



The
University
Of
Sheffield.

Access to Electronic Thesis

Author: Andrew James Pearson
Thesis title: Correlating Structure with Optoelectronic Functionality in Polymer:
Fullerene Blend Films
Qualification: PhD

This electronic thesis is protected by the Copyright, Designs and Patents Act 1988. No reproduction is permitted without consent of the author. It is also protected by the Creative Commons Licence allowing Attributions-Non-commercial-No derivatives.

If this electronic thesis has been edited by the author it will be indicated as such on the title page and in the text.

Correlating Structure with Optoelectronic Functionality in Polymer:Fullerene Blend Films

Andrew James Pearson

Department of Physics and Astronomy
University of Sheffield



The
University
Of
Sheffield.

Thesis submitted for the degree of
Doctor of Philosophy

April 2012

Declaration

The work presented in this thesis was carried out between October 2008 and December 2011. All data is my own except where explicitly stated. This thesis has not been submitted in whole or in part for a degree at this or any other University. It does not exceed 50,000 words in length.

Andrew Pearson, April 2012

ACKNOWLEDGEMENTS

I would not have been able to undertake a PhD were it not for the help of so many others: friends, family and work colleagues. First and foremost I wish to thank Frazer Pearce at the University of Nottingham, a tutor who persistently suggested going onto a PhD after I graduated. Well, here I am! Without your confidence I would not be in this position today. And to my supervisor David Lidzey, thank you for giving me the opportunity to study in your group, your guidance and most importantly of all your words of encouragement over three and a half years.

When I first arrived at the Physics Department, it was the students, post-docs and staff that trained and guided my work in the labs. Your continued support and combined ability to never provide a dull moment have been of enormous value to me. To James, David Mohamed, David Coles, Karen, Ben, Francesca, Ashley, Paul, Tao, Darren, Adam, Jonathan, Alan, Andy and Nic, for all of the meals, after-work drinks, movie nights and BBQ's, cheers!

To my parents and grandparents, thank you for all your love and support and for having faith in me to pursue this degree. To grandad, thank you for giving me the inspiration to consider a career in research. To my sisters Gemma and Magenta, thank you for showing me that I don't have to grow up as I grow old. I'm so proud to have all of you as family.

To my friends, as much as it's true that each PhD is a course for one I honestly wouldn't have been able to get this far without all of you. Thank you so much for being there for me, getting me through the lows and building me back up again so that I can enjoy the highs, with so many cups of tea along the way. To Amanda, Helen, Russell and Deja, thank you for helping me find my feet when I first moved here, and for keeping them grounded since.

Helen and Amanda, you're simply awesome. Amanda, I cannot thank you enough for introducing me to climbing.

To Kate, thank you for reaching out to me when you did. I think I'm slowly getting better! To Jon, Barry, Alex, Emily and Des, thank you for letting me be part of the walking club with you. Realising the beauty that sits on Sheffield's doorstep, and further afield too, has been a source of endless joy for me. To Lauren, Pete, Hugh, Chris, Mahati, Christine, Joseph, Kiri and Helen, thank you for welcoming me into the post-graduate society with such kindness and for giving me so many warm memories.

To Mahati, Chris, Christine and Hugh, I hope you understand why I always have done and always will say 'thank you' for your time. It really is that special.

And lastly to Becky, thank you for being wonderful and for making the last few months some of the happiest I've ever known.

ABSTRACT

In this thesis the influence of processing conditions on the structure and optoelectronic properties of conjugated polymer:methanofullerene blend thin-films has been investigated. These conditions strongly impact upon the efficiency with which blend films may produce a photocurrent when fabricated into an Organic Photovoltaic (OPV) device. Using the model system P3HT:PCBM, it is shown that films undergo a three-stage drying process upon casting. Heterogeneous growth of P3HT crystallites occurs once the solid fraction in the film exceeds 50 wt%. Measurements from spectroscopic ellipsometry (SE) and grazing-incidence wide-angle X-ray scattering (GIWAXS) suggest a correspondence between enhanced polymer crystallinity and the strength of the π - π^* electronic transition in the polymer absorption spectrum. In-situ measurements of a blend during thermal annealing evidence the evolution of residual solvent loss upon heating, volume relaxation, phase separation and increased electronic conjugation of P3HT upon cooling. The glass transition of P3HT:PCBM blend films, measured in a thin-film geometry, is found to correlate with the minimum effective annealing temperature for improving the power conversion efficiency of thermally annealed OPVs. As-cast films with 20 to 60 wt% PCBM exhibit two glass transitions, an observation that may indicate the existence of two compositionally distinct amorphous phases. Studies on a different polymer:fullerene blend system (PCDTBT:PC₇₁BM), indicate a greater miscibility between materials compared to blends of P3HT:PCBM. In this system, thermal annealing is found to result in increased disorder in the polymer phase of the film, and also to drive excessive phase separation of PC₇₁BM. It is argued that thermal annealing is unlikely to be an appropriate treatment for optimising the efficiency of OPVs based on PCDTBT:PC₇₁BM blends. Finally, Helium Ion Microscopy (HeIM) is used to image the chemical composition of OPV applicable blend films with nanometer resolution, providing a powerful technique to correlate film morphology with device functionality in a range of organic opto-electronic devices.

PUBLICATIONS

1. Kingsley, J. W.; Pearson, A. J.; Harris, L.; Weston, S. J.; Lidzey, D. G., Detecting 6 MV X-rays using an organic photovoltaic device. *Org. Electron.* 2009, 10 (6), 1170-1173.
2. Parnell, A. J.; Dunbar, A. D. F.; Pearson, A. J.; Staniec, P. A.; Dennison, A. J. C.; Hamamatsu, H.; Skoda, M. W. A.; Lidzey, D. G.; Jones, R. A. L., Depletion of PCBM at the Cathode Interface in P3HT/PCBM Thin Films as Quantified via Neutron Reflectivity Measurements. *Advanced Materials* 2010, 22 (22), 2444-2447.
3. Wang, T.; Dunbar, A. D. F.; Staniec, P. A.; Pearson, A. J.; Hopkinson, P. E.; MacDonald, J. E.; Lilliu, S.; Pizzey, C.; Terrill, N. J.; Donald, A. M.; Ryan, A. J.; Jones, R. A. L.; Lidzey, D. G., The development of nanoscale morphology in polymer: fullerene photovoltaic blends during solvent casting. *Soft Matter* 2010, 6 (17), 4128-4134.
4. Hopkinson, P. E.; Staniec, P. A.; Pearson, A. J.; Dunbar, A. D. F.; Wang, T.; Ryan, A. J.; Jones, R. A. L.; Lidzey, D. G.; Donald, A. M., A Phase Diagram of the P3HT:PCBM Organic Photovoltaic System: Implications for Device Processing and Performance. *Macromolecules* 2011, 44 (8), 2908-2917.
5. Wang, T.; Pearson, A. J.; Lidzey, D. G.; Jones, R. A. L., Evolution of Structure, Optoelectronic Properties, and Device Performance of Polythiophene: Fullerene Solar Cells During Thermal Annealing. *Advanced Functional Materials* 2011, 21 (8), 1383-1390.
6. Staniec, P. A.; Parnell, A. J.; Dunbar, A. D. F.; Yi, H. N.; Pearson, A. J.; Wang, T.; Hopkinson, P. E.; Kinane, C.; Dalgliesh, R. M.; Donald, A. M.; Ryan, A. J.; Iraqi, A.; Jones, R. A. L.; Lidzey, D. G., The Nanoscale Morphology of a PCDTBT: PCBM Photovoltaic Blend. *Advanced Energy Materials* 2011, 1 (4), 499-504.
7. Pearson, A. J.; Boden, S. A.; Bagnall, D. M.; Lidzey, D. G.; Rodenburg, C., Imaging the Bulk Nanoscale Morphology of Organic Solar Cell Blends Using Helium Ion Microscopy. *Nano Letters* 2011, 11 (10), 4275-4281.
8. Pearson, A. J.; Wang, T.; Jones, R. A. L.; Lidzey, D. G.; Staniec, P. A.; Hopkinson, P. E.; Donald, A. M., Rationalizing Phase Transitions with Thermal Annealing Temperatures for P3HT:PCBM Organic Photovoltaic Devices. *Macromolecules* 2012, 45 (3), 1499-1508.
9. Wang, T.; Pearson, A. J.; Dunbar, A. D. F.; Staniec, P. A.; Watters, D. C.; Yi, H.; Ryan, A. J.; Jones, R. A. L.; Iraqi, A.; Lidzey, D. G., Correlating Structure with Function in Thermally Annealing PCDTBT:PCBM Photovoltaic Blends. *Advanced Functional Materials* 2012, 22 (7), 1399-1408

CONFERENCE PRESENTATIONS

European Optical Society Annual Meeting (EOSAM). Paris, France. October 2010
(Oral Presentation)

European Materials Research Society (E-MRS) Spring Meeting. Nice, France. May
2011 (Poster Presentation)

Opto-Electronic Processes in Organic Materials (OEPOM). Oxford, UK. April 2011
(Poster Presentation)

Materials Research Society (MRS) Spring Meeting. San Francisco, USA. April 2012
(Poster Presentation)

CONTENTS

Chapter 1: Introduction

1.1: Thesis Summary and Motivation.....	5
1.2: References.....	7

Chapter 2: Background

2.1: Introduction.....	9
2.2: Electronic Characteristics of Hybridised Carbon Bonds.....	9
2.2.1: Electronic Properties of Fullerenes.....	14
2.3: Photoexcitation of Conjugated Polymers.....	15
2.4: Photocurrent Generation in Organic Photovoltaic Devices.....	23
2.4.1: Exciton Diffusion.....	23
2.4.2: Exciton Dissociation.....	24
2.4.3: Charge Transport.....	28
2.4.4: Charge Extraction and Injection.....	33
2.4.5: Space Charge Limited Current.....	35
2.5: Characterising OPV Device Efficiency.....	37
2.6: Influence of Active Layer Materials and Nanostructure of the Efficiency of Organic Photovoltaic Devices.....	41
2.7: References.....	54

Chapter 3: Methods

3.1: Introduction.....	65
3.2: Materials, Solution and Thin film Preparation.....	65
3.3: Device Preparation.....	69
3.4: Experimental Techniques	
3.4.1: UV-Visible Spectroscopy.....	71
3.4.2: Atomic Force Microscopy.....	74
3.4.3: Spectroscopic Ellipsometry.....	76
3.4.4: Grazing Incidence Wide Angle X-Ray Scattering.....	79
3.4.5: Device Characterisation.....	85
3.4.6: Helium Ion Microscopy.....	87
3.4.7: Neutron Reflectivity.....	88

3.4.8: Dynamic Mechanical Thermal Analysis.....	89
---	----

Chapter 4: In-Situ Characterisation of Blend Thin Film Formation & Influence of the Casting Solvent on Device Performance of P3HT:PCBM OPVs

4.1: Introduction.....	91
4.2: The Evolution of Structure During Thin film Formation.....	93
4.3: Influence of the Casting Solvent on OPV Device Efficiency.....	105
4.4 Conclusions.....	116
4.5 References.....	117

Chapter 5: Evolution of Structure and Optoelectronic Properties of P3HT:PCBM Blend Thin Films During Thermal Annealing

5.1: Introduction.....	121
5.2: Monitoring Thickness Changes During a Thermal Annealing Cycle Using Spectroscopic Ellipsometry.....	122
5.3: Optical Characteristics of Films During Thermal Annealing.....	133
5.4: Photovoltaic Properties of P3HT:PCBM Thin films.....	141
5.5: Conclusions.....	144
5.6: References.....	146

Chapter 6: Rationalising Phase Transitions with Thermal Annealing Temperatures for P3HT:PCBM OPV Devices

6.1: Introduction.....	149
6.2: Impact of Thermal Annealing on the Photovoltaic Efficiency of P3HT:PCBM OPV Devices.....	151
6.3: Origin of the Minimum Effective Annealing Temperature.....	157
6.4: Origin of the Optimum Annealing Temperature.....	168
6.5: Conclusions.....	177
6.6: References.....	178

Chapter 7: Correlating Phase Behaviour with Optical and Electronic Properties in PCDTBT:PC₇₀BM OPV Devices

7.1: Introduction.....	183
7.2: Optical and Structural Properties of PCDTBT Thin films.....	186
7.3: Optical, Structural and Electronic Properties of PCDTBT:PC ₇₀ BM Blend Thin films.....	189
7.4: Influence of Thermal Annealing on Film Nanostructure and Photovoltaic Properties of PCDTBT:PC ₇₀ BM Blends.....	200
7.5: Determining the Onset of PC ₇₀ BM Aggregation in PCDTBT:PC ₇₀ BM Blend Thin films.....	213
7.6: Conclusions.....	220
7.7: References.....	221

Chapter 8: Imaging the Bulk Nanoscale Morphology of Solar Cell Blends Using Helium Ion Microscopy

8.1: Introduction.....	226
8.2: Identifying the Origin of Contrast in HeIM Images.....	228
8.3: Calculating the Domain Size in P3HT:PCBM Blend Thin films from HeIM Measurements.....	236
8.4: Conclusions.....	244
8.5: References.....	245

Chapter 9: Conclusions.....	248
-----------------------------	-----

Appendix.....	252
---------------	-----

CHAPTER 1: INTRODUCTION

Renewable energy technologies are at the forefront of an international effort to transition the global economy away from fossil fuels as its primary energy source. The motivation for this is two-fold, (1) the finite supply of conventional fuels (e.g. coal, oil and natural gas) and (2) the negative impact of these fuels on the environment ¹. The term ‘renewables’ can be ascribed to a wide range of energy sources, including wind, biomass and hydroelectric. Arguably, however, it is energy converted directly from sunlight, i.e. photovoltaics and solar thermal, that has the greatest potential to meet a significant fraction of global energy demand. This is primarily due to the fact that sunlight can theoretically provide vastly more energy than global consumption compared to wind or biomass. Thus only a small fraction needs to be ‘harvested’ in order to meet demand ². The power density (i.e. the energy converted per unit area) of the technology is also believed to be greater. As an example, it is estimated that to power the city of San Jose in California (population 1,000,000) through a single renewable energy source, an area equal to one sixth of the city size would need to be covered using a photovoltaic energy system, compared to an area ~1.1 times as large for wind and 6 times as large for biomass ². Whilst it is clear that in practice, a mix of sources will be required to adequately meet our energy needs (due to intrinsic variations in power output for each), solar power is likely to provide the largest contribution ³. Indeed, the significant potential of solar power has led to it being the primary technology for the Desertec initiative which aims to build an infrastructure for renewable energy generation across Europe and North Africa ⁴.

Photovoltaic (PV) technologies are appealing since a large amount of mankind's energy consumption is in the form of electricity. The first practical demonstration of the technology was at Bell Labs³, where a silicon based solar cell achieved a power conversion efficiency (PCE) of approximately 6%. Subsequent research has focused on increasing the PCE of devices whilst reducing their cost in order to compete economically with conventional energy sources. The efficiency of a PV device is ultimately limited by the amount of light absorbed that can subsequently generate a photocurrent. Figure 1.1 presents a standardised spectral profile of sunlight incident upon the Earth's surface overlaid with the integrated solar flux.

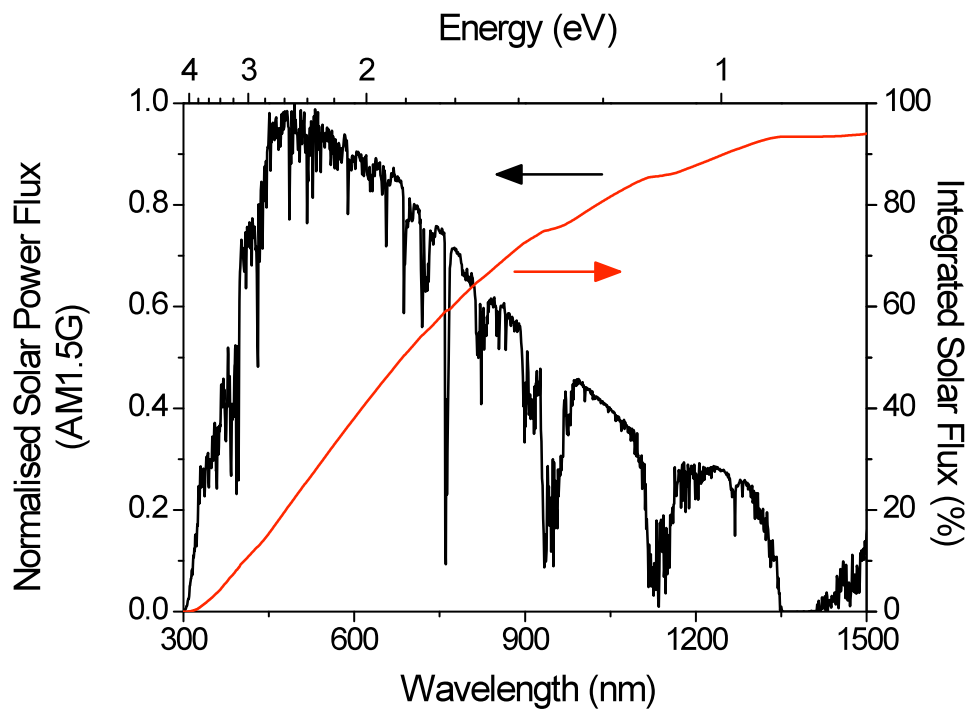


Figure 1.1: Profile of the AM1.5 G solar spectrum over the wavelength region 300-1500 nm (photon energies of 4.13 to 0.82 eV). The integrated flux is overlaid in red. Note the absolute maximum power density is $\sim 1.6 \text{ Wm}^{-2}$ at 495 nm.

The solar spectrum extends through to the infra-red ($\sim 4 \mu\text{m}$). It can be seen from Figure 1.1 however that over 90% of the total solar flux occurs at a wavelength below 1300 nm. However, owing to the necessity of a PV to provide power, the optimum band-gap for a single junction solar cell is in the region of 1.1-1.4 eV in order to balance photocurrent with photovoltage⁵. Single crystal silicon, having a band-gap of 1.1 eV is a semiconductor well suited for PV application. Because it has an indirect band-gap, however, thick layers ($\sim 100 \mu\text{m}$) are needed to provide an adequate optical density. In order to reduce the volume of material used in a practical application, thin-film ($\sim 10 \mu\text{m}$) PV utilising direct band-gap semiconductors (e.g. amorphous silicon, GaAs and CdTe) have been developed. Silicon based PV remains the most popular commercial technology owing to the larger raw material availability and greater processing infrastructure.

Inorganic semiconductors are well suited for large-scale PV arrays and in solar concentrator devices due to their ability to withstand high temperatures. Organic semiconductors, either conjugated polymers or small molecules, have been developed as an alternative PV material, particularly for applications where mechanical flexibility and semi-transparency may be required⁶. Perhaps the biggest cost advantage of Organic Photovoltaics (OPVs) is the ability of the active semiconducting materials to be processed from solution, thereby offering the potential for large volume manufacture using, for example, reel-to-reel printing techniques⁷. The absorption coefficients of these materials ($\sim 10^5 \text{ cm}^{-1}$) are much larger than the absorption coefficients of inorganic semiconductors. This advantage offsets the relatively low mobility of charge carriers in organic semiconductors with active layers of only $\sim 100\text{-}200 \text{ nm}$ in thickness being necessary for OPVs with high PCE, meaning

that far less material is needed in the device fabrication process compared to inorganic thin-film PV.

A fundamental difference between OPVs and conventional inorganic solar cells is the nature of the photoexcited state. Instead of free charge generation following absorption of a photon, light absorption typically creates a bound electron-hole pair (termed an exciton) in an organic semiconductor. In order to be useful for photocurrent generation, a relatively large internal field must exist within the semiconducting layer to dissociate this state. To create high efficiency OPVs, this is achieved by blending two semiconductors with differing electron affinities (thus acting as a molecular scale heterojunction). Following exciton dissociation, charge transport occurs through the p-type semiconductor (for the hole) and through the n-type semiconductor (for the electron) towards the electrodes of the device. Whilst OPVs have not yet reached the level of technological maturity sufficient for their widespread commercialisation (i.e. by combining high efficiency, long lifetime and low cost), rapid growth in the research and development of OPVs has occurred over the past decade. Current results are promising; using proprietary materials, OPVs with a power conversion efficiency of 10% have recently been measured for a 1 cm² device, and a PCE of over 4% has been measured for a module cell with an area of 294.5 cm², approximately the size of an A5 sheet of paper ⁸. In the literature, the published record PCE now stands at over 8% ⁹ for a device with an active area of 0.16 cm². OPVs with lifetimes approaching seven years have also been demonstrated ¹⁰.

A current trend in OPV research is the design and synthesis of organic semiconductors having low energy-gaps, in order to extend their photosensitivity into the IR region of the solar spectrum and thus harvest more sunlight (c.f. Figure 1.1). The breadth of materials available presents two challenges. From an applied perspective, the challenge is to understand the interdependence between the molecular structures of these semiconductors and the processing protocols (i.e. design rules) needed to optimise the active layer structure (or ‘morphology’) and therefore maximise the power conversion efficiency and operational stability of a fully fabricated OPV. Of equal importance, however, is to understand the fundamental processes by which photocurrent generation occurs, and how this may be influenced by film structure.

SECTION 1.1: THESIS SUMMARY AND MOTIVATION

The purpose of this thesis is to develop our understanding of the mechanisms of film structure formation and modification of a PV applicable thin organic film and to understand how this impacts upon the photovoltaic efficiency of an OPV device. The structure of this thesis is as follows. In chapter 2 the necessary background is presented, giving an overview of semiconducting behaviour in conjugated systems and outlining the steps involved in photocurrent generation. A brief literature review is also included to highlight the major developments in the research field. The experimental methods used in this work are described in chapter 3.

In chapter 4, it is shown from *in-situ* measurements how film formation in a polythiophene:methanofullerene (P3HT:PCBM) blend film occurs over a three stage process. The results indicate the existence of an intermediate stage in the drying process that is responsible for significant self-organisation in the film. This stage occurs when the concentration of solids in the drying solution exceeds a certain threshold weight concentration. Furthermore, this process limits the degree to which further improvements can be expected in OPV device performance.

Chapters 5 and 6 present the effects of thermal annealing for modifying the structure of P3HT:PCBM blend thin-films. By monitoring the process of thermal annealing *in-situ*, the effects of heating, isothermal annealing and cooling can be identified. The loss of trapped solvent in the blend film, by heating a film above its blend glass transition temperature, permits us to gain a rational insight into the effects of thermal annealing at low temperatures. Later it is shown how the glass transition itself is influenced by blend composition, a result that indicates a strong correlation between this transition and the minimum temperature necessary to drive self-organisation in blend films and generate improved photovoltaic properties. These chapters permit us to develop a rational framework by which to design annealing protocols in new and as yet unexplored OPV blends.

In chapter 7 the role of thermal annealing in modifying film structure of a poly(2,7-) carbazole:fullerene (PCDTBT:PCBM) blend system is investigated. This blend exhibits promising thermal stability against excessive phase separation. However, it is found that thermal annealing does not apparently improve the photovoltaic properties

of this blend, instead it acts as a driving force for increased disorder in the polymer phase of the films. In contrast to blends of P3HT:PCBM, fullerene molecules are relatively more miscible in PCDTBT and quench photoexcitations generated on the polymer with greater efficiency.

Finally, in chapter 8, the use of Helium Ion Microscopy (HeIM) for imaging the nanoscale structure of P3HT:PCBM blend thin-films is evaluated. It is shown that the mechanism for contrast in HeIM is strongly influenced by the chemical distribution of P3HT and PCBM, and can therefore provide a measure of the length-scale for phase separation in films optimised for photocurrent generation.

REFERENCES

1. (a) Parry, M. L., *Climate change 2007 : impacts, adaptation and vulnerability : contribution of Working Group II to the fourth assessment report of the Intergovernmental Panel on Climate Change*. Cambridge University Press: Cambridge, 2007; p ix, 976 p; (b) Metz, B., *Climate change 2007. Mitigation of climate change : contribution of Working Group III to the Fourth assessment report of the Intergovernmental Panel on Climate Change*. Cambridge University Press: Cambridge, 2007; p x, 851 p.
2. Cho, A., Energy's Tricky Tradeoffs. *Science* **2010**, 329 (5993), 786-787.
3. Kerr, R. A., Do We Have the Energy For the Next Transition? *Science* **2010**, 329 (5993), 780-781.

4. Clery, D., Sending African Sunlight To Europe, Special Delivery. *Science* **2010**, 329 (5993), 782-783.
5. (a) Shockley, W.; Queisser, H. J., DETAILED BALANCE LIMIT OF EFFICIENCY OF P-N JUNCTION SOLAR CELLS. *Journal of Applied Physics* **1961**, 32 (3), 510-&; (b) Scharber, M. C.; Wühlbacher, D.; Koppe, M.; Denk, P.; Waldauf, C.; Heeger, A. J.; Brabec, C. L., Design rules for donors in bulk-heterojunction solar cells - Towards 10 % energy-conversion efficiency. *Advanced Materials* **2006**, 18 (6), 789-794.
6. Krebs, F. C.; Jorgensen, M.; Norrman, K.; Hagemann, O.; Alstrup, J.; Nielsen, T. D.; Fyenbo, J.; Larsen, K.; Kristensen, J., A complete process for production of flexible large area polymer solar cells entirely using screen printing-First public demonstration. *Solar Energy Materials and Solar Cells* **2009**, 93 (4), 422-441.
7. Krebs, F. C., Fabrication and processing of polymer solar cells: A review of printing and coating techniques. *Solar Energy Materials and Solar Cells* **2009**, 93 (4), 394-412.
8. Green, M. A.; Emery, K.; Hishikawa, Y.; Warta, W.; Dunlop, E. D., Solar cell efficiency tables (Version 38). *Progress in Photovoltaics* **2011**, 19 (5), 565-572.
9. He, Z. C.; Zhong, C. M.; Huang, X.; Wong, W. Y.; Wu, H. B.; Chen, L. W.; Su, S. J.; Cao, Y., Simultaneous Enhancement of Open-Circuit Voltage, Short-Circuit Current Density, and Fill Factor in Polymer Solar Cells. *Advanced Materials* **2011**, 23 (40), 4636-4643.
10. Peters, C. H. S.-Q., I. T. ; Kastrop, J. P. ; Beaupre, S. ; Leclerc, M. ; McGehee, M. D. ;, High Efficiency Polymer Solar Cells with Long Operating Lifetimes. *Advanced Energy Materials* **2001**, 1 (4), 491-494.

CHAPTER 2: BACKGROUND

SECTION 2.1: INTRODUCTION

In this chapter some of the physical properties and phenomena exhibited by the materials studied in this thesis are discussed. Starting from the origin of semiconducting behaviour in conjugated polymers in Section 2.2, a brief overview of the photophysics in organic semiconductors is presented in Section 2.3. In Section 2.4 a model is constructed to explain the working principles of a photovoltaic device and to highlight the key factors that determine the efficiency of photocurrent generation. Section 2.5 considers how the points discussed in all preceding sections impact upon the efficiency of an Organic Photovoltaic Device (OPV). Finally, Section 2.6 contains a brief review of key results from the literature that have developed the understanding of organic photovoltaics and increased the efficiency of OPV devices towards the level deemed necessary for widespread commercial adoption.

SECTION 2.2: ELECTRONIC CHARACTERISTICS OF HYBRIDISED CARBON BONDS

The building block for all organic materials is carbon. Of the six electrons present in the neutral atom (adopting the configuration $1s^2 2s^2 2p^2$), the outermost four participate in chemical bonding. Upon bonding with other carbon atoms to form a molecule, the nature of the bonds alters to lower the total energy of the system. The precise nature of these *hybrid* bonds determine whether the molecule exhibits insulating or semiconducting behaviour.

Before hybridisation of the carbon bonds it is necessary to promote one electron from the $2s$ orbital into the $2p$ orbital. The resulting configuration then becomes $1s^2 2s^2 2p^3$. From here, the s and p orbitals may combine to form four sp^3 hybrid orbitals, which adopt a tetragonal structure. Figure 2.1 presents the structure of polyethylene, arguably the simplest polymer to adopt this type of hybrid bonding. A simplified structure is presented here, in practice the true bond angles are $\sim 110^\circ$ between atoms.

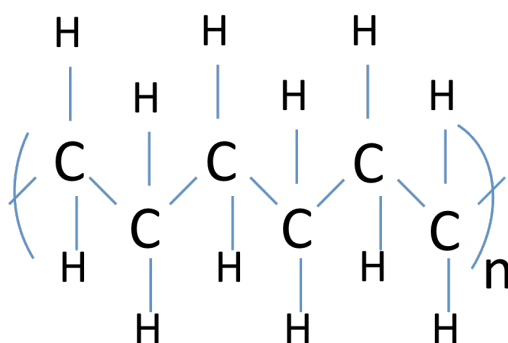


Figure 2.1: The chemical structure of polyethylene. Here each carbon atom forms four bonds, two to neighbouring carbon atoms and two to hydrogen atoms. The bond lengths between atoms are approximately 0.154 \AA (C-C) and 0.110 \AA (C-H).

The hybrid bonding structure presented above is insulating as all valence (outermost) electrons are covalently bound and immobile. Conducting behaviour is achieved by an electron in the $2s$ orbital hybridising with 2 electrons from the $2p$ orbital to form three sp^2 hybrid orbitals. These bonds form a planar structure, each separated 120° apart from each other. These σ bonds form the backbone of any molecular structure (example structures of benzene and polyacetylene are shown in Figure 2.2). Critically, the remaining p orbital orientates perpendicular to the plane of the sp^2 σ bonds (for simplicity it is referred hereafter as a p_z orbital, the sp^2 bonds aligning in the x,y plane).

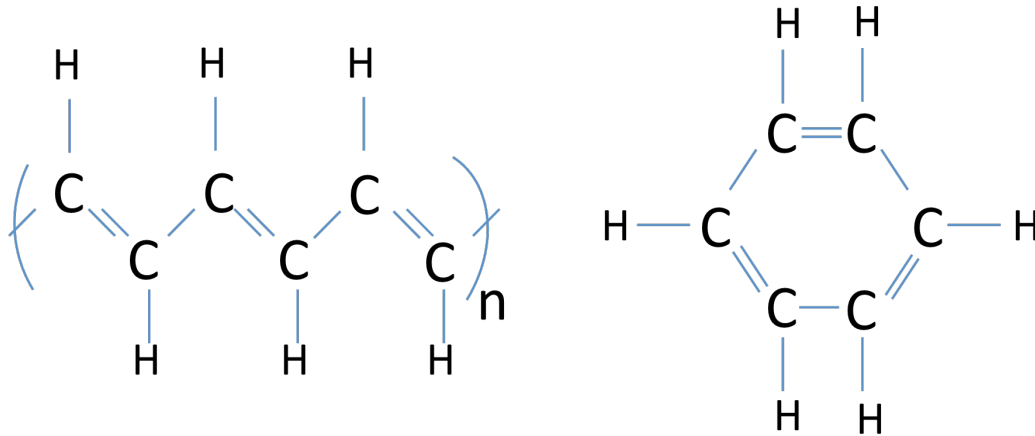


Figure 2.2: The chemical structures of polyacetylene (left) and benzene (right). Note that the p_z orbitals will orientate perpendicular to the page. The bond lengths between adjacent carbon atoms are approximately 0.147 Å.

In a molecule, the p_z orbitals combine to form a π bond, the electron density remaining above and below the plane of the σ bonds. Whereas the density of electrons in a σ bond are highly localized, π electrons can be relatively delocalised across several neighboring molecular units. Systems in which sp^2p_z hybridised carbon bonds form chains of alternating single and double bonds are said to be conjugated, with electrons belonging to the p_z orbitals delocalising across neighbouring aligned molecules. Thus it is not possible to associate a π electron with a single atom; rather they belong to a group of atoms. It is the properties of these π electrons that determine the electronic and optical properties of the material.

So far only the bonding orbitals of organic semiconductors have been considered. Hereafter the nature of antibonding orbitals are discussed in order to develop the band structure of these materials. This permits us to understand the processes of photoexcitation that are discussed in the following section. The simplest system for understanding electronic behaviour in solids is

a crystal; i.e. a structure with a well-defined periodicity. For a crystal with many atoms present, and where electrons may be shared between neighbouring atoms, conservation laws lead to the development of a *band* structure in momentum (k) space which governs the allowed states for delocalised electrons¹. Revisiting the structure of polyacetylene in Figure 2.2, it is clear that if the chain is initially empty of electrons, any electrons added would occupy the lowest energy states closest to the polymer backbone. Thus they would be highly localised. As more electrons are added to the structure, thereby tending it towards its neutral state, they reside further from the parent nuclei. The outermost electrons define the highest occupied molecular orbital (HOMO) level. This is analogous to the valence band present in inorganic semiconductors. The top of the HOMO level corresponds to the ionisation potential (I_P) of the molecule. By definition the band immediately above the HOMO level is the lowest unoccupied molecular orbital (LUMO) level. These are antibonding orbitals as the electron wavefunctions combine out-of-phase, lowering the electrostatic attraction between the negative charge of the electrons and the positively charged atomic nuclei. Consequently antibonds raise the potential energy of the system and cause it to become relatively unstable. Here, the bottom of the LUMO level corresponds to the electron affinity (E_A). Again in analogy to inorganic semiconductors the LUMO level can be viewed in a similar way to a conduction band. It is important to recognise that both σ and π bonds have associated HOMO and LUMO levels. For σ bonds, however, moving an electron into an antibonding σ^* orbital (the LUMO level) will cause structural instability and possibly degradation of the polymer. In π bonds, however, moving an electron into an antibonding π^* orbital results in the structural integrity being maintained as these transitions are of lower energy than $\sigma - \sigma^*$ transitions. Consequently it is these $\pi - \pi^*$ transitions that are interesting from a technological perspective.

It is apparent that if polyacetylene were truly characterised by carbon-carbon bonds of constant length, it would act as a 1-dimensional metal owing to the delocalization of electrons along the chain. Experimentally however polyacetylene bears all the characteristics of a semiconductor. This inconsistency, i.e. the assumption of structural stability in a 1-D metal, results from an over-simplification of the true structure of conjugated polymer chains. Polyacetylene and other conjugated polymer backbones instead form a dimerised structure, whereby $\pi - \pi$ bonds alternate between being relatively weak and relatively strong. In polyacetylene these bond lengths have been measured and found to vary between $\sim 1.35\text{\AA}$ and 1.45\AA ². The characteristic is known as Peierls instability³, with the displacement of atoms leading to an energy gap opening at the Fermi level. The magnitude of the gap is proportional to the extent of the displacement. The energy ‘cost’ of distorting the lattice is recovered by a decrease in the total energy of the valence electrons. Dimerised polyacetylene is therefore stable and semiconducting with a band gap of approximately 1.4 eV ⁴.

Although this discussion provides a first principles description of the origin for semiconducting behaviour in conjugated materials, the true behaviour is perhaps understandably more complex. Conjugated systems, including those explored in this thesis, are typically disordered (for example through chain entanglement) and therefore the concept of a well-defined electronic band structure, as is the case for inorganic semiconductors, is not applicable here. Due to disorder the electron states become further localised and transitions between bands become ‘broader’ and less well defined. A second feature of organic semiconductors is the relatively strong coupling interaction between the chemical structure of the molecule (i.e. the atomic lattice) and the excited state that can lead to the formation of pseudoparticles e.g. polarons. These describe the coupling between a charge carrier and the deformation and resulting polarisation of the atomic lattice.

SECTION 2.2.1: ELECTRONIC PROPERTIES OF FULLERENES

Fullerenes are an allotrope of carbon first synthesised by Kroto *et al.* in 1985⁵. The first structure formed was C₆₀ (buckminsterfullerene), named after the geodesic spheres that it resembles. Although fullerenes are commonly considered as small molecules, it is important to recognise that bonding between carbon atoms in C₆₀ and higher fullerenes occurs via sp^2 hybridisation. Fullerenes can therefore be considered as conjugated, albeit with a caged instead of an elongated chain structure. The p_z π bonds in C₆₀ orientate perpendicular to the fullerene cage, thus the delocalization of electrons occurs above and below the entire carbon cage. Two LUMO levels, approximately 1.5 to 2 eV above their respective HOMO levels are responsible for most of the photophysics involving this molecule⁶. Each level is triply degenerate, thus each C₆₀ molecule is capable of accepting up to six electrons. As will be discussed in Section 2.6 this makes C₆₀ a strong acceptor material in OPVs.

SECTION 2.3: PHOTOEXCITATION OF CONJUGATED POLYMERS

Photoexcitation describes the process in which a photon interacts with a semiconductor having sufficient energy to promote an electron into an excited state. An alternative definition is *photoinduced doping*, since mobile charges can result from the process ^{3a}.

Consider the potential energy level diagram in Figure 2.3, which shows the ground state and first excited state for an idealised system. The lowest energy curve represents the ground state (HOMO level) of the molecule, with the higher energy curve corresponding to the first excited state (LUMO level). Vibrational energy levels within each state are illustrated by dashed lines. Note that the minima of each curve corresponds to the equilibrium bond length between molecules in that state.

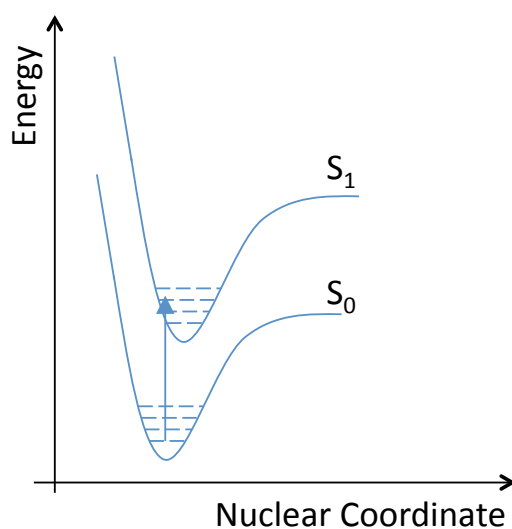


Figure 2.3: Energy level diagram illustrating the ground and first excited states of a molecule. Dashed lines correspond to vibrational energy levels within each state, whilst the vertical arrow illustrates an electronic transition.

It can be seen that if a photon with energy equal to or greater than the energy gap between the HOMO and LUMO levels is absorbed an electron will be promoted into the LUMO level, leaving a hole residing in the HOMO level. According to the Frank-Condon principle this transition is defined by a vertical arrow in Figure 2.3. As nuclear motion occurs over much slower time scales than electronic transitions, the nuclei can be considered stationary upon photoexcitation of electrons ⁷. If the energy of the photon exceeds the energy gap between HOMO and LUMO, an electron will be initially promoted into one of the vibrational modes of the energetic state. These states can be labeled $S_{1,m}$ (taking vibrational modes in the first excited state as an example) where m is an integer.

The bound electron-hole pair created through photoexcitation is termed an exciton. This excited state is overall electrically neutral and, owing to the generally high spatial localisation of the state, will recombine on a typical timescale of 1 ns. Preceding this step is a rapid (approximately 1 ps or less) radiationless relaxation of the excited state towards the lowest vibronic energy level. From here a photon may be re-emitted in a process called fluorescence. Note that this occurs at the same or lower energy than the excitation (i.e. it is Stokes shifted) due to the internal relaxation process described previously. To illustrate this process, the absorption and fluorescence spectra from perylene dissolved in cyclohexane ⁸ is presented in Figure 2.4.

For photocurrent generation (discussed in more detail in Section 2.4) the exciton is composed of the charges that can potentially be extracted from a device. However the relatively short lifetime of the state makes it relatively difficult to separate into a free electron and hole. In order to achieve this, an amount corresponding to the binding energy E_B of the exciton must

be expended. The magnitude of E_B will be determined by the Coulombic attraction between the charges and interactions between the exciton and the atomic lattice (i.e. polaron interactions). For example, the excited state on a phenylene – vinylene chain leads to a relaxation of the benzene structure into a quinodal structure in the vicinity of the exciton. The magnitude of the distortion is greatest in the middle of the exciton, as illustrated in Figure 2.5.

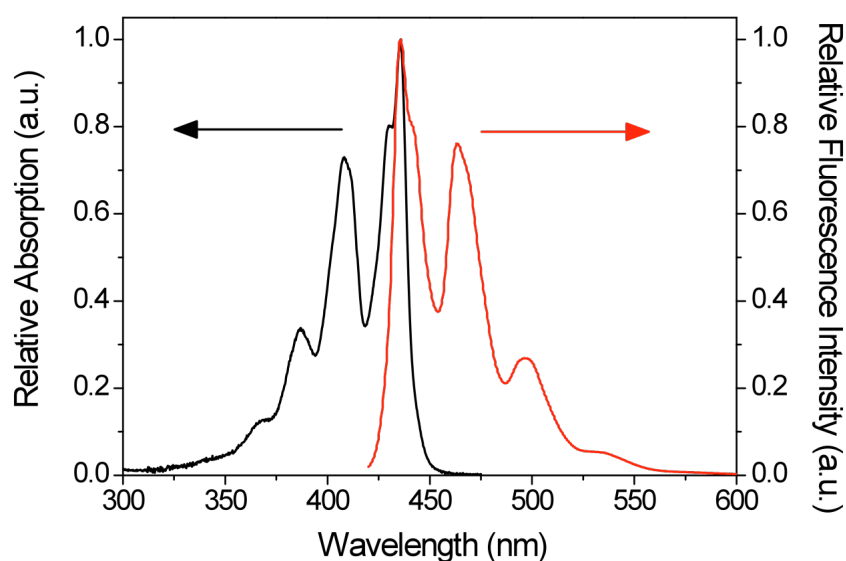


Figure 2.4: Absorption and fluorescence spectra of perylene dissolved in cyclohexane, using data provided by the PhotochemCAD library⁸. Emission was collected after excitation at 410 nm. The peak at 430 nm corresponds to the principle transition between the lowest vibrational levels of the ground and first excited state. Transitions between modes of higher vibrational energy manifest themselves as peaks at relatively lower intensity.

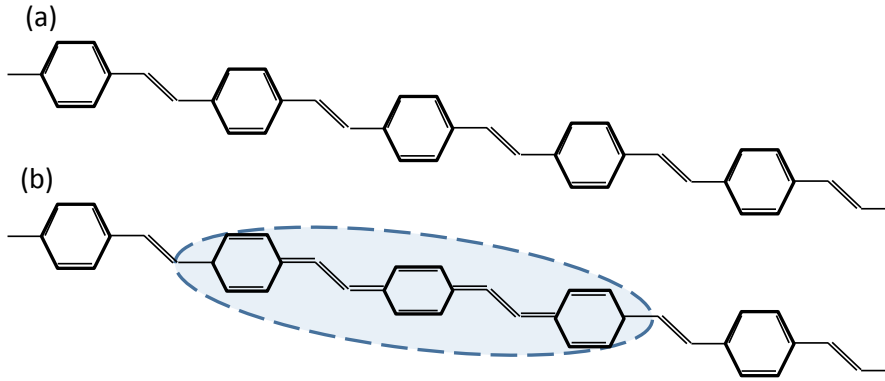


Figure 2.5: (a) the chemical structure of phenylene-vinylene in the ground state. If excited, the presence of an exciton, illustrated by the blue ellipse in (b), distorts the atomic lattice from an aromatic into a quinodal structure.

The relatively strong exciton coupling to the atomic lattice is one reason why excitons are relatively difficult to dissociate in organic semiconductors. A second reason is the relatively low dielectric constant ϵ_r of these materials, which is approximately 3-4⁹. In inorganic semiconductors ϵ_r is much higher (~ 12 for silicon¹⁰), consequently the Coulombic attraction between charges is efficiently screened in these materials. The relatively large dielectric constant in inorganic semiconductors and the delocalisation of the exciton results in a low binding energy. Excitons of this character are sometimes referred to as Mott-Wigner excitons. Excitons that are characterised by a large binding energy and relatively high degree of localisation are in contrast termed Frenkel excitons. For an inorganic semiconductor photovoltaic device operating at ambient temperatures, the thermal energy $k_B T$ (~ 25 meV at 300 K) is sufficient to dissociate the exciton. Consequently the primary photoexcited states in inorganic semiconductors are commonly considered as free charge carriers and exciton physics is generally of limited relevance. In contrast, the binding energy for excitons in organic semiconductors has been measured to be of the order of 0.3 eV¹¹ and therefore

Frenkel excitons cannot dissociate via ambient thermal energies alone. In order to dissociate the exciton into free charges before it recombines, the exciton must reach an interface with an energy offset greater than E_B . This can either be a semiconductor/metal interface or a semiconductor/semiconductor interface with sufficient offset in HOMO and LUMO levels (i.e. a donor/acceptor interface).

The process of exciton generation discussed here represents the first step in generating a photocurrent. Exciton dissociation and the subsequently steps required to generate a photocurrent in an organic photovoltaic device are discussed in Section 2.4. It is first worthwhile to consider other radiative transitions that may occur between the ground and excited states of a molecule. A separate mechanism to fluorescence (radiative recombination of a singlet excited state) is phosphorescence, which describes radiative recombination of an excited triplet state, which resides at a lower energy than the first excited singlet state in a material. To understand the circumstances in which phosphorescence may occur (alternatively the selection rules that govern whether a transition is allowed or forbidden) it is helpful to invoke a quantum mechanical description for the electron wavefunctions and to consider the spin states of the exciton and the orbital angular momentum changes of the system that occur upon light absorption. For simplicity, here the system corresponds to two coupled charge carriers (i.e. the hole and the electron) interacting in the atomic lattice environment. Electrons have a spin $s = \frac{1}{2}$ and may combine with another electron (or hole) to give a total angular momentum S of 0 or 1.

The wavefunction of the former ($S = 0$) case can be written as,

$$\psi_{s_0} = \frac{1}{\sqrt{2}}(|\uparrow\downarrow\rangle - |\downarrow\uparrow\rangle) \quad \{2.1\}$$

Which is asymmetric under particle exchange. For the case where two spin $\frac{1}{2}$ particles combine in parallel (i.e $S = 1$), three (symmetric) configurations are possible, referred hereafter as triplet states,

$$\psi_{s_1} = \frac{1}{\sqrt{2}}(|\uparrow\downarrow\rangle + |\downarrow\uparrow\rangle), \quad \psi_{s_1} = |\uparrow\uparrow\rangle, \quad \psi_{s_1} = |\downarrow\downarrow\rangle \quad \{2.2\}$$

Note that ground state is given by,

$$\psi_{s_0} = |\uparrow\downarrow\rangle \quad \{2.3\}$$

The symmetry of each wavefunction determines whether a transition between states is allowed. According to the Pauli exclusion principle, for a two particle system the total wavefunction (spin and spatial components) must be asymmetric under particle exchange. Thus either the spatial component must remain symmetric (for the singlet state) or be asymmetric (for the triplet states) to allow the exciton wavefunction to remain asymmetric overall.

In order for an optical transition to be allowed the change in spatial angular momentum ΔL must equal 1. For absorption, the photon provides the necessary angular momentum to allow the S_0 to S_1 transition, i.e. between the ground state symmetric state with $L = 0$ and the first excited antisymmetric state with $L = 1$. The opposite holds true for fluorescence with emission of a photon providing the necessary change in L . From the previous discussion the $S_0 - T_0$ is forbidden because both states are spatially symmetric, $\Delta L = 0$. However it is possible for the transition to occur by means of spin-orbit coupling, which describes the interactions between the spin and spatial components of a particle's angular momentum. The transition between a singlet and triplet state requires one particle to undergo a spin flip. Such a process is intrinsically weaker than singlet-singlet transition – as a result the lifetime is significantly longer (μs to ms or greater timescale). The efficiency (i.e. quantum yield) of the process is heavily influenced by the spatial angular momentum of the atomic lattice – atoms that are much heavier than carbon increase the efficiency of the spin-orbit coupling process. This mechanism is of far greater significance for organic electroluminescent devices than organic photovoltaic devices, however a number of studies have addressed triplet generation in OPVs to potentially increased the yield of photogenerated charges, owing to the lower energy required to move an electron from the S_0 to T_0 state.

To summarise the processes discussed in this section, a Jablonski diagram is presented in Figure 2.6. Here, the horizontal axis corresponds to states of different spin (that is, total angular momentum) and not molecular coordinate as previously presented in Figure 2.3. In addition to highlighting the nature (radiative or non-radiative) of the transitions that may occur within a molecule upon photoexcitation, the approximate lifetime of each process is also included to distinguish relatively dominant from relatively weak processes.

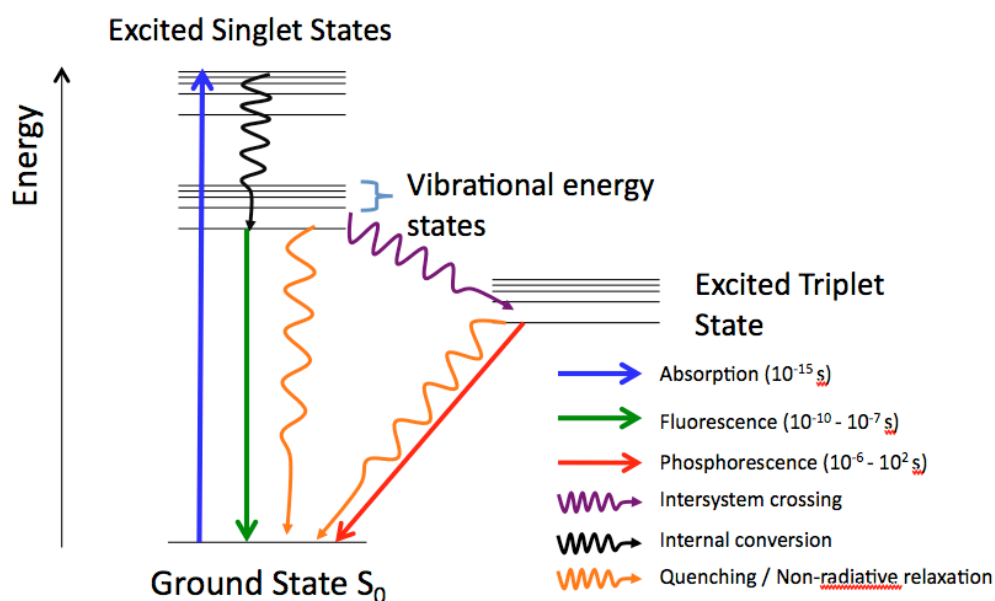


Figure 2.6: Jablonski diagram illustrating the nature and approximate timescales of the radiative processes discussed in this section. Radiative and non-radiative transitions are labeled by straight and squiggly lines respectively.

SECTION 2.4: PHOTOCURRENT GENERATION IN ORGANIC PHOTOVOLTAIC DEVICES

The principle steps in photocurrent generation in a polymer/fullerene photovoltaic device after exciton generation are discussed in this section. These are exciton diffusion, exciton dissociation into free charges, charge transport and charge extraction. For simplicity, the impact of the structure of a blend film and its influence on these steps is not considered here and is left until Section 2.6.

SECTION 2.4.1: EXCITON DIFFUSION

As mentioned briefly in the preceding section, an exciton of Frenkel character must reach an interface to dissociate into free charges in order to be able to contribute to a photocurrent. The question arises therefore as to how such a process occurs in a typically disordered system where wavelike propagation of the excited state is unlikely to occur. In order to reach an interface, the exciton must undergo a process of diffusion. Owing to the disorder in the system, exciton diffusion is typically described as a random ‘hopping’ process (the exciton is overall electrically neutral) either along a molecular chain (intrachain hopping) or between chains (interchain hopping) towards sites lower in energy. Two common mechanisms by which excitons may diffuse are Förster resonance energy transfer¹² (FRET) and Dexter electron transfer. Förster energy transfer occurs via a resonant coupling between neighbouring atomic dipoles and typically occurs over a lengthscale of a few nm. The efficiency of FRET (i.e. the transfer rate) is sensitive to the separation distance r between donor and acceptor (varying as r^{-6}), the overlap between the absorption spectrum of the donor and the emission spectrum of the acceptor and the relative alignment between donor and

acceptor dipoles. Dexter electron transfer involves the direct transfer of charge carriers between neighbouring moieties. Here the efficiency of the process is determined by the wavefunction overlap between the donating and accepting molecules, and therefore occurs over much shorter distances than FRET (e^{-r} dependence), typically less than 2 nm.

The exciton diffusion length L_D is used to characterise the hopping process (i.e. the average distance travelled by the exciton prior to recombination) and set the appropriate length scale for donor / acceptor phase separation to efficiently dissociate excitations into electrons and holes (free charge generation) within an OPV. A common method to estimate L_D is via fluorescence quenching measurements¹³, whereby the relative intensity of emission is measured from a material as a function of distance away from a well defined (i.e. smooth) quenching interface (for example C₆₀ or titania). Values of L_D are typically within the range of 5-10 nm for spin-cast films of conjugated polymers^{13a, 14}.

SECTION 2.4.2: EXCITON DISSOCIATION

Upon reaching an interface an exciton can undergo charge transfer between two materials if the energy offset between LUMO levels is sufficiently large to overcome the exciton binding energy. For brevity only the dissociation mechanism at organic semiconductor interfaces is considered here. The condition for charge transfer is that the free energy of the system must be lowered as a result. Consider the idealised energy level diagram for a donor/acceptor system in Figure 2.6, with the HOMO and LUMO levels of the acceptor material positioned at lower energy than those of the donor material. Recall from section 2.3 that an exciton corresponds to an electron residing in the LUMO level of the molecule and a hole residing in the HOMO level. This picture however ignores any coupling interactions between the

charges and the atomic lattice. If instead the electron (hole) is treated as an electron (hole) polaron, the state will reside at a slightly different energy to the molecular orbitals. Specifically, a hole polaron E_{p^+} will be at a higher energy with respect to the HOMO level, and the electron polaron E_{p^-} will reside at a slightly lower energy with respect to the LUMO level. These polaron energy levels are represented by the dashed lines in Figure 2.6. Electron transfer from the donor molecule to the acceptor molecule between LUMO levels (or between the HOMO levels for hole transfer) will occur if the energy difference ΔE between the two levels exceeds the binding energy of the exciton. For electron transfer the donor LUMO should be at a higher energy relative to the acceptor LUMO. For hole transfer the donor HOMO should be at a higher energy relative to the acceptor HOMO. From the previous section this offset should be at least 0.3 eV. It is important to recognise that the rate of electron transfer does not continually increase as ΔE is increased, but rather reaches a maximum when the reorganization energy of the transfer process equals the Gibbs free energy¹⁵. In addition, an energy offset that is too great also has a negative impact on the maximum voltage which a photovoltaic device can produce¹⁶. As will be discussed later, it is therefore preferable to have a donor acceptor combination in which the energy level offset is just sufficient to dissociate the exciton.

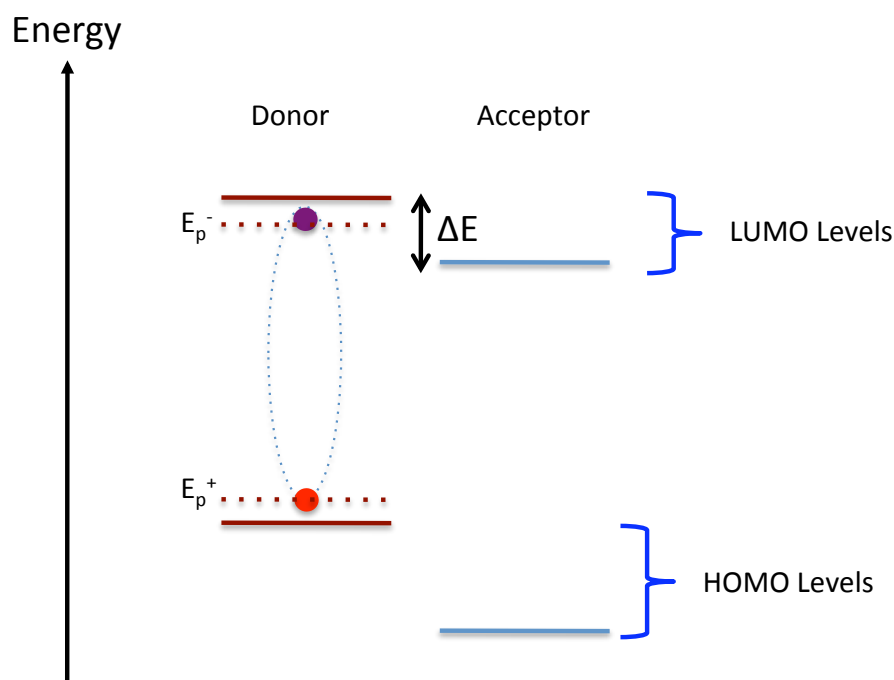


Figure 2.6: Diagram illustrating schematically the energy levels (HOMO and LUMO) at a donor acceptor interface. If an exciton, represented here as mutually bound electron polaron (purple circle) and hole polaron (red circle) pair, reaches a donor/acceptor interface, the separation energy ΔE between LUMO levels must exceed the binding energy of the exciton in order for electron transfer to take place.

In polymer:fullerene blend thin-films charge transfer is fast and has been measured experimentally for both electron and hole transfer at up to 45¹⁷ and 30 fs¹⁸ respectively. This timescale is significantly faster than the principle loss mechanism of photoluminescence which occurs over timescales of 100's of ps. Provided the donor and acceptor are suitably mixed, such that an interface can be found within L_D , exciton dissociation will occur with a quantum yield of almost unity.

Prior to the formation of charge carriers that can be considered 'free' and subsequently undergo the process of charge transport, the electron and hole must first escape their mutual

Coulombic attraction. This is the so-called ‘charge-transfer’ or CT state in donor/acceptor systems, with the electron now present on the LUMO level of an acceptor molecule and the hole remaining on the HOMO level of the donor molecule. To a first approximation, breaking the charge transfer state can be described using Onsager’s theory¹⁵; here an electron and hole are deemed to be fully separated when their thermal energy exceeds their Coulomb attraction. The critical distance r_c between charges that needs to be exceeded is given by the following expression,

$$r_c = \frac{e^2}{4\pi\epsilon_r\epsilon_0k_B T} \quad \{2.4\}$$

Here e is the elementary charge, ϵ_r and ϵ_0 represent the relative and vacuum electric permittivity respectively, k_B is Boltzmann’s constant and T is the temperature of the system. For simplicity this model assumes that one charge is considered stationary, with the second mobile (or ‘hot’) charge interacting with the potential energy of the first charge. For a CT state present at ambient conditions in a conjugated polymer:fullerene system the critical escape radius is roughly 15 – 20 nm. Consequently, unless the electron and hole are separated by at least this distance they will recombine germinately. This defines recombination of charge carriers from the same initial state (i.e. an exciton). Non-germinate recombination, in contrast, describes the recombination of charges from separate initial states.

The limitation of the Onsager model is that the lifetime of the state, the reversibility of the process and structural disorder are not considered; effects that are believed to reduce r_c to

only a few nm. In addition, external electric fields are neglected which may also help to drive the charged species apart. Consequently it is difficult to construct a comprehensive picture of the CT state, with a large body of literature devoted to understating its character. Providing a conclusive character of the CT state is beyond the scope of this work, nevertheless the model included here gives a semi-quantitative understanding of the true nature of the state. In analogy to the binding energy of the exciton, a CT state can also be thought of as having a binding energy, $E_{B,CT}$. If this state is emissive it is possible to estimate $E_{B,CT}$ using conventional photoluminescence or electroluminescence measurements. In general, the binding energy of the CT state is less than the binding energy of the singlet exciton which precedes it. The potential energy of the CT state – approximately the difference between the LUMO level of the acceptor and the HOMO level of the donor on which the charge species reside – will have an impact on the maximum attainable voltage from an OPV¹⁹.

SECTION 2.4.3: CHARGE TRANSPORT

After separation of a CT state, the electron and hole can be considered ‘free’ of each other and attention now turns to how these charge carriers can be transported from the donor:acceptor interface towards the electrodes of a device. As organic semiconductors are typically disordered, with relatively low coupling energies between molecules, it is appropriate to describe charge transport as occurring via a series of ‘hops’ instead of coherent band like charge transport as would be applicable for inorganic semiconductors with well defined lattice structures. The simplest model to describe charge transport is a Gaussian disorder model that assumes charge transport with a Gaussian distribution of disordered states. This concept can also be used to describe the distribution of energy levels (HOMO and LUMO) in a molecule; an effect that leads to a broadening of the optical transitions of the

material. The exact analytical description of the energetic state distribution is dependent upon the system under examination. The distribution of energetic states $g(E)$ can however be represented as follows ²⁰,

$$g(E) = \frac{1}{\sqrt{2\pi\sigma}} \exp\left(-\frac{E^2}{2\sigma^2}\right) \quad \{2.5\}$$

Here, σ represents the distribution width of the energetic states E , and is larger for systems with greater disorder. Because of disorder, it is possible for charge transport to occur via diffusion towards states of lower energy in the absence of an electric field, however the direction of this process is likely to be random. The presence of an electric field, either built in or externally applied in addition to the temperature of the environment, will influence the mobility of charge carriers. Each of these factors are considered in turn.

The hopping rate ν_{ij} between two molecular sites i and j can be described using the following expression ²¹,

$$\begin{aligned} \nu_{ij} &= \nu_0 \exp(-2\gamma\Delta r_{ij}) \exp\left(-\frac{E_j - E_i}{k_b T}\right) & E_j > E_i \\ \nu_{ij} &= \nu_0 \exp(-2\gamma\Delta r_{ij}) & E_j < E_i \end{aligned} \quad \{2.6\}$$

Here, ν_0 represents the frequency at which charges attempt to move between sites, γ is the coupling strength, Δr_{ij} is the distance between sites and E_j and E_i are the energy of each site. In the absence of temperature activated hopping, a charge will only be able to move from site i to site j if $E_j < E_i$. Note that charges may become trapped if, before reaching an interface to undergo charge extraction, they hop onto a site at significantly lower energy than its neighbours. Such a scenario can lead to recombination if a charge of opposite polarity moves within the vicinity of the trapped charge and becomes Coulombically bound.

In the presence of an electric field, charge transport is conventionally described by the mobility μ of each charge carrier; this is defined as the speed of a charge carrier per unit of electric field applied. Where disorder is present in a system, it is not possible to completely define an analytical expression to relate semiconductor structure to charge mobility. Consequently phenomenological models are used instead. One description by Bässler describes the electric field F and temperature T dependence of μ as²⁰

$$\mu(T, F) = \mu_0 \exp\left[\left(-\frac{2}{3k_b T}\right)^2\right] \cdot \begin{cases} \exp[A(\sigma^2 - \Sigma^2)\sqrt{F}], & \Sigma > 1,5 \\ \exp[A(\sigma^2 - 2.25)\sqrt{F}], & \Sigma \leq 1,5 \end{cases} \quad \{2.7\}$$

Here μ_0 is the zero-field mobility, A is a constant related to the spacing between molecules and σ and Σ parameterise the energetic (from Equation 2.6) and spatial disorder of the system. From Equation 2.7 it can be seen that charge mobility can increase with a reduction in either σ or Σ or both. Except in exceptional circumstances, organic semiconductors will always

exhibit lower charge carrier mobilities (typically by several orders of magnitude) than that of inorganic semiconductors.

From Equations 2.6 and 2.7 it can also be seen that charge mobility may be improved via thermal activation. The extent to which charge mobility may increase depends upon the thermal stability of the semiconductor – at elevated temperatures, if the semiconductor undergoes a transition into a structurally more disordered state then charge mobility will reduce. Recent studies have also looked at the mobility dependence of the intensity of light incident on an OPV ²². This measurement clearly determines the effect of the density of charge carriers in the thin-film on charge mobility ²³. Indeed, the actual mobility of charge carriers within a device is related to a number of internal and external factors. Consequently measuring the mobility of charge carriers is non-trivial, with a number of techniques used to approximate the mobility under certain conditions, or to highlight relative differences between samples or materials. Three methods are commonly used to determine charge carrier mobility in organic semiconductors:

1. Field-Effect Transistor (FET): Here the mobility is calculated from the saturation current through a device (that is, at large source-drain bias voltage) as a function of gate voltage. Note that for FETs the calculated mobility is strongly influenced by the interface between the semiconducting layer and the insulating gate dielectric. Thus FETs are not ideal device architectures for determining bulk electronic transport characteristics of a semiconductor.

2. Time-of-Flight (ToF): Here, a device with an architecture identical to an OPV (anode/active layer/cathode) is illuminated with a short pulse of light whilst under applied bias. The time taken for charge carriers to traverse the device is used to determine the carrier mobility. In order to accurately determine μ , the duration of the light pulse should be sufficiently shorter than the carrier transit time. Also, the initial region within the semiconductor where charges are photogenerated should be small in relation to the total film thickness. For these two reasons, the semiconducting layers studied are typically several microns in thickness. The ToF technique offers the advantage that charge carrier mobilities of either polarity may be measured in the same device, in addition to the extracted value representing the probable 'bulk' property of the material.

3. Space Charge Limited Current (SCLC): Here, a device is prepared in an identical manner to an OPV, with the exception that both electrodes are chosen to match the HOMO level of the donor or the LUMO level of the acceptor. This suppresses the transport of either electrons (for the first case) or holes (for the second case) due to the large energetic barrier that forms at the semiconductor/metal interface. An SCLC device in principle allows for the mobility of a single charge carrier (holes or electrons) to be determined. As will be discussed at the end of this section, the mobility is determined from dark-current/voltage measurements where space charge effects may be observed. As SCLC devices are prepared in an almost identical manner to OPVs, the technique is used in this thesis to measure relative differences in charge carrier mobilities between samples.

An important length-scale associated with the charge mobility is the drift length, L_{drift} at a particular electric field F , which is given by the following expression,

$$L_{drift} = \mu\tau F \quad \{2.8\}$$

Here τ represents the carrier lifetime, that is the average time a charge carrier is expected to exist before recombining. As will be discussed in the following section, the drift length is an important length-scale in determining the optimum thickness for an OPV. L_{drift} approximately defines the maximum thickness of a semiconducting thin-film that can successfully be employed in an OPV device before charge transport becomes inefficient and charge recombination becomes problematic. This distance may be lower than the thickness required for efficient absorption of light.

SECTION 2.4.4: CHARGE EXTRACTION AND INJECTION

In order for efficient charge extraction to occur, charges must first be transported from the bulk of the semiconducting film toward the interfaces via appropriate pathways, i.e. regions of pure or almost pure electron or hole transporting material. Consequently the efficiency of charge extraction will be determined by the choice of suitable electrodes in the device and the local composition of the active semiconducting layer in the vicinity of interface.

Charge extraction can be considered in two distinct cases, where the electrodes are either Ohmic or non-Ohmic in nature. The distinction relates to whether or not the work function of the electrodes match the energy levels of the semiconductors. Specifically for Ohmic contacts the cathode should be matched to the LUMO level of the electron transporter and the anode should be matched to the HOMO of the hole transporter. The type of contact determines whether the open circuit voltage V_{oc} (the maximum voltage a solar cell can produce) of the device is interface or bulk limited. For non-Ohmic contacts the V_{oc} is set by the difference between the work functions of the two electrodes²⁴. This potentially introduces considerable energetic barriers for charge extraction; for example an electrode with a work function further away from the vacuum level than the HOMO level of the hole transporter will require holes to spend energy in order to leave the device.

When Ohmic contacts are present the bulk properties of the semiconductor becomes the limiting factor in determining V_{oc} ²⁴. Several studies have shown that in this regime, V_{oc} is correlated with the energy difference between the LUMO level of the acceptor and the HOMO level of the donor semiconductors^{16, 25}, this difference representing the built-in voltage potential of the device, V_{BI} . This model gives a reasonable estimate of the open-circuit voltage attainable from a device. Deviations from V_{BI} are generally ascribed to band pinning¹⁶ or band bending²⁶ effects at the metal/semiconductor interface, the degree of energetic disorder within the blend and charge recombination in the semiconducting layer²⁷. The open circuit voltage is also influenced by the intensity of incident light on the solar cell²⁸ – a characteristic that sets apart organic solar cell devices from inorganic p-n heterojunction solar cells which can be described by Shockley diode characteristics. It is believed that the maximum open circuit voltage attainable is determined from the potential energy of the charge transfer state introduced earlier^{19, 29}.

SECTION 2.4.5: SPACE CHARGE LIMITED CURRENT

The dark current-voltage characteristics of a typical polymer:fullerene blend in a SCLC device is shown in Figure 2.7. The data is plotted on a logarithmic scale in order to highlight the different regimes of current flow. In addition, the applied bias has been offset by an amount V_B to give the effective applied bias across the semiconducting layer. Here, V_B represents the work function difference between the two electrodes.

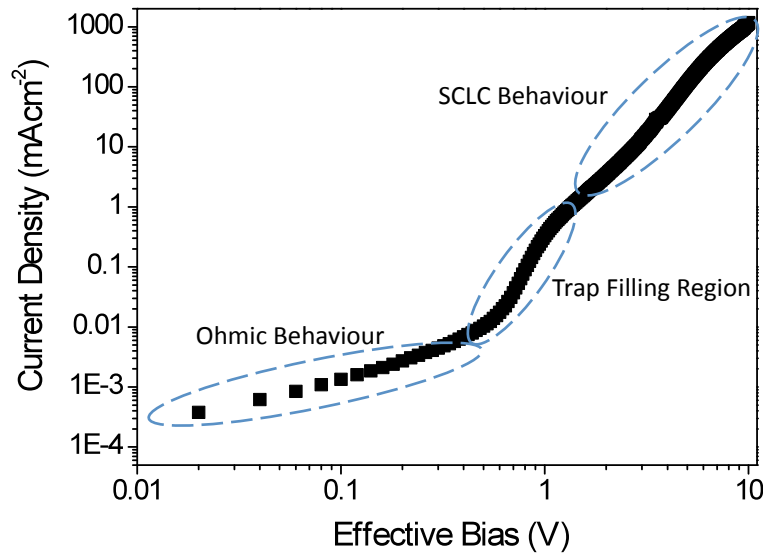


Figure 2.7: Typical dark current-voltage characteristics for a PCDTBT:PC₇₀BM blend (1:4 wt%) diode device. Here, the architecture of the device was ITO/PEDOT:PSS/Blend Layer/Au.

It can be seen from Figure 2.7 that the current dependence on the effective bias can be split into three mechanistically different regions³⁰. At low effective bias the current rises in a linear fashion and corresponds to an Ohmic regime (i.e. – the current is determined by charges which move freely across the device). At larger effective bias the current undergoes a

rapid increase. This trap-filling transition corresponds to the filling of insulating sites (trap states), reducing the number of conductive (Ohmic) pathways through the device. The current undergoes a relatively rapid increase in this phase owing to the transition of the Fermi level to an energy above that of the trap level³⁰. During the trap-filling transition, trapped charges can be considered immobile and the field within the device becomes weaker as the effective applied bias increases still further. This is a result of the trapped charges ‘screening’ the applied electric field. At higher bias, once most of the trap sites have been filled the rate of increase in current flow is reduced i.e. it becomes space charge limited.

The relationship between current flow and effective bias in the SCLC regime is given as:

$$J_{SCLC} = \frac{9}{8} \epsilon_0 \epsilon_r \mu \frac{V^2}{L^3} \quad \{2.9\}$$

Here V is the effective bias, L is the thickness of the semiconducting layer and ϵ_0 and ϵ_r represent the vacuum and relative electric permittivity respectively. Here, μ represents a steady state mobility and is thus only an approximate measure of charge carrier mobility within a sample. Although not used in this thesis, it is possible to use a modified form of Equation 2.9 to account for the dependence of μ on charge carrier density³¹. Note however that under SCLC, conditions the electric field across the device will be significantly higher than for an OPV under conventional operation³².

SECTION 2.5: CHARACTERISING OPV DEVICE EFFICIENCY

The previous section discussed the individual steps in photocurrent generation. For an operating OPV the power conversion efficiency (PCE) will be determined by the product of the efficiency of these individual steps. The standard method for determining the PCE of an OPV, as with any type of solar cell, is via measurement of the photocurrent response of the device as a function of applied bias. In Figure 2.8 the current voltage (JV) characteristics for a typical solar cell under illumination is shown.

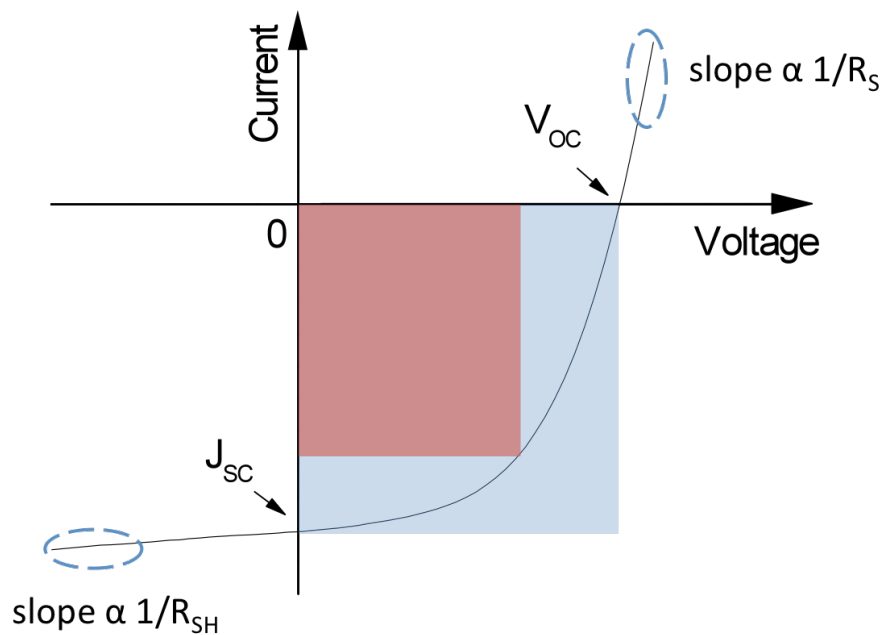


Figure 2.8: Current voltage characteristics of a solar cell under illumination. The terms R_{SH} , J_{SC} , V_{OC} and R_S and the blue and red squares are defined and referred to in the text.

The parameters from which the power conversion efficiency is calculated are

1. The short circuit current (J_{SC}) – the extracted current at zero applied bias.
2. The open circuit voltage (V_{OC}) – the largest voltage attainable from the solar cell. It is the point at which no current flows through the device.
3. The fill factor (FF) – the ratio between the area defined by the maximum product of JV (maximum power point) and the product of J_{sc} & V_{oc} . To optimise the efficiency of a solar cell this value should be as close to unity as possible. This is illustrated by the ratio of the area between the red and blue squares in Figure 2.8.

The PCE is defined as follows:

$$PCE = \frac{J_{SC} V_{OC} FF}{P_{IN}} \quad \{2.9\}$$

$$FF = \frac{J_{MP} V_{MP}}{J_{SC} V_{OC}} \quad \{2.10\}$$

Here P_{IN} represents the power incident upon the solar cell. At short-circuit conditions, when no bias is applied to the device, charges may be extracted by the built-in field determined by the work function difference of the electrodes. Thus the magnitude of J_{sc} will be related to the amount of light absorbed by the device (dependent on the band gaps of the semiconducting materials and the optical density of the active layer) and the subsequent efficiency of charge generation, transport and extraction. If a voltage is applied in the direction of this field (i.e. in

reverse bias as defined in Figure 2.8) charge extraction becomes easier and the device can be operated as a photodetector.

In forward bias, the applied voltage opposes the direction of the built-in field, reducing the ability of the solar cell to provide power. Eventually the applied bias becomes sufficient to balance the built-in field. Beyond this point (the open circuit voltage) the solar cell no longer provides electrical power.

It is possible to describe the current-voltage characteristics of a solar cell using the following equation,

$$J = J_0 \left\{ \exp\left(\frac{e}{nk_B T}(V - JR_S)\right) - 1 \right\} + \frac{V - JR_S}{R_{SH}} - J_{PH} \quad \{2.11\}$$

Here J_0 is the dark current, n is the diode ideality factor, J_{PH} is the photocurrent and R_S and R_{SH} are the series and shunt resistances across the device respectively. It is possible to relate the resistive terms R_S and R_{SH} to the fill-factor described earlier. A large fill-factor correlates with a low series resistance and high shunt resistance (necessary to minimise leaks from the device). From Figure 2.8 it can be seen that R_S is inversely proportional to the gradient of the JV curve at high forward bias and R_{SH} is inversely proportional to the gradient of the JV curve at large reverse bias. This provides a simplistic representation of the FF in terms of an electric circuit. It is also possible to relate, albeit indirectly, the fill-factor to the nanoscale structure of

the active semiconducting layer and the likelihood of charge recombination (which can also be thought of as a resistive loss). Solar cells with more balanced charge transport and low recombination rates will have larger fill factors³²⁻³³.

A second method to characterise a device is to measure its quantum efficiency. The *external quantum efficiency* (EQE) relates the number of charges extracted from a device to the number of photons incident upon it. This can be calculated as a function of incident light at wavelength λ using the following expression,

$$EQE(\lambda) = \frac{Jhc}{P(\lambda)\lambda e} \quad \{2.12\}$$

Here, $P(\lambda)$ is the incident power as a function of wavelength, and all other terms have their usual meaning. The *internal quantum efficiency* (IQE) relates the number of charges extracted to the number of photons absorbed by the active semiconducting layer. Both measurements allow the spectral response of an OPV to be determined, however it is apparent that the EQE also takes into account light that is not absorbed by the solar cell. Consequently OPVs with very thin (< 100 nm) active layers will always have a low EQE even if the internal quantum efficiency is high. Due to optical interference effects that occur within a device, accurate measurements of IQE are typically calculated using absorption measurements obtained in a reflection geometry.

SECTION 2.6: INFLUENCE OF ACTIVE LAYER MATERIALS AND NANOSTRUCTURE ON THE EFFICIENCY OF ORGANIC PHOTOVOLTAIC DEVICES

From Section 2.4 one may expect that in order to maximise the power conversion efficiency of an OPV, the efficiency of each of the individual steps (light absorption, free charge generation, charge transport and extraction) should be maximised. Although this is true, in practice however the best OPVs work by finding the best balance between the steps in photocurrent generation, and although undesirable, certain losses are often accepted in order to maximise the overall device efficiency. For example, in an OPV incorporating a thin organic semiconducting film the internal efficiencies of charge generation and transport may be high, however the device will be limited by the amount of light that can be harvested. An alternative description to this example is that L_{drift} , as defined in section 2.4.3, becomes the limiting factor in the design of an efficient OPV. In this section the development of OPVs is discussed, from the first proof of concept devices to the most efficient devices reported at the time of writing.

The first OPVs incorporated a single semiconductor sandwiched between two electrodes, each with a different work function. As described in section 2.4.4, one electrode is chosen to match to the LUMO level to enable electron extraction, with the other matched to the HOMO level to enable hole extraction / electron injection. Oxidised tetramethyl p-phenylenediamine³⁴, polyacetylene³⁵ and magnesium phthalocyanine³⁶ are all early examples of semiconductors used in single layer OPVs. The charge collection efficiencies of these devices were low (less than 0.1%), the most probable reason being due to an insufficient internal electric field being present within the device to dissociate excitons into free charge carriers.

Nevertheless these studies proved that a photovoltaic effect could be observed in organic semiconductors (either conjugated polymers or small molecules).

A seminal contribution to OPV research was made in 1986 when the first heterojunction OPV was demonstrated³⁷. This consisted of a bilayer system of copper phthalocyanine (as electron donor) and a perylene tetracarboxylic derivative (as electron acceptor) in the device architecture ITO/Active layer/Ag. In this configuration ITO operates as the anode and Ag as the cathode. The device demonstrated a power conversion efficiency of 1% under simulated solar radiation. Here, as with all conventional bilayer OPVs, the acceptor layer is deposited after deposition of the donor layer to form pure layers of each within the device. This work demonstrated one of the key requirements for OPVs that has remained to the present day; the substantial improvement in free charge generation provided by a donor:acceptor interface. Nevertheless one of the principle drawbacks of the bilayer heterojunction architecture is the mismatch between two characteristic length scales in organic semiconductors; the diffusion length of excitons (approximately 10 nm) and the length scale for efficient light absorption (roughly 100 nm of material for 50% light dissipation). This forces a trade off between efficient charge transport and free charge generation, as only photogenerated excitons in the vicinity of the interface will dissociate, the rest undergoing recombination. Nevertheless, owing to the purity of donor and acceptor layers, the bi-layer concept does allow for the relatively efficient transport of charge carriers towards the electrical contacts without significant recombination losses. Indeed the device reported in ref. 37 had a fill factor of 65%, indicating a relatively low series resistance across the device.

The principle drawback with bi-layer OPVs was overcome with the introduction of the bulk-heterojunction (BHJ) concept in 1995. Demonstrated independently by Halls *et al.*³⁸ and Yu *et al.*³⁹, the ability to intimately mix donor and acceptor materials via casting a blend thin-film from a common solvent creates an interpenetrating network of donor and acceptor material. This massively increases the interfacial donor:acceptor area and consequently improves the dissociation efficiency of photogenerated excitons. For example, in the work of Yu *et al.* a blend of poly[2-methoxy, 5-(2-ethylhexoxy)-1,4-phenylene vinylene] (MEH-PPV) as electron donor and C₆₀ as electron acceptor was cast from xylene or dichlorobenzene. Power conversion efficiencies of ~2% were achieved under 380-480 nm illumination. In addition to the BHJ structure of the active layer, the use of C₆₀ also contributed to the efficient generation of free charge carriers. Work by Sariciftci *et al.* in 1992⁴⁰ demonstrated that photoinduced charge transfer from MEH-PPV to C₆₀ is ultrafast (< 60 ps) owing to the strong affinity of C₆₀ towards electrons as discussed earlier. Later work estimated the electron transfer rate to be of the order of $\sim 10^{12} - 10^{13} \text{ s}^{-1}$ ¹⁷.

The BHJ concept and the use of fullerene acceptors have been common to all of the highest reported efficiency solution processable OPVs following the proof-of-concept work in 1995. Since then, a combination of material synthesis (to obtain materials with promising absorption and charge transport characteristics) and process development (to obtain film structures that balance the steps in photocurrent generation discussed in section 2.4) has pushed the technology towards commercial viability. Poly(3,4-ethylenedioxythiophene):poly(styrenesulfonate) (PEDOT:PSS) became an appropriate blend system with which to coat ITO as the semi-transparent anode layer in OPVs. This affords a work function of the anode that is more closely (but not precisely) matched to the HOMO

level of many conjugated polymers. In addition, the coating may also improve the wettability and film quality of the active blend film by smoothing the ITO surface⁴¹.

For several years, the efficiency of OPVs under white light illumination remained at ~1%. The issue of poor solubility of C₆₀ was overcome via functionalisation with a methyl-ester group to form PCBM³⁹ thereby allowing more uniform blend thin-films to be deposited. The importance of the casting solvent was realized by Shaheen *et al.*⁴² who were able to increase the power conversion efficiency of MEH-PPV:PCBM solar cells from 0.9 to 2.5% by preparing blend thin-films from a good solvent (chlorobenzene) as opposed to a poor solvent (toluene) that caused aggregation of PCBM. This allowed much finer phase separation of donor and acceptor materials - from 100's to 10's of nm - to a length scale more commensurate with the diffusion length of excitons. This change in processing protocol further improved the efficiency of the charge generation step in photocurrent generation, whilst still allowing for some degree of phase separation between donor and acceptor domains to support efficient charge transport.

Ultimately, when mixing two materials in a common solvent and subsequently casting a film, the structures formed will depend upon the miscibility between each of the components and the drying dynamics. During film preparation, the evaporation of solvent will cause the materials to partially de-mix in order to lower the free energy of the system. For thin-films prepared via spin-casting, solvent loss is a relatively rapid process which 'vitrifies' or locks-in a solid structure that can be far from thermodynamic equilibrium, or does not necessarily represent the best morphology for photocurrent generation. It is important therefore to determine the conditions under which a large interfacial area can be achieved between donor

and acceptor materials, albeit with a small degree of phase separation present in order to provide percolated pathways throughout the film for charge transport and charge extraction.

As an example of the necessity to balance light absorption with charge extraction as discussed at the start of this section, OPVs based on a blend of MEH-PPV or MDMO-PPV with PCBM have highest efficiency when the semiconducting layer contains approximately 80wt% PCBM⁴². This result is slightly counterintuitive, as PCBM does not strongly absorb visible light⁴³. However, later studies on this system identified a significant increase in hole mobility through the polymer phase upon addition of large wt% of PCBM⁴⁴. This improvement in charge transport efficiency was large enough to offset the loss of light absorption by reducing the wt% of polymer in the active semiconducting layer.

The different blend ‘systems’ which followed –PPV:PCBM based devices had a higher efficiency and a conceptually different approach to the fabrication methodology. Figure 2.9 presents the chemical structures of several key polymers and functionalised fullerenes. P3HT was considered a suitable substitute for MEH-PPV and similar PPV derivatives owing to its lower band gap (1.95 eV compared to 2.1 to 2.2 eV⁴⁵). Additionally, P3HT based OFETs were demonstrated to have hole mobilities of up to 0.1 cm²/Vs⁴⁶. This promising result suggested that OPVs with P3HT as the donor material could incorporate thicker active layers compared to OPVs with –PPV derivatives, owing to the likelihood of a longer charge carrier drift length as discussed in section 2.4.3. Thus in addition to a lower energy gap, it was likely that P3HT:PCBM could more efficiently transport charge over longer distances compared to previous blend systems, thereby enabling the use of optically denser active layers.

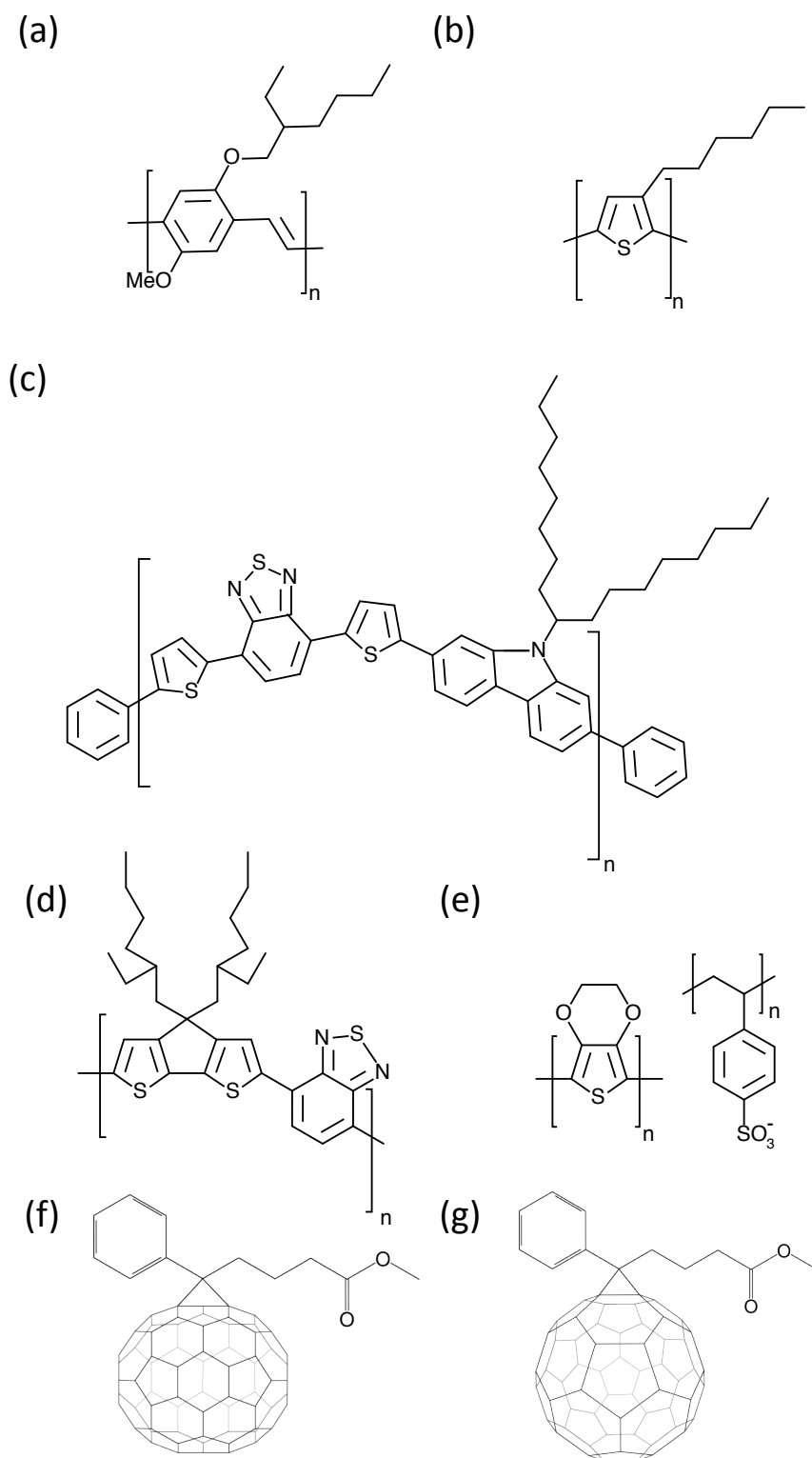


Figure 2.9: The chemical structures of several key materials used in OPV research. (a) MEH-PPV, (b) P3HT, (c) PCDTBT and (d) PCPDTBT, all of which are electron donor materials. The structures of PEDOT and PSS, which blended together act as a hole transport material in OPVs is shown in (e), whilst the structures of the electron acceptors PC₇₀BM and PCBM are shown in (f) and (g) respectively.

In P3HT:PCBM blend OPVs, it was found that post film deposition treatments were the key to obtain optimised devices. These have included thermal annealing⁴⁷ and solvent vapour annealing; the latter describing either the removal of a deposited but partially wet thin-film into a solvent rich environment to alter the drying kinetics⁴⁸, or the exposure of dry films to one⁴⁹ or two⁵⁰ solvents in order to swell the film and encourage the crystallisation and self organisation of both components⁵¹. Apparently optimised PCEs of between 4 and 5% could be obtained for devices with similar electrodes to –PPV:PCBM OPVs⁴⁷⁻⁴⁸, rising to 5.5% upon substitution of PEDOT:PSS with a metal oxide as anode to improve the extraction efficiency of holes⁵².

The principle effect of these post film-deposition treatments (which are explored in depth in Chapters 4 - 6) is to coarsen the phase separation between P3HT and PCBM in order to benefit from the improved photovoltaic characteristics of both materials in their semi-crystalline phase. For example, when P3HT is partially crystalline, it has improved light absorption in the red wavelength region of the visible spectrum and greater hole mobility. However, the optimum processing parameters for either thermal post-treatment or solvent vapour assisted post treatment have generally been empirically derived, with several studies following in the wake of optimised device studies attempting to provide a partial explanation for why the optimised processing conditions work. In addition, the blend system became a test-bed for exploring the interdependence between material properties (for example, the regioregularity or molecular weight of P3HT) and optimum processing conditions, and for evaluating new characterisation techniques.

A key advancement in polymer synthesis was the gradual move towards donor-acceptor copolymers as a means to obtain materials with smaller energy gaps. These polymers contain alternating units along the conjugated backbone with strong electron or donating characteristics⁵³. This allows a band-gap to form between the HOMO of the donor moiety and the LUMO of the acceptor moiety, as the proximity of the units makes it energetically favorable to transfer an electron between these two neighboring energy levels. The positions of these levels (i.e. the absolute electron affinity and ionization potential of each unit, and therefore the bandgap of the overall copolymer) can be tuned by the chemical structure of each unit and the position of solubilising side groups⁵⁴. The copolymer approach also allows for the synthesis of donors with HOMO and LUMO levels that are well matched to the energy levels of PCBM, thereby allowing the open-circuit voltage to be maximised.

In 2007 the best OPV system reported was based on the polymer poly[2,1,3-benzothiadiazole-4,7-diyl[4,4-bis(2-ethylhexyl)-4H-cyclopenta[2,1-b:3,4-b']dithiophene-2,6-diyl]] (PCPDTBT) as the donor material, the latter being an example of a copolymer⁵⁵. The band gap of PCPDTBT is ~1.4 eV, and when blended with PC₇₀BM can efficiently absorb light throughout the visible and near IR spectrum. Efficiencies of 5.5% were obtained⁵⁵, however here thermal annealing was found to be detrimental. Instead, solvent additives were used to tune the degree of phase separation during the film casting process. These additives have a significantly higher boiling point than the primary solvent (typical vol% of the additive in the host solvent is 5% or less) and preferential solubility for one material (either polymer or fullerene). The higher boiling point and lower vapour pressure of the additive relative to the primary solvent allows it to remain in the film after the majority of solvent has left (defining the film thickness) and thus partially aggregate one component. This approach allows for the partial control of phase separation and crystallisation during the drying process

without the need for post-treatment. After demonstrating this effect for PCPDTBT:PC₇₀BM OPVs, Moulé *et al.* looked at its suitability for the P3HT:PCBM system and showed promising results⁵⁶.

Poly(2,7-) carbazole copolymers started to attract interest as new OPV donor materials due to their relative stability against photooxidation (achieved by deep HOMO levels) and the range of band-gaps that could be obtained by varying the chemical composition of the electron donating and accepting units⁵⁷. In particular, poly[[9-(1-octylnonyl)-9H-carbazole-2,7-diyl]-2,5-thiophenediyl-2,1,3-benzothiadiazole-4,7-diyl-2,5-thiophenediyl] (PCDTBT) based OPVs started to attract interest in 2009 after demonstrating PCEs of 4.6%⁵⁸. A later study, focusing on the optimisation of the donor:acceptor blend, the casting solvent, careful control of the light management within the device (specifically, designing the thin-film stack to provide maximum light dissipation within the active semiconducting layer) and electrode materials meant that internal quantum efficiencies approaching unity could be achieved⁵⁹. This implies that under short-circuit conditions, almost each photon absorbed by the active layer produces an electron and hole which are eventually extracted from the device. Further optimisation of this system produced PCEs above 7%⁶⁰.

At the time of writing (January 2012), the best OPVs continue to use donor-acceptor copolymers as the donor material. Efficiencies of just over 8% have been achieved using blends of poly[[4,8-bis[(2-ethylhexyl)oxy]benzo[1,2-b:4,5-b']dithiophene-2,6-diyl][3-fluoro-2-[(2-ethylhexyl)carbonyl]thieno[3,4-b]thiophenediyl]] (PTB7), a copolymer, and PC₇₀BM^{60b}. An apparent trend of optimising the active layer morphology through the drying process alone has been established with these material blends. Work has also focused on optimising the

anode and cathode and any layers which precede them, which act as blocking layers for unwanted charge (for example holes in the vicinity of the cathode)⁶¹. These interfacial layers are typically thin (< 20 nm) and highly transmissive, however the incorporation of such layers affects the position at which light dissipation occurs within the device (and thus charge generation). In addition to maximising the efficiency of charge extraction therefore, hole or electron blocking layers can also increase the amount of light absorbed within the active layer of the solar cell^{61c, 62}. This is a promising method for increasing light absorption in semiconducting materials with low charge carrier mobility (consequently small L_{drift}) that cannot operate efficiently when deposited as thick layers.

Although most of the attention in materials synthesis has been towards new donor polymers, alternative acceptor materials (polymers and functionalised fullerenes) have also been produced and tested. Higher fullerenes (e.g. C_{70}) exhibit stronger absorption in the visible region relative to C_{60} and show the largest relative improvement over C_{60} when blended with donor polymers with relatively limited absorption at ~ 500 nm⁴³. Whereas many polymers have been synthesised to match the energy levels of PCBM or $PC_{70}BM$ in order to maximise V_{OC} , Zhao and coworkers studied the reverse approach of tuning the energy levels of the acceptor to the donor⁶³. Using indene- C_{60} bisadduct, PCEs of 6.5% could be obtained using P3HT as the donor material, demonstrating that for the right blend combination, high efficiencies can be obtained using a relatively high band-gap semiconducting material. However, the embedded energy of fullerene synthesis and functionalisation is considerably higher than for conjugated polymer synthesis⁶⁴. In order to reduce the embedded energy and cost of OPVs therefore, alternatives to fullerene acceptors have been proposed. Whilst some conjugated polymer acceptors have been demonstrated to display promising characteristics, high power conversion efficiencies have yet to be obtained⁶⁵. This is most likely due to a

poor donor:acceptor morphology and/or limited acceptor strength, leading to increased charge recombination.

The evolution of donor:acceptor blends for OPVs has led to the development of a number of models that link efficient photocurrent generation to the nanoscale structure, or ‘morphology’ of the blend thin-film⁶⁶, and also for predicting some of the processing conditions for optimising unexplored donor/acceptor blends. The optimum donor/acceptor composition is thought to be strongly influenced by the miscibility between the two components⁶⁷ and the ability of the either material to crystallise. The former point can be clarified by considering the chemical structure of the conjugated polymer and in particular whether the fullerene molecules can ‘sit’ between the solubilising alkyl side groups of the polymer. Where this is possible, a typically relatively high wt% of fullerene is required in the blend thin-film in order to ‘fill’ the polymer phase with molecules and still provide sufficient material to form the pure acceptor regions needed for efficient electron transport⁶⁷⁻⁶⁸. Blends of –PPV:PCBM and PCDTBT:PCBM fall into this category, with optimised blends containing ~66-80wt% fullerene. For blends of P3HT:PCBM, the relatively higher density of alkyl chains on the thiophene backbone of P3HT do not permit the same degree of molecular mixing. Consequently, and owing to their ability to self-organise with relative ease, P3HT and similar polymers have a propensity to form relatively pure domains in a blend thin-film. This suggests that the best morphology is a two-phase system, with processing routes designed to maximise the crystallinity of each phase without driving overly coarse phase separation, i.e. limiting the phase separation to nanoscale crystallites of a size commensurate with the exciton diffusion length. To an extent this model is correct; several studies have correlated improved opto-electronic characteristics with improved packing of the polymer, particularly along the π - π plane – thereby facilitating efficient interchain charge transport⁶⁹. However,

some degree of mixing between donor and acceptor in their amorphous phases is encouraged in order to connect these nanocrystals. Detailed measurements on the phase behaviour of P3HT:PCBM films have suggested that PCBM is relatively soluble in amorphous P3HT (disrupting π - π stacking), indicating that a three-phase picture may be a better representation of donor:acceptor morphologies⁷⁰.

The diagram in Figure 2.10 provides a schematic of the likely networks present in a polymer:fullerene BHJ OPV. To elucidate and quantify the nanostructure of these blend films, a number of techniques have been used, some of which are discussed in the following chapter. From Section 2.3 it is apparent that the length scales associated with exciton diffusion can give indirect information about the morphology of blend thin-films. For example, a relatively high degree of fluorescence quenching from a blend thin-film relative to a sample of pure donor material may indicate efficient mixing of donor and acceptor. Thus spectroscopic techniques can provide indirect information on the nanoscale morphology of blend films⁷¹.

The theory and literature outlined in this chapter provides the necessary background for interpreting the work presented in the rest of this thesis. In particular, the concepts of absorption and fluorescence, introduced in section 2.3, are discussed for both blend systems explored, and are used as indirect probes of film nanostructure. Additionally, the overview of key literature presented in this section provides a context for the thesis by highlighting the differences in processing conditions needed to optimise different OPV blend systems.

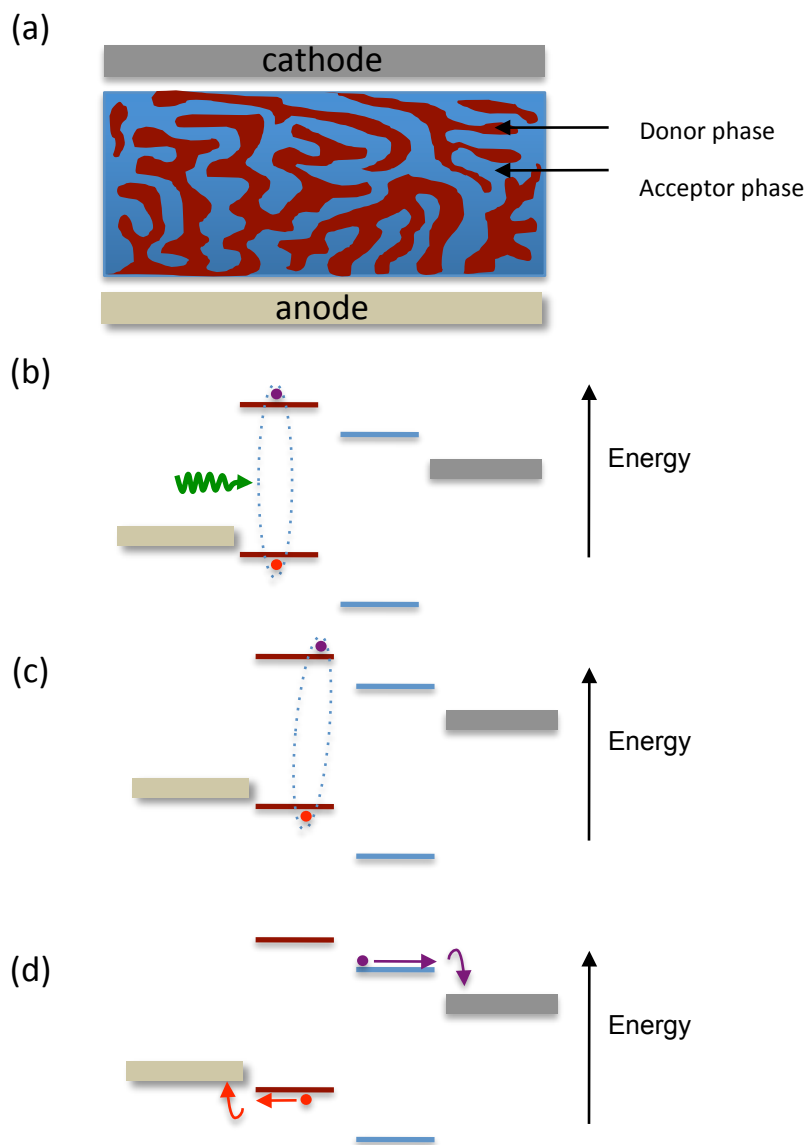


Figure 2.10: (a) schematic illustration of a bulk-heterojunction donor:acceptor morphology. The condition for efficient photocurrent generation is approximately met by the intimate mixing throughout the blend layer of donor and acceptor materials, in addition to a percolated network of each phase to connect the bulk of the layer to the electrodes. In parts (b) to (d) the steps of photocurrent generation are outlined from an energy level perspective: (b) light absorption (green line) leads to exciton generation on the donor phase, (c) exciton diffusion towards a donor/acceptor interface prior to separation, (d) free charge generation, transport and extraction into the electrodes. These diagrams follow the same format as Figure 2.6.

SECTION 2.7: REFERENCES

1. Kittel, C., *Introduction to solid state physics*. 8th ed. ed.; John Wiley: Hoboken, N.J., 2005; p xix, 680 p.
2. Yannoni, C. S.; Clarke, T. C., Molecular-Geometry of Cis-Polyacetylene and Trans-Polyacetylene by Nutation Nmr-Spectroscopy. *Physical Review Letters* **1983**, *51* (13), 1191-1193.
3. (a) Heeger, A. J.; Sariciftci, N. S.; Nanddas, E. B., *Semiconducting and metallic polymers*. Oxford University Press: Oxford, 2010; p ix, 278 p., [4] p. of plates; (b) Peierls, R. E., *Quantum theory of solids*. Clarendon Press: Oxford, 1955; p 238p.
4. Chien, J. C. W., *Polyacetylene : chemistry, physics and material science*. Academic: Orlando ; London, 1984; p xiv,634p.
5. Kroto, H. W.; Heath, J. R.; O'Brien, S. C.; Curl, R. F.; Smalley, R. E., C-60 - Buckminsterfullerene. *Nature* **1985**, *318* (6042), 162-163.
6. Pope, M.; Swenberg, C. E.; Pope, M. E. p. i. o. c., *Electronic processes in organic crystals and polymers*. 2nd ed. ed.; Clarendon: Oxford, 1999; p xxix, 1328 p.
7. McNaught, A. D.; Wilkinson, A., *Compendium of chemical terminology : IUPAC recommendations*. 2nd ed / compiled by Alan D. McNaught and Andrew Wilkinson. ed.; Blackwell Science: Oxford, 1997; p vii, 450p.
8. Du, H.; Fuh, R. C. A.; Li, J. Z.; Corkan, L. A.; Lindsey, J. S., PhotochemCAD: A computer-aided design and research tool in photochemistry. *Photochem Photobiol* **1998**, *68* (2), 141-142.
9. Blythe, A. R.; Bloor, D., *Electrical properties of polymers*. 2nd ed., New ed., fully rev. and expanded. ed.; Cambridge University Press: Cambridge, 2005; p xi, 480 p., [2] p. of plates.

10. Kaye, G. W. C.; Laby, T. H., *Tables of physical and chemical constants*. 16th ed / now prepared under the direction of an editorial committee. ed.; Longman: Harlow, 1995; p xi,611p.
11. (a) Bredas, J. L.; Cornil, J.; Heeger, A. J., The exciton binding energy in luminescent conjugated polymers. *Advanced Materials* **1996**, *8* (5), 447-&; (b) Alvarado, S. F.; Seidler, P. F.; Lidzey, D. G.; Bradley, D. D. C., Direct determination of the exciton binding energy of conjugated polymers using a scanning tunneling microscope. *Physical Review Letters* **1998**, *81* (5), 1082-1085.
12. Forster, T., 10th Spiers Memorial Lecture - Transfer Mechanisms of Electronic Excitation. *Discuss Faraday Soc* **1959**, (27), 7-17.
13. (a) Shaw, P. E.; Ruseckas, A.; Samuel, I. D. W., Exciton Diffusion Measurements in Poly(3-hexylthiophene). *Advanced Materials* **2008**, *20* (18), 3516-3520; (b) Markov, D. E.; Amsterdam, E.; Blom, P. W. M.; Sieval, A. B.; Hummelen, J. C., Accurate measurement of the exciton diffusion length in a conjugated polymer using a heterostructure with a side-chain cross-linked fullerene layer. *J Phys Chem A* **2005**, *109* (24), 5266-5274; (c) Haugeneder, A.; Neges, M.; Kallinger, C.; Spirkl, W.; Lemmer, U.; Feldmann, J.; Scherf, U.; Harth, E.; Gugel, A.; Mullen, K., Exciton diffusion and dissociation in conjugated polymer fullerene blends and heterostructures. *Physical Review B* **1999**, *59* (23), 15346-15351.
14. Scully, S. R.; McGehee, M. D., Effects of optical interference and energy transfer on exciton diffusion length measurements in organic semiconductors. *Journal of Applied Physics* **2006**, *100* (3).
15. Clarke, T. M.; Durrant, J. R., Charge Photogeneration in Organic Solar Cells. *Chemical Reviews* **2010**, *110* (11), 6736-6767.

16. Brabec, C. J.; Cravino, A.; Meissner, D.; Sariciftci, N. S.; Fromherz, T.; Rispen, M. T.; Sanchez, L.; Hummelen, J. C., Origin of the open circuit voltage of plastic solar cells. *Advanced Functional Materials* **2001**, *11* (5), 374-380.
17. Brabec, C. J.; Zerza, G.; Cerullo, G.; De Silvestri, S.; Luzzati, S.; Hummelen, J. C.; Sariciftci, S., Tracing photoinduced electron transfer process in conjugated polymer/fullerene bulk heterojunctions in real time. *Chemical Physics Letters* **2001**, *340* (3-4), 232-236.
18. Bakulin, A. A.; Hummelen, J. C.; Pshenichnikov, M. S.; van Loosdrecht, P. H. M., Ultrafast Hole-Transfer Dynamics in Polymer/PCBM Bulk Heterojunctions. *Advanced Functional Materials* **2010**, *20* (10), 1653-1660.
19. Deibel, C.; Strobel, T.; Dyakonov, V., Role of the Charge Transfer State in Organic Donor-Acceptor Solar Cells. *Advanced Materials* **2010**, *22* (37), 4097-4111.
20. Hertel, D.; Bassler, H., Photoconduction in amorphous organic solids. *Chemphyschem* **2008**, *9* (5), 666-688.
21. (a) Bassler, H.; Schonherr, G.; Abkowitz, M.; Pai, D. M., Hopping Transport in Prototypical Organic Glasses. *Physical Review B* **1982**, *26* (6), 3105-3113; (b) Miller, A.; Abrahams, E., Impurity Conduction at Low Concentrations. *Phys Rev* **1960**, *120* (3), 745-755.
22. Shuttle, C. G.; Hamilton, R.; Nelson, J.; O'Regan, B. C.; Durrant, J. R., Measurement of Charge-Density Dependence of Carrier Mobility in an Organic Semiconductor Blend. *Advanced Functional Materials* **2010**, *20* (5), 698-702.
23. Tanase, C.; Blom, P. W. M.; de Leeuw, D. M.; Meijer, E. J., Charge carrier density dependence of the hole mobility in poly(p-phenylene vinylene). *Phys Status Solidi A* **2004**, *201* (6), 1236-1245.

24. Mihailetschi, V. D.; Blom, P. W. M.; Hummelen, J. C.; Rispen, M. T., Cathode dependence of the open-circuit voltage of polymer : fullerene bulk heterojunction solar cells. *Journal of Applied Physics* **2003**, *94* (10), 6849-6854.
25. (a) Gadisa, A.; Svensson, M.; Andersson, M. R.; Inganas, O., Correlation between oxidation potential and open-circuit voltage of composite solar cells based on blends of polythiophenes/fullerene derivative. *Applied Physics Letters* **2004**, *84* (9), 1609-1611; (b) Kooistra, F. B.; Knol, J.; Kastenberg, F.; Popescu, L. M.; Verhees, W. J. H.; Kroon, J. M.; Hummelen, J. C., Increasing the open circuit voltage of bulk-heterojunction solar cells by raising the LUMO level of the acceptor. *Organic Letters* **2007**, *9* (4), 551-554.
26. Steim, R.; Kogler, F. R.; Brabec, C. J., Interface materials for organic solar cells. *Journal of Materials Chemistry* **2010**, *20* (13), 2499-2512.
27. Maurano, A.; Hamilton, R.; Shuttle, C. G.; Ballantyne, A. M.; Nelson, J.; O'Regan, B.; Zhang, W. M.; McCulloch, I.; Azimi, H.; Morana, M.; Brabec, C. J.; Durrant, J. R., Recombination Dynamics as a Key Determinant of Open Circuit Voltage in Organic Bulk Heterojunction Solar Cells: A Comparison of Four Different Donor Polymers. *Advanced Materials* **2010**, *22* (44), 4987-4992.
28. Koster, L. J. A.; Mihailetschi, V. D.; Ramaker, R.; Blom, P. W. M., Light intensity dependence of open-circuit voltage of polymer : fullerene solar cells. *Applied Physics Letters* **2005**, *86* (12).
29. Vandewal, K.; Tvingstedt, K.; Gadisa, A.; Inganas, O.; Manca, J. V., On the origin of the open-circuit voltage of polymer-fullerene solar cells. *Nature Materials* **2009**, *8* (11), 904-909.
30. Carbone, A.; Kotowska, B. K.; Kotowski, D., Space-charge-limited current fluctuations in organic semiconductors. *Physical Review Letters* **2005**, *95* (23) 236601.

31. Tanase, C.; Blom, P. W. M.; de Leeuw, D. M., Origin of the enhanced space-charge-limited current in poly(p-phenylene vinylene). *Physical Review B* **2004**, *70* (19) 193202.
32. Blom, P. W. M.; Mihailetschi, V. D.; Koster, L. J. A.; Markov, D. E., Device physics of polymer : fullerene bulk heterojunction solar cells. *Advanced Materials* **2007**, *19* (12), 1551-1566.
33. Mihailetschi, V. D.; Wildeman, J.; Blom, P. W. M., Space-charge limited photocurrent. *Physical Review Letters* **2005**, *94* (12) 126602.
34. Kearns, D.; Calvin, M., Photovoltaic Effect and Photoconductivity in Laminated Organic Systems. *J. Chem. Phys.* **1958**, *29* (4), 950-951.
35. Weinberger, B. R.; Akhtar, M.; Gau, S. C., Polyacetylene Photo-Voltaic Devices. *Synthetic Metals* **1982**, *4* (3), 187-197.
36. Ghosh, A. K.; Morel, D. L.; Feng, T.; Shaw, R. F.; Rowe, C. A., Photovoltaic and Rectification Properties of Al-Mg Phthalocyanine-Ag Schottky-Barrier Cells. *Journal of Applied Physics* **1974**, *45* (1), 230-236.
37. Tang, C. W., 2-LAYER ORGANIC PHOTOVOLTAIC CELL. *Applied Physics Letters* **1986**, *48* (2), 183-185.
38. Halls, J. J. M.; Walsh, C. A.; Greenham, N. C.; Marseglia, E. A.; Friend, R. H.; Moratti, S. C.; Holmes, A. B., Efficient Photodiodes from Interpenetrating Polymer Networks. *Nature* **1995**, *376* (6540), 498-500.
39. Yu, G.; Gao, J.; Hummelen, J. C.; Wudl, F.; Heeger, A. J., Polymer Photovoltaic Cells - Enhanced Efficiencies Via a Network of Internal Donor-Acceptor Heterojunctions. *Science* **1995**, *270* (5243), 1789-1791.
40. Sariciftci, N. S.; Smilowitz, L.; Heeger, A. J.; Wudl, F., Photoinduced Electron-Transfer from a Conducting Polymer to Buckminsterfullerene. *Science* **1992**, *258* (5087), 1474-1476.

41. Kim, Y.; Ballantyne, A. M.; Nelson, J.; Bradley, D. D. C., Effects of thickness and thermal annealing of the PEDOT:PSS layer on the performance of polymer solar cells. *Org. Electron.* **2009**, *10* (1), 205-209.
42. Shaheen, S. E.; Brabec, C. J.; Sariciftci, N. S.; Padinger, F.; Fromherz, T.; Hummelen, J. C., 2.5% efficient organic plastic solar cells. *Applied Physics Letters* **2001**, *78* (6), 841-843.
43. Wienk, M. M.; Kroon, J. M.; Verhees, W. J. H.; Knol, J.; Hummelen, J. C.; van Hal, P. A.; Janssen, R. A. J., Efficient methano[70]fullerene/MDMO-PPV bulk heterojunction photovoltaic cells. *Angewandte Chemie-International Edition* **2003**, *42* (29), 3371-3375.
44. (a) Melzer, C.; Koop, E. J.; Mihailetschi, V. D.; Blom, P. W. M., Hole transport in poly(phenylene vinylene)/methanofullerene bulk-heterojunction solar cells. *Advanced Functional Materials* **2004**, *14* (9), 865-870; (b) Mihailetschi, V. D.; Koster, L. J. A.; Blom, P. W. M.; Melzer, C.; de Boer, B.; van Duren, J. K. J.; Janssen, R. A. J., Compositional dependence of the performance of poly(p-phenylene vinylene): Methanofullerene bulk-heterojunction solar cells. *Advanced Functional Materials* **2005**, *15* (5), 795-801.
45. Thompson, B. C.; Frechet, J. M. J., Organic photovoltaics - Polymer-fullerene composite solar cells. *Angewandte Chemie-International Edition* **2008**, *47* (1), 58-77.
46. Sirringhaus, H.; Brown, P. J.; Friend, R. H.; Nielsen, M. M.; Bechgaard, K.; Langeveld-Voss, B. M. W.; Spiering, A. J. H.; Janssen, R. A. J.; Meijer, E. W.; Herwig, P.; de Leeuw, D. M., Two-dimensional charge transport in self-organized, high-mobility conjugated polymers. *Nature* **1999**, *401* (6754), 685-688.
47. Ma, W. L.; Yang, C. Y.; Gong, X.; Lee, K.; Heeger, A. J., Thermally stable, efficient polymer solar cells with nanoscale control of the interpenetrating network morphology. *Advanced Functional Materials* **2005**, *15* (10), 1617-1622.

48. Li, G.; Shrotriya, V.; Huang, J. S.; Yao, Y.; Moriarty, T.; Emery, K.; Yang, Y., High-efficiency solution processable polymer photovoltaic cells by self-organization of polymer blends. *Nature Materials* **2005**, *4* (11), 864-868.
49. (a) Zhao, Y.; Xie, Z. Y.; Qu, Y.; Geng, Y. H.; Wang, L. X., Solvent-vapor treatment induced performance enhancement of poly(3-hexylthiophene): methanofullerene bulk-heterojunction photovoltaic cells. *Applied Physics Letters* **2007**, *90* (4), -; (b) Park, J. H.; Kim, J. S.; Lee, J. H.; Lee, W. H.; Cho, K., Effect of Annealing Solvent Solubility on the Performance of Poly(3-hexylthiophene)/Methanofullerene Solar Cells. *J. Phys. Chem. C* **2009**, *113* (40), 17579-17584.
50. Tang, H. W.; Lu, G. H.; Li, L. G.; Li, J.; Wang, Y. Z.; Yang, X. N., Precise construction of PCBM aggregates for polymer solar cells via multi-step controlled solvent vapor annealing. *Journal of Materials Chemistry* **2010**, *20* (4), 683-688.
51. (a) Huttner, S.; Sommer, M.; Chiche, A.; Krausch, G.; Steiner, U.; Thelakkat, M., Controlled solvent vapour annealing for polymer electronics. *Soft Matter* **2009**, *5* (21), 4206-4211; (b) Miller, S.; Fanchini, G.; Lin, Y. Y.; Li, C.; Chen, C. W.; Su, W. F.; Chhowalla, M., Investigation of nanoscale morphological changes in organic photovoltaics during solvent vapor annealing. *Journal of Materials Chemistry* **2008**, *18* (3), 306-312.
52. Irwin, M. D.; Buchholz, B.; Hains, A. W.; Chang, R. P. H.; Marks, T. J., p-Type semiconducting nickel oxide as an efficiency-enhancing anode interfacial layer in polymer bulk-heterojunction solar cells. *P Natl Acad Sci USA* **2008**, *105* (8), 2783-2787.
53. Havinga, E. E.; Tenhoeve, W.; Wynberg, H., A New Class of Small Band-Gap Organic Polymer Conductors. *Polym Bull* **1992**, *29* (1-2), 119-126.
54. Bundgaard, E.; Krebs, F. C., Low band gap polymers for organic photovoltaics. *Solar Energy Materials and Solar Cells* **2007**, *91* (11), 954-985.

55. Peet, J.; Kim, J. Y.; Coates, N. E.; Ma, W. L.; Moses, D.; Heeger, A. J.; Bazan, G. C., Efficiency enhancement in low-bandgap polymer solar cells by processing with alkane dithiols. *Nature Materials* **2007**, *6* (7), 497-500.
56. Moule, A. J.; Meerholz, K., Controlling morphology in polymer-fullerene mixtures. *Advanced Materials* **2008**, *20* (2), 240-245.
57. (a) Blouin, N.; Michaud, A.; Leclerc, M., A low-bandgap poly(2,7-carbazole) derivative for use in high-performance solar cells. *Advanced Materials* **2007**, *19*, 2295-2300; (b) Blouin, N.; Michaud, A.; Gendron, D.; Wakim, S.; Blair, E.; Neagu-Plesu, R.; Belletete, M.; Durocher, G.; Tao, Y.; Leclerc, M., Toward a rational design of poly(2,7-carbazole) derivatives for solar cells. *Journal of the American Chemical Society* **2008**, *130* (2), 732-742.
58. Wakim, S.; Beaupre, S.; Blouin, N.; Aich, B. R.; Rodman, S.; Gaudiana, R.; Tao, Y.; Leclerc, M., Highly efficient organic solar cells based on a poly(2,7-carbazole) derivative. *Journal of Materials Chemistry* **2009**, *19* (30), 5351-5358.
59. Park, S. H.; Roy, A.; Beaupre, S.; Cho, S.; Coates, N.; Moon, J. S.; Moses, D.; Leclerc, M.; Lee, K.; Heeger, A. J., Bulk heterojunction solar cells with internal quantum efficiency approaching 100%. *Nat. Photonics* **2009**, *3* (5), 297-U5.
60. (a) Chu, T. Y.; Alem, S.; Tsang, S. W.; Tse, S. C.; Wakim, S.; Lu, J. P.; Dennler, G.; Waller, D.; Gaudiana, R.; Tao, Y., Morphology control in polycarbazole based bulk heterojunction solar cells and its impact on device performance. *Applied Physics Letters* **2011**, *98* (25); (b) He, Z. C.; Zhong, C. M.; Huang, X.; Wong, W. Y.; Wu, H. B.; Chen, L. W.; Su, S. J.; Cao, Y., Simultaneous Enhancement of Open-Circuit Voltage, Short-Circuit Current Density, and Fill Factor in Polymer Solar Cells. *Advanced Materials* **2011**, *23* (40), 4636-4643.
61. (a) Kim, J. Y.; Lee, K.; Coates, N. E.; Moses, D.; Nguyen, T. Q.; Dante, M.; Heeger, A. J., Efficient tandem polymer solar cells fabricated by all-solution processing. *Science*

- 2007**, 317 (5835), 222-225; (b) Cho, S.; Lee, K.; Heeger, A. J., Extended Lifetime of Organic Field-Effect Transistors Encapsulated with Titanium Sub-Oxide as an 'Active' Passivation/Barrier Layer. *Advanced Materials* **2009**, 21 (19), 1941-1944; (c) Roy, A.; Park, S. H.; Cowan, S.; Tong, M. H.; Cho, S. N.; Lee, K.; Heeger, A. J., Titanium suboxide as an optical spacer in polymer solar cells. *Applied Physics Letters* **2009**, 95 (1) 013302.
62. Andersson, B. V.; Huang, D. M.; Moule, A. J.; Inganäs, O., An optical spacer is no panacea for light collection in organic solar cells. *Applied Physics Letters* **2009**, 94 (4) 043302.
63. Zhao, G. J.; He, Y. J.; Li, Y. F., 6.5% Efficiency of Polymer Solar Cells Based on poly(3-hexylthiophene) and Indene-C(60) Bisadduct by Device Optimization. *Advanced Materials* **2010**, 22 (39), 4355-4358.
64. (a) Anctil, A.; Babbitt, C. W.; Raffaele, R. P.; Landi, B. J., Material and Energy Intensity of Fullerene Production. *Environ Sci Technol* **2011**, 45 (6), 2353-2359; (b) Garcia-Valverde, R.; Cherni, J. A.; Urbina, A., Life cycle analysis of organic photovoltaic technologies. *Progress in Photovoltaics* **2010**, 18 (7), 535-558.
65. Moore, J. R.; Albert-Seifried, S.; Rao, A.; Massip, S.; Watts, B.; Morgan, D. J.; Friend, R. H.; McNeill, C. R.; Srinivasan, H., Polymer Blend Solar Cells Based on a High-Mobility Naphthalenediimide-Based Polymer Acceptor: Device Physics, Photophysics and Morphology. *Advanced Energy Materials* **2011**, 1 (2), 230-240.
66. (a) Li, G.; Shrotriya, V.; Yao, Y.; Huang, J. S.; Yang, Y., Manipulating regioregular poly(3-hexylthiophene): [6,6]-phenyl-C-61-butyric acid methyl ester blends - route towards high efficiency polymer solar cells. *Journal of Materials Chemistry* **2007**, 17 (30), 3126-3140; (b) Yang, X.; Loos, J., Toward high-performance polymer solar cells: The importance of morphology control. *Macromolecules* **2007**, 40 (5), 1353-1362.

67. Mayer, A. C.; Toney, M. F.; Scully, S. R.; Rivnay, J.; Brabec, C. J.; Scharber, M.; Koppe, M.; Heeney, M.; McCulloch, I.; McGehee, M. D., Bimolecular Crystals of Fullerenes in Conjugated Polymers and the Implications of Molecular Mixing for Solar Cells. *Advanced Functional Materials* **2009**, *19* (8), 1173-1179.
68. Cates, N. C.; Gysel, R.; Beiley, Z.; Miller, C. E.; Toney, M. F.; Heeney, M.; McCulloch, I.; McGehee, M. D., Tuning the Properties of Polymer Bulk Heterojunction Solar Cells by Adjusting Fullerene Size to Control Intercalation. *Nano Letters* **2009**, *9* (12), 4153-4157.
69. (a) Chu, C. W.; Yang, H. C.; Hou, W. J.; Huang, J. S.; Li, G.; Yang, Y., Control of the nanoscale crystallinity and phase separation in polymer solar cells. *Applied Physics Letters* **2008**, *92* (10), -; (b) Szarko, J. M.; Guo, J. C.; Liang, Y. Y.; Lee, B.; Rolczynski, B. S.; Strzalka, J.; Xu, T.; Loser, S.; Marks, T. J.; Yu, L. P.; Chen, L. X., When Function Follows Form: Effects of Donor Copolymer Side Chains on Film Morphology and BHJ Solar Cell Performance. *Advanced Materials* **2010**, *22* (48), 5468-5472; (c) Kim, Y.; Cook, S.; Tuladhar, S. M.; Choulis, S. A.; Nelson, J.; Durrant, J. R.; Bradley, D. D. C.; Giles, M.; McCulloch, I.; Ha, C. S.; Ree, M., A strong regioregularity effect in self-organizing conjugated polymer films and high-efficiency polythiophene: fullerene solar cells. *Nature Materials* **2006**, *5* (3), 197-203.
70. (a) Collins, B. A.; Gann, E.; Guignard, L.; He, X.; McNeill, C. R.; Ade, H., Molecular Miscibility of Polymer, ð Fullerene Blends. *The Journal of Physical Chemistry Letters* **2010**, *1* (21), 3160-3166; (b) Muller, C.; Bergqvist, J.; Vandewal, K.; Tvingstedt, K.; Anselmo, A. S.; Magnusson, R.; Alonso, M. I.; Moons, E.; Arwin, H.; Campoy-Quiles, M.; Inganäs, O., Phase behaviour of liquid-crystalline polymer/fullerene organic photovoltaic blends: thermal stability and miscibility. *Journal of Materials Chemistry* **2011**, *21* (29), 10676-10684; (c) Treat, N. D.; Brady, M. A.; Smith, G.; Toney, M. F.; Kramer, E. J.; Hawker, C. J.; Chabynyc,

M. L., Interdiffusion of PCBM and P3HT Reveals Miscibility in a Photovoltaically Active Blend. *Advanced Energy Materials* **2011**, *1* (1), 82-89.

71. (a) Cabanillas-Gonzalez, J.; Grancini, G.; Lanzani, G., Pump-Probe Spectroscopy in Organic Semiconductors: Monitoring Fundamental Processes of Relevance in Optoelectronics. *Advanced Materials* **2011**, *23* (46), 5468-5485; (b) Westenhoff, S.; Howard, I. A.; Friend, R. H., Probing the Morphology and Energy Landscape of Blends of Conjugated Polymers with Sub-10 nm Resolution. *Physical Review Letters* **2008**, *101* (1), 016102.

CHAPTER 3: METHODS

SECTION 3.1: INTRODUCTION

In this chapter the procedures for sample preparation and the techniques for sample characterisation are described. In Section 3.2 the materials used in this thesis are presented, after which the methods for preparing solutions and thin films are outlined. The fabrication process for Organic Photovoltaic Devices (OPVs) and hole-only devices is discussed in section 3.3. The experimental techniques are covered in section 3.4. Where collaborative work has been included or referred to in this thesis, a summary of the technique used is given for the aid of the reader.

SECTION 3.2: MATERIALS, SOLUTION AND THIN FILM PREPARATION

All of the materials for the work in this thesis were used as-received from the supplier. P3HT was supplied by Rieke Metals (Product 4002E). The molecular weight of the polymer was 13,510 g/mol as determined by gel permeation chromatography (GPC). The regioregularity was between 90% and 95%, according to manufacturer specifications. PCBM and PC₇₀BM were supplied by Solenne to purities of 99% and 95% respectively. PCDTBT was synthesised by the Department of Chemistry at the University of Sheffield, and had a molecular weight of 33,100 g/mol as determined by GPC. Except where stated, sample preparation was conducted

under glove box conditions, with the dry nitrogen atmosphere typically containing water and O₂ content of between 2 and 5 ppm.

To prepare thin films either of pure materials or blends, the materials were first dissolved into a chlorinated solvent (anhydrous with greater than 98% purity) supplied by Aldrich. For P3HT and PCBM, chlorobenzene, 1,2-dichlorobenzene or 1,4-trichlorobenzene were used. Chloroform was used as casting solvent for studies on PCDTBT and PCDTBT:PC₇₀BM. Solutions were prepared in borosilicate amber glass vials to minimise the risk of solvent photo-degradation. Materials were weighed out using a calibrated microbalance in ambient conditions before mixing with solvent in a glove box environment. For studies on P3HT:PCBM the concentration of P3HT and PCBM precursor solution was kept constant at 25 mg/ml in all solvents. Blend solutions were subsequently prepared by mixing precursor solutions by volume in order to obtain the desired solid weight composition (wt%). For studies on PCDTBT and PCDTBT:PC₇₀BM thin films, the concentration of PCDTBT and PC₇₀BM precursor solutions was 4 mg/ml and 25 mg/ml respectively. To encourage dissolution of material, solutions were placed onto a hotplate held at 70°C for a period of up to 24 hrs. The final step in solution preparation was filtration, through a 0.25 µm PTFE filter after the solutions were cooled down to room temperature. Following filtration solutions were typically used within one hour to minimise gelation or aggregation of solid contents.

Thin films were prepared by spin-coating, or for the work presented in chapter 4, section 4.1, by bar-coating. For spin-coating, a droplet (30-50 µl) of solution is deposited via pipette tip onto a substrate that can either be stationary or already rotating. For samples in this thesis the second method was used throughout. Spin-coating is a relatively rapid film forming process,

owing to the amount of excess solution which is initially expelled from the substrate. Any remaining solution that has wetted the substrate subsequently dries to form a relatively smooth and uniform film. The following relationship is used to relate film thickness, d , to experimental conditions in spin coating,

$$d \propto cv / \sqrt{\omega} \quad \{3.1\}$$

Here c and v are the solution concentration and solution viscosity respectively and ω is the rotation speed (rad s^{-1}) of the substrate.

For thin films prepared by bar-coating, 90 μl of solution was deposited via a computer controlled syringe pump in front of a wire bound steel rod resting on a silicon / native oxide substrate. Capillary action allows the solution to wick along the length of the bar, which is subsequently spread by translating the bar across the substrate. In this work, the translation of the bar was controlled by computer. In addition, small weights were placed at either end of the bar to ensure a uniform pressure was applied across the substrate. In contrast to spin-coating, a far smaller percentage of the deposited solution is wasted and the drying time (typically) is far greater. A schematic of the bar coater used in this thesis is presented in Figure 3.1.

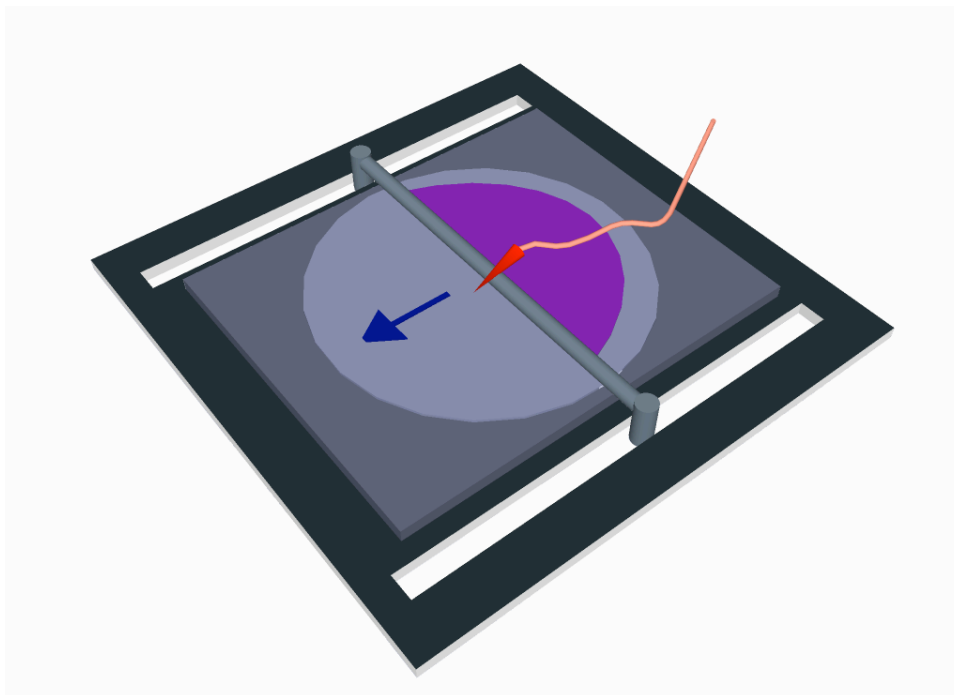


Figure 3.1: Schematic of a bar-coater illustrating the film deposition process. A pipette tip (here illustrated in red) is attached to the bar and connected to a syringe pump (not shown). Solution deposition occurs prior to translation of the bar across the substrate. The direction of film spreading is indicated by the blue arrow.

Thin films for microscopy or spectroscopy characterisation were cast onto glass or silicon/native oxide substrates. Prior to film casting, substrates were sonicated in warm isopropanol (IPA), dried under N_2 flow and subject to a brief (5 to 10 minutes) O_2 plasma to remove any residual organic material. Film thicknesses were determined across a scratch made into the film using either profilometry (Dektak 3) or atomic force microscopy.

SECTION 3.3: DEVICE PREPARATION

A schematic of the devices fabricated in this thesis, illustrating the different layers present, is presented in Figure 3.2. All devices were fabricated onto 15 x 20 mm² glass substrates, pre-patterned with a 100 nm layer of Indium Tin Oxide (ITO). Prior to use, these substrates were sonicated in warm NaOH (10 wt% in water)ⁱ, deionised water and IPA. An aqueous dispersion of PEDOT:PSS (Baytron 4083 Special Grade) was used to spin-cast the hole transport layer in ambient conditions after passing through a 0.25 μm PVDF filter. For all devices this layer had a thickness of 30 ± 4 nm.

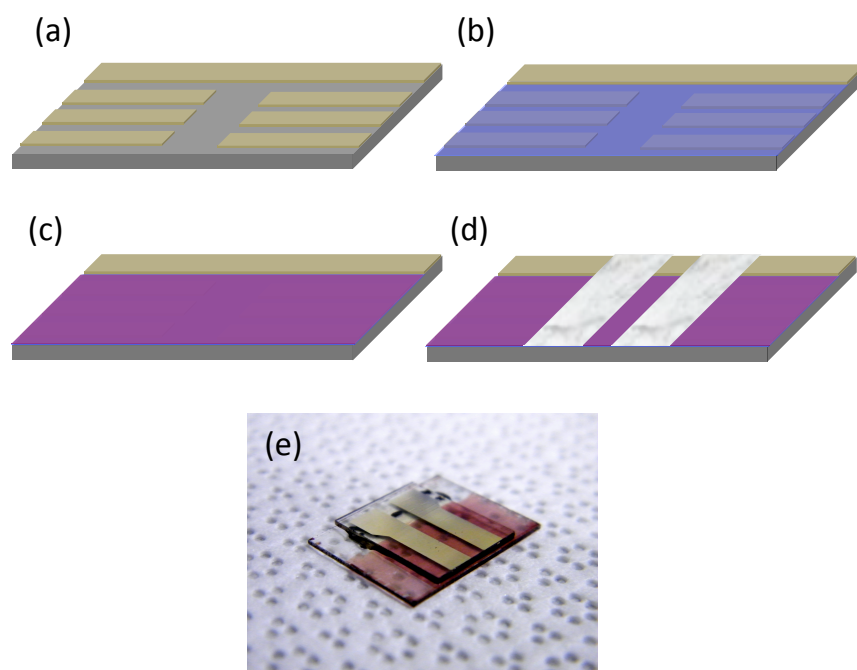


Figure 3.2: Diagram illustrating the architecture and different layers present in OPVs fabricated for this thesis. Part (a) shows the glass/pre-patterned ITO substrate, subsequently coated with PEDOT:PSS (b), active semiconducting layer (c) and aluminium cathode through a shadow mask (d). A photograph of a complete device, after encapsulation with a glass cover slip is presented in (e).

ⁱ For removal of a protective resist on the ITO.

Before deposition of the active semiconducting layer, the PEDOT:PSS coated substrates were transferred into a dry glove box environment and baked at 115°C for two minutes to remove any residual water content. Semiconducting thin films were prepared by spin-casting solution onto a substrate, with spin speeds between 750 rpm and 2500 rpm typically used. For blend thin films of P3HT:PCBM the thickness was kept constant at 70 ± 4 nm, with the substrate spin-speed used as a variable to compensate for variations in solution viscosity. After preparing the active layer, any semiconducting material in contact with the top ITO electrical contact was removed via gentle wiping using a cotton bud dipped in IPA (or, for PCDTBT samples, chloroform). This step was necessary to allow for electrical contact between the cathode and ITO strip (as shown in Figure 3.2(d)). Following this step, samples were transferred within the glove box to a high-vacuum system for thermal evaporation of a cathode. Note that for samples subject to a solvent vapour anneal, samples were transferred into a metal containerⁱⁱ prior to cathode deposition. Within the container the samples were held on a rack raised above the container base. A small quantity (~5 ml) of neat solvent at the container base provided a solvent rich atmosphere.

For all OPVs 100 nm of aluminium was used as the cathode. This was typically deposited at a rate of $1-2 \text{ \AA s}^{-1}$ at a pressure of $\sim 10^{-6}$ mbar. For hole only devices, 100 nm of gold was used, deposited at a rate of approximately 5 \AA s^{-1} at a pressure of 10^{-5} mbar. Samples for hole only devices were subject to approximately 10 minutes exposure to ambient conditions during transfer from a glove box environment to a thermal evaporator. During electrode deposition a shadow mask was used to define two stripes across each device. The overlap of ITO and top electrode defined the active area of each pixel, which was $1.5 \times 3 \text{ mm}^2$.

ⁱⁱ Cylindrical, approximately 15 cm in height and 10 cm in diameter.

Thermal annealing, where used, was carried out on samples after deposition of the top electrode. Samples were placed onto a hot plate held at the required temperature, thus facilitating a rapid heating process. After isothermal annealing, samples were immediately transferred onto a copper plate held at ambient temperature, thereby facilitating a rapid cooling process.

The final step in device fabrication was encapsulation of the central area of each substrate, to improve the stability of the device when transferred and subsequently tested under ambient conditions. For encapsulation, a glass slide and curable epoxy was used. Devices were placed under UV light for 30 minutes in order to set the epoxy.

SECTION 3.4: EXPERIMENTAL TECHNIQUES

SECTION 3.4.1: UV-VISIBLE SPECTROSCOPY

The mechanisms for light absorption and emission from organic semiconductors are covered in chapter 2, section 2.3. For both absorption and photoluminescence (PL) measurements, spectra were acquired under steady state conditions using a Horiba Fluoromax 4 Spectrofluorimeter. All samples were measured under ambient conditions. To minimise any effects of sample degradation upon exposure to air, samples were measured immediately after transfer from a dry nitrogen glovebox. A schematic of the Fluoromax 4 is shown in Figure 3.3. The instrument allows for continuously variable excitation (200 to 950 nm, optimised in the UV) by means of a xenon arc lamp and monochromator. A photomultiplier tube (PMT) is

used to measure emission (200 to 850 nm, optimised in the visible). A photodiode placed prior to the sample monitors the output of the lamp, thereby providing a correction factor for any temporal or wavelength variations in lamp power.

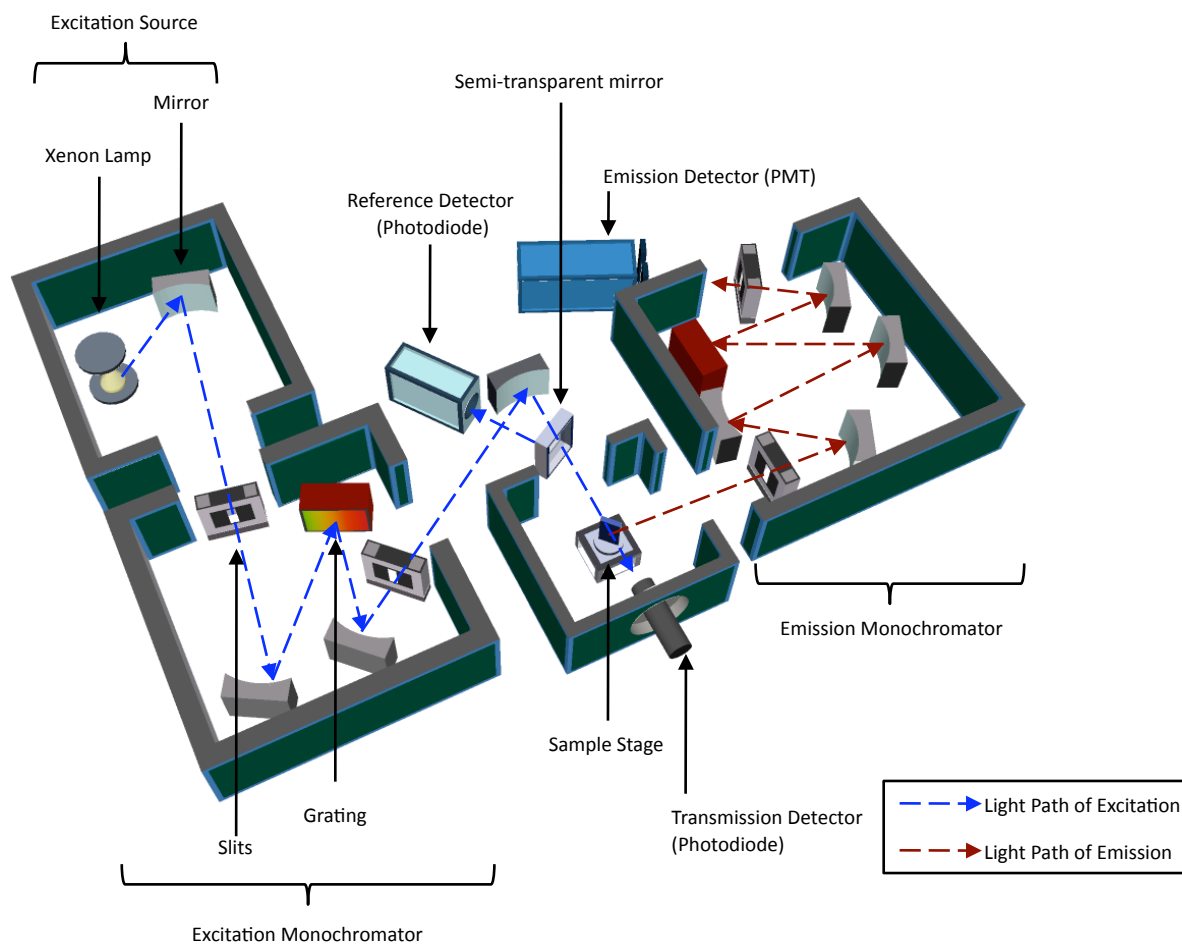


Figure 3.3: Layout of the optical components within the Horiba Fluoromax 4. For clarity, only the first instance of each component (i.e. mirror, slits and grating) is labeled. The light path of the excitation and emission beams are given in blue and red respectively.

Absorption spectra were obtained in transmission geometry i.e. a silicon photodiode was placed in the path of the light incident upon a sample.

The absorbance A , or optical density $O.D.$ for a thin film can be calculated using the following expression,

$$A = O.D. = -\log_{10} \left(\frac{I(\lambda)}{I_0(\lambda)} \right) \quad \{3.2\}$$

where $I(\lambda)$ and $I_0(\lambda)$ are the sample transmittance and reference transmittance (as a function of wavelength) respectively over the wavelength range of interest. For the reference spectrum, an uncoated substrate was placed in front of the photodiode. In addition, both transmittance spectra were normalised against the power output recorded by the reference detector to account for any potential variations in light output between the separate measurements.

PL spectra were obtained in reflection geometry, with any emission collected at 90° relative to the excitation beam. Emission was detected using a photomultiplier tube (PMT) and normalised against the signal from the reference detector (proportional to incident light intensity). To minimise any specular reflection of the excitation light onto the collection optics, samples were orientated at 30° away from the beam. A long-pass filter was also placed before the collection optics to prevent second-order reflections of the excitation light reaching the PMT.

The PL spectrum for a thin film was first calculated by subtracting from the raw data any signal from an uncoated substrate measured under identical conditions. To calculate the corrected emission intensity $I_{Corrected}$ from the thin film, absorption effects from either the

filter or sample itself (through self-absorption) were accounted for by using the following expression,

$$I_{Corrected} = I_{Measured} 10^{-\left(\frac{OD_{ex} + OD_{em}}{2}\right)} \quad \{3.3\}$$

Here $I_{Measured}$ is the raw emission data, and OD_{ex} and OD_{em} represent the optical densities of the excitation and emission attenuation respectively.

SECTION 3.4.2: ATOMIC FORCE MICROSCOPY

Atomic Force Microscopy (AFM) is a scanning probe microscopy technique whereby a cantilever with a sharp (several nm in curvature) tip on one end is rastered across the surface of a sample. AFM can be performed by keeping the tip in direct contact with the sample throughout the measurement ('contact mode') or oscillating the cantilever to provide intermittent contact between tip and sample ('tapping mode'). Owing to the relative softness of the materials studied in this thesis, tapping mode AFM was used throughout. Although spatial resolution is reduced and data acquisition times are increased, sample damage is minimised. A schematic of the setup is presented in Figure 3.4. In tapping mode AFM, the cantilever is driven close to its resonance frequency, with the tip coming into contact with the sample at its maximum displacement. The displacement of the tip is monitored via a laser beam directed to the top of the cantilever and deflected onto a split four-quadrant photodiode. An electronic feedback loop maintains constant oscillation amplitude by monitoring the RMS

of the amplitude signal on the photodetector. A topographic ‘image’ of a sample surface is constructed by recording the relative height of the scanner at each position in the scan area which is needed to maintain a constant ‘setpoint’ amplitude. A series of piezoelectric motors are used for scanning the cantilever along the sample surface (x,y), with a separate piezoelectric motor used for adjusting the vertical position (z) of the cantilever or sample.

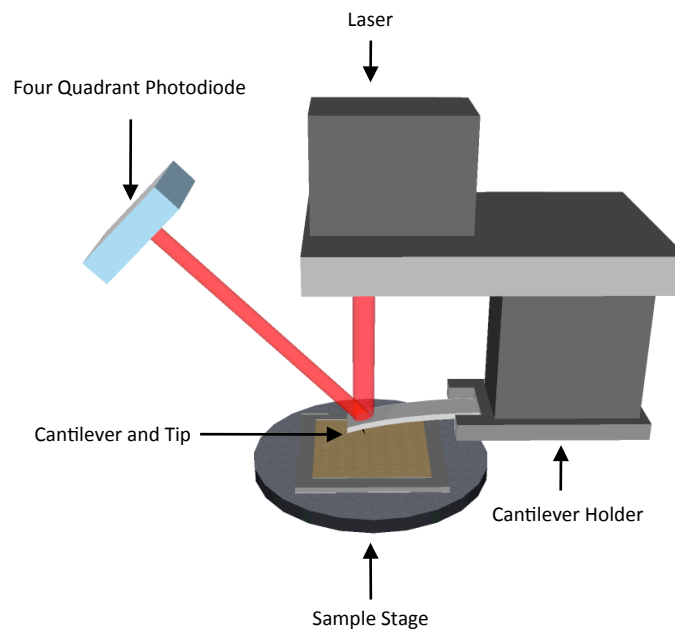


Figure 3.4: Schematic of the principle components in an AFM. Relative motion between sample and tip may be achieved via orthogonal (x,y and z direction) piezo-electric motors which displace either the cantilever (i.e. motors placed above the sample) or the sample stage (motors placed below the sample). Note that an electronic feedback loop (not shown) exists between the detector electronics and the controller electronics linked to the cantilever.

For phase imaging, a separate controller module monitors the phase lag between the cantilever oscillation signal and the signal sent to the piezoelectric motors at each position (x,y) in a scan. This quantity is sensitive to material properties (for example adhesion), thus

providing a contrast mechanism in samples containing more than one material, or a single material in different phases (e.g. amorphous and semi-crystalline). The resolution of phase imaging through tapping mode AFM is comparable to contact mode AFM, with the added benefit that boundaries on a sample surface that are potentially obscured by large height variations can be seen with greater clarity. A Veeco Instruments Dimension 3100 or Multimode 4 was used to perform AFM. Aluminium coated silicon tips from Budget Sensors (Tap 300 Al-G) with a resonance frequency of 300kHz and spring constant of 40 N/m were used throughout. The obtained data was processed using the Gwyddion software package.

SECTION 3.4.3: SPECTROSCOPIC ELLIPSOMETRY

Spectroscopic Ellipsometry (SE) measures the change in polarisation of a light beam reflected from a sample relative to a reference signal. These changes are sensitive to the optical properties and thickness of the sample under investigation. Consequently it is these characteristics that can be extracted in an ellipsometry experiment. In this work a J A Wollam M2000v instrument was used, which is illustrated schematically in Figure 3.5. The wavelength range of the instrument is 370 to 1000 nm. Light from a xenon lamp is passed through a monochromator, fixed angle polariser and mechanical chopper before reaching the sample. Upon reflection, the light is passed through a rotating polariser analyser before reaching a detector. Note that both the light source and detector are positioned at the same angle above the plane of the sample surface. Two quantities are measured, r_s and r_p , which represent the amplitude of light orientated perpendicular and parallel to the plane of incidence respectively. These quantities are normalised to their initial values.

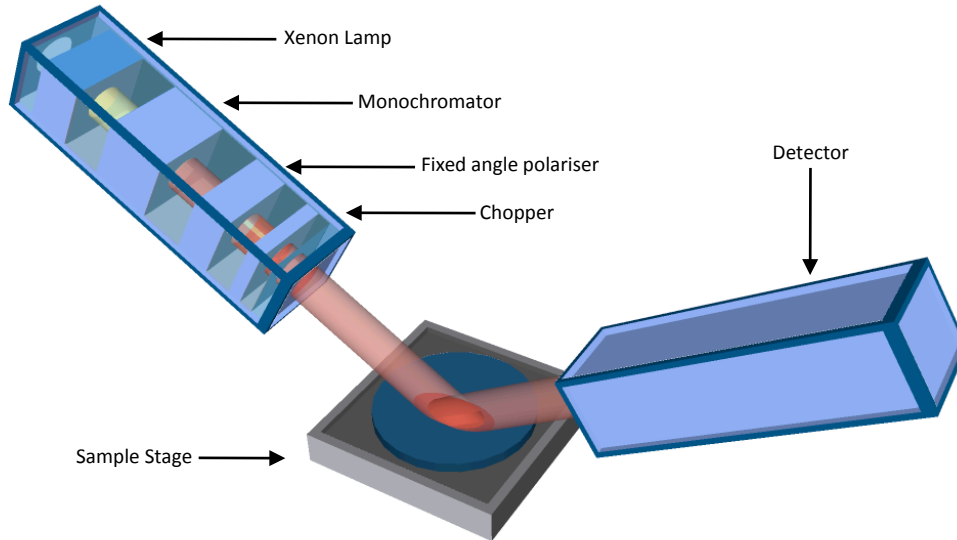


Figure 3.5: Schematic of the principle components inside a spectroscopic ellipsometer. Components inside the source head (left module) are labeled individually. Note that a rotating polariser-analyser is contained within the detector head.

The ratio of r_s to r_p is the reflectance ratio, ρ , which can be written as follows,

$$\rho = \frac{r_s}{r_p} = \tan(\Phi)e^{i\Delta} \quad \{3.4\}$$

Note that ρ is a complex quantity. From the quantities Φ and Δ it is possible to determine the thickness of the sample and its complex refractive index, $\tilde{n} = n + ik$, by building a model to best match Φ and Δ as a function of wavelength. Here n and k represent the refractive index and extinction coefficient respectively.

Film thicknesses were estimated using a Cauchy dispersion model, which considers the real component of \tilde{n} only. This is expressed as,

$$n = A + \frac{B}{\lambda^2} + \frac{C}{\lambda^4} \quad \{3.5\}$$

where A , B and C are positive constants to be determined through the fitting process. A limitation of the model is that it can only be applied to data corresponding to a transmissive ($k \approx 0$) wavelength region of a material, for example below the band-gap of a semiconductor.

To model ρ for wavelengths at which a film is absorbing, both n and k must be accounted for. To minimise the number of fitting parameters, the thickness determined by the Cauchy model is used as an input. A Lorentz oscillator model can be used as a spline model to fit to the data, which can be written in the following form,

$$\tilde{\varepsilon} = \varepsilon_{offset} + \frac{AE_C}{E_C - E^2 - iBE} \quad \{3.6\}$$

Here E is the photon energy and A , B , E_C and ε_{offset} represent the amplitude, broadening, center energy and offset respectively for a modeled absorption band.

The CompleteVASE software package was used to collect and model the ellipsometry data. The quality of the fit is quantified by its mean squared error (MSE), which considers the difference between modeled and measured data sets. It is important to acknowledge that the modeling process is regressive and thus has the potential to settle into a local MSE ‘minima’, away from the best apparent fit (global minimum MSE). Also the fitting procedure may yield values of n or k that are non-physical. Thus complimentary techniques (for example, profilimetry or absorbance measurements) are used to judge the goodness of any modeled fits.

SECTION 3.4.4: GRAZING INCIDENCE WIDE ANGLE X-RAY SCATTERING

Grazing Incidence Wide Angle X-Ray Scattering (GIWAXS) is a diffraction technique for characterising structural features in a thin film at a length scale ranging from a few Angstroms up to several nanometers. As with conventional WAXS, from a GIWAXS experiment it is possible to characterise the unit cell dimensions of a material, crystallite size and overall material crystallinity (i.e. the relative fraction of amorphous to crystalline material). Using a 2D detector it is also possible to measure and characterise the texture (orientation with respect to a reference plane) of any crystalline domains present. The advantage of GIWAXS over WAXS is the substantial increase in sampling volume that is achieved by illuminating the sample at a low angle of incidence. If the sample covers a sufficiently large area, X-rays will typically interact with the sample over a path length of several cm in a GIWAXS experiment. In contrast, the path length will equal the sample thickness for a WAXS experiment performed in a transmission geometry. Thus GIWAXS is

more suited for probing the crystal structure of materials which weakly scatter X-rays, for example organic semiconductors. By using X-rays from a synchrotron source, the high flux of incident photons improves the signal-to-noise ratio and permits relatively short data acquisition times for the types of materials studied here, or for the possibility for tracking dynamic processes that occur over short time intervals. The experimental beam lines I07 and I22 at the Diamond Light Source were used to collect GIWAXS data for the samples investigated in this thesis, using X-rays with energy of 8 to 12 keV. A schematic of the set-up used is presented in Figure 3.6.

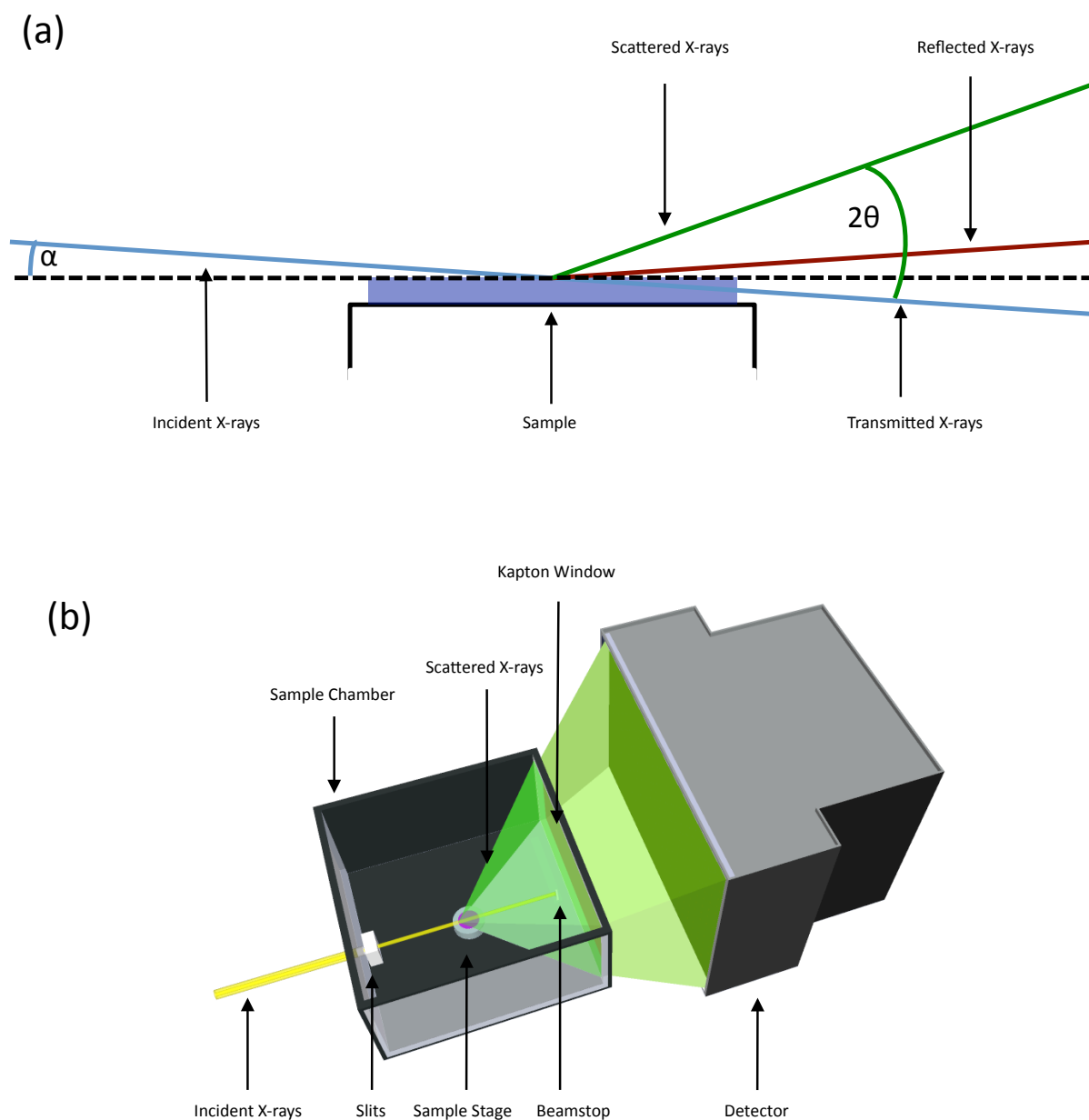


Figure 3.6: The geometry of a GIWAXS measurement is presented in part (a), highlighting the different paths light may take upon interaction with the sample. Here α represents the angle of incidence between the incident X-rays and the plane of the sample surface. The angle 2θ is defined as the scattering angle between the scattered and transmitted X-rays. A top-down view of the experimental layout is presented in (b) with principle components labeled. Note that in order to reduce the scatter of X-rays by air the sample is housed within a closed cell through which He gas may be pumped. For the same reason, the detector sample distance should be minimised.

As shown, the sample (a thin film deposited onto silicon / native oxide substrate) is tilted at a shallow angle α relative to the path of an X-ray beam. These samples are prepared in a similar manner to samples prepared for the other characterisation techniques used in this thesis. Typically, the sample is tilted at a critical angle α_c in order to maximise the intensity of the scattered X-rays from the thin film, which roughly corresponds to the point at which incident X-rays undergo total internal reflection. Below this angle the incident beam the penetration depth of X-rays is restricted to the surface of the film, and thus the sampling volume of material is relatively small. Above α_c incident X-rays may penetrate through to the sample substrate, which eventually dominates any scattering signal. The angle α_c varies from material to material. However for conjugated polymers it is of the order of 0.1° . It can be seen that by varying α in an experiment, it is possible to selectively scatter X-rays from either the surface of a film or its bulk. Consequently, although not the focus of this work, it is possible to build a vertical profile of structural order within a thin film.

A 2D detector is placed in the path of the incident X-rays to collect any light that has interacted with the sample. The incident X-ray photons may undergo transmission, reflection or diffraction upon interaction with the sample, or scatter from the sample surface. It is possible that the detector will collect light that has undergone each of these processes. Because it is only the diffracted and scattered light which is of interest, appropriate attenuation must be included in the experimental set up to minimise the other signals, which can potentially be significantly more intense and swamp any useful data. A beam stop is used for this purpose – a small metal (typically lead) point several mm in thickness is positioned between sample and detector to attenuate the transmitted and specularly reflected X-ray beams. To reduce the amount of X-ray scatter by air, the signal-to-noise ratio of the diffracted light is improved by housing samples within a chamber containing a helium atmosphere.

Bragg diffraction governs the conditions under which X-rays undergo coherent diffraction with an ordered material. This can be described using Bragg's Law, where

$$n\lambda = 2d \sin(\theta) \quad \{3.7\}$$

Here n (an integer) is the order of the reflection, λ is the wavelength of X-ray photons, d is the distance between planes in a crystal lattice and θ is the angle between the incident X-ray beam and the scattering plane. It is apparent that a diffraction experiment yields information in reciprocal space (i.e. diffraction peaks at relatively high angles correspond to planes that have relatively small separation). In order to extract real space information, X-ray light as a function of scattering angle is instead considered as a reciprocal space quantity Q , using the following transformation,

$$Q = \frac{4\pi \sin(\theta)}{\lambda} = \frac{2\pi}{d} \quad \{3.8\}$$

Here the terms θ , λ and d have the same definition as in Equation 3.7. In order to set this scale on a detector, a material with well characterised Bragg peaks is used as a calibrant. For data presented in this thesis, Silver Behenate powder was used to calibrate the detector.

The full-width at half-maximum (FWHM) of a diffraction peak can yield information regarding the size of crystalline domains. The coherence length L is given simply as $L = 2\pi/\Delta$

where Δ is the FWHM of a diffraction peak. L estimates the distance over which crystal planes maintain a constant orientation with respect to a reference plane (e.g. the sample substrate).

Alternatively, the Scherrer Equation may be used to determine the mean domain size τ , given by,

$$\tau = \frac{K\lambda}{\beta \cos(\theta)} \quad \{3.9\}$$

Here K is a factor relating to the shape of the crystallite, λ is the wavelength of X-ray photons, β is the FWHM of a peak and θ is the diffraction angle. The shape factor is dependent upon the aspect ratio of the crystals and therefore may vary from material to material. It is common practice to set $K = 0.9$ to provide a relative domain size between different samples. Note that both L and τ will estimate a lower bound to the actual crystal domain size as other factors (e.g. instrumental effects) may broaden the diffraction peaks. GIWAXS data was collected using custom-written Diamond software and analysed using the FiberFix software package.

SECTION 3.4.5: DEVICE CHARACTERISATION

Three techniques are used in this work for device characterisation: photocurrent and dark current measurements (both as a function of applied bias) and photocurrent measurements at short-circuit conditions as a function of incident light wavelength. As discussed in chapter 2, section 2.5 it is the technique which can be used to determine the power conversion efficiency (PCE) of a device, whilst the third determines its external quantum efficiency (EQE). Dark current measurements are used to calculate the mobility of charge carriers within a device under the space charge limited regime, as discussed in chapter 2, section 2.4.5.

For PCE measurements, an OPV is connected to a custom-built test board via metal connections to each ITO strip. This board is placed beneath a Newport Lot Oriel 91159 Solar Simulator. The light from the simulator is filtered to approximate the AM 1.5G solar spectrum which was presented in Figure 1.1. A silicon photovoltaic device traceable to National Renewable Energy Laboratory (NREL) is used to calibrate the power output of the simulator to 1 sun (100 mW/cm^2) and the ambient temperature of the illuminated area to 25°C . A Keithly 237 source measure unit, controlled via computer, is used to measure the current from an OPV as a function of applied bias. The same setup is employed for dark current measurements, albeit with the simulator off and the device covered with black-out fabric.

For EQE measurements an OPV is mounted onto electrical contacts in front of a monochromated tungsten lamp. The setup is illustrated schematically in Figure 3.7. Over the wavelength range of interest, the current from the device is measured using the same equipment for the PCE measurement. Here however no voltage bias is applied to the device. For each experiment the current response of a silicon photodiode (with known quantum efficiency) is also measured. The ratio between the measured OPV current and photodiode current, normalised to the quantum efficiency of the photodiode, determines the external quantum efficiency of a device.

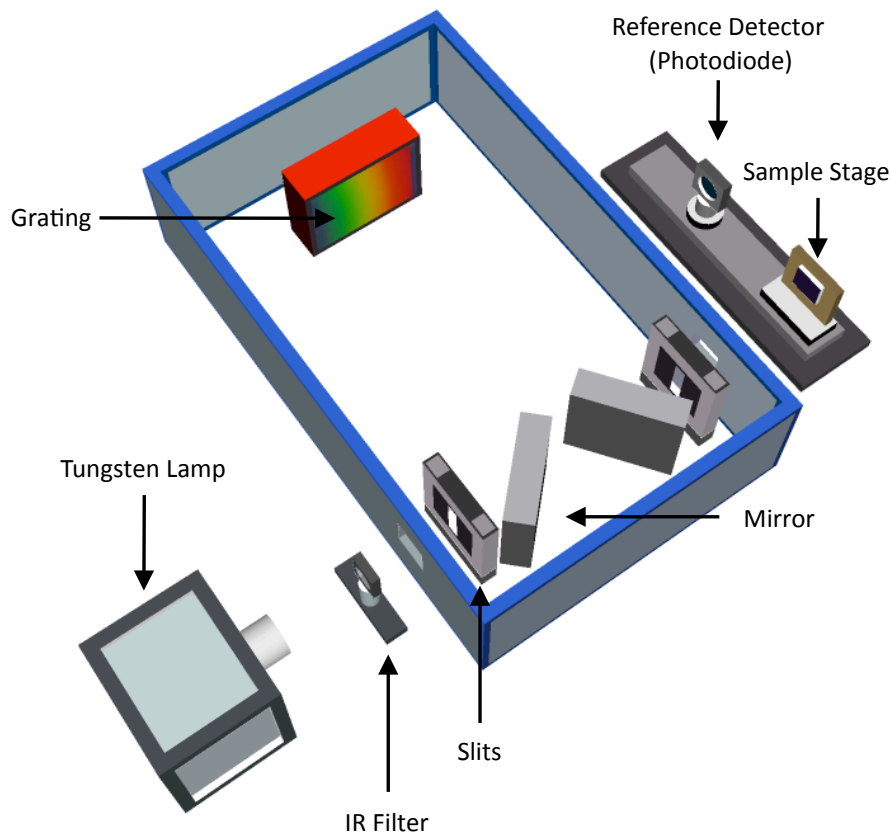


Figure 3.7: Schematic of the EQE setup, with principle components labeled. Note that the sample and photodiode are mounted onto a translation stage in order to move either element into the path of light exciting the monochromator.

SECTION 3.4.6: HELIUM ION MICROSCOPY

Helium Ion Microscopy (HeIM) is a surface characterisation technique whereby a focussed beam of He ions are rastered across a sample. The microscope is illustrated schematically in Figure 3.8. The ion beam is generated by ionisation of the imaging gas in the vicinity of a source. The source is constructed from a metal needle, which is manipulated by application of a high voltage until the apex of the needle resembles an atomically sharp tip. The most stable tip structure consists of three atoms in a trimer formation, and it is only these atoms that generate the ion beam. The ion beam emission from one atom is selected for imaging. Upon exit from the source chamber, the ion beam is collimated, apertured, directed and then focused onto the surface of a sample. Secondary electrons are one by-product of the interactions between He ions and the material(s) studied, and it is the generation rate / yield of secondary electrons that are measured as a function of position. This quantity is used to provide a contrast mechanism for the constructed grey scale images.

HeIM was performed using a Carl Zeiss Orion PLUS at the Department of Electronics & Computer Science, University of Southampton. Secondary electrons are measured with an Everheart-Thornley detector (a positively biased scintillator coupled to a photomultiplier tube) housed within the microscope. Data analysis was performed using the ImageJ software package.

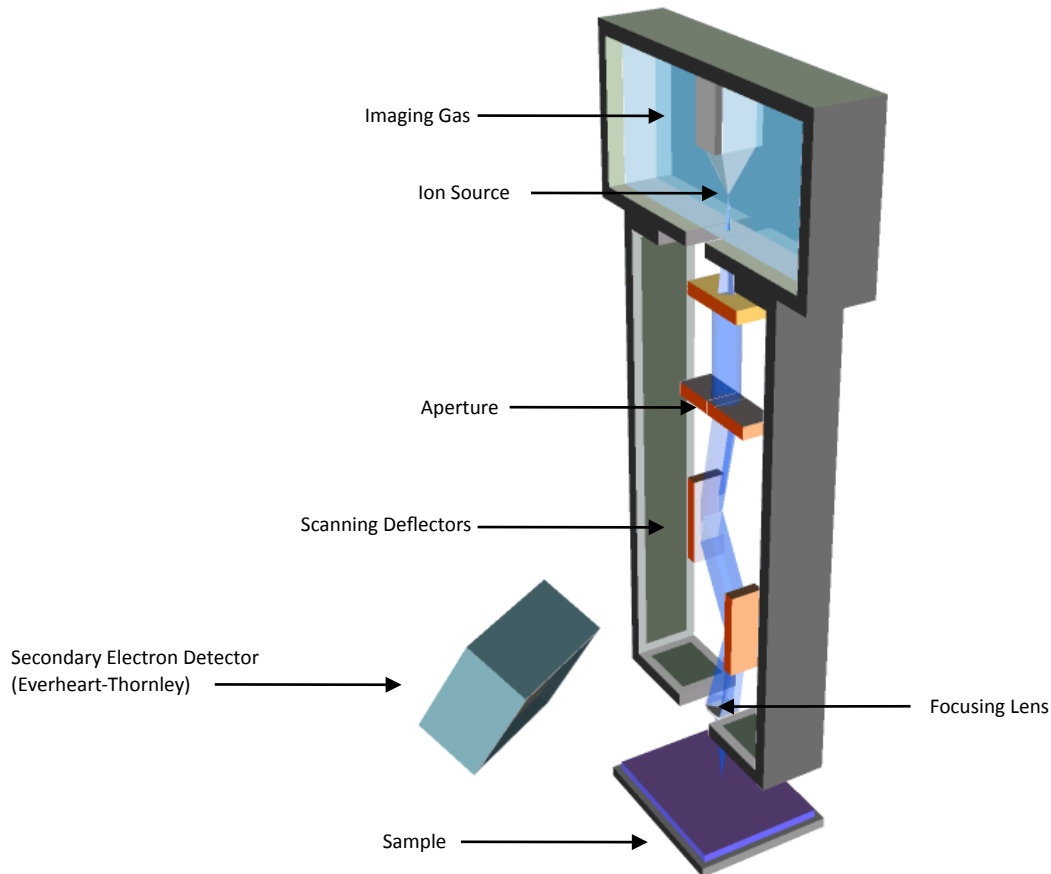


Figure 3.8: Principle components within a HeIM. Note that the optics, sample and detector are all enclosed within a high-vacuum environment.

SECTION 3.4.7: NEUTRON REFLECTIVITY

Neutron Reflectivity (NR) is a diffraction technique that can be used to determine the vertical composition of thin films. Reference is made to NR measurements in chapter 7. Andy Parnell, Christy Kinane and Robert Dalglish performed these experiments at the ISIS Neutron Source on thin film samples prepared by myself. In an NR experiment, a collimated beam of neutrons with a pre-defined distribution in momenta are directed onto a sample at a low angle of incidence ($\sim 1-2^\circ$). Neutrons to have undergone specular reflection from the

sample surface are measured using a time of flight detector, with neutrons of greatest velocity arriving first. A requirement of the sample is that the surface be extremely flat in order to maximise the intensity of the specularly reflected light. The layout of the experiment is similar to GIWAXS (see Figure 3.6). Here however the detector is raised to be at the same angle relative to the sample surface as the incident neutron beam.

A reflectivity profile is generated by measuring the relative intensity of neutrons as a function of momentum transfer i.e. the change in momentum upon reflection. Contrast in a sample is obtained because neutrons are sensitive to variations in nuclei density. In an analogous manner to Spectroscopic Ellipsometry, a model must be constructed to interpret the reflectivity profile. As an input to the model, the scattering length density (SLD) of neutrons by each material(s) within the sample must be known. Subsequently a model profile can be constructed by considering the sample as a number of layers, each characterised by a particular thickness, roughness and SLD composition.

SECTION 3.4.8: DYNAMIC MECHANICAL THERMAL ANALYSIS

Dynamic Mechanical Thermal Analysis (DMTA) is a complimentary technique to Spectroscopic Ellipsometry for determining phase transitions in polymers. Reference is made to DMTA measurements on P3HT:PCBM blend films in chapter 6 that were performed by Paul Hopkinson at the University of Cambridge. In a DMTA experiment the sample of interest is clamped between two metal plates, one connected to a linear motor and the other to a differential transformer. A temporally varying sinusoidal stress is applied to the system and

its strain is measured as a function of sample temperature. Practically, a stress is applied to the system by the linear motor. Any strain is measured by relating a voltage change across the transformer to the displacement of its magnetic core. A glass transition will manifest itself as a maximum in a plot of $\tan \delta$ vs temperature, where δ is the phase lag between stress and strain signals. Physically, exceeding the glass transition temperature corresponds to a decrease in material stiffness and an increase in material viscosity.

CHAPTER 4: IN-SITU CHARACTERISATION OF BLEND THIN FILM FORMATION & INFLUENCE OF THE CASTING SOLVENT ON DEVICE PERFORMANCE OF P3HT:PCBM OPVS

SECTION 4.1: INTRODUCTION

In this chapter the evolution of structure during the casting of P3HT:PCBM blend thin-films and the influence of the casting solvent on the efficiency of P3HT:PCBM OPVs is discussed. As the casting process represents one of the earliest steps in the construction of an OPV, understanding the processes that occur provides a suitable starting point for discussing the various stages in the fabrication of an OPV; subjects that are addressed both in this chapter and in later parts of this thesis. In section 4.2, a summary of results from a collaborative investigation into the in-situ characterisation of bar-coated P3HT:PCBM thin-films using spectroscopic ellipsometry (SE) and grazing-incidence wide-angle X-ray scattering (GIWAXS) are presented ¹. The evolution of film drying is shown to occur over a three stage process, with crystallisation of P3HT observed once the P3HT:PCBM mass fraction of the blend solution exceeds approximately 50 wt%. P3HT crystallisation then proceeds at a relatively rapid pace until the fraction of residual solvent falls below 20 wt%. The final period of residual solvent removal is correlated with a reduction in the rate of

crystallisation. These processes were shown to be general for a range of different casting conditions investigated¹.

The insight gained into the formation of structure within an as-cast blend thin films provides a starting point for a study on the influence of the casting solvent on the photovoltaic efficiency of P3HT:PCBM blend OPVs. In section 4.3, a device study for P3HT:PCBM OPVs having a fixed blend composition, but cast from one of three different solvents is presented. These films were treated to a post-deposition ‘solvent anneal’ and thermal bake, processes that can be used to further improve device efficiency over untreated controls. It is shown how films that initially result in relatively low efficiency devices can eventually be used to create relatively efficient OPVs following exposure of the active semiconducting film to a solvent rich vapour. This trend persists for devices subject to a post cathode-deposition thermal anneal. The sensitivity of device efficiency to initial casting conditions demonstrates the fine-tuning of the fabrication process that is needed to maximise the efficiency of the P3HT:PCBM OPVs, and shows that a film having a relatively high initial degree of crystallinity is not necessarily the most promising starting point to create a high efficiency OPV.

SECTION 4.2: THE EVOLUTION OF STRUCTURE DURING THIN FILM DEPOSITION

The following section summarises work conducted as part of a collaboration between the Universities of Sheffield, Cambridge, Cardiff and staff of the Diamond Light Source in Oxfordshire. I took part in the experiments at Diamond, helping with the preparation of samples and with the acquisition of data. I also contributed to the interpretation of the data gathered at Diamond. The SE data presented here was recorded by Dr Tao Wang.

To observe the processes that occur during the drying process, thin-films of P3HT:PCBM were deposited using a bar-coating technique, illustrated schematically in chapter 3, section 3.2 (Figure 2.1). By adopting bar-coating as the film-deposition method for in-situ characterisation, films cast under ambient conditions with relevant (i.e. chlorinated) solvents dry on the timescale of 10's seconds, allowing for a relatively high temporal resolution monitoring of the process using SE or GIWAXS. Given the sensitivity of P3HT:PCBM blend thin film structure to the drying process, a subject discussed in section 4.3, this approach does not allow for the direct comparison between films prepared using bar-coating or spin-coating. However we can compare samples cast using the same technique but using different casting solvents. In Figure 4.1, the thicknesses of P3HT:PCBM blend films (1:0.8 wt%) cast from CB at different substrate temperatures are presented. Here the thickness has been estimated from a Cauchy model of the raw ellipsometry data as discussed in chapter 3, section 3.4.3.

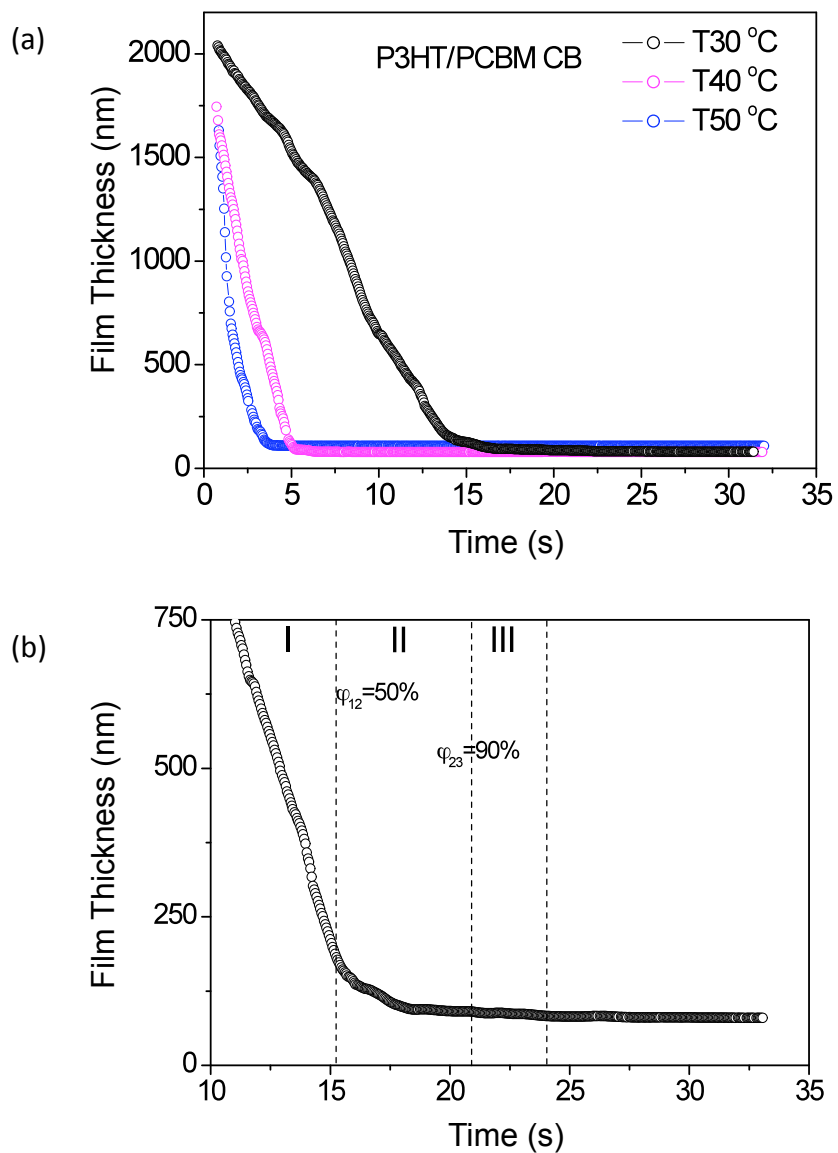


Figure 4.1: Thickness changes of for P3HT:PCBM (1:0.8 wt%) blend thin-films cast from CB onto silicon / native oxide substrates as a function of drying time. Part (a) shows the influence of substrate temperature (30, 40 or 50 °C) on film drying time, whilst part (b) focuses on the final stages of drying for a blend thin-film cast onto a substrate held at 30 °C. The definition of the labelled stages (I, II, III) will be discussed in the following section.

From Figure 4.1(a), it can be seen that the drying time for a P3HT:PCBM blend thin film can be reduced by casting a film onto a substrate held at an elevated temperature. It is apparent that the drying process at all substrate temperatures is dominated by an approximately linear decrease in sample thickness. This stage accounts for over half of the total drying time. The results presented here are in good agreement with the study by Schmidt-Hansberg *et al.*², who monitored the drying of P3HT:PCBM blend thin-films using laser reflectometry. In both studies, this process (defined here as Stage I) is attributed to the loss of solvent by evaporation from the blend thin films.

For the remainder of this section only the evolution in structure for the blend thin film cast at 30°C is discussed. The sensitivity of SE to detect small variations in film thickness permits the observation of two additional stages in the latter parts of the drying process. These are presented more clearly in Figure 4.1(b). As will be discussed later, these stages are believed to be the most important with regard to the self-organisation of P3HT molecules within the film, and directly affect the final degree of relative crystallinity. Compared to Stage I of the drying process, the drying rate in Stage II is significantly reduced, from 146 ± 2 nm/s to 34 ± 2 nm/s. In stage III the drying rate is reduced further still to 1.5 ± 0.2 nm/s.

Having considered the thickness changes for a number of films cast from different solvents and at different substrate temperatures, the optical absorption characteristics of the films during drying are presented. These are calculated using a b-spline model with the sample thickness (as inferred from the Cauchy modeling) used as a boundary condition. This allows the optical extinction coefficient k to be determined for the

sample. Data is presented in Figure 4.2 and describes the evolution of k during the three stages of the thin film drying process.

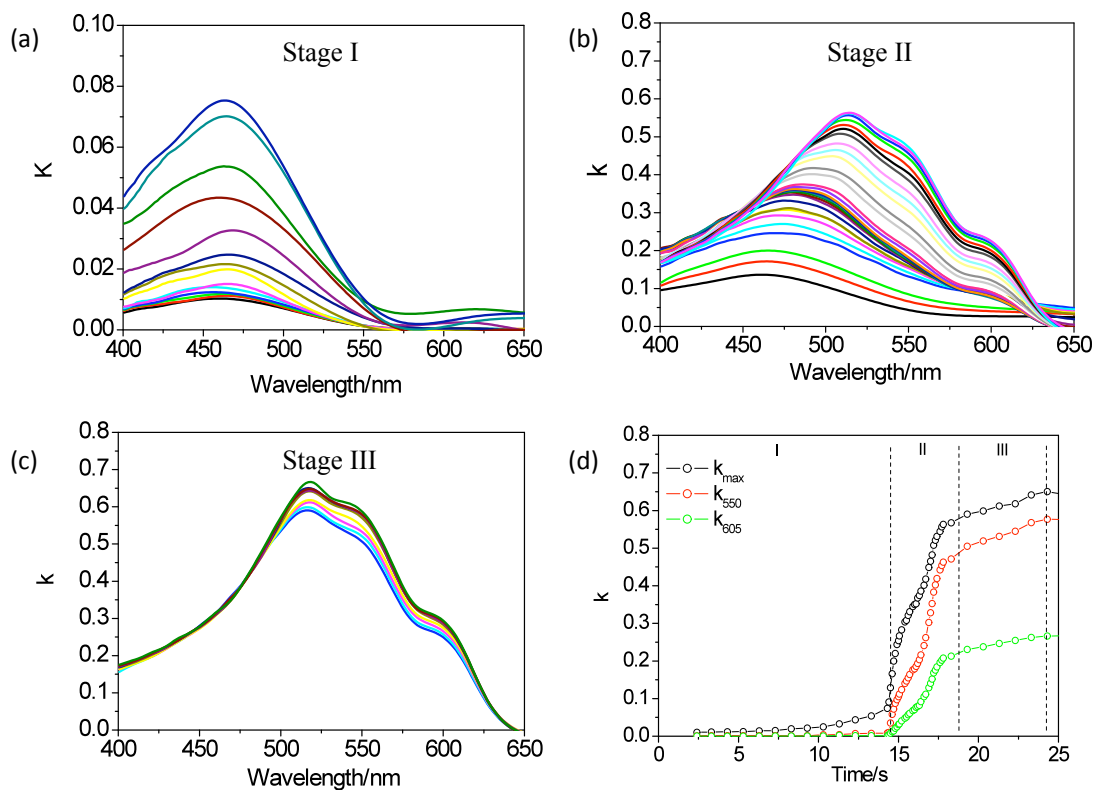


Figure 4.2: Evolution of the increase in extinction coefficient (k) spectrum during drying for a 1:0.8 (wt%) P3HT:PCBM blend thin film cast from CB onto a substrate held at 30°C. Spectra are grouped according to different stages in the drying process, Stage I (a), Stage II (b), Stage III (c). In parts (a)-(c), each spectra is separated by a time interval of 1s, 0.1s and 1s respectively. In part (d), the evolution of k at its maximum wavelength, 550 nm and 605 nm is presented over the entire drying process.

During Stage I of the drying process (Figure 4.2(a)), the relative magnitude of the modeled extinction coefficient remains small. The structure of the spectra is characterised by a broad peak centered at ~ 460 nm, which closely resembles that of

dilute P3HT in solution, where inter-molecular interactions are weak³. Indeed, over the timescale considered in Figure 4.2(a) (~15s), the maximum absorption wavelength P3HT does not undergo any significant shift towards longer wavelengths. This suggests that during this stage free solvent evaporation does not apparently correspond to any significant self-organisation of the polymer.

In Stage II of the drying process, a relatively large increase in the magnitude of k accompanies a significant red-shift and appearance of vibronic features in the spectrum (note the y-axis scale to parts (a) and (b) in Figure 4.2). This results from an enhancement in the electronic conjugation length (planarisation) of the P3HT via increased intermolecular interactions⁴. This increase in optical density and red-shift of absorption is correlated with a significant reduction in the rate of solvent loss. At the end of Stage II the structure of the extinction coefficient spectrum is almost coincident with that of a fully dried film. As shown from Figure 4.2(c), during the final stage of film drying process the magnitude of k continues to increase, albeit at a slower rate than during Stage II. The wavelength of the main optical absorption transition and vibrational shoulders however remain constant.

To summarise the dynamic changes in extinction coefficient, k at a number of different wavelengths is presented as a function of film drying time in Figure 4.2(d). The development of the extinction coefficient at 605 nm can be used as an approximate measure of the degree of polymer crystallisation⁵. It can be seen that significant changes in k_{605} occur only in Stage II of the drying process, with k_{605}

initially undergoing a rapid increase followed by a slow convergence in Stage III to a value which corresponds to that measured in a dry film.

From Figures 4.1 and 4.2 it is apparent that the drying process for the blend thin films studied is not uniform, but rather takes place over a number of distinct stages. By simply monitoring the process as a function of the drying time, it is difficult to determine the mechanisms that induce the onset of each of the three stages, given that the drying time can be influenced by external factors such as the substrate temperature (as shown in Figure 4.1(b)). To overcome this problem the data is reconsidered as a function of solid concentration φ in the sample. This quantity is inferred from the relative decrease in sample thickness during film drying, alongside the boundary conditions of $\varphi = 2.5\%$ at $t = 0\text{s}$ (corresponding to the material concentration in solution) and $\varphi = 100\%$ at $t = 25\text{s}$ (film is fully dry). This data is presented in Figure 4.3.

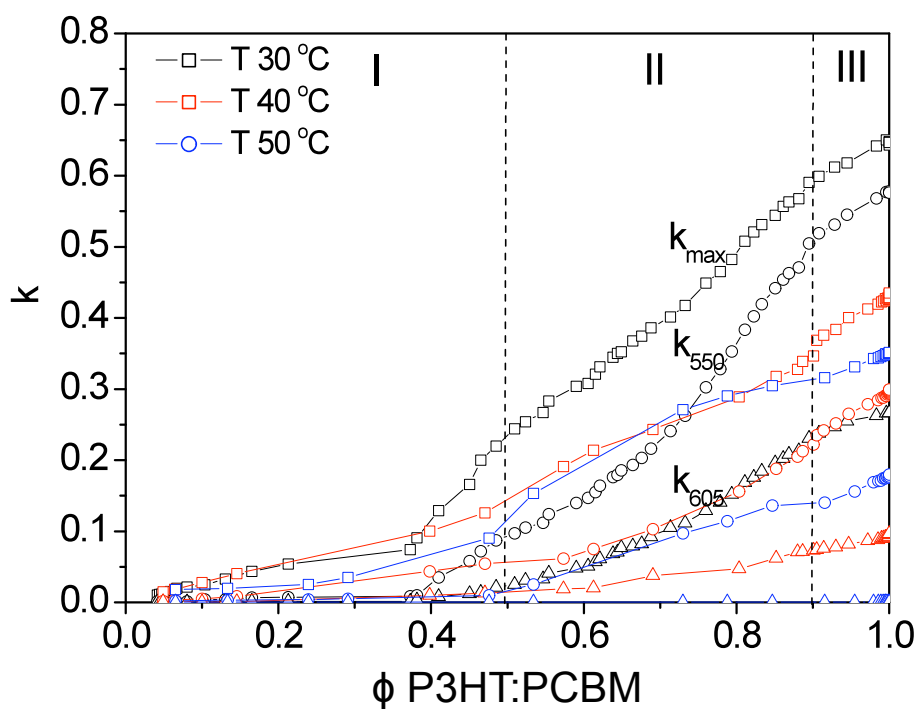


Figure 4.3: Evolution of k_{max} , k_{550} and k_{605} during film drying for a 1:0.8 (wt%) P3HT:PCBM blend thin film cast from CB at different substrate temperatures, plotted as a function of total solid concentration in the sample ϕ .

In Figure 4.1, the influence of substrate temperature on sample drying time is clearly demonstrated. If however changes to the optical density of the films are recorded as a function of total solid concentration, it is apparent that the onset for significant changes in k_{550} or k_{605} only occur above a solids concentration of $\sim 50\%$ (see Figure 4.3).

It is permissible to describe the drying of thin films of P3HT:PCBM in terms of the following picture:

1. For over half the total drying time, the loss of solvent from the wet film does not significantly induce changes in the conformation or interaction between polymer chains. From Figure 4.2(a), the relatively featureless extinction coefficient spectrum is characteristic of P3HT molecules in solution.
2. Above a threshold concentration of material in the wet film, the rate of solvent loss drops by ~70%. This rapid slowdown takes place simultaneously with a rapid change in the extinction coefficient characteristics of the sample. A significant enhancement and relative red-shift in k suggests P3HT chains in the partially wet film undergo self-organisation into more ordered structures, permitting improved intermolecular interaction.
3. The rate of self-organisation slows when the wt% of solids in the film reaches ~80%. Beyond this wt% the rate of film thinning slows once more, with the structure of the film tending towards its final state.

To confirm this picture, GIWAXS has been used to gain further insight into the crystallisation kinetics of P3HT in blend thin films. In Figure 4.4, a 2D GIWAXS image is presented of a P3HT:PCBM blend thin film to provide a reference for the following discussion. Recall from chapter 3, section 3.4.4 that information about a sample from a GIWAXS measurement is in reciprocal-space. Thus signals at larger scattering vector q correspond to smaller distances in real-space.

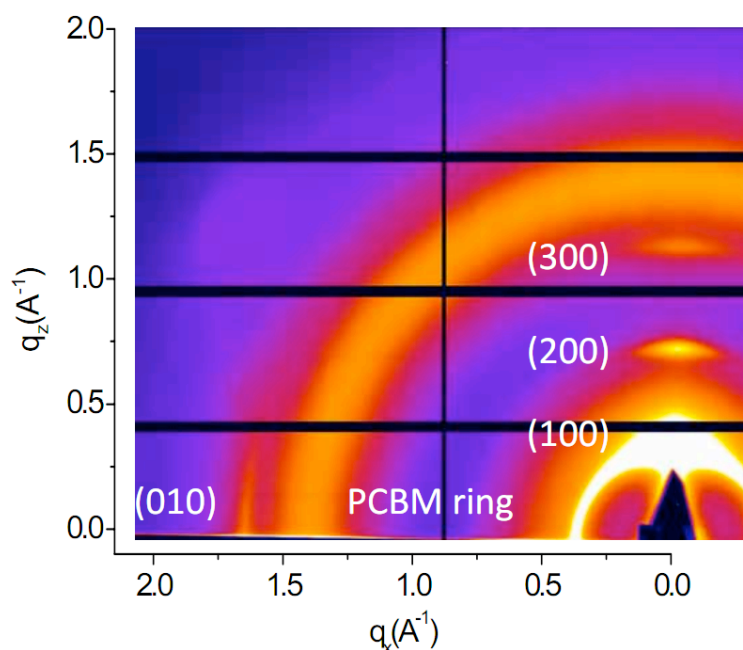


Figure 4.4: 2D GIWAXS pattern from a P3HT:PCBM (1:0.8 wt%) blend film cast from trichlorobenzene. A number of features are labeled on the image that are referred to in the text.

As can be seen, a number of features are present that originate from the coherent diffraction of X-rays from the film. In the out-of-plane (i.e. with respect to the sample substrate) q_z direction, from $q_x = 0 \text{ \AA}^{-1}$ the intense peak at $q_z = 0.36 \text{ \AA}^{-1}$ corresponds to the [100] plane of the P3HT unit cell, which is the spacing between adjacent polymer chains along the direction of the alkyl side groups. The presence of higher order reflections from this plane ([200] and [300] peaks) indicates the P3HT fraction in this film is relatively crystalline along this plane. As can be seen along the in-plane ($q_z = 0 \text{ \AA}^{-1}$) direction, the feature at $q_x = 1.65 \text{ \AA}^{-1}$ corresponds to the [010] plane of the P3HT unit cell, which is the spacing between adjacent polymer chains along the direction of the π - π stacks. Lastly, the halo at $q = 1.4 \text{ \AA}^{-1}$ is due to scatter from the PCBM molecules within the film. As this feature has no preferential direction (the

intensity of the ring is uniform across the image), this implies the PCBM domains within the film do not preferentially align in any direction with respect to the sample substrate.

Hereafter the kinetics of the film drying process are discussed, specifically the evolution of the diffraction signal corresponding to the [100] axis of the P3HT unit cell during film casting. This is due to its inherently greater intensity compared to other diffraction signals (see Figure 4.4). Data is presented in Figure 4.5 that shows the evolution of the [100] peak at $q_z = 0.36 \text{ \AA}^{-1}$ as a function of time after film casting. It can be seen that this peak grows in relative intensity over a period of ~ 15 s. The integrated scattering intensity, normalised to the final signal intensity is presented in Figure 4.5(b). Here, it can be seen that the development of the signal is qualitatively similar to the time evolution of k_{605} as presented in Figure 4.2(d).

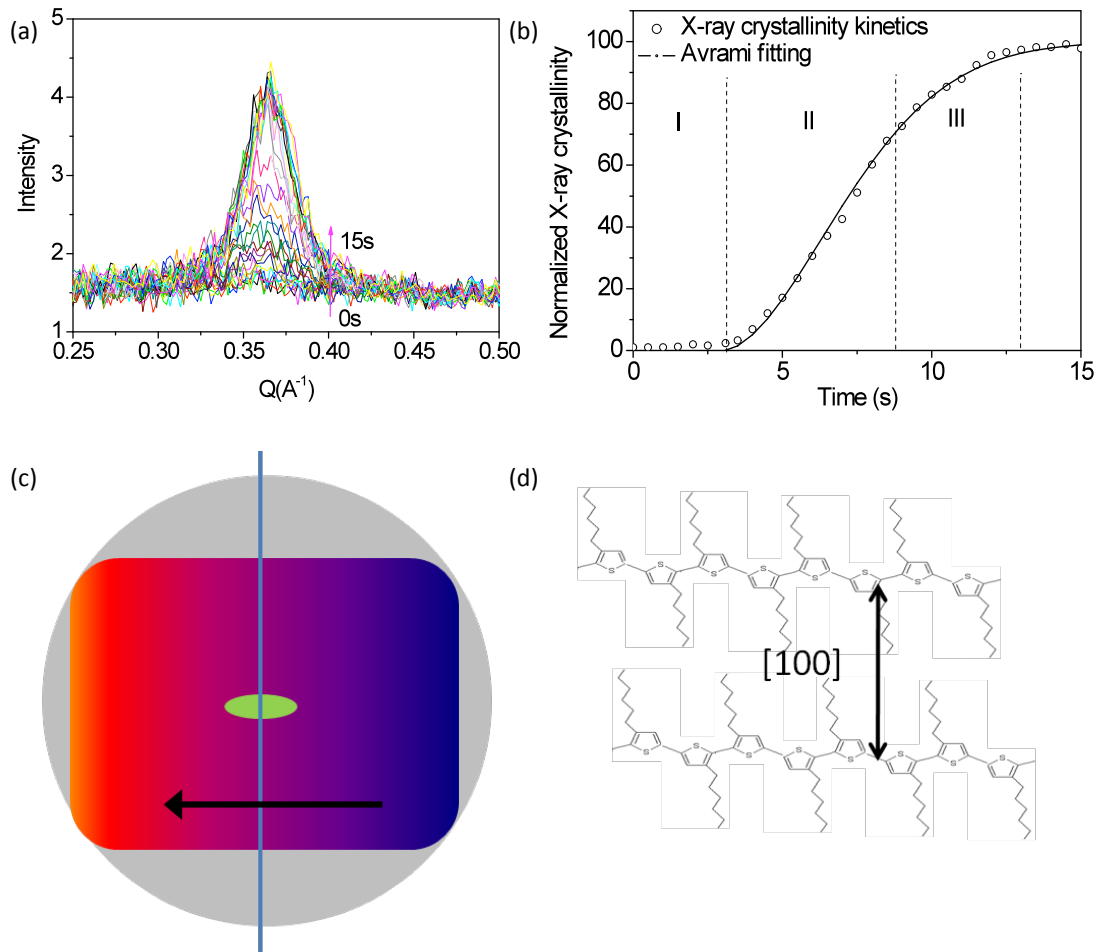


Figure 4.5: (a) Out-of-plane GIWAXS signal from a 1:0.8 (wt%) P3HT:PCBM blend thin film cast from CB onto silicon at 30°C over a period of 15s. In part (b) the integrated signal intensity is plotted as a function of time, alongside an Avrami model fit to the data with $n = 1.8$. Here the data has been normalised to the final integrated signal. Part (c) shows schematically (not to scale) the differences in sampling area between SE (green ellipse) and GIWAXS (blue line) on a drying blend thin film cast onto silicon. The black arrow defines the drying direction of the thin film. The definition of the [100] unit cell axis is shown in part (d).

To estimate the growth kinetics of the P3HT crystallites, the integrated data in Figure 4.5(d) is fitted to an Avrami model ⁶ which takes the form $Y = 1 - e^{-Kt^n}$. Here, Y represents the volume fraction of the crystalline component as a function of time t within the sample, and K and n represent fitted constants. The data closely follows this equation when $n = 1.8 \pm 0.1$. The magnitude of n suggests the crystallisation of P3HT is heterogeneous in nature, with nucleation sites likely to be impurities or aggregates of P3HT already present in the sample. Note however that both SE and GIWAXS probe different volumes of the drying sample (SE probes a $(8 \times 3 \text{ mm}^2)$ ellipse in the centre of the sample, whilst GIWAXS probes a $\sim 300 \text{ }\mu\text{m}$ wide beam across the entire width of the film (see Figure 4.5(c)). Hence the absolute start and end of each drying stage will not necessarily be the same. However the period of rapid signal growth in GIWAXS measurements is in good agreement to the timescale inferred from SE.

The data obtained from in-situ GIWAXS supports therefore the picture of a three-stage drying process for the polymer component in thin films of P3HT:PCBM. Furthermore, during the latter parts of the drying process, a relative decrease in d-spacing and peak FWHM suggest P3HT lamella undergo a partial self-annealing process, reducing distortions and kinks between chains ¹. Through use of the Scherrer Equation (see chapter 3 section 3.4.4, equation 3.9), after casting P3HT domains approximately 30 nm in size were thought to exist in the blend thin film discussed here.

SECTION 4.3: INFLUENCE OF THE CASTING SOLVENT ON OPV DEVICE EFFICIENCY

In section 4.2 the in-situ characterisation of blend thin films recorded during the casting process was discussed in order to give a partial insight into how nanoscale structure is initially formed. Here, it is shown how the power conversion efficiency (PCE) of as-cast thin films fabricated into OPVs is influenced by the casting solvent, and how this affects the extent to which the efficiency can be improved using common post-deposition annealing techniques. A side-by-side comparison of casting solvents with annealing treatments demonstrates the sensitivity of the blend system to processing conditions.

A series of OPV devices (P3HT:PCBM 1.0.7 wt%) were fabricated from films subjected to a range of different post-deposition treatments. Specifically, untreated films were cast from different solvents, which are termed as 'as cast' samples. A selection of these films were solvent annealed after casting, through exposure of the film to a solvent rich vapour (identical to the casting solvent used) for 30 minutes. Finally, a series of devices were subjected to a solvent and thermal annealing step. Here, thermal annealing was conducted at 140°C for 30 minutes. Figure 4.6 shows the JV characteristics for each of the devices fabricated, alongside their EQE spectra. The performance metrics of the devices are summarised in Table 4.1.

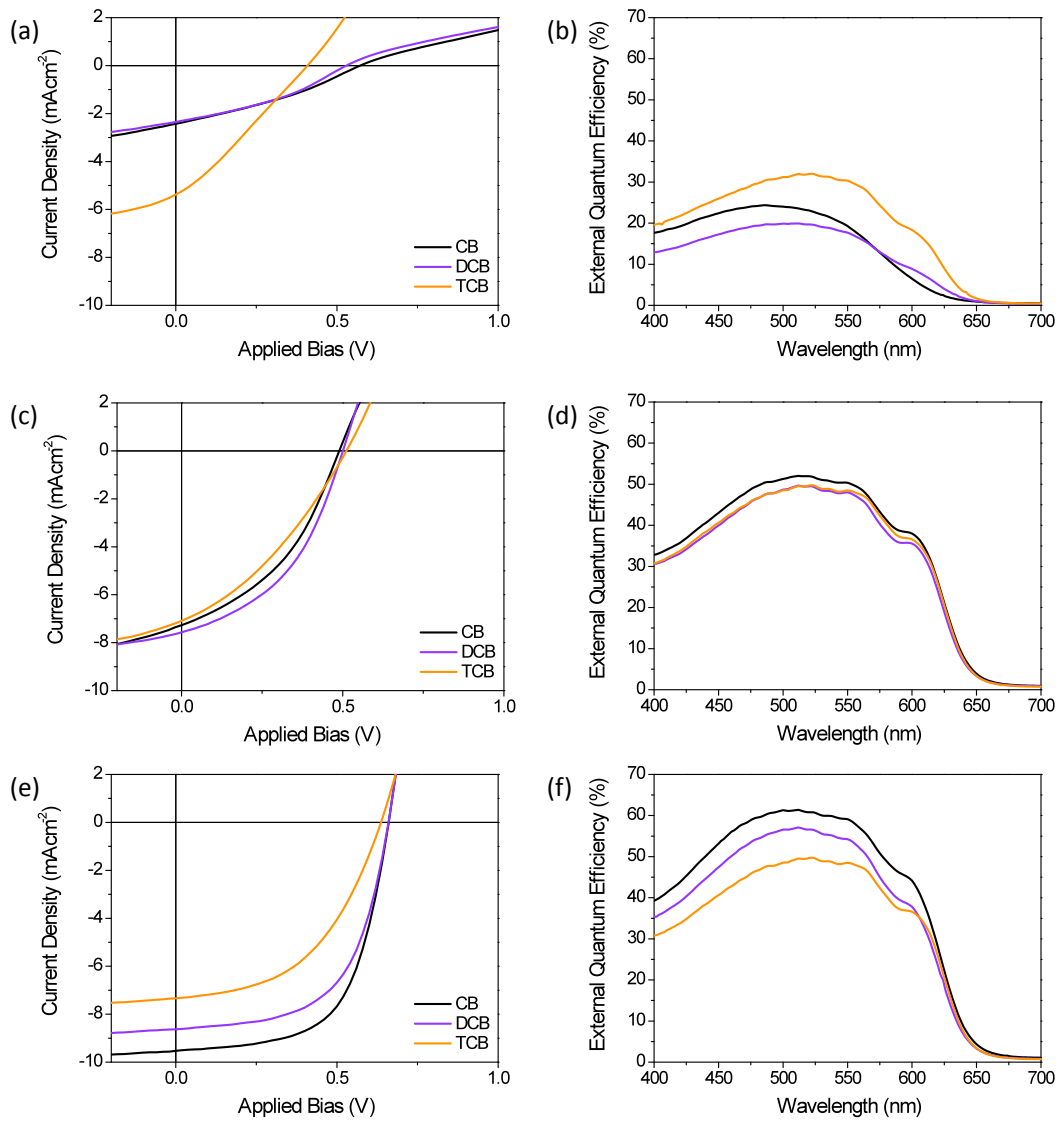


Figure 4.6: JV curves (left) and EQE spectra (right) for all devices investigated in this work. Specifically, data is shown for thin films that have been either as-cast (unannealed) (parts (a),(b)), solvent vapour annealed ((c),(d)), or solvent vapour and thermally annealed ((e), (f)). These films have been cast from CB (black), DCB (violet) and TCB (orange) solvents.

	PCE (%)	J_{sc} (mA/cm ²)	FF (%)	V_{oc} (V)
Solvent	As-cast			
CB	0.44 ± 0.03	-2.41	32	0.57
DCB	0.46 ± 0.04	-2.42	37	0.51
TCB	<u>0.63 ± 0.03</u>	-5.19	28	0.44
	Solvent Annealed			
CB	1.42 ± 0.02	-7.26	40	0.49
DCB	<u>1.66 ± 0.02</u>	-7.73	43	0.50
TCB	1.20 ± 0.05	-7.16	33	0.51
	Solvent & Thermally Annealed			
CB	<u>3.83 ± 0.05</u>	-9.54	61	0.66
DCB	3.13 ± 0.04	-8.17	59	0.65
TCB	2.20 ± 0.10	-7.27	48	0.63

Table 4.1: Average device metrics for samples in this work. For each treatment set, the best device PCEs are underlined. The uncertainty in each PCE measurement is calculated from the standard deviation in PCE of 12 pixels.

It can be seen that devices that are cast from TCB and do not undergo further treatment (i.e. as-cast) are more efficient than those similarly prepared from the other solvents (0.63% and ~0.45% PCE respectively). The higher PCE results from a larger

short-circuit current density (J_{sc}) although the fill-factor (FF) and open-circuit voltage (V_{oc}) is lower than that observed in DCB and CB cast devices. The variation in J_{sc} values between samples is consistent with measurements of the External Quantum Efficiency (EQE) of each device. As shown in Figure 4.6(b), the peak EQE for the TCB device left as-cast is 32% at 525 nm. For the CB and DCB cast devices the peak EQEs are lower (24% and 20% respectively) and shifted to shorter wavelengths.

The drying times for the spin-coated CB, DCB and TCB films in this study were approximately 15s, 45s and 300s respectively. The significantly longer drying time of the TCB cast-films results from its higher boiling point and lower vapour pressure at the film casting temperature compared to the other solvents. Several studies have correlated a greater degree of relative crystallinity in P3HT with an extended drying time of the film^{1,7}. For the spin-cast samples investigated here, this is supported by UV-Vis measurements presented in Figure 4.7. It can be seen that films spin-cast from a TCB solution initially have an Optical Density (O.D.) spectrum with more prominent structural features at relatively long wavelengths. In contrast the O.D. spectra of films cast from CB or DCB are relatively blue-shifted, suggesting less ordered P3HT.

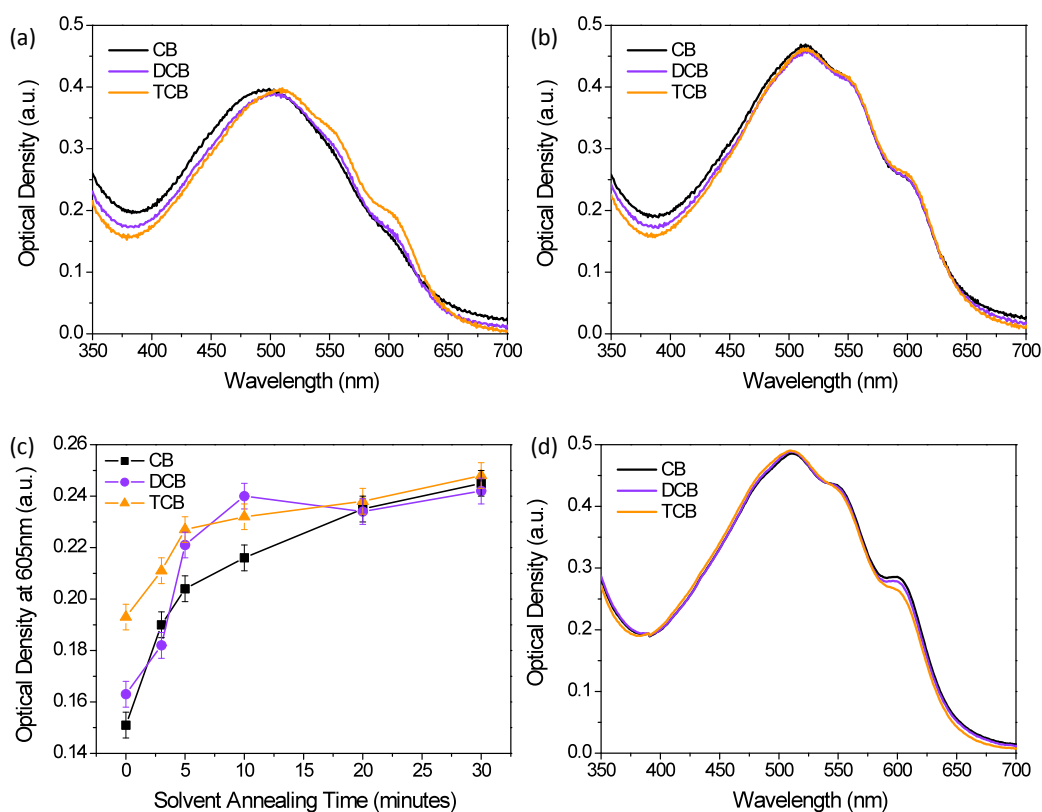


Figure 4.7: (a) O.D. spectra of as-cast thin films of P3HT:PCBM cast from CB (black) DCB (violet) and TCB (orange) solvents. In part (b) O.D. spectra are plotted for blend thin films after exposure to a solvent rich atmosphere for 30 minutes. Part (c) shows the change in O.D. at 605 nm as a function of exposure time (minutes). Part (d) shows O.D. spectra for blend thin films to have undergone solvent-vapour exposure for 30 minutes followed by thermal annealing for 30 minutes at 140°C and rapidly cooled down.

To further support the suggestion that as-cast blend thin films from TCB solvent contain a relatively greater population of semi-crystalline P3HT domains, I consider the photoluminescence intensity from each sample. The photoluminescence (PL) emission intensity of a series of thin films cast from different solvents, or exposed to different post-deposition treatments are presented in Figure 4.8. Variations in PL

efficiency can be linked qualitatively to the degree of phase separation in a blend film, since a stronger signal suggests a lower interfacial area of donor:acceptor interfaces within a film⁸. For the as-cast films (Figure 4.8(a)) the most intense luminescence is emitted by the films cast from TCB. The relatively red-shifted absorption and larger PL yield for the TCB cast films therefore support the existence of semi-crystalline phase separated P3HT domains. In contrast, the faster drying time for films cast from CB and DCB do not apparently allow the P3HT to undergo the same degree of phase separation and crystallisation, providing a partial explanation for the relatively lower efficiencies measured for this set of devices.

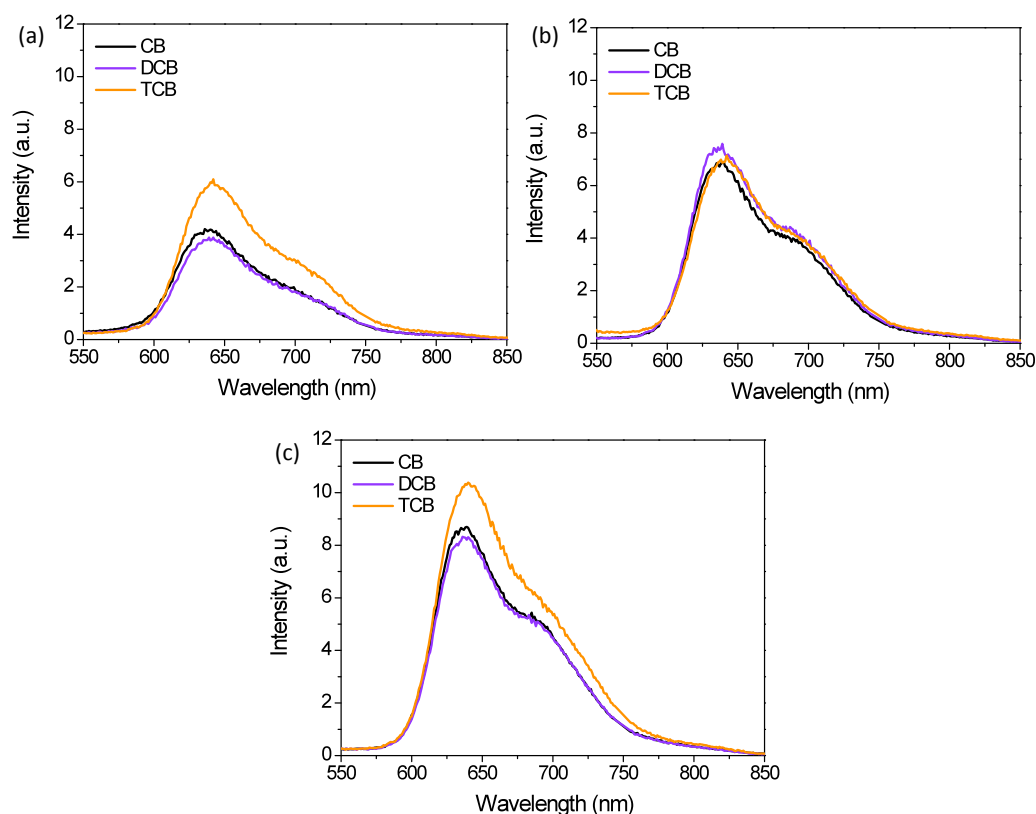


Figure 4.8: PL spectra recorded from films cast from CB (black), DCB (violet) and TCB (orange) during excitation at 500nm. For each group, spectra have been normalised to the absorption at the excitation wavelength and corrected for thin film absorption effects. Here, data is plotted from films that have been (a) as-cast, (b) solvent vapour annealed and (c) solvent vapour and thermally annealed.

It appears therefore that the extended drying time of TCB cast films permits the formation of a film morphology in which there is a significant degree of self-order of the polymer (and consequently suggests favourable OPV characteristics); however the photovoltaic efficiency of the resultant devices is below 1%. This suggests that the PCBM molecules within the thin films have not had the opportunity to form a partially phase separated network from P3HT to allow for the transport and extraction of electrons within the blend film and to balance with the transport of holes within the P3HT phase.

From the data presented in Table 4.1, it can be seen that exposing films to a solvent rich atmosphere results in an improvement in device efficiency. Devices that have been cast and then annealed in a DCB solvent atmosphere have an average PCE of 1.6%, compared to that of CB and TCB cast and solvent vapour annealed devices that have an efficiency of 1.4% and 1.2% respectively. From UV-Vis measurements however, near identical absorption and PL spectra for all films are obtained (see Figures 4.7(b) and 4.8(b)), suggesting that a solvent anneal using a volatile solvent (e.g. CB) can drive P3HT molecules into structures similar to those created using a slow drying process (e.g. by preparing a film from a TCB solvent). This trend is supported by the data shown in Figure 4.7(c), which shows the evolution of the optical density at 605 nm as a function of solvent exposure time. It can be seen that in all cases, the OD of solvent vapour annealed films at this wavelength converge to almost identical values. From the results presented in section 4.2, these films may therefore contain P3HT domains within the blend thin films that exhibit a comparable level of self-organisation.

Interestingly, the similarities in O.D. and PL evidenced in Figures 4.7(b) and 4.8(b) respectively are not reflected in device performance. The relative improvement in PCE gained by solvent vapour annealing a film cast from a non-volatile solvent is significantly lower than that observed in films cast and annealed using a more volatile solvent. It is possible that during casting of a film from, e.g. TCB, the extended drying process promotes a network of relatively self-organised P3HT domains that are relatively stable with respect to further solvent exposure. In contrast, the solvent annealing step when applied to quickly-dried films (which are relatively amorphous in nature) results in a greater improvement in efficiency as the polymer has yet to undergo significant crystallisation. This may also permit the diffusion of PCBM molecules into a network of nanodomains during the solvent annealing step to improve the transport of electrons. Indeed, we find that the measured fill-factors of solvent annealed devices cast from CB and DCB are larger than those cast from TCB (40%, 43% and 33% respectively), suggesting the charge transport characteristics are relatively more balanced in a rapidly cast film which is subsequently annealed^{7a,9} and further supports the idea that films cast from TCB are initially structured in a manner which limits further improvement.

It has been shown therefore how the processing history of a thin film influences the extent to which solvent annealing can improve device efficiency, with devices fabricated from quickly dried films apparently undergoing the largest improvement from a post-deposition treatment. The results support the findings of a previous study in which a single solvent vapour was used to anneal a film¹⁰. However here this analysis has been extended to a number of different casting solvents. When solvent vapour annealing is conducted using the same solvent as used to cast the film, its

benefits are lower than using a different solvent. For example, efficiencies of 3.3% have been reported for CB-cast thin films exposed to an acetone vapour rich atmosphere¹⁰⁻¹¹.

Attention now turns to the use of thermal annealing to improve the efficiency of P3HT:PCBM films when made into an OPV. Here, a 30 minute anneal at 140°C is used followed by a rapid return to room temperature. As discussed in chapters 5 and 6, thermal annealing offers an alternative mechanism for P3HT to undergo partial self-organisation. From Table 4.1, devices cast from a CB solvent benefit the most from this process, with efficiencies of 3.8 ± 0.05 % obtained. Devices prepared from DCB or TCB and subject to thermal annealing step have a lower PCE (3.13 ± 0.04 % and 2.2 ± 0.1 % respectively) than devices prepared using CB cast active layers.

In Figure 4.7(d) the O.D. spectra of blend thin films after being subject to both solvent vapour and thermal annealing steps are presented. It can be seen that there is very little difference in any of the spectra, suggesting the differences in device efficiencies measured are not related to the amount of light absorbed by the P3HT:PCBM layer. Rather, such differences must reflect variations in the charge separation, transport and collection efficiencies within the layer. PL measurements for thermally annealed films (see Figure 4.8(c)) show that TCB-cast films have the highest fluorescence intensity. This observation suggests a greater fraction of photo-generated excitons recombine radiatively before undergoing separation into free charge carriers. This observation is not necessarily inconsistent with the positive correlation between increased PL and device efficiency discussed earlier, since a

partially phase separated network of P3HT is required to facilitate efficient hole transport. Here the relatively low PCE of TCB cast OPVs which have been annealed suggests that an overly coarse degree of phase separation between polymer and fullerene has developed after the thermal annealing step.

To explore this possibility further, optical microscopy images of samples that have undergone solvent-vapour and thermal annealing are shown in Figure 4.9. In the same figure AFM topography scans of the same sample surface are shown, taken over an area of $10 \times 10 \mu\text{m}^2$. From Figure 4.9(a) it can be seen that blend thin films cast from TCB are characterised by a large surface density of PCBM aggregates¹². At much shorter length scales (Figure 4.9(b)) the surface of the sample is relatively rough and features a number of structures that are 1-2 μm in diameter. Note the peak-to-peak height variation in the AFM scan of the TCB cast film (30 nm) and RMS roughness (4 nm) is relatively large with respect to the thickness of the active layer ($70 \pm 4 \text{ nm}$). In contrast, for samples cast from either DCB or CB solvent and subsequently annealed do not appear to contain a significant number of PCBM aggregates. Furthermore, the AFM data shows that the surface of these samples is much smoother (RMS roughness of 1.9 and 2 nm respectively). Given the ideal length scale for phase separation should be comparable to the diffusion length of photo-generated excitons ($\sim 5\text{-}10 \text{ nm}$ ¹³), the presence of relatively large (micron-scale) PCBM structures is a clear indication of a poor device morphology. These observations are consistent with the PL spectra shown in Figure 4.8(c) and help to rationalise the relatively high photoluminescence intensity emitted from TCB cast thin films that have undergone both solvent vapour and thermal annealing treatments. In addition to a depletion of PCBM from the bulk of the thin film, the presence of micron-scale aggregates

increases the likelihood of creating electrical shorts across the device ¹⁴. A smaller PCBM aggregate density in DCB and CB is also consistent with the higher power conversion efficiencies observed in devices in which the active P3HT:PCBM layer has been both solvent annealed and thermally annealed.

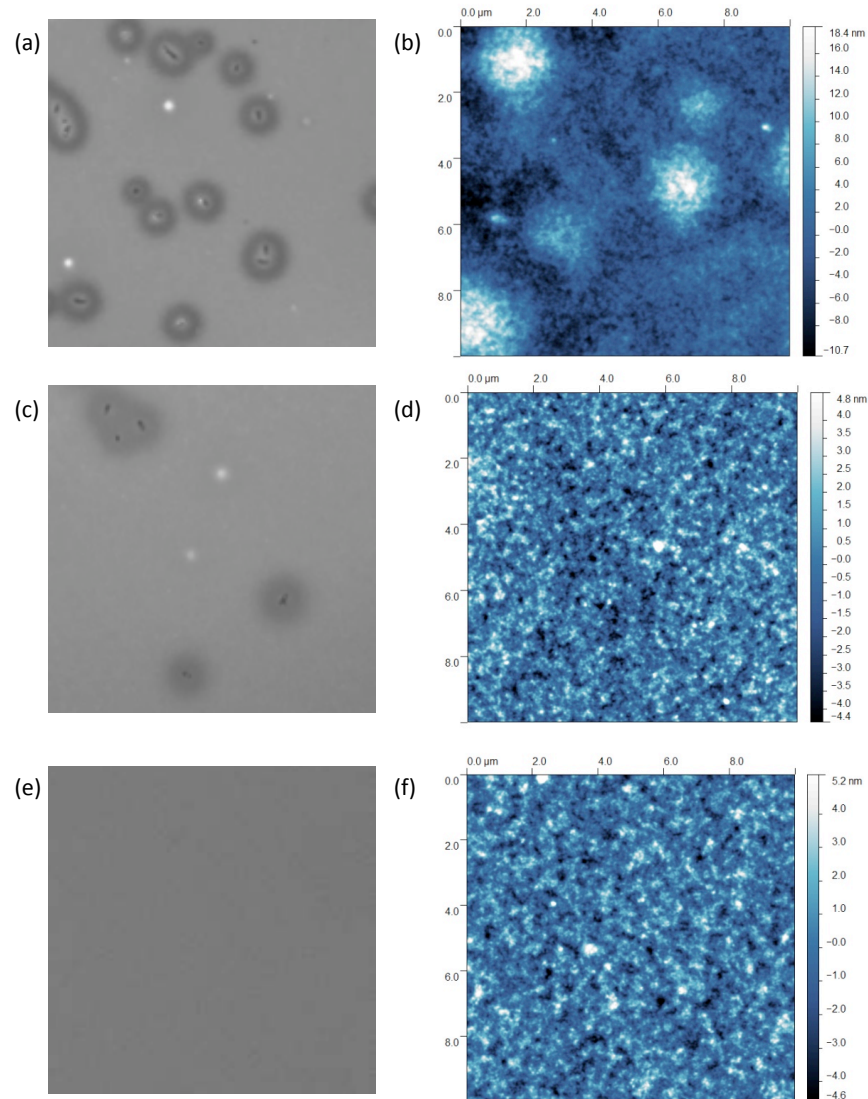


Figure 4.9: Optical microscopy images ($500 \times 500 \mu\text{m}^2$ field of view) and AFM topography scans ($10 \times 10 \mu\text{m}^2$) of P3HT:PCBM blend thin films after solvent-vapour and thermal annealing treatments. Images correspond to films cast from TCB (parts (a) and (b)), DCB ((c) and (d)) and CB ((e) and (f)). Note that the colour (height) scales to parts (b), (d) and (f) correspond to height differences about a mean height (set individually for each scan) of 0 nm.

SECTION 4.4: CONCLUSIONS

In section 4.2 of this chapter, it was shown how the polymer component of P3HT:PCBM blend thin films undergoes phase separation and self-organisation during the film casting process. The data shows how the drying process takes place in three distinct stages, with polymer organisation only occurring above a solid concentration threshold of approximately 50 wt% in the film, which is accompanied by a significant drop in the evaporation rate of casting solvent. The crystallisation of P3HT occurs over a relatively short period of the total film drying time, with the growth kinetics of x-ray scatter from the [100] plane of the P3HT unit-cell in good agreement with changes in the optical extinction coefficient of the material, particularly at wavelengths corresponding to the π - π^* electronic transition. The experiment offers insight into how the relative self-organisation of organic semiconductor thin films could be actively controlled during film casting, or monitored (via SE) as a process-control technique. Although the evolution of PCBM domain formation has not been discussed here, the work of Schmidt-Hansberg *et al.*¹⁵ has shown it is delayed with respect to P3HT crystallite formation i.e. occurring during the latter stages of the drying process.

The effect of casting solvent (CB, DCB & TCB) and common annealing treatments on the efficiency of a solar cell fabricated from a blend of P3HT and PCBM has also been explored. It has been shown how the casting solvent has a significant effect on the final efficiency of the device, affecting the extent to which solvent vapour and thermal annealing processes are beneficial. It is noted that previous studies using

DCB as a casting solvent in which a thermal anneal at a lower temperature (110°C) has resulted in efficiencies of 4% ^{7a}. Separate studies have shown that when the active layer is cast from a TCB solvent, efficiencies of 2.5% have been reported when using a thermal annealing treatment that is similar to that used for optimised DCB cast devices ¹⁶. However without thermal annealing, efficiencies of 3.3 and 3.8% have been achieved using spin-cast TCB ¹⁶, suggesting that under certain drying conditions the solvent can give relatively efficient devices without the need for post-treatment. The results in section 4.3 of this chapter demonstrate the complexity of the optimisation process for P3HT:PCBM OPVs and show that the choice of casting solvent is likely to require separate optimisation protocols in order to maximise the PCE of fabricated devices.

SECTION 4.5: REFERENCES

1. Wang, T.; Dunbar, A. D. F.; Staniec, P. A.; Pearson, A. J.; Hopkinson, P. E.; MacDonald, J. E.; Lilliu, S.; Pizzey, C.; Terrill, N. J.; Donald, A. M.; Ryan, A. J.; Jones, R. A. L.; Lidzey, D. G., The development of nanoscale morphology in polymer: fullerene photovoltaic blends during solvent casting. *Soft Matter* **2010**, *6* (17), 4128-4134.
2. Schmidt-Hansberg, B.; Klein, M. F. G.; Peters, K.; Buss, F.; Pfeifer, J.; Walheim, S.; Colsmann, A.; Lemmer, U.; Scharfer, P.; Schabel, W., In situ monitoring the drying kinetics of knife coated polymer-fullerene films for organic solar cells. *Journal of Applied Physics* **2009**, *106* (12).

3. Berson, S.; De Bettignies, R.; Bailly, S.; Guillerez, S., Poly (3-hexylthiophene) fibers for photovoltaic applications. *Advanced Functional Materials* **2007**, *17* (8), 1377-1384.
4. Brown, P. J.; Thomas, D. S.; Kohler, A.; Wilson, J. S.; Kim, J. S.; Ramsdale, C. M.; Sirringhaus, H.; Friend, R. H., Effect of interchain interactions on the absorption and emission of poly(3-hexylthiophene). *Physical Review B* **2003**, *67* (6).
5. Erb, T.; Zhokhavets, U.; Gobsch, G.; Raleva, S.; Stuhn, B.; Schilinsky, P.; Waldauf, C.; Brabec, C. J., Correlation between structural and optical properties of composite polymer/fullerene films for organic solar cells. *Advanced Functional Materials* **2005**, *15* (7), 1193-1196.
6. (a) Avrami, M., Kinetics of phase change I - General theory. *J. Chem. Phys.* **1939**, *7* (12), 1103-1112; (b) Avrami, M., Granulation, Phase Change, and Microstructure - Kinetics of Phase Change. III. *J. Chem. Phys.* **1941**, *9* (2), 177-184.
7. (a) Li, G.; Shrotriya, V.; Huang, J. S.; Yao, Y.; Moriarty, T.; Emery, K.; Yang, Y., High-efficiency solution processable polymer photovoltaic cells by self-organization of polymer blends. *Nature Materials* **2005**, *4* (11), 864-868; (b) Sanyal, M.; Schmidt-Hansberg, B.; Klein, M. F. G.; Colsmann, A.; Munuera, C.; Vorobiev, A.; Lemmer, U.; Schabel, W.; Dosch, H.; Barrena, E., In Situ X-Ray Study of Drying-Temperature Influence on the Structural Evolution of Bulk-Heterojunction Polymer-Fullerene Solar Cells Processed by Doctor-Blading. *Advanced Energy Materials* **2011**, *1* (3), 363-367.
8. (a) Clarke, T. M.; Ballantyne, A. M.; Nelson, J.; Bradley, D. D. C.; Durrant, J. R., Free Energy Control of Charge Photogeneration in Polythiophene/Fullerene Solar Cells: The Influence of Thermal Annealing on P3HT/PCBM Blends. *Advanced Functional Materials* **2008**, *18* (24), 4029-4035; (b) Kim, Y.; Cook, S.; Tuladhar, S.

- M.; Choulis, S. A.; Nelson, J.; Durrant, J. R.; Bradley, D. D. C.; Giles, M.; McCulloch, I.; Ha, C. S.; Ree, M., A strong regioregularity effect in self-organizing conjugated polymer films and high-efficiency polythiophene: fullerene solar cells. *Nature Materials* **2006**, *5* (3), 197-203.
9. Blom, P. W. M.; Mihailetschi, V. D.; Koster, L. J. A.; Markov, D. E., Device physics of polymer : fullerene bulk heterojunction solar cells. *Advanced Materials* **2007**, *19* (12), 1551-1566.
10. Zhao, Y.; Guo, X. Y.; Xie, Z. Y.; Qu, Y.; Geng, Y. H.; Wang, L. X., Solvent Vapor-Induced Self Assembly and its Influence on Optoelectronic Conversion of Poly(3-hexylthiophene): Methanofullerene Bulk Heterojunction Photovoltaic Cells. *J Appl Polym Sci* **2009**, *111* (4), 1799-1804.
11. Park, J. H.; Kim, J. S.; Lee, J. H.; Lee, W. H.; Cho, K., Effect of Annealing Solvent Solubility on the Performance of Poly(3-hexylthiophene)/Methanofullerene Solar Cells. *J. Phys. Chem. C* **2009**, *113* (40), 17579-17584.
12. Watts, B.; Belcher, W. J.; Thomsen, L.; Ade, H.; Dastoor, P. C., A Quantitative Study of PCBM Diffusion during Annealing of P3HT: PCBM Blend Films. *Macromolecules* **2009**, *42* (21), 8392-8397.
13. Shaw, P. E.; Ruseckas, A.; Samuel, I. D. W., Exciton Diffusion Measurements in Poly(3-hexylthiophene). *Advanced Materials* **2008**, *20* (18), 3516-3520.
14. Chirvase, D.; Parisi, J.; Hummelen, J. C.; Dyakonov, V., Influence of nanomorphology on the photovoltaic action of polymer-fullerene composites. *Nanotechnology* **2004**, *15* (9), 1317-1323.
15. Schmidt-Hansberg, B.; Sanyal, M.; Klein, M. F. G.; Pfaff, M.; Schnabel, N.; Jaiser, S.; Vorobiev, A.; Muller, E.; Colsmann, A.; Scharfer, P.; Gerthsen, D.; Lemmer, U.; Barrena, E.; Schabel, W., Moving through the Phase Diagram:

Morphology Formation in Solution Cast Polymer-Fullerene Blend Films for Organic Solar Cells. *Acs Nano* **2011**, 5 (11), 8579-8590.

16. Chu, C. W.; Yang, H. C.; Hou, W. J.; Huang, J. S.; Li, G.; Yang, Y., Control of the nanoscale crystallinity and phase separation in polymer solar cells. *Applied Physics Letters* **2008**, 92 (10), -.

CHAPTER 5: EVOLUTION OF STRUCTURE AND OPTOELECTRONIC PROPERTIES OF P3HT:PCBM BLEND THIN FILMS DURING THERMAL ANNEALING

SECTION 5.1: INTRODUCTION

In this chapter the role of thermal annealing in modifying the structure and optoelectronic properties of P3HT:PCBM blend thin films is discussed, via in-situ monitoring of the process using Spectroscopic Ellipsometry (SE) ¹. The discussion is split into three parts. In section 5.2 the mechanisms through which the sample thickness changes during the thermal annealing process are explored. In section 5.3 the role of thermal annealing on altering the optical extinction coefficient spectrum of the sample is discussed. The data presented here builds upon the results from chapter 4, and in particular explores the link between the relative crystallinity of P3HT and the structure of its optical absorption spectrum. UV-Visible spectroscopy and optical microscopy techniques are used support the SE measurements, and allows the identification of four distinct processes during thermal annealing: (1) the removal of residual casting solvent above the glass transition temperature of P3HT in the blend, (2) the volume relaxation in non-equilibrium structures formed during spin-casting, (3) indirect evidence for the crystallisation and (4) phase separation of both P3HT and PCBM.

In section 5.4 of this chapter, these results are related to the power conversion efficiency of OPVs subject to identical annealing protocols. For blend thin films and OPVs annealed at 150°C, it is shown how the cooling rate - often overlooked in the literature - has a small but not insignificant effect on the final structure of the blend film, and therefore affects the power conversion efficiency of OPV devices.

SECTION 5.2: MONITORING THICKNESS CHANGES DURING A THERMAL ANNEALING CYCLE USING SPECTROSCOPIC ELLIPSOMETRY

P3HT (cast from a 25 mg/ml in chlorobenzene solution) or P3HT:PCBM thin films (1:0.67 wt%, cast from a 25 mg/ml total solids concentration in chlorobenzene solution) were annealed at temperatures ranging from below the glass transition temperature (T_g) through to the melt temperature (T_m) of the blend. These transitions are related to the P3HT phase of the blends and not to PCBM. However, it is important to recognise the influence of PCBM on the thermal transitions of P3HT. A number of studies have shown that the addition of PCBM can raise the T_g of P3HT², indeed this is explored in more detail in chapter 6 in this thesis. Here, the T_g for the P3HT used in these experiments is measured for a pure thin film and a blend. The data is presented in Figure 5.1. As can be seen, a change in the thermal expansion rate occurs for both samples at a temperature of 20 ± 2 °C (for pure P3HT) and 60 ± 2 °C (for the blend). These transitions correspond to the glass transition of the polymer. As will be shown in chapter 6, the T_g of the blend can vary for a constant film composition, providing an indirect measure of different thin film morphologies. The T_g values determined from Figure 5.1 are inferred from the first heating cycle and are

therefore representative of ‘as-cast’ film morphologies only. The observed increase in the apparent T_g between pure and blend thin films is an agreement with results reported elsewhere ^{2b}. For the blend sample it is apparent that the nature of the transition is qualitatively different compared to the pure polymer. Indeed, a ‘shoulder’ - corresponding to a reduction in the film expansion rate - is apparent above the apparent T_g of the blend. In contrast, for pure P3HT the T_g marks two regions of linear thermal expansion.

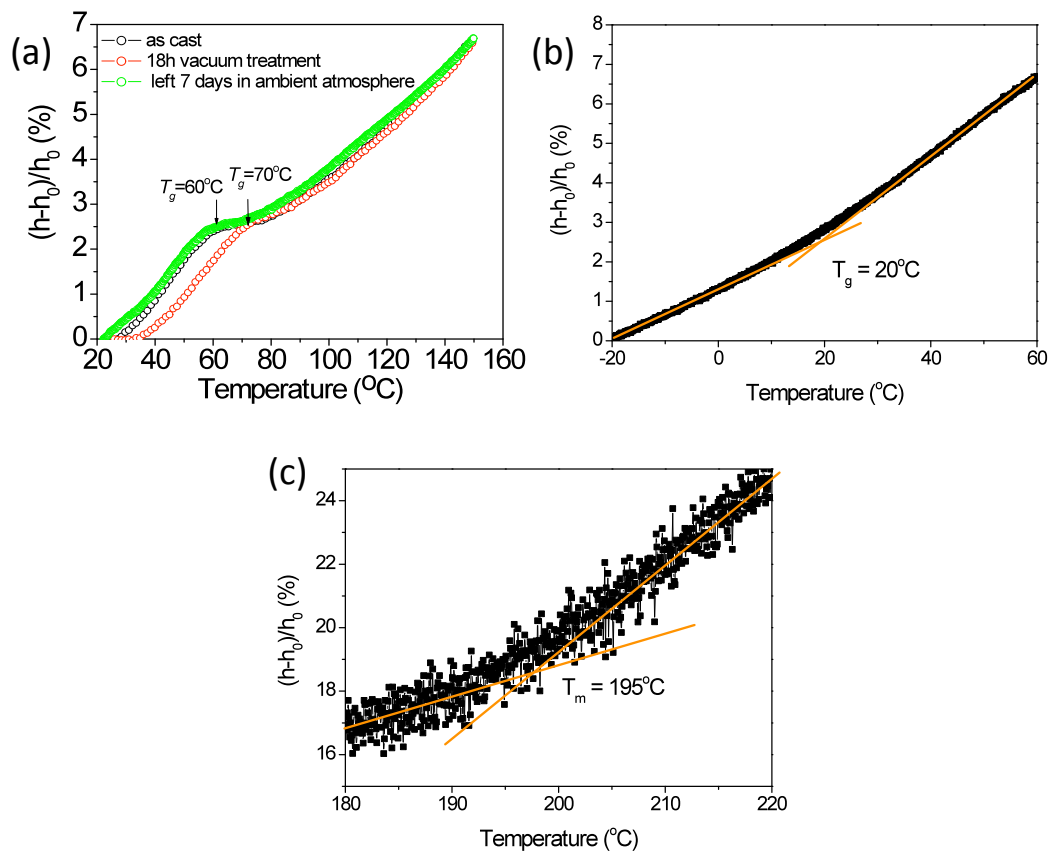


Figure 5.1: Glass Transition (T_g) temperatures for a P3HT:PCBM blend film (1:0.67 wt%) (a) and a pure P3HT film (b) as determined from the first heating cycle by spectroscopic ellipsometry. The melt temperature (T_m) of the P3HT used in this study is presented in (c). All transitions have been determined by spectroscopic ellipsometry. The initial thicknesses of the samples were 120 ± 4 nm and 70 ± 4 nm for the pure and blend films respectively.

In Figure 5.1(a), I plot the measured thickness changes for a freshly prepared blend thin film, the thickness changes of identical samples stored either in ambient conditions for 7 days, or held under vacuum (10^{-7} mbar) for 18 hrs. For all blend samples it is apparent that the films undergo a reduction in the rate of expansion when heated to between 60 and 70°C, which marks the apparent T_g for the blend³. The reduction in the thermal expansion rate around T_g for the blend samples most probably results from solvent loss from the film. This process occurs once the film is heated past the glass transition of the polymer. Note that this process occurs at a temperature below the boiling point of the casting solvent used (132°C). It is likely that a few percent of solvent remains in the glassy blend films after spin-casting. When these films are heated above their glass transition temperature, trapped solvent may evaporate over the time scale of the experiment. As shown in chapter 4, section 4.1, solvent loss leads to a relative decrease in sample thickness. Consequently this process competes with thermal expansion caused by heating to decrease the thermal expansion rate³. At such a time where the mechanisms triggered by solvent loss become relatively weak, thermal expansion again becomes the dominant mechanism and the sample expands once more.

It can be seen that the temperature at which the shoulder appears in the as-cast blend thin film and the thin film left for 7 days in atmosphere is identical. This indicates that the T_g for P3HT:PCBM blend films subjected to such different (ambient) ageing treatments is the same. This implies that the removal of trapped solvent is a relatively inefficient process from the film when left under ambient conditions, as solvent loss is opposed by the very slow volume relaxation of the glassy film. For the sample held under high vacuum, the temperature onset of the shoulder in the thermal expansion

rate shifts to 70°C. This increase in temperature occurs because trapped solvent in the film acts as plasticizer and will therefore decrease its T_g ⁴. Thus when some (but not all) solvent is lost during the vacuum treatment, the T_g shifts to a higher temperature, consequently delaying the onset of the shoulder. Previous work has shown that such a vacuum treatment can remove some of the trapped solvent from a polymer thin film³, a result confirmed qualitatively here. It appears therefore that freshly cast P3HT:PCBM blends trap some fraction of the casting solvent which can be subsequently removed by thermal annealing or exposure to high vacuum.

To explore the entire thermal annealing process, P3HT:PCBM blend films were heated at a rate of 90°C/min to either 50°C (below T_g of the blend), 150°C (between T_g and T_m of the blend) and 200°C (at the T_m of the blend). Following isothermal annealing at these temperatures for periods of up to one hour, thin films were cooled either linearly or exponentially, the latter achieved by switching off the temperature controller. In Figure 5.2, a number of plots of film thickness change (normalised to thickness at time $t = 0$) as a function of time are presented for samples subject to different annealing protocols. In all cases the entire timescale covers the initial heating, isothermal annealing and cooling processes. In Figure 5.2(a) it is apparent that film expansivity increases as the isothermal annealing temperature is raised. The maximum expansivity for blend thin films heated to 50°C, 150°C or 200°C is 2, 7 and 13% respectively.

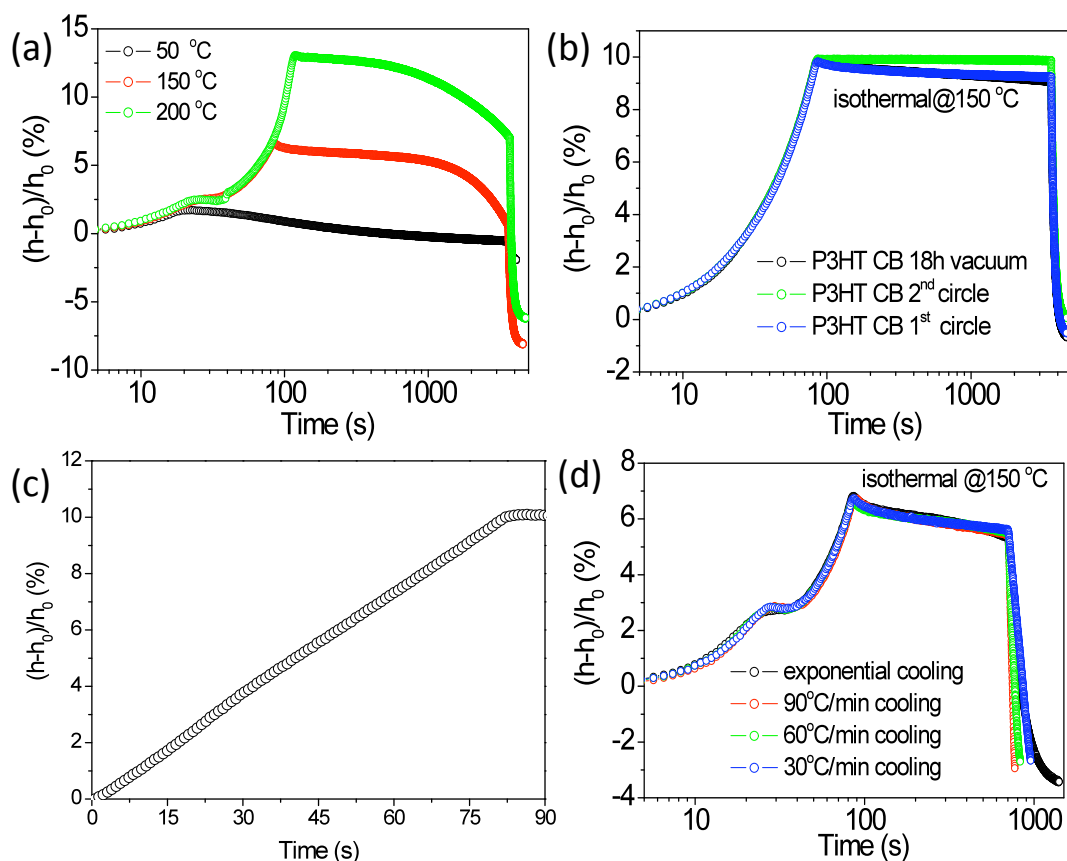


Figure 5.2: a) The relative changes in P3HT:PCBM film thickness during heating, isothermal annealing, and cooling processes. b) Thickness changes on heating, annealing and cooling of a pure P3HT films. c) Thickness change of a pure P3HT film during heating on a linear time scale. d) The changes in P3HT:PCBM film thickness under the same heating and isothermal treatments but with different linear cooling rates. The isothermal annealing period is 60 minutes in part a) and b) and 10 minutes in part c).

Before proceeding to discuss the properties of the blend during isothermal annealing, it is instructive to first compare the heating of blend thin films (Figure 5.2(a)) and films of pure P3HT (Figure 5.2(b)). As can be seen, upon heating to 150 °C, all P3HT films undergo a linear expansion of ~10% without any evidence of the shoulder seen in the blend films. This can be seen more clearly in Figure 5.2(c). As shown in part

(a), the thickness evolution during heating of pure P3HT films either held in vacuum for 18 hrs or heated for a second time, are identical to that recorded from a freshly cast film. If any solvent were trapped in a freshly cast film, one would expect it to be removed by the annealing protocol used, or by a lesser extent from exposure to vacuum. As no difference is observed between the linear thickness expansion in the three samples measured, it strongly suggests that there is very little solvent trapped in an as-cast P3HT thin film. Since the film casting process occurs at a temperature above the apparent T_g of the polymer, the results indicate that as-cast P3HT thin films are rubbery in nature at ambient conditions, thus having relatively high chain mobility. Consequently this reduces the ability of a pure P3HT film to trap solvent.

The discussion now turns to the properties of the blend and pure polymer thin films during isothermal annealing. As mentioned in chapter 2, section 2.6, it is known that during a spin-casting (or quenching) process, a large free volume can be “frozen in” to a vitrified amorphous polymer thin film as a result of insufficient time being available for molecular relaxation⁵. Upon heating, such thin films can undergo a molecular scale relaxation process involving a structural rearrangement that permits the film to reduce in volume until it reaches an equilibrium state. This does not necessarily imply self-organisation; structural relaxation can also occur in the amorphous phase of a semi-crystalline polymer. As is shown in Figure 5.2(a), it can be seen that volume relaxation (i.e. a relative reduction in film thickness towards a plateau) occurs during the early stage of the isothermal annealing process of the P3HT:PCBM thin film for all temperatures. This process occurs more slowly at lower temperatures. It is likely that the volume relaxation of P3HT:PCBM thin film at 50°C occurs due to the rearrangement of the amorphous regions within the film, given the

driving force for P3HT crystal formation is weak. As the isothermal annealing temperature is raised however, volume relaxation will result from a combination of structural rearrangement *and* crystallisation of amorphous P3HT. It can be seen that volume relaxation also occurs in an as-cast semi-crystalline P3HT film (Figure 5.2(b)) during its first annealing treatment. During the second heating cycle however to an identical temperature, no volume relaxation is observed – the thickness of the sample remains constant over the course of the isothermal annealing process. It is likely that the first heating cycle promotes further self-organisation within the thin film, thus any remaining amorphous regions within such a relatively high crystallinity polymer film can be regarded as being constrained ^{5a}. Consequently, any remaining amorphous regions cannot undergo volume relaxation with the same degree of freedom compared to amorphous regions that exist in low crystallinity P3HT films.

From Figure 5.2(a), it is apparent that during the isothermal annealing process of P3HT:PCBM blend films at 150 and 200°C, there is a significant reduction in film thickness that occurs at time $t > 1000$ s. From Figure 5.2(b) no significant decrease in film thickness for pure P3HT is observed during isothermal annealing.

The mechanism that results in the reduction in sample thickness is now considered. In a blend system, it is not possible to precisely decouple the processes of volume relaxation and phase separation, or accurately determine their onset or end. However, several studies have shown that PCBM molecules diffuse during annealing at a temperature above the T_g of the film to eventually form aggregates or needle-like crystals ⁶. Indeed, recent work using high resolution transmission electron microscopy

(HRTEM) ⁷ has been used to track the aggregation and crystallisation of PCBM during thermal annealing, concluding that aggregation results from the agglomeration of pre-existing PCBM nanodomains in the as-cast films, rather than phase-separation of PCBM from mixed amorphous P3HT:PCBM phases. Figure 5.3 shows a series of optical microscopy images of P3HT:PCBM films recorded before and after thermal annealing. Micron-scale PCBM crystals with an average length around 10 μm , or needle-like crystals around 200 to 400 μm in length appear in the blend films after annealing at 150°C and 200°C for 1 hr, respectively. As the total amount of PCBM within each sample can be considered constant under the conditions reported here, the formation of any micron-scale PCBM crystals occurs at the expense of a depletion of the remaining material in the bulk. Consequently, the average film thickness decreases whilst film roughness increases.

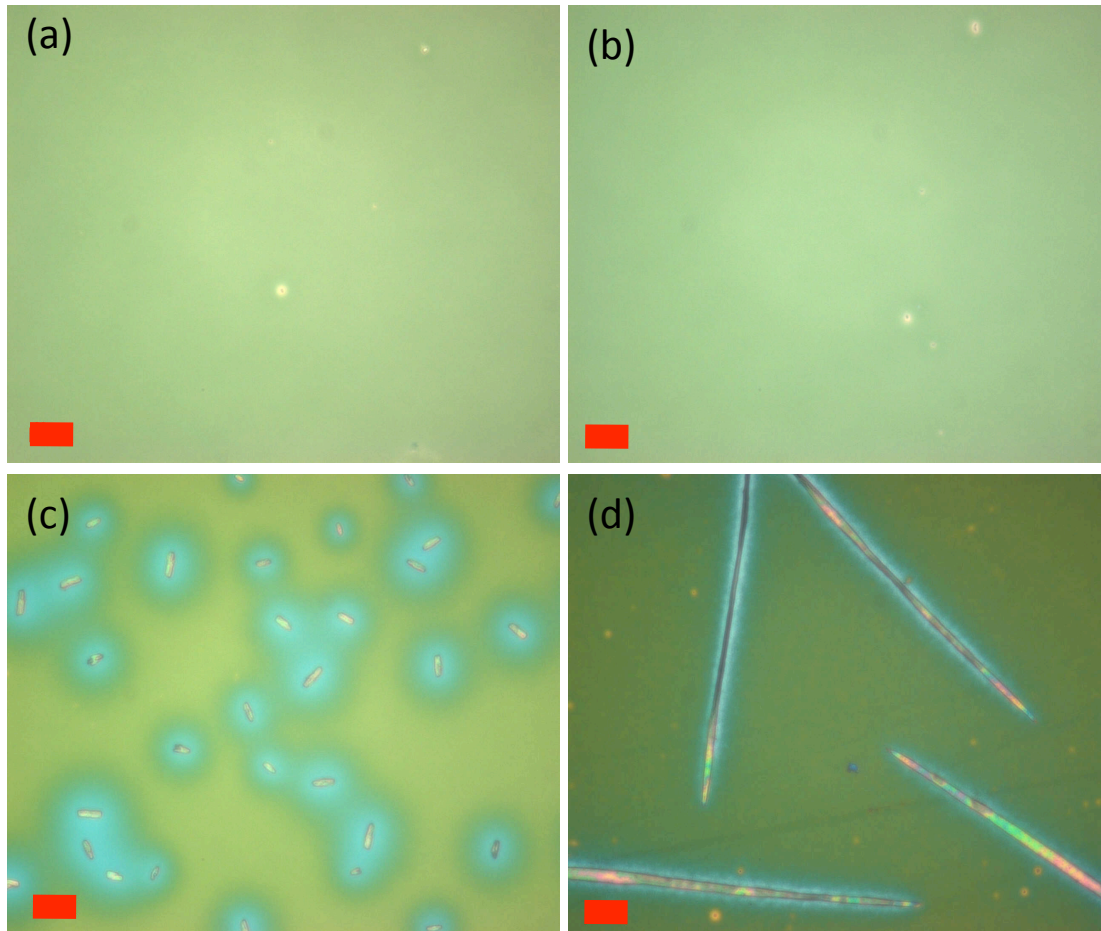


Figure 5.3: Optical microscopy images of P3HT:PCBM blend films (a) as-cast and after annealing for 60 minutes at (b) 50°C, (c) 150°C and (d) 200°C. The scale bar in each image corresponds 20 μm.

To support the idea that coarse phase separation reduces average film thickness, AFM has been used to characterise the depletion region around a PCBM crystallite. The results are presented in Figure 5.4. As shown, a region of relatively lower height (~15 nm) surrounds the crystallite, extending approximately 15 μm either side of the feature. Note that the thickness of the film before annealing was 70 ± 4 nm, indicating that mass transfer of PCBM has reduced the thickness of the thin film in the vicinity of a crystallite by ~20%.

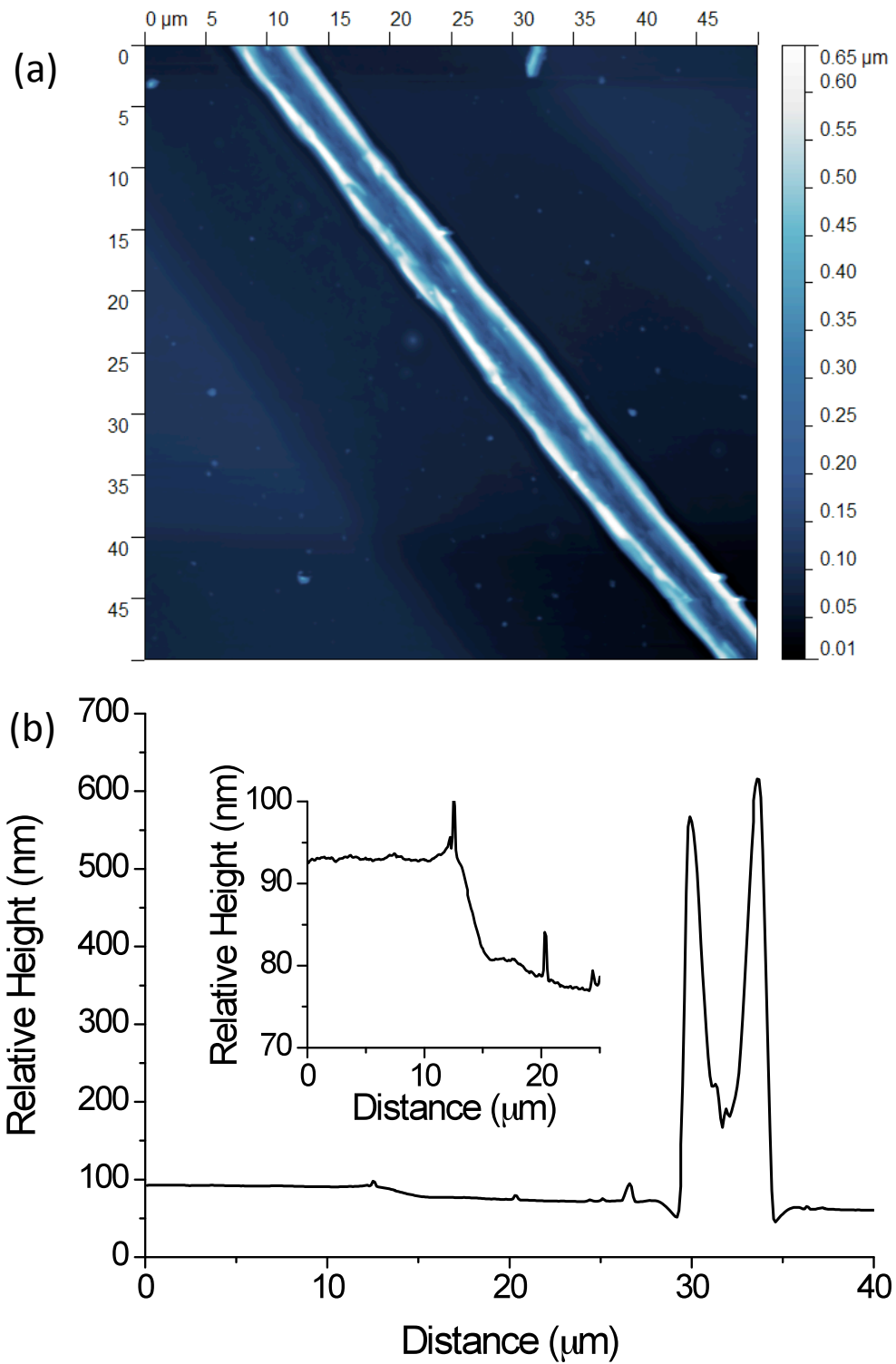


Figure 5.4: (a) AFM height scan of a PCBM crystallite. The sample is a blend thin film of P3HT:PCBM that has undergone isothermal annealing at 200°C for 1hr. In (b) a line profile of the AFM data taken across the crystallite. The depth of the depletion region is shown more clearly in the inset.

From Figure 5.3(b) no evidence for coarse (μm scale) phase separation in the blend thin film that has undergone annealing at 50°C is found. At this temperature – which is below the T_g of the blend – P3HT molecular chains are likely to remain relatively rigid and, as a consequence, the PCBM molecules will have difficulty in diffusing through the polymer matrix to form crystals. This observation further supports the argument that the thickness change of the P3HT:PCBM blend film upon isothermal annealing at 50°C , which is comparable in relative magnitude to that observed in pure P3HT films as shown in Figure 5.2(b), is due to volume relaxation of non-equilibrium amorphous P3HT conformations.

Following the isothermal annealing step, as expected both P3HT and P3HT:PCBM films shrink as they cool. From Figure 5.2(d) a linear cooling process reduces the thickness linearly whilst an exponential cooling rate reduces the film thickness exponentially. It can be seen that once the films are returned to room temperature, a significant reduction in sample thickness has occurred. Here, a combination of solvent loss, volume relaxation, crystallisation, and phase separation together adequately account for this phenomenon in P3HT:PCBM blends. Recent studies on P3HT:PCBM thin films using grazing incidence X-ray scattering reported a reduction in average interchain spacing when the films were returned from annealing temperature to room temperature⁸, a result in qualitative agreement with the observations presented here.

SECTION 5.3: OPTICAL CHARACTERISTICS OF FILMS DURING THERMAL ANNEALING

In this section the optical properties of the thin films, monitored during thermal annealing, are discussed. In Figure 5.5, the modeled extinction coefficient (k) spectra are presented for a thin film of pure P3HT recorded during heating, isothermal annealing at 150°C and subsequent cooling. It can be seen that before annealing (i.e. at room temperature) the k -spectrum exhibits a peak at 510 nm and two shoulders at 550 and 600 nm, thus indicating the presence of relatively self-organised P3HT domains. Upon heating to 150°C (Figure 5.5(a)), the peak absorption blue-shifts to 495 nm and undergoes a relative reduction in intensity. As the total number of polymer molecules in a thin film can be regarded as constant, the thermal expansion increases the volume space between polymer chains. The reduction in the peak value of k therefore most likely indicates increased free volume and decreased intermolecular order between polymer chains. The associated blue-shift also suggests a reduction in the overall degree of electronic conjugation.

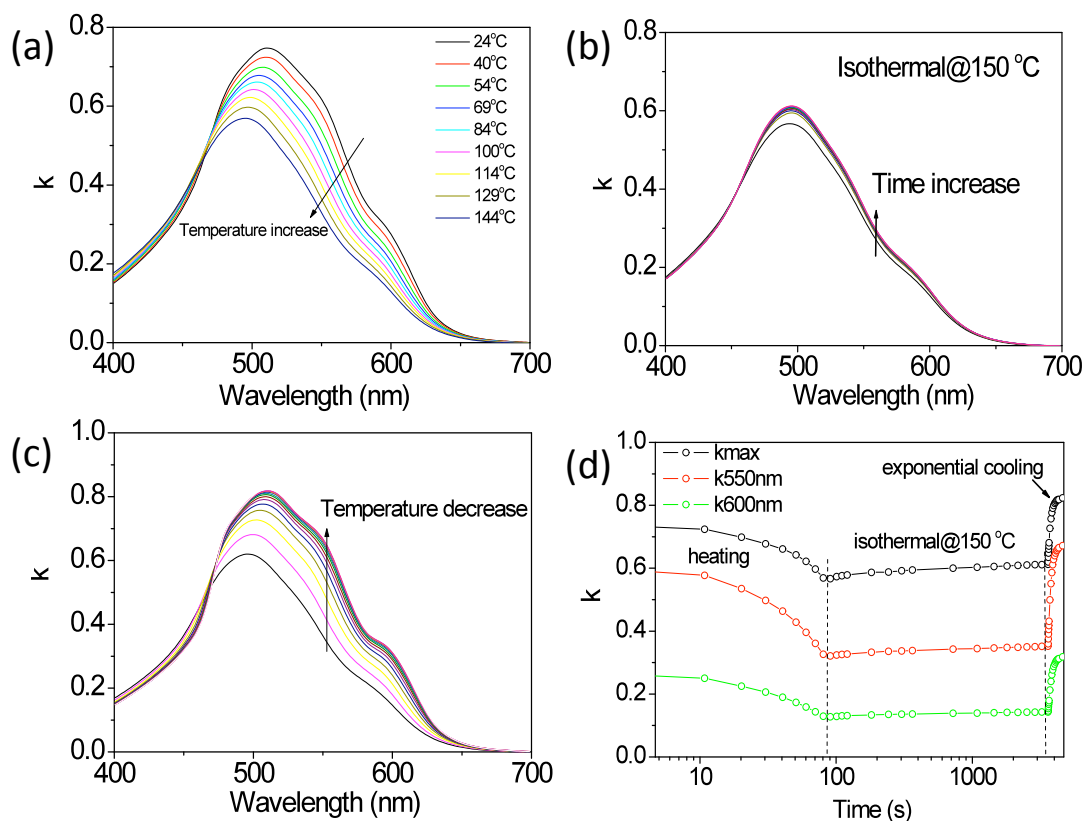


Figure 5.5: The extinction coefficient spectra of a P3HT thin film during a) heating to 150°C, b) isothermal annealing at 150°C, and c) exponential cooling to 25°C. Time intervals between spectra in parts b) and c) are 720 and 120 seconds, respectively. d) The kinetics of k_{max} , k_{550nm} and k_{600nm} of P3HT as a function of time during the thermal annealing cycle.

From Figure 5.5(b), it can be seen that during isothermal annealing the wavelength location of the peak absorption (k) and shoulders at 550 nm and 600 nm undergo very little change. It is apparent however that there is a small increase in the magnitude of k , which may well result from volume relaxation of the film during the isothermal annealing process, as shown Figure 5.2(b). Note the relative increase in k over the course of the isothermal step (see Figure 5.5(d)) is $\sim 8.7\%$, a value in reasonable agreement with the relative reduction in sample thickness ($\sim 7.6\%$). During the cooling process (Figure 5.5(c)), the main absorption peak red-shifts from 495 nm to

510 nm. This shift occurs simultaneously with a relative strengthening in the magnitude of k at 600 nm. In chapter 4, section 4.1 a strong correlation between the strength of k_{605} and the relative crystallinity of P3HT was shown. The overall red-shift and enhanced absorption at 600 nm on cooling measured in this study therefore suggests that the planarisation of P3HT and electronic conjugation increase significantly during this process.

The evolution of k in a blend thin film of P3HT:PCBM during a thermal anneal (to 150°C) is presented in Figure 5.6. During heating (Figure 5.6(a)) it is apparent that the changes in k are qualitatively more complex than the evolution in k for pure P3HT (Figure 5.5(a)). As can be seen, upon heating to below T_g the k spectrum blue-shifts and decreases in intensity. It then red-shifts and increases in intensity when the temperature is above T_g of the blend (between 60 and 70°C). Finally, at temperatures much greater than T_g , the k spectrum blue shifts and decreases in intensity once more. This can be seen more clearly in Figure 5.6(c) where the magnitude and wavelength of k_{max} is presented for the pure and blend thin films as a function of temperature during the initial heating cycle. To compare the evolution of k over the thermal annealing process at different temperatures, the modeled k values from blend thin films to have undergone isothermal annealing at 50°C or 200°C are presented in Figure 5.7. Here a plot of k after annealing at 150°C for 10 minutes, for both P3HT and P3HT:PCBM blend films is also included to highlight the effect of PCBM content in the film.

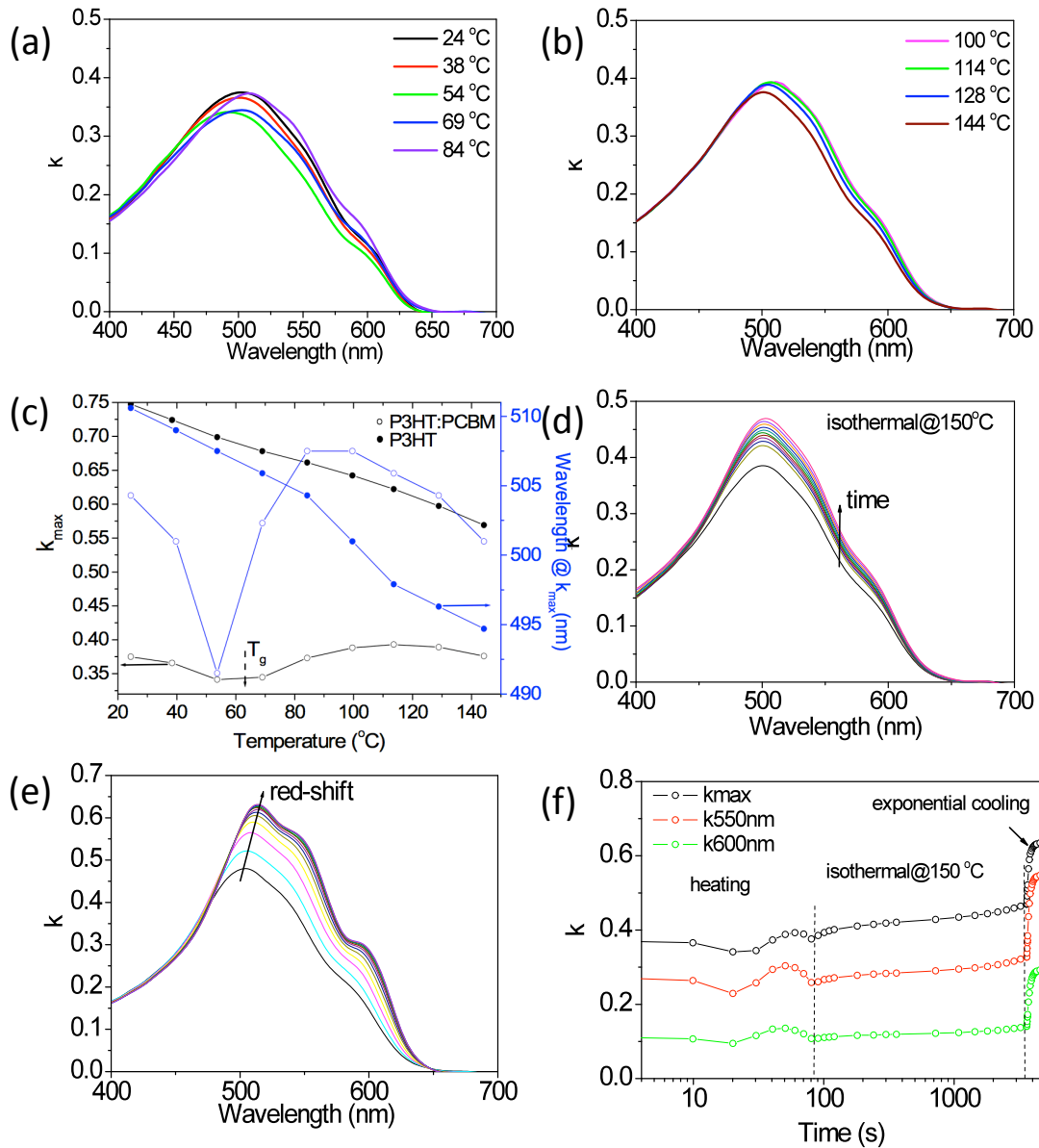


Figure 5.6: The absorption spectra of a P3HT:PCBM film a) during heating around T_g of the blend and b) when the temperature is heated far above T_g of the blend. c) The evolution of k_{\max} and the wavelength of k_{\max} of pure P3HT and P3HT:PCBM films during the initial heating process as a function of temperature. d) A plot of k during the isothermal annealing at 150 °C, and e) during exponential cooling to 25 °C. The time interval between spectra in parts d) and e) is 720 and 120 seconds, respectively. f) The evolution of k_{\max} , $k_{550\text{nm}}$ and $k_{600\text{nm}}$ of a P3HT:PCBM blend film during heating, isothermal annealing and cooling.

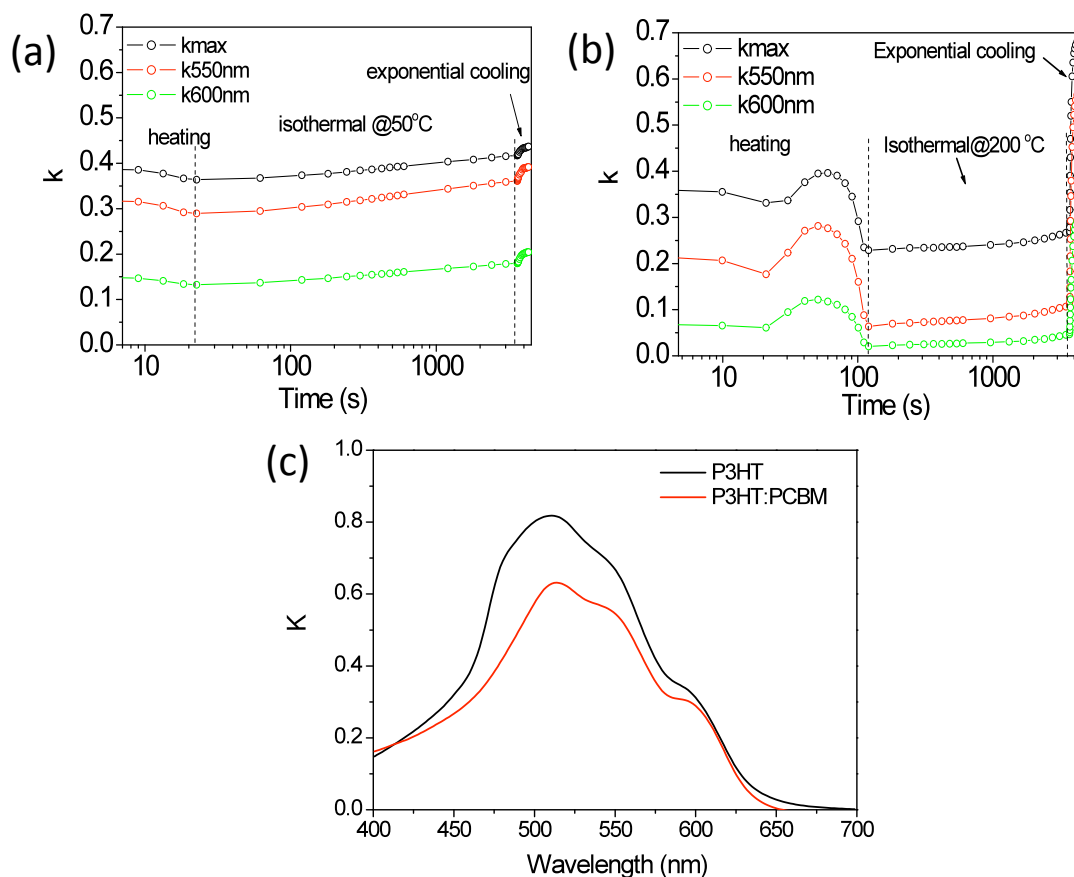


Figure 5.7: The evolution of k_{\max} , k_{550} and k_{600} of a P3HT:PCBM blend film during heating, isothermal annealing and cooling. Thin films were annealed for 1 hr at 50°C (a) or 200°C (b) respectively. In part (c) the final k spectra for P3HT and P3HT:PCBM blend films after annealing at 150°C for 10 minutes.

As discussed in section 5.2 of this chapter, P3HT:PCBM thin films trap a small fraction of the casting solvent, that is subsequently lost once the films are heated above T_g . This suggests that the red-shift and increase in absorption intensity observed when a P3HT:PCBM blend film is heated just above its T_g results from solvent loss. This will cause a spectral red-shift and an increase in the intensity of the k_{\max} as a result of improved molecular organisation. In contrast, when a blend film is heated and held to a temperature below its T_g (at 50°C) for 1 hr, the absorption spectra show

monotonic changes only with the intensity of absorption reducing and the spectra undergoing a blue shift (Figure 5.7(a)). During isothermal annealing at 150°C, the absorption spectrum of the blend increases in intensity without undergoing any obvious wavelength shift. Spectra also undergo a relatively greater increase in intensity and red-shift during film cooling as shown in Figure 5.6(e). Figure 5.6(f) summarises the evolution of k_{\max} , $k_{550 \text{ nm}}$, and $k_{600 \text{ nm}}$ as a function of time during the entire annealing process.

The discussion now considers the optical properties of the blend thin films after the annealing process. In Figure 5.8, absorption spectra of P3HT:PCBM blend thin films are presented after annealing to different temperatures. Relative to the absorption spectrum of an unannealed (as-cast) blend thin film, it can be seen k_{\max} red-shifts from 505 to 512 nm as a result of annealing, and the shoulders at k_{550} and k_{600} increase in intensity; a result indicative of increased P3HT crystallinity.

In Figure 5.8(b) the photoluminescence (PL) emission recorded a P3HT:PCBM blend film following annealing is presented. It is apparent that the PL intensity of P3HT is reduced significantly when blended with PCBM. However, upon annealing a partial recovery in PL emission intensity of the P3HT:PCBM blend is detected. The significant (~90%) reduction in emission intensity of the as-cast P3HT:PCBM blend thin film compared to the pure P3HT thin film implies efficient quenching of P3HT photoluminescence by the PCBM. Annealing above T_g promotes phase separation between P3HT and PCBM, with higher temperatures correlated with a relative increase in P3HT emission intensity. This observation suggests that after annealing,

fewer excitons generated within P3HT domains diffuse to an interface with PCBM to undergo dissociation into free charges⁹.

Figure 5.8(c) shows the absorption of blend films that have either been slowly cooled to room temperature (at 90 or 30°C min⁻¹), or quenched to room temperature over a period of a few seconds. For comparison, the absorption spectrum of an as-cast film is also included. It can be seen that the cooling rate has a pronounced effect on the absorption spectrum. Films cooled slowly (> 30°C min⁻¹) are apparently highly crystallised, however the film quenched to room temperature has a lower and relatively blue-shifted value of k_{max} , indicative of a lower degree of crystallinity. In Figure 5.8(d) the relative photoluminescence intensity of films either cooled slowly to room temperature or rapidly quenched is presented. There is little difference between the emission intensity, suggesting a similar distribution of domain sizes within these films.

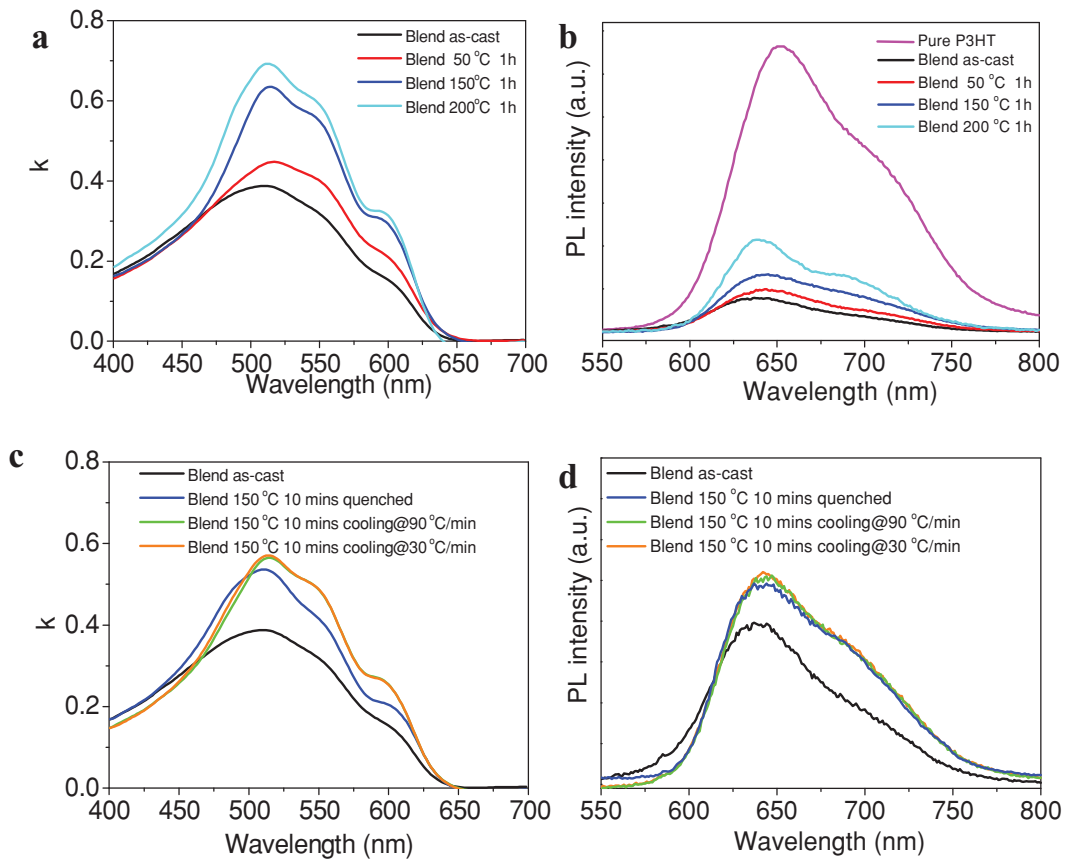


Figure 5.8: In parts (a) & (c) are extinction coefficient spectra for blend thin films after a number of thermal annealing protocols explored in this chapter. In parts (b) and (d) the relative photoluminescence (PL) intensity from blend thin films after thermal annealing is presented. Spectra have been corrected for thin film absorption effects. In part (b) the PL spectrum of pure P3HT is included to highlight the quenching efficiency of PL from the blend samples.

SECTION 5.4: PHOTOVOLTAIC PROPERTIES OF P3HT:PCBM THIN FILMS

A series of OPV devices were fabricated in order to correlate device efficiency with the apparent morphological differences between blend thin films that were subjected to different annealing protocols. A series of selected illuminated JV characteristics are shown in Figure 5.9, with average efficiency metrics for all devices investigated presented in Table 5.1.

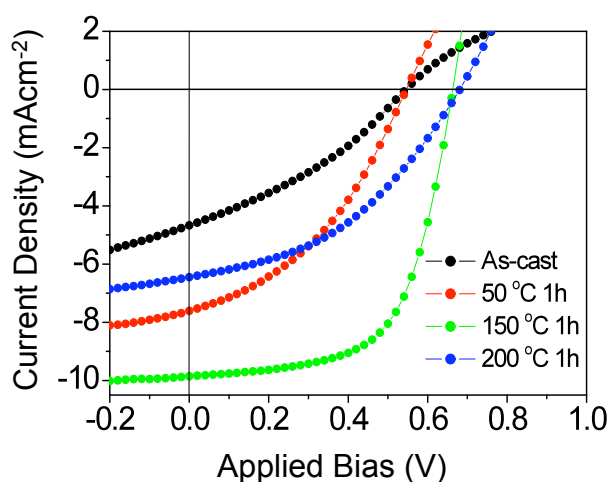


Figure 5.9: JV characteristics of a series of P3HT:PCBM devices under white light illumination following different thermal annealing treatments.

It can be seen that the average PCE of an as-cast device increases from $0.85 \pm 0.04 \%$ to $1.64 \pm 0.04 \%$ after annealing at 50°C for 1 hr. As significant crystallisation and phase separation of P3HT and PCBM is unlikely to occur at this temperature, the near doubling in device PCE is tentatively attributed to volume relaxation that develops an equilibrium amorphous morphology. The PCE further improves to $4.00 \pm 0.1\%$ when

the device is annealed at 150°C for 1 hr. Annealing at 200°C results in a significant degradation in performance, with devices having an average PCE of $1.83 \pm 0.1\%$.

Annealing Temperature (°C)	Annealing Time (min)	Cooling Rate (°C min ⁻¹)	V _{oc} (V)	J _{sc} (mAcm ⁻²)	FF (%)	PCE (%)
as-cast	-	-	0.53	4.65	34.4	0.85±0.04
50	60	exponential	0.54	7.62	40.0	1.64±0.04
200	60	exponential	0.68	6.63	42.6	1.83±0.10
150	60	exponential	0.66	9.92	61.4	4.00±0.15
150	30	exponential	0.66	10.04	59.5	3.95±0.05
150	10	exponential	0.65	9.71	62.5	3.93±0.08
150	10	90	0.66	9.77	62.3	4.02±0.11
150	10	80	0.65	9.83	62	3.94±0.10
150	10	8	0.64	10.01	60.7	4.03±0.02
150	10	quenched	0.66	9.48	60.1	3.75±0.11

Table 5.1: Average device performance metrics of all the devices following a range of annealing treatments. The uncertainty in PCE values represented the standard deviation of 6 pixels. Note that to quench devices from 150°C, samples were transferred from a hot-plate onto a metal plate at room temperature, facilitating cooling in ~5-10s.

For thin films that have undergone annealing at this temperature, the peak optical density (Figure 5.8(a)) is the largest of all the annealed samples, suggesting the most efficient solar harvesting. However, PL emission intensity (Figure 5.8(b)) and optical microscopy (Figure 5.3(d)) indicate that annealing at 200°C has resulted in overly developed phase separation between P3HT and PCBM. The coarsening of domains and depletion of PCBM from the bulk of the thin film will clearly hinder the process of efficient exciton dissociation, as shown earlier in chapter 4, section 4.2. As this process is one of the most important steps in photocurrent generation¹⁰, its impact on the PCE is highly detrimental.

The results show that annealing at 150°C for times between 10 minutes and 1 hr represents an optimal treatment condition, as it results in the creation of devices having a PCE between 3.9 ± 0.1 % to 4.0 ± 0.1 %. As discussed, the linear cooling rates (varied from $90^\circ\text{C min}^{-1}$ to 8°C min^{-1}) investigated in this work have little impact upon either optical absorption or PL intensity, with resultant devices all behaving identically within experimental uncertainty. Importantly however, devices annealed at 150°C for 10 minutes and subsequently quenched (over the course of a few seconds) to room temperature have a significantly lower average PCE of 3.75 ± 0.1 %. This lower efficiency mainly results from a lower J_{sc} and a slightly smaller FF compared to devices that were cooled either linearly or exponentially. As shown in Figure 5.8(c) the optical density of the blend film that was quenched to room temperature after isothermal annealing is smaller compared to films that were cooled linearly. This suggests that the thermal quench does not provide sufficient time for P3HT to undergo crystallization and results in a greater fraction of relatively amorphous P3HT domains being present. These phases will have reduced optical

density, which will clearly reduce J_{sc} , whilst the relatively poor charge transport efficiencies of amorphous material will likely reduce the FF ¹⁰⁻¹¹. Another possibility is that molecules can freeze into non-equilibrium states during the rapid thermal quench. Such assumed non-equilibrium morphological states clearly have a detrimental affects on device efficiency, as their removal (e.g., by annealing at 50°C for 1 hr) results in a relatively significant improvement in device power conversion efficiency (from 0.85% to 1.64%). Such states may act to reduce device efficiency by reducing the overall mobility of charge-carriers within the film resulting from reduced π - π stacking, or by acting as charge traps.

SECTION 5.5: CONCLUSIONS

In this chapter spectroscopic ellipsometry has been used to give a detailed insight into the processes which occur during the thermal annealing of blend thin films of P3HT and P3HT:PCBM. As the T_g of pure P3HT is below the ambient temperature at which the thin films were cast, casting solvent is unlikely to remain trapped after the film has vitrified. In contrast, the relatively elevated T_g of P3HT in the blend samples causes a small fraction of solvent to become trapped inside the thin film. By exceeding the T_g of the blend during thermal annealing, trapped solvent may escape; a process that leads to a reduction in the expansion rate of the film and associated changes in the optical absorption characteristics of the blend. During isothermal annealing and cooling, thin film blends undergo volume relaxation, phase separation and crystallisation. By subjecting blend thin films to a range of annealing

temperatures, annealing times and cooling rates, a series of apparently morphologically distinct samples were created.

OPV devices were subsequently fabricated using active layers that had undergone identical annealing protocols in order to correlate apparent morphological differences in thin film blends to their photovoltaic efficiency. It is important to acknowledge that the presence of a cathode on the free surface of the OPV devices prior to thermal annealing may introduce morphological differences between these samples and annealed blend films. However, it is not possible to measure the properties of a blend thin film using SE when the film is covered by an opaque metallic layer. Whilst the results were in agreement with previous studies, the cooling rate was found to have a small impact on device efficiency, with devices rapidly cooled having an apparently reduced content of semi-crystalline P3HT. Thus light absorption and charge transport efficiency will likely be lower compared to devices to have been slowly cooled to room temperature.

The results presented here use the link between P3HT crystallinity and optical absorption characteristics, as discussed in the previous chapter, to develop a mechanistic understanding of the thermal annealing process for polymer:fullerene blend OPVs. The results here provide a backdrop for the following chapter, in which the phase behaviour of several P3HT:PCBM blend compositions are explored and related to the photovoltaic properties of films and devices subject to thermal annealing. This helps to rationalise and provide a general overview of the processing step.

SECTION 5.6: REFERENCES

1. Wang, T.; Pearson, A. J.; Lidzey, D. G.; Jones, R. A. L., Evolution of Structure, Optoelectronic Properties, and Device Performance of Polythiophene: Fullerene Solar Cells During Thermal Annealing. *Advanced Functional Materials* **2011**, *21* (8), 1383-1390.
2. (a) Zhao, J.; Swinnen, A.; Van Assche, G.; Manca, J.; Vanderzande, D.; Van Mele, B., Phase Diagram of P3HT/PCBM Blends and Its Implication for the Stability of Morphology. *J Phys Chem B* **2009**, *113* (6), 1587-1591; (b) Hopkinson, P. E.; Staniec, P. A.; Pearson, A. J.; Dunbar, A. D. F.; Wang, T.; Ryan, A. J.; Jones, R. A. L.; Lidzey, D. G.; Donald, A. M., A Phase Diagram of the P3HT:PCBM Organic Photovoltaic System: Implications for Device Processing and Performance. *Macromolecules* **2011**, *44* (8), 2908-2917.
3. Richardson, H.; Sferrazza, M.; Keddie, J. L., Influence of the glass transition on solvent loss from spin-cast glassy polymer thin films. *Eur Phys J E* **2003**, *12*, S87-S91.
4. Wang, T.; Dunbar, A. D. F.; Staniec, P. A.; Pearson, A. J.; Hopkinson, P. E.; MacDonald, J. E.; Lilliu, S.; Pizzey, C.; Terrill, N. J.; Donald, A. M.; Ryan, A. J.; Jones, R. A. L.; Lidzey, D. G., The development of nanoscale morphology in polymer: fullerene photovoltaic blends during solvent casting. *Soft Matter* **2010**, *6* (17), 4128-4134.
5. (a) Hutchinson, J. M., Physical Aging of Polymers. *Prog Polym Sci* **1995**, *20* (4), 703-760; (b) Kawana, S.; Jones, R. A. L., Effect of physical ageing in thin glassy polymer films. *Eur Phys J E* **2003**, *10* (3), 223-230; (c) Richardson, H.; Lopez-Garcia, I.; Sferrazza, M.; Keddie, J. L., Thickness dependence of structural relaxation in spin-cast, glassy polymer thin films. *Phys Rev E* **2004**, *70* (5).

6. (a) Campoy-Quiles, M.; Ferenczi, T.; Agostinelli, T.; Etchegoin, P. G.; Kim, Y.; Anthopoulos, T. D.; Stavrinou, P. N.; Bradley, D. D. C.; Nelson, J., Morphology evolution via self-organization and lateral and vertical diffusion in polymer: fullerene solar cell blends. *Nature Materials* **2008**, *7* (2), 158-164; (b) Watts, B.; Belcher, W. J.; Thomsen, L.; Ade, H.; Dastoor, P. C., A Quantitative Study of PCBM Diffusion during Annealing of P3HT: PCBM Blend Films. *Macromolecules* **2009**, *42* (21), 8392-8397.
7. Beal, R. M.; Stavrinadis, A.; Warner, J. H.; Smith, J. M.; Assender, H. E.; Watt, A. A. R., The Molecular Structure of Polymer-Fullerene Composite Solar Cells and Its Influence on Device Performance. *Macromolecules* **2010**, *43* (5), 2343-2348.
8. (a) Verploegen, E.; Mondal, R.; Bettinger, C. J.; Sok, S.; Toney, M. F.; Bao, Z. A., Effects of Thermal Annealing Upon the Morphology of Polymer-Fullerene Blends. *Advanced Functional Materials* **2010**, *20* (20), 3519-3529; (b) Lilliu, S.; Agostinelli, T.; Pires, E.; Hampton, M.; Nelson, J.; Macdonald, J. E., Dynamics of Crystallization and Disorder during Annealing of P3HT/PCBM Bulk Heterojunctions. *Macromolecules* **2011**, *44* (8), 2725-2734.
9. van Bavel, S. S.; Barenklau, M.; de With, G.; Hoppe, H.; Loos, J., P3HT/PCBM Bulk Heterojunction Solar Cells: Impact of Blend Composition and 3D Morphology on Device Performance. *Advanced Functional Materials* **2010**, *20* (9), 1458-1463.
10. Blom, P. W. M.; Mihailetchi, V. D.; Koster, L. J. A.; Markov, D. E., Device physics of polymer : fullerene bulk heterojunction solar cells. *Advanced Materials* **2007**, *19* (12), 1551-1566.
11. Mihailetchi, V. D.; Xie, H. X.; de Boer, B.; Koster, L. J. A.; Blom, P. W. M., Charge transport and photocurrent generation in poly (3-hexylthiophene):

Methanofullerene bulk-heterojunction solar cells. *Advanced Functional Materials* **2006**, *16* (5), 699-708.

CHAPTER 6: RATIONALISING PHASE TRANSITIONS WITH THERMAL ANNEALING TEMPERATURES FOR P3HT:PCBM OPV DEVICES

SECTION 6.1: INTRODUCTION

In this chapter the composition of the active layer in P3HT:PCBM OPVs is demonstrated to determine the range of thermal annealing temperatures that can be used to increase device performance ¹. By comparing device studies with the thermal transitions of the blend, the results develop a mechanistic understanding of this processing step, potentially providing a framework to design effective annealing protocols for future polymer:fullerene blend OPVs. For certain as-cast P3HT:PCBM blend thin-films two glass transitions related to the polymer are evidenced, which most likely correspond to the existence of two compositionally different amorphous states. It is shown that an improvement in device efficiency only occurs once the film has been heated above its upper apparent glass transition temperature. If annealing is performed above an optimum temperature, excessive phase-separation and a partial reduction in film optical density leads to a general decrease in device efficiency.

A number of studies have attempted to construct a phase diagram for blends of P3HT:PCBM in order to elucidate the thermal properties of the system and relate these to the properties of OPVs ². Given the sensitivity of P3HT:PCBM film

morphology to processing conditions, it is not always clear if the samples prepared for thermal characterisation are representative of samples prepared for OPV fabrication. For example, the phase behaviour of a drop-cast film may differ from the phase behaviour of a film that has been prepared by spin-casting, owing to differences in the drying dynamics of either sample ^{2a}.

In this chapter, a phase diagram for P3HT:PCBM blend thin-films is constructed using spectroscopic ellipsometry (SE), focusing on transitions at relatively low temperatures (below 100°C) only. Here, the methodology employed in the previous chapter is followed. The results are in close qualitative agreement with a phase diagram for the same system determined using Dynamic Mechanical Thermal Analysis (DMTA) by Hopkinson *et al.* ^{2b} Specifically, the relative increase in the glass transition temperature (T_g) of the P3HT phase within the blend films increased with increasing weight fraction of PCBM (wt%), until the PCBM undergoes partial phase separation in the as-cast film. Beyond this threshold concentration (measured at 66 wt% PCBM), a relative reduction in the T_g of the P3HT phase suggested a reduced concentration of PCBM mixed within the polymer phase.

In this chapter, SE is used to monitor the thermal expansion of blend thin films prepared identically to those used in OPVs. This demonstrates that the T_g of P3HT containing phases within the blend thin-films increases as the relative fraction of PCBM in the blend is increased from 20 to 60 wt%. However a relative decrease is observed in T_g in a blend thin-film containing a PCBM loading of 80 wt%. For blends compositions in which two T_g s can be detected, the higher temperature T_g apparently

defines the minimum annealing temperature for which an improvement in device efficiency can occur. Above this temperature, residual casting solvent is removed and the film is driven by phase separation between P3HT and PCBM into a nanoscale morphology that is more favourable for efficient device operation. Annealing at temperatures in excess of optimal processing conditions however results in both excessive phase separation of PCBM and a relative blue shift in the optical density of the film, limiting its ability to efficiently harvest light.

SECTION 6.2: IMPACT OF THERMAL ANNEALING ON THE PHOTOVOLTAIC EFFICIENCY OF P3HT:PCBM OPV DEVICES

To begin with, the effects of thermal annealing on the power conversion efficiency (PCE) of a P3HT:PCBM device are revisited. Although it has been previously established that the film composition range that yields the best devices utilising this blend system is between 40 and 50 wt% PCBM³ it is instructive to probe a broader region of parameter space to give greater insight into the thermal response of P3HT:PCBM OPVs to thermal annealing.

First, to determine an appropriate isothermal annealing time, OPVs with an active layer containing between 40 and 60 wt% PCBM were annealed at 150°C for times ranging from 5 to 60 minutes. The PCEs of these annealed devices as a function of isothermal annealing time are presented in Figure 6.1. It can be seen that the PCE of all device compositions is significantly increased after only a short isothermal

annealing step. Within the uncertainty of device efficiencies (estimated as the standard deviation across 12 pixels), the PCE for each device composition appears to be relatively stable to annealing times ranging from 5 minutes up to 1 hr, an observation in accord with other studies⁴. From this preliminary experiment an isothermal annealing time of 10 minutes was chosen to further explore the impact of isothermal annealing temperature on device efficiency.

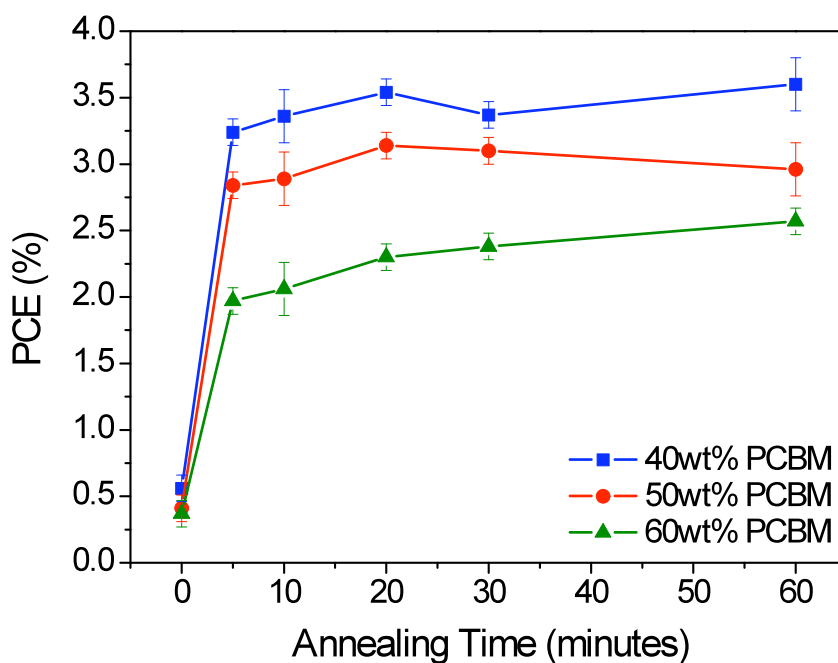


Figure 6.1: Power conversion efficiency of P3HT:PCBM blend OPVs (40 to 60 wt% PCBM) after annealing at 150°C for between 5 and 60 minutes.

In Figure 6.2 (a) the measured PCEs of devices having a PCBM content between 40 and 60 wt% as a function of annealing temperature is presented. The PCEs of devices containing 20 wt% and 80 wt% PCBM are shown in Figure 6.2(b). Average device metrics (FF , J_{sc} and V_{oc}) are presented in Figure 6.3.

In Figure 6.2(a), it can be seen that significant improvements in device efficiency can result from thermal annealing^{3a, 5}. For example, PCEs can be improved from less than 1% for all blend ratios, to up to 3.4% in a device containing a blend composed of 60:40 wt% P3HT:PCBM. The driving force for the improvement in device PCE come principally from changes in the short-circuit current density (J_{SC}), which can be seen from Figure 6.3. It can be seen that the J_{sc} of each device blend composition qualitatively follows the same trend with annealing temperature as the PCE, increasing and then decreasing at temperatures that are apparently characteristic of the blend composition. I quantify this by defining T_{onset} as the temperature beyond which device efficiency is improved compared to an equivalent unannealed control. T_{onset} increases from $45 \pm 5^\circ\text{C}$ in devices with a film composition of 40 wt% PCBM, to $70 \pm 5^\circ\text{C}$ in devices containing 60 wt% PCBM. At temperatures beyond T_{onset} , the PCE further increases, reaching an optimum value at a particular temperature, hereafter defined as $T_{optimum}$. When annealed at a temperature above $T_{optimum}$, the PCE of the devices is seen to decrease. $T_{optimum}$ is also apparently dependent on relative film composition, reducing from $130 \pm 5^\circ\text{C}$ in a 40 wt% PCBM film to $110 \pm 5^\circ\text{C}$ in film containing 60 wt% PCBM. Films containing a higher PCBM loading undergo a larger reduction in PCE when annealed at a temperature above $T_{optimum}$. For example, devices containing 40%, 50% and 60% (wt%) PCBM within the active layer that have been annealed at 40°C above $T_{optimum}$ have an efficiency that is 57, 47 and 42% of the efficiency of a device annealed at $T_{optimum}$.

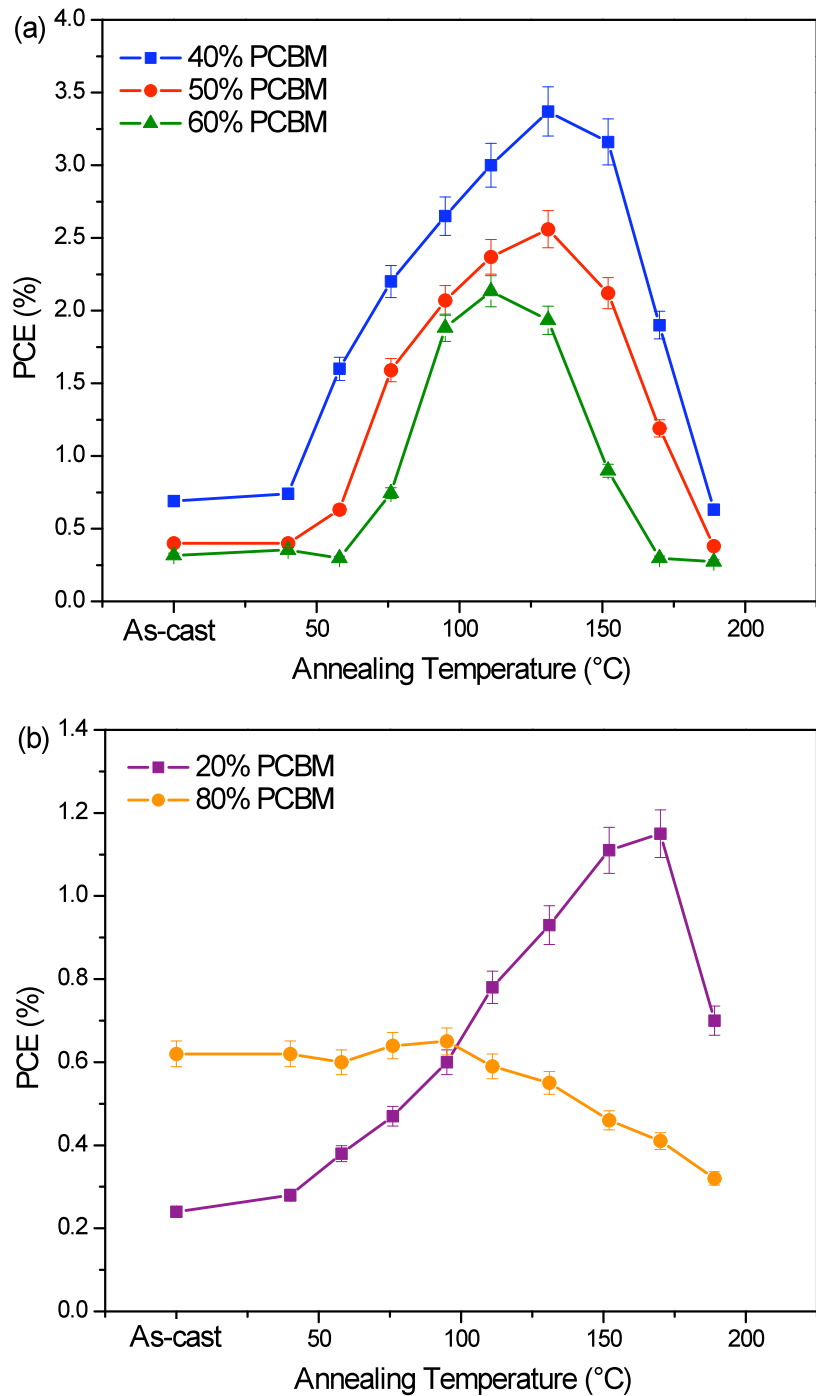


Figure 6.2: Power conversion efficiency (PCE) values for P3HT:PCBM blend devices as a function of annealing temperature. Data for devices having between 40 and 60 wt% PCBM in the active layer are shown in part (a), whilst part (b) shows data for devices with 20 wt% and 80 wt% PCBM. Lines are provided as a guide to the eye.

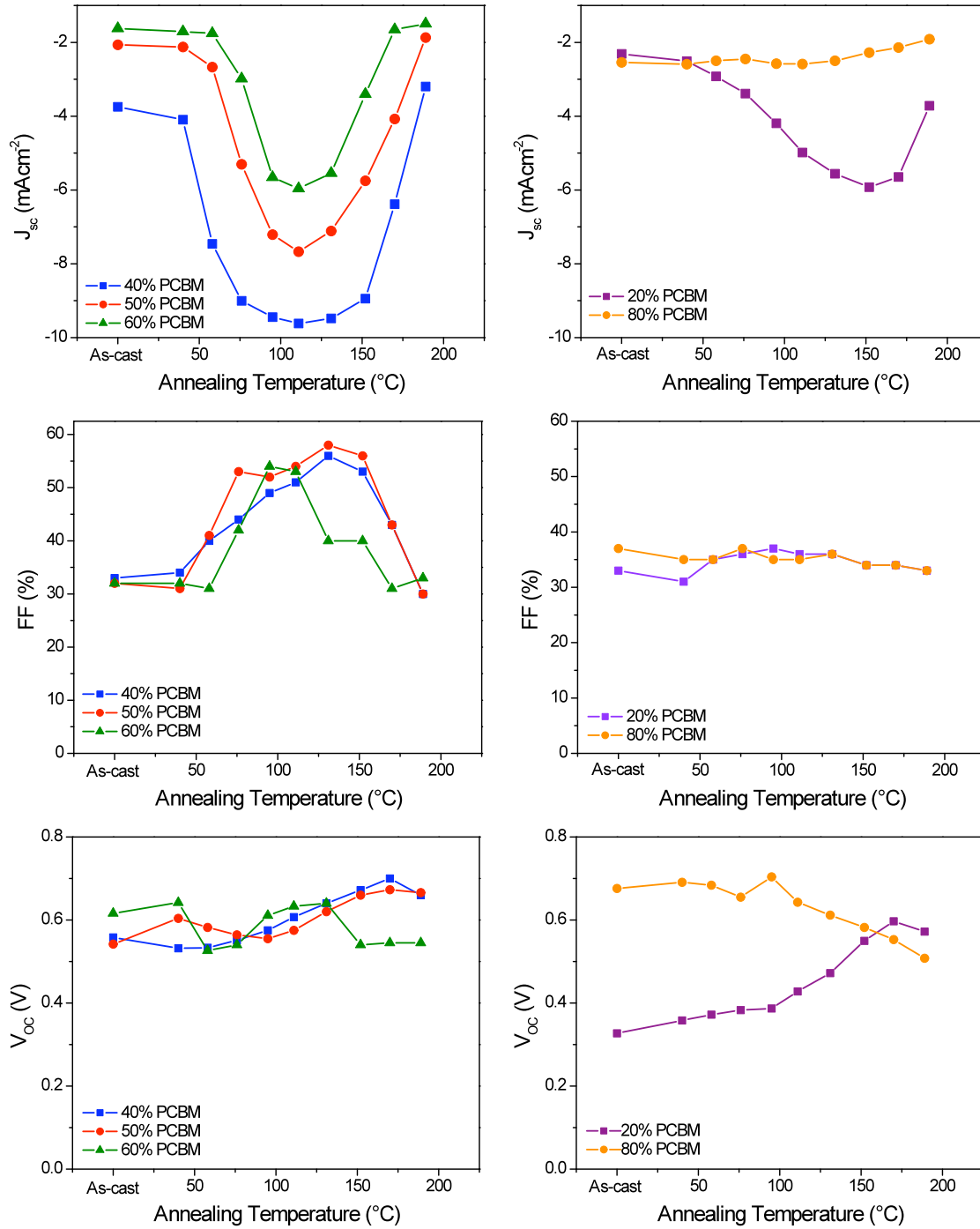


Figure 6.3: Average short-circuit current densities (J_{sc}) (top row), fill factors (FF) (middle row) and open circuit voltages (V_{oc}) (bottom row) for all the devices measured for this work. Data is split in the same manner as Figure 6.2 for ease of comparison. Lines are provided as a guide to the eye only.

In Figure 6.2(b), I plot the efficiency of devices having either a high or a low fraction of PCBM in its active layer. In both cases, the PCE of the devices are low; devices containing 20 wt% PCBM have a maximum efficiency of 1.2%. The origins of such low efficiencies are well understood ⁶, as films composed predominantly of P3HT have favourable absorption characteristics. However exciton dissociation and extraction of electrons is inefficient due to an insufficient concentration of PCBM acceptor molecules. At high PCBM concentration however, the transport and extraction of holes becomes problematic together with a reduced absorption overlap of the active layer with the solar spectrum ⁷. Nevertheless, for devices containing either 20% or 80 wt% PCBM, thermal annealing also modifies device PCE; for 20 wt% PCBM loading, values of T_{onset} and $T_{optimum}$ are found to be $50 \pm 5^\circ\text{C}$ and $170 \pm 5^\circ\text{C}$ respectively. When the device contains 80 wt% PCBM, there is an apparently negligible benefit from the thermal annealing process. Indeed, beyond approximately 105°C , the treatment becomes detrimental with a monotonic decrease in PCE as the annealing temperature is increased.

From Figure 6.3, it can also be seen that the fill-factor (FF) of the annealed devices is also improved by a factor of up to 2 times compared to that of the equivalent controls. Devices containing either a high or a low fraction of PCBM undergo a smaller relative improvement compared to devices having a PCBM loading between 40 and 60 wt%. The relative magnitude of the FF provides an approximate measure of the relative balance between electron and hole mobilities ^{3b}, as discussed in chapter 2 section 2.5, with a smaller FF indicating imbalanced charge-carrier mobility. Indeed, a number of studies have suggested that a FF less than $\sim 42\%$ indicates that charge-extraction is limited by space-charge ⁸. The data in Figure 6.2 shows that for blend

devices containing 20 wt% and 80 wt% PCBM, the FF never exceeds 37%, suggesting that such devices have intrinsically imbalanced charge-carrier mobility.

To summarise; Figures 6.2(a) and 6.2(b) demonstrate that a composition-dependent annealing range exists. The onset temperature for improved device efficiency (T_{onset}) increases with increasing PCBM wt%, whilst the optimum annealing temperature ($T_{optimum}$) decreases with increasing PCBM wt%. The effect of these two processes suggests that the annealing window for improving device PCE narrows with increasing PCBM wt%. Indeed, for devices containing the highest wt% of PCBM, thermal annealing is detrimental to device efficiency. The remainder of this chapter proceeds to rationalise these findings on the basis of the various thermal transitions (including the apparent glass-transition temperature T_g) and properties of the active layer materials.

SECTION 6.3: ORIGIN OF THE MINIMUM EFFECTIVE ANNEALING TEMPERATURE

To rationalise the thermal annealing of P3HT:PCBM OPVs, it is necessary to construct a phase diagram for the blends studied. Blend thin-films were prepared in the same manner to those used in devices and were cast onto silicon / native oxide substrates. These samples were monitored during the first heating cycle using spectroscopic ellipsometry. This approach provides an opportunity to test the conclusions drawn from the phase diagram constructed by Hopkinson *et al.* using

DMTA^{2b}. A summary of the SE data is presented in Figure 6.4, alongside values for T_{onset} and $T_{optimum}$ as determined from the data in Figure 6.1.

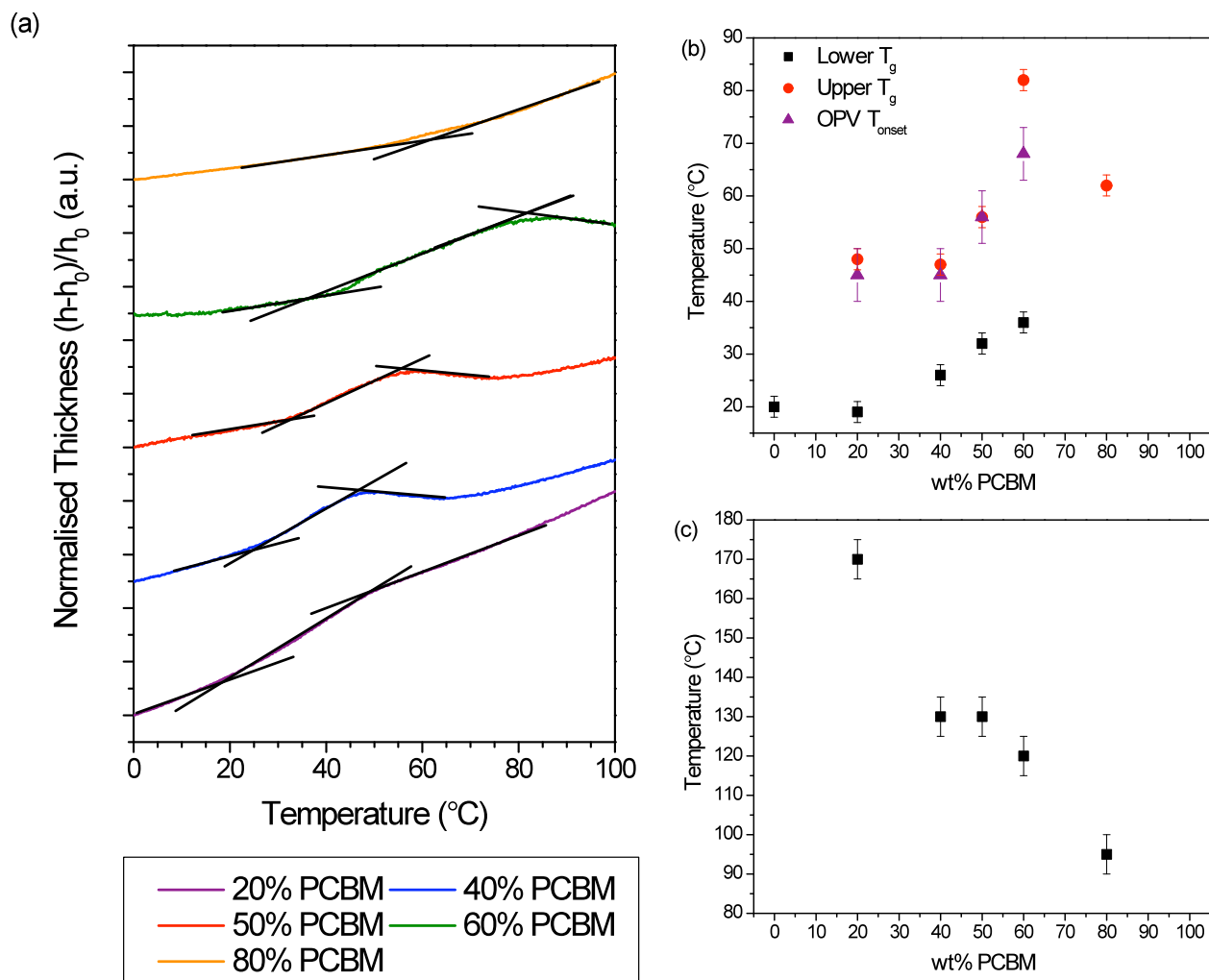


Figure 6.4: (a) Normalised thickness (of P3HT:PCBM (wt%) thin films) as a function of temperature measured during the first heating cycle. Data is offset for clarity. For each sample a number of straight lines are fitted to the temperature-dependent expansion of the sample, with the intersection of such lines marking the apparent glass transitions of the blend. (b) The onset annealing temperature for PCE improvement in P3HT:PCBM OPVs as a function of the active layer composition, plotted alongside the T_g values extracted from part (a). Optimum annealing temperatures for P3HT:PCBM OPVs as a function of the composition of the active layer composition are plotted in part (c).

In Figure 6.4(a) the relative change in thickness of a series of blend thin films as they are subjected to a thermal ramp is presented. This can be quantified using $(h-h_0)/h_0$, where h is the film thickness at temperature T and h_0 is the film thickness prior to thermal annealing. As shown, a number of changes occur in the thermal expansion rate as the films are annealed. To estimate the temperature at which these changes in expansion rate occur, each data set is considered as a being composed as a series of regions having linear thermal expansion coefficients. An intersection of a fit to these linear regions permits the apparent glass transitions of the blends to be determined during the first heating cycle, a method commonly used to extract T_g values for other polymer thin-films⁹. In Figure 6.4(b), the T_g values extracted from part (a) are shown, together with values for T_{onset} as determined from Figure 6.1, with $T_{optimum}$ values plotted in Figure 6.4(c).

From chapter 5 it was shown that thin films of the P3HT batch used in this thesis have a T_g of 20°C. It can be seen in Figure 6.4(a) that in a blend containing 20 wt% PCBM, there is a change in the thermal expansion rate that approximately coincides with this temperature with an additional higher temperature transition observed at 50°C. For blend thin-films with 40 to 60 wt% PCBM, two transitions are again detectable, however the temperature of the T_g apparently increases as the relative content of PCBM within the blend is increased. At 80 wt% PCBM, a single transition is observed that occurs at a temperature that is relatively lower than that observed in the 60 wt% blend film.

In many cases, as a film is heated above the thermal transitions identified, the expansion rate remains positive. It is speculated that these transitions correspond to glass-transitions, where an expansion in film thickness occurs as molecules acquire sufficient thermal energy to undergo a transition to a more mobile state and thus explore a greater free volume, i.e. the material undergoes a transition from a glassy to a rubbery state⁹. A notable exception to this occurs in blends with a PCBM loading of 40 to 60 wt%, in which the films undergo an apparent contraction in thickness when heated above the second T_g . Comparing these results to those discussed in chapter 5, section 5.2, it is likely that the glass transition over this relatively small composition range is convoluted with the effects of the removal of residual casting solvent that occurs during the first heating cycle. As the film is heated above the higher temperature T_g , solvent loss occurs as the polymer chains have sufficient thermal energy to allow the expulsion of trapped solvent molecules. This loss of solvent will clearly lead to a partial self-organisation of the polymer that will manifest itself by a reduction in film thickness, as discussed in chapter 4, section 4.2. This volume-reduction process will dominate over the competing process of thermal expansion until such a time where the majority of the solvent has been removed. At this stage the expansion rate of the sample becomes positive once more.

It can be seen that this solvent loss process is not observed in blend films containing either 20 wt% or 80 wt% of PCBM. I speculate that this phenomenon has two different origins. Firstly the absence of solvent loss effects in blend films containing 80wt% PCBM blend reflects the fact the relatively low concentration of P3HT molecules within the film limits its ability to trap solvent. Secondly, it has been shown that as the difference between the temperature at which a film is cast and the T_g of film

increases, a larger volume of the casting solvent is trapped¹⁰. As the lower T_g of films containing 20 wt% PCBM lies below room temperature, it suggests that the majority of casting solvent evaporates as the film is cast and thus little solvent remains to be expelled as the film is annealed.

As can be seen in Figure 6.4(b), the T_g of P3HT:PCBM blend thin-films is larger than that of the pure polymer. Furthermore this temperature increases as the relative wt% of PCBM in the blend is increased. This result is in good agreement with the study of this system using DMTA, confirming the fact that PCBM molecules act as an anti-plasticiser for P3HT. Importantly however, in the blend thin film having the highest loading of PCBM (80 wt%), the T_g of the blend undergoes a reduction, an observation also in line with the observations and conclusions reported in ref [2]. The measurements presented here however indicate that in blends with a PCBM wt% between 20 to 60%, there are in fact two distinct glass transitions. This is tentatively ascribed to the blend film comprising at least two compositionally distinct, amorphous, P3HT phases within the as-cast blend thin film. It is important to emphasise that these phases co-exist with the pure semi-crystalline P3HT and PCBM phases; however the relative volume fraction of each phase will likely depend on the sample composition and will be dependent on any phase separation that occurs during spin-casting.

To gain confidence in the existence of a phase associated with the relatively low temperature T_g , the thermal expansion of a blend thin film (50 wt% PCBM) during first heating was measured as a function of heating rate, to determine how the

experimental conditions affect the temperature associated with the transition. Additionally, to explore the reversibility of the system a blend sample was monitored over the course of two heating and cooling cycles.

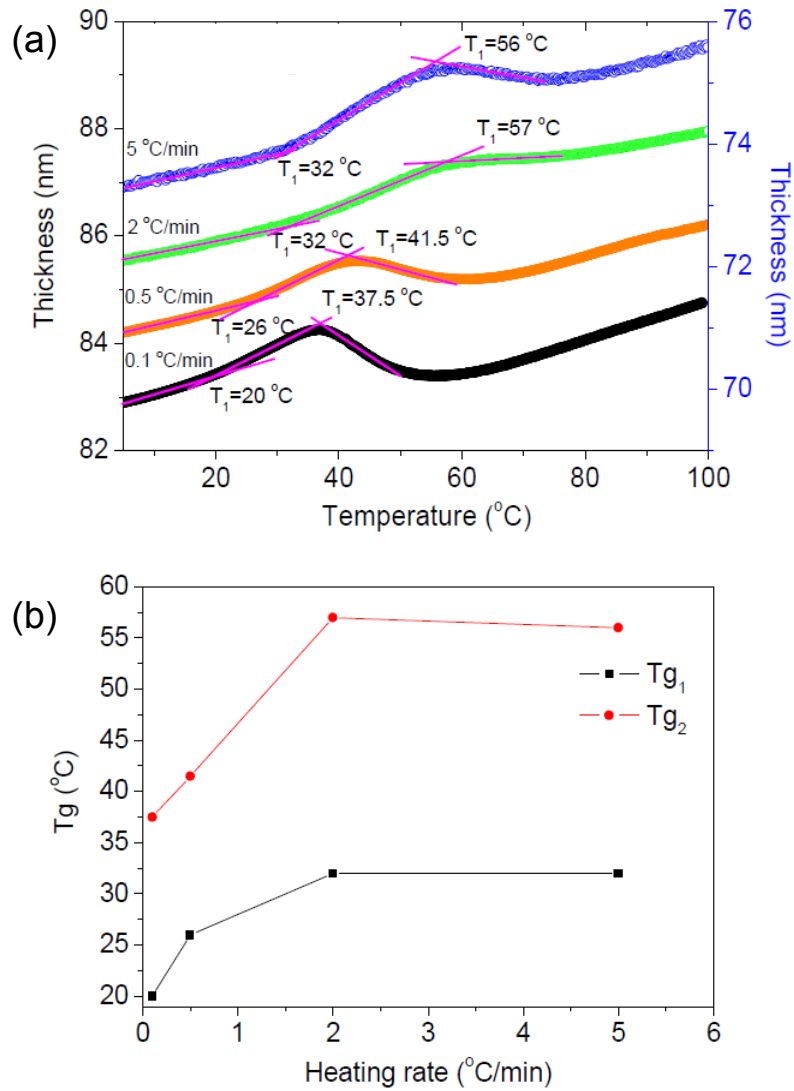


Figure 6.5: (a) Thickness change of an as-cast P3HT:PCBM (50:50 wt%) blend thin-film during the first heating cycle, for different heating rates. For clarity, the data corresponding to the sample heated at $5^{\circ}\text{C}/\text{min}$ is plotted on a second y-axis. The temperature at which each transition is observed as a function of sample heating rate is presented in part (b).

As can be seen in Figure 6.5, two T_g s are detectable for all heating rates used. However the lower temperature transition only results in a minor modification to the film expansion rate. In all cases the effects related to solvent loss only occur when the temperature of the thin film exceeds the second, higher temperature T_g . The relative decrease in T_g temperatures at low ($< 2^\circ\text{C}/\text{min}$) heating rates have also been observed in other polymer thin films. For polystyrene, the relaxation dynamics are Arrhenius in nature, with an activation energy that decreases as the heating rate slows¹¹. It is possible that the same effects are being observed in this system.

The thickness changes of a blend thin-film recorded over the course of two heating and cooling cycles are presented in Figure 6.6. Parts (a) and (b) correspond to the first heating and cooling cycle respectively of the film when raised to a temperature of 50°C . Parts (c) and (d) similarly correspond to the second heating and cooling cycle of the same film when raised to 100°C . SE has also been used to model the wavelength-dependent extinction coefficient of the film as shown in part (e). As can be seen in Figures 6.6(a) to (c), at transition ($T_{g,1}$) at 36°C is measureable during heating, which shifts to 25°C as the sample is cooled. The apparent reversibility of this transition (recorded at 30°C during the second heating cycle) within the range of heating temperatures applied suggests its origin is a glass transition. Note that in part (c) the sample is heated to a higher temperature than during the first heating cycle. It can be seen that the effects of solvent loss are observed when the temperature of the film is above 60°C corresponding to the blend undergoing a second glass transition ($T_{g,2}$), as shown previously in this section and in chapter 5. Upon cooling the film from 100°C (see Figure 6.6(d)), only a single transition ($T_{g,3}$) at 50°C can be detected.

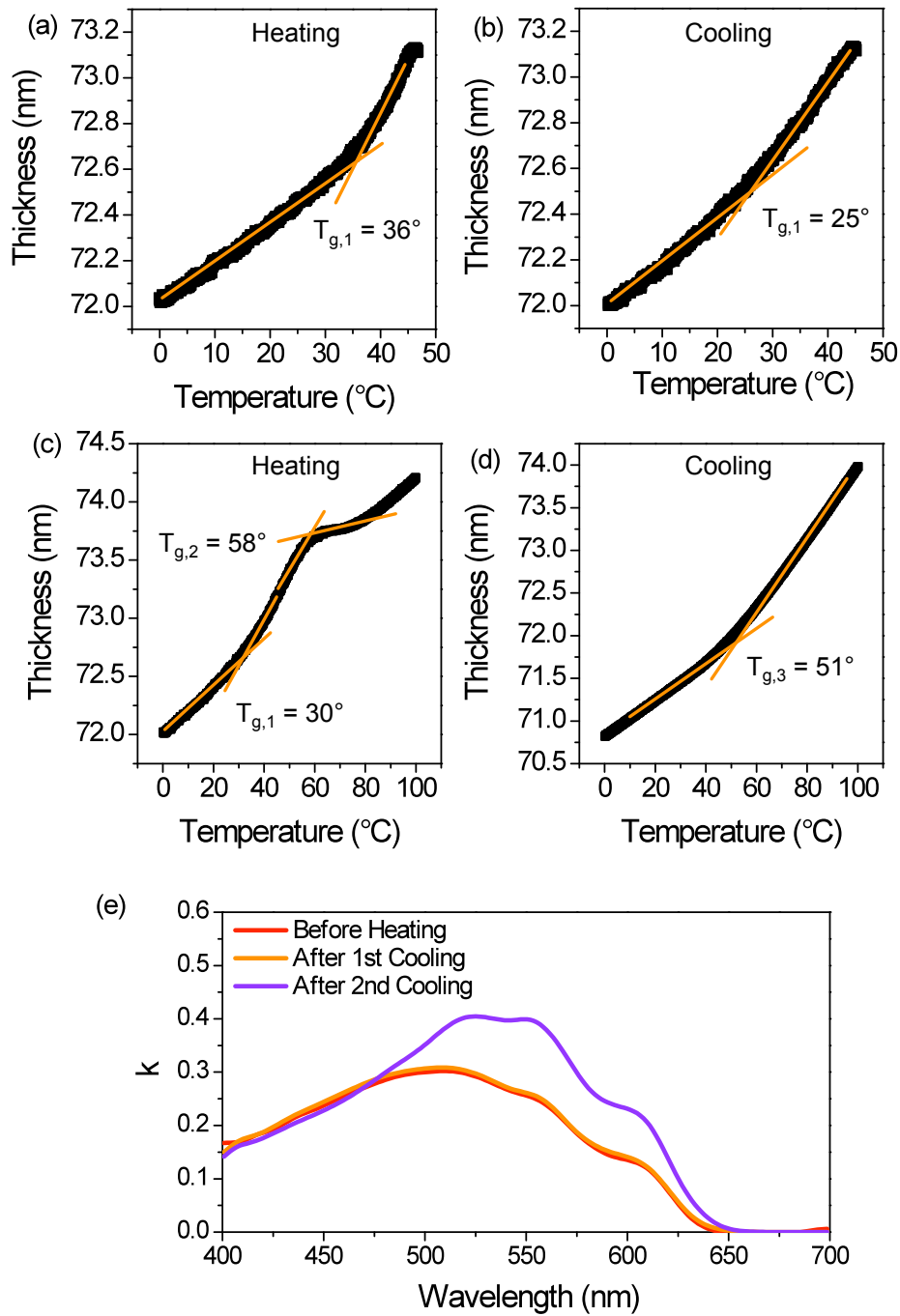


Figure 6.6: Thickness changes for a P3HT:PCBM (50:50 wt%) blend thin film during (a) first heating, (b) first cooling, (c) second heating & (d) second cooling. Heating & cooling rate was kept at $5^\circ\text{C}/\text{min}$ throughout. The intersections of the orange lines mark the apparent T_g (s) of the sample. In (e) the modeled extinction coefficient spectrum for the blend before heating and after the first and second heating cycles.

In Figure 6.6(e), it can be seen that the extinction coefficient of the film remains relatively unchanged after the first heating cycle, but undergoes a significant enhancement in strength that is accompanied by a red-shift after the second heating cycle. This suggests that heating the film above the low temperature T_g does not induce significant morphological changes within the film, an observation that suggests the phase associated with this transition comprises a relatively low volume-fraction of the film. In contrast, upon heating and subsequently cooling the sample from a temperature above the upper T_g of the blend, the film undergoes a significant degree of self-organisation, inferred from the structure of the k spectrum. The observation of a single glass transition at 50°C after cooling from an elevated temperature suggests the amorphous polymer phase of the thin-film has become relatively more homogeneous.

As shown by Parnell *et al.*¹², using Neutron Reflectivity as-cast thin films of P3HT:PCBM (40 wt% PCBM) exhibit a surface layer rich in P3HT (~85% volume fraction). The depth of this layer was measured to be 25 nm for a total film thickness of 150 nm. Other studies have also shown that as-cast blend thin films of P3HT:PCBM undergo vertical stratification, whereby the surface and the buried interface of a P3HT:PCBM blend film may be compositionally different to the bulk phase. Germack *et al.* estimated that P3HT forms an almost pure layer ~6 nm thick at the top of blend thin-films (50wt% PCBM) (total thickness 80 nm) onto silicon / native oxide substrates, increasing to ~15 nm for a blend thin film cast onto PEDOT:PSS¹³. Tillack *et al.* concluded the surface of as-cast blend thin-films is almost exclusively composed of P3HT for a 1:0.95 wt% blend thin film¹⁴. However the limitations of the technique used (Near-Edge X-Ray Absorption Fine Structure)

mean that the estimated thickness of this layer is likely to be a lower bound. Although a positive verification is not possible at this stage, considering these studies the observations reported here suggest that the relatively lower temperature T_g may originate from a thermal transition of the surface-layer of the blend films in which the concentration of PCBM molecules is low.

To determine if a correlation exists between the device data presented in section 6.2 and the SE data presented in this section, Figure 6.4(b) presents T_g values extracted from the SE data as a function of PCBM wt% in the blend, alongside the onset temperature for OPV device improvement, as determined from the data in Figure 1. Notably, a close coincidence is found between T_{onset} (for the OPVs) and the upper temperature T_g of the blends. This agreement confirms that the T_g of the blend defines the minimum effective temperature for improving the photocurrent generating efficiency of the blend and, in the most efficient blend compositions, for the removal of residual solvent. The absence of a link between the relatively low temperature T_g and T_{onset} supports the hypothesis that the low-temperature T_g is associated with a volume of the blend film in which the concentration of PCBM molecules is low.

It is important to acknowledge the differences between the samples prepared for SE and for OPVs. It has been endeavored to replicate in the samples for SE as closely as possible the morphology of P3HT:PCBM blends as would exist in an OPV prior to thermal annealing. However, for SE samples a free surface exists which is not present during the annealing process for OPVs. Additionally the films are cast onto native silicon oxide and not PEDOT:PSS. It is not possible to model both thickness changes

and optical characteristics of films beneath 100 nm of aluminum, which would fully resemble a device and so would be the ideal sample. I have monitored a blend thin film cast onto PEDOT:PSS during heating, in addition to a control sample of PEDOT:PSS only, with results presented in Figure 6.7.

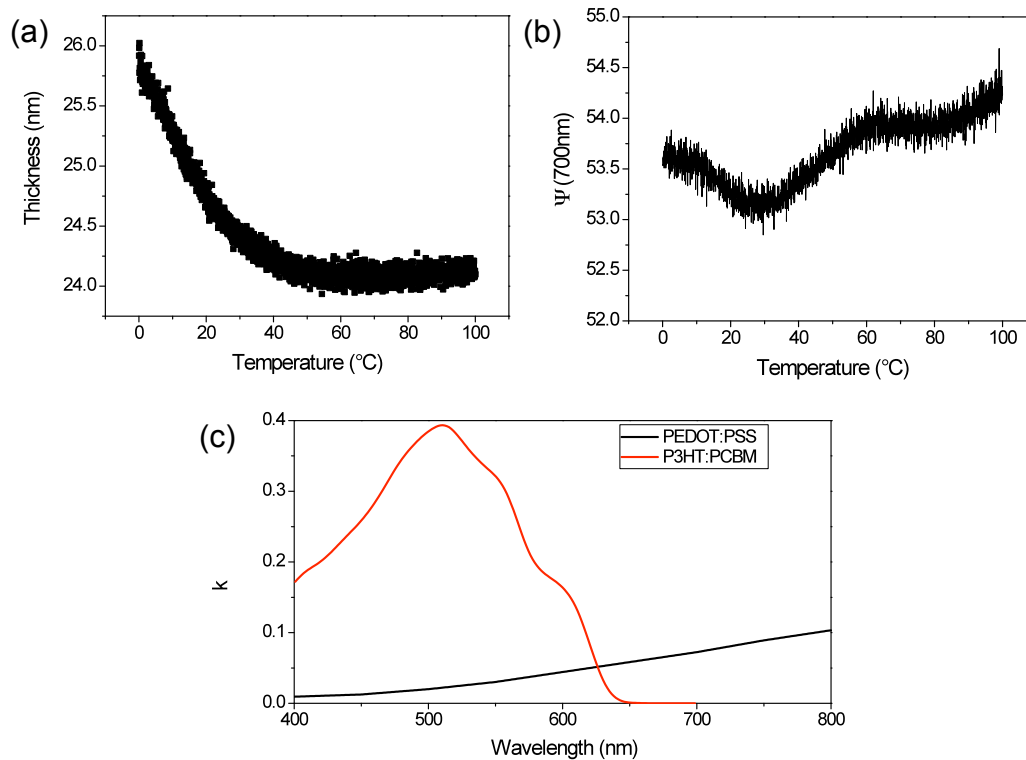


Figure 6.7: (a) Thickness evolution of a PEDOT:PSS film on silicon / native oxide during a first heating cycle. The heating rate used was $5^{\circ}\text{C}/\text{min}$. In part (b), a P3HT:PCBM (50:50 wt%) film deposited onto PEDOT:PSS is shown for a first heating cycle, highlighting the effect of the thickness contraction in PEDOT:PSS at relatively low temperatures on the raw ellipsometry data. The modeled extinction coefficient spectra for a P3HT:PCBM (50:50 wt%) film and a PEDOT:PSS film is shown in part (c).

It can be seen in Figure 6.7(a) that PEDOT:PSS undergoes a thickness contraction in the low temperature range up to 60°C. For blend thin films cast onto PEDOT:PSS the thickness contraction overlaps with the low T_g transitions identified for samples on native silicon oxide, which effects the raw SE data as shown in Figure 6.7(b). As discussed in chapter 3, section 3.4.3, the Cauchy model used to calculate film thicknesses requires the film to be transmissive. In the wavelength region where P3HT:PCBM does not strongly absorb light ($\lambda > 700$ nm) PEDOT:PSS is weakly absorbing (see Figure 6.7(c)), thus deconvolution of the SE data is not possible. Nonetheless, the good correlation between SE data and OPV measurements suggests that structural changes within the bulk of the blend films are the dominant driving force for improvements in OPV device efficiency, with interfacial effects playing a relatively minor role.

SECTION 6.4: ORIGIN OF THE OPTIMUM ANNEALING TEMPERATURE

I now discuss the effect of annealing a blend above its T_g . With the exception of the devices based on a blend containing 80 wt% PCBM, thermal annealing at temperatures up to $T_{optimum}$ increase device efficiency by driving phase separation and increasing the crystallinity of each phase¹⁵. Beyond $T_{optimum}$ it is possible for at least one of the materials within the film to undergo excessive phase separation or a phase-transition, resulting in a morphology that is less favourable for efficient device operation. From Figure 6.4(c), the optimum annealing temperature as a function of PCBM wt% was shown. It can be seen that this temperature undergoes a progressive

reduction as the fraction of PCBM is increased. As will be discussed in this section, this temperature is most likely defined by the kinetics of the annealing process, rather than being associated with any one thermal transition.

To explore the apparent observation of an optimum annealing temperature, I have performed optical microscopy on a series of P3HT:PCBM blend films having a range of different relative compositions that were annealed at a series of temperatures above 140°C and subsequently cooled rapidly to room temperature. A selection of representative images is shown in Figure 6.8. As can be seen, after thermal annealing at 140°C, (a temperature that just exceeds $T_{optimum}$ for all devices with the exception of the 20:80 wt% P3HT:PCBM active layer blend) relatively few structures are present that can be resolved optically in all of the films studied.

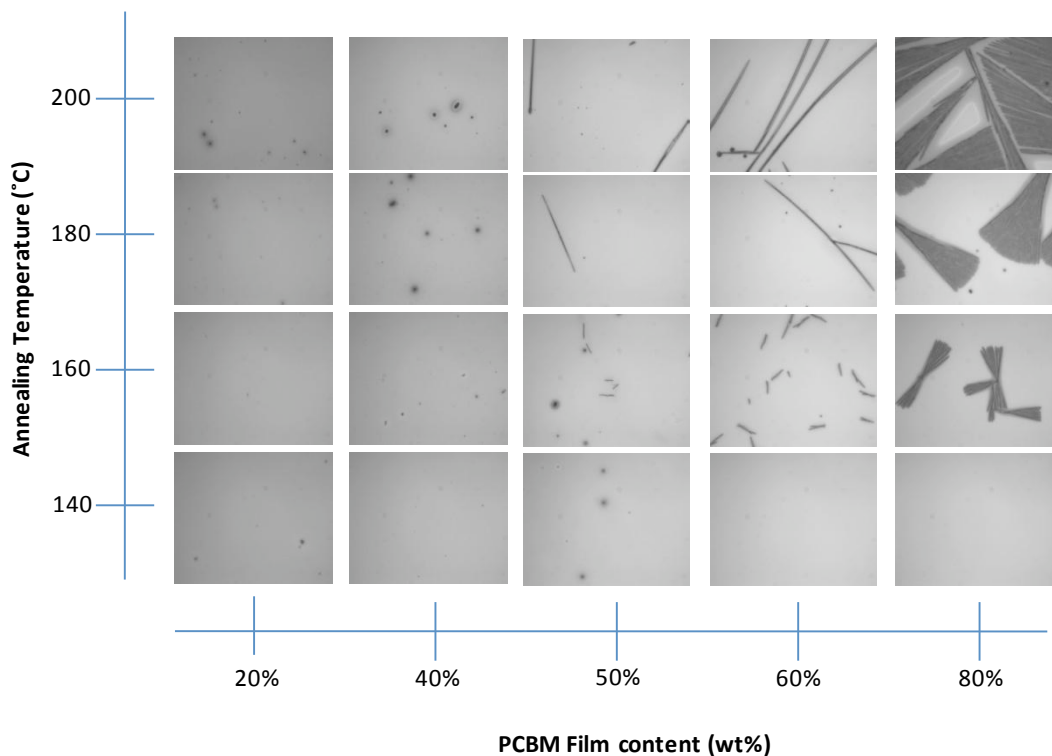


Figure 6.8: Optical micrographs (60 μm x 80 μm field of view) for P3HT:PCBM blend thin-films annealed and subsequently cooled from a temperature above 140°C.

These observations suggest that films annealed below this temperature mainly consist of nanoscale domains of P3HT and PCBM together with a molecularly mixed phase. However as the annealing temperature is raised above 140°C, it can be seen that excessive phase separation between the blend components occurs. Indeed, aggregates having a size of 10 to 100s of microns, identified as polycrystalline PCBM¹⁶, form in films composed of 80 wt% PCBM that have been annealed at a temperature at or above 160°C. As the relative fraction of PCBM is reduced, fewer microscopic PCBM crystallites are observed at any given annealing temperature, reflecting the fact that a smaller number of PCBM molecules are present in the sample. This observation provides a partial explanation for the relative stability of devices having a low PCBM

fraction when annealed at a temperature just above $T_{optimum}$ as discussed in section 6.2, since excessive phase separation is clearly hindered by the relatively low concentration of PCBM.

In an attempt to ascribe a thermal transition to the onset of PCBM phase separation in the blend thin films, I note that a solid-solid transition was measured for pure PCBM by DMTA at 155°C^{2b}. Verploegen *et al.* have identified this transition as the cold crystallisation temperature¹⁶. This transition apparently exists in films having a PCBM wt% above ~66%, suggesting that below this concentration, the transition may be suppressed. Several studies have however demonstrated that PCBM in pure and blend thin-films can form aggregates or crystals at temperatures below 131-134°C¹⁶⁻¹⁷. It is also important to acknowledge the influence of the substrate (specifically its surface energy) in determining the extent of the phase separation (i.e. the kinetics of the aggregation process) at the micron length-scale. Indeed, He *et al.*¹⁸ observed that in P3HT:PCBM blend thin films cast from 1,2-dichlorobenzene, PCBM may phase separate earlier and at a lower temperature than if the blend thin film is deposited onto silicon / native oxide, compared to PEDOT:PSS. It appears therefore that isothermal annealing at a temperature above 130°C may be the minimum temperature required to drive PCBM aggregation, however kinetics and interfacial energy effects are likely to play an important role, particularly since film thickness and polymer regioregularity¹⁹ will also influence the diffusion rate of PCBM through a polymer matrix.

The existence of microscopic PCBM aggregates in P3HT:PCBM blend films is a clear indication that the film has been over-annealed, resulting in reduced operational

efficiency, as shown in chapters 4 and 5. Such structures may also be sufficiently large to exceed film thickness, thereby creating a short-circuit or possibly damaging the device electrode²⁰. The formation of such microscopic structures by annealing above $T_{optimum}$ will be accompanied by a relative depletion of acceptor material within the bulk of the film; an effect that will reduce both the efficiency of exciton dissociation and the extraction of electrons from the device. However, it is apparent that the optimum annealing temperature for OPVs occurs before the onset on PCBM micron-scale aggregation. To further characterise the effects of annealing on the properties of P3HT:PCBM based devices, I have measured both the optical density and relative photoluminescence efficiency of a series of representative films. UV-Visible spectroscopic techniques provide a useful probe to qualitatively explore structure-property relationships of the blend films at a resolution of a few nm, a length scale that cannot be accessed using conventional optical microscopy techniques. These measurements thereby provide a useful complement to the earlier discussion.

In Figure 6.9, I present a summary of the optical characteristics of the blend thin-films as a function of annealing temperature. For ease of comparison, the data is split in the same manner as in Figure 6.2. Specifically, Figures 6.9(a) and 6.9(b) show the wavelength at which blend thin-films have their peak optical density (here defined as λ_{max}), whilst 6.9(c) and 6.9(d) show the integrated photoluminescence emission intensity of the same films. Representative spectra from which this data is extracted are shown in the Appendix, Figures A1-2.

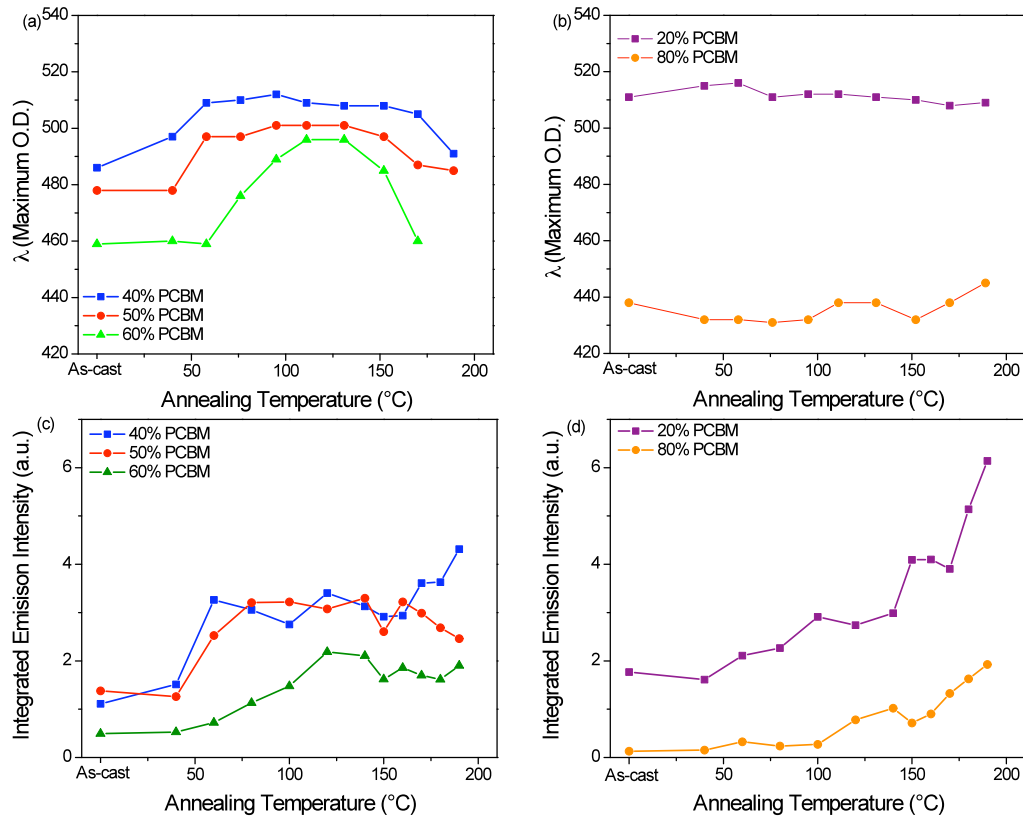


Figure 6.9: The wavelength at which blend thin-film optical density is maximised, λ_{max} , after thermal annealing for: (a) blends with 40-60wt% PCBM and (b) 20wt% and 80wt% PCBM. In (c) and (d) the integrated photoluminescence emission from samples after annealing for blends with 40-60 wt% PCBM and 20 wt% or 80 wt% PCBM respectively. Lines are provided as a guide only.

It can be seen that annealing films containing between 40 and 60 wt% PCBM at a relatively low temperature, results in a red-shift of λ_{max} . For example, a film containing 40 wt% PCBM undergoes a shift in λ_{max} from 485 nm to 515 nm after being annealed at 130°C. In Figure A1, it can be seen that this red-shift is also accompanied by an increase in optical density. This trend reverses (i.e. the optical density decreases and λ_{max} undergoes a relative blue-shift) after a film is annealed

beyond a temperature approximately coincident with $T_{optimum}$. In fact, a clear correlation is found between the data in Figures 6.2(a) and 6.8(a), showing that the increased device PCE on annealing above T_{onset} (upper T_g) is correlated with a red-shift of λ_{max} and an increase in OD, whilst annealing above $T_{optimum}$ is correlated with a blue-shift of λ_{max} and a reduction in OD. This demonstrates that annealing a P3HT:PCBM film at a temperature between T_{onset} and $T_{optimum}$, followed by rapidly cooling to room-temperature provides a driving force for P3HT crystallisation, providing a partial explanation for improvements in device efficiency (for example, improved harvesting of the solar spectrum). On annealing a film above $T_{optimum}$, followed by a rapid return to room temperature, the observed blue-shift of λ_{max} and relative weakening in film OD suggests that a significant fraction of the P3HT polymer is quenched into a largely amorphous state. Note that this process occurs without the film being partially melted, as the melt temperature of P3HT is expected to be above 200°C for all the blend compositions explored in this work ^{2b, c}. Nevertheless, this rapid return to room-temperature generates a film having poor light harvesting capability and predicted lowered charge mobility ²¹. Note that in the previous chapter, it was demonstrated that by slowly cooling blend thin films even from a relatively high (>150°C) temperature, polymer crystallisation is further encouraged; a process that corresponded to relative improvements device PCE of up to ~5%.

It is apparent that the maximum OD of a film on annealing is inversely correlated with the relative PCBM concentration. As the maximum absorption wavelength λ_{max} is a measure of the degree of crystallization, this effect shows that an increased PCBM concentration hinders P3HT crystallisation. Interestingly, Figure 6.9(b)

demonstrates that films containing either a high or low PCBM weight fraction only undergo small changes in λ_{max} on annealing. On closer inspection of the absorption spectra recorded from films containing a relatively low (20 wt%) concentration of PCBM (see Figure A1), it can be seen that even in as-cast films, there is a relative high fraction of crystalline P3HT present (as evidenced by the peak corresponding to the 0-0 electronic transition, seen around 600 nm) that is not significantly increased by subsequent thermal annealing. In films containing a high fraction (80 wt%) of PCBM, the packing and partial crystallization of P3HT is clearly restricted by the PCBM under the annealing protocol used in this work.

In Figures 6.8(c) and (d) I plot the integrated PL intensity from a series of thin-film blends as a function of annealing temperature. It can be seen that the relative PL intensity is inversely proportional to the fraction of PCBM as anticipated. It can be seen that for each of the film compositions, the PL emission intensity increases once the annealing temperature exceeds a certain threshold temperature, again closely correlated to the upper T_g of the blend and T_{onset} . The effect is particularly evident in films containing either 40 or 50 wt% PCBM, where PL emission intensity increases significantly on annealing above 50°C, whilst emission from films containing 60 wt% PCBM increases in a linear fashion when annealed above 60°C. The temperature at which the PL emission intensity increases also correlates well with observed changes in the absorption spectra (Figures 6.9(a) and (b)) and device efficiency (Figure 6.2). Such correlated trends further suggest that annealing above T_{onset} permits the film morphology to undergo a transition from a largely mixed phase in which excitons are efficiently quenched, to a morphology in which nanoscale phase separation reduces the efficiency of exciton dissociation.

When thin films containing a relatively low fraction of PCBM are annealed at temperatures above 150°C, a marked increase in PL intensity is observed. This increase in PL intensity is indicative of reduced exciton quenching resulting from the formation of larger (or purer) P3HT domains. In contrast, the fluorescence emission intensity of films containing 50 wt% by mass PCBM does not increase significantly on being annealed above 150°C. From Figure A.1, measurements of the absorption spectra indicate that P3HT has limited ability to undergo self-organisation in films containing a relatively high fraction of PCBM and thus such films are likely to contain a greater (relative) fraction of amorphous P3HT. This suggests that the relatively small increases in P3HT PL emission intensity from films containing a relatively high fraction of PCBM upon annealing and subsequently rapid cooling results from PCBM molecules that have become mixed in regions dominated by amorphous polymer²². Such amorphous material may hinder the ability of PCBM in the bulk of the blend film to coalesce into nanoscale networks, with such molecular-mixed phases being associated with relatively efficient exciton quenching.

In summary, the data presented in Figures 6.8 and 6.9 demonstrate that annealing a P3HT:PCBM film beyond $T_{optimum}$ results in both P3HT and PCBM blend fractions that have unfavourable OPV characteristics. This may arise from reduced optical density and overlap with the solar spectrum (limiting the ability of the device to harvest sunlight), as shown in Figure 3.8, and from the creation of microscopic PCBM aggregates, resulting in an overly coarse degree of phase separation as shown in Figure 6.8. As discussed, it is not possible to ascribe a composition dependent thermal transition to $T_{optimum}$, as has been demonstrated when correlating T_{onset} with the higher temperature T_g of P3HT. It is instead likely that $T_{optimum}$ is instead

determined by the kinetics of PCBM diffusion during isothermal annealing and the relative crystallinity of both P3HT and PCBM during annealing and cooling.

SECTION 6.5: CONCLUSIONS

I have explored the impact of thermal annealing on the photovoltaic efficiency of P3HT:PCBM OPVs across a range of active layer compositions and annealing temperatures. These results are related to the phase transition behaviour of the blends. Measurements on the glass transition of the blends in a thin-film geometry suggest that two distinct compositional amorphous phases exist. I demonstrate a positive correlation between the highest temperature apparent glass transition and the minimum temperature necessary to improve the efficiency of an OPV device. This confirms that annealing a film above its glass transition temperature (for that particular blend composition) will permit molecules to undergo cooperative motion, forming a morphology that can promote efficient photocurrent generation.

I have also identified a blend-ratio dependent optimum annealing temperature for efficient device operation. This has been correlated with excessive phase separation by PCBM, and the reduced ability of the blend thin-film to harvest sunlight. As the wt% of PCBM within the blend increases, the optimum temperature decreases, from 170°C to as low as 100°C. Thermally annealing devices that contain a high weight fraction of PCBM apparently results in a reduction in operational efficiency; a result that may be particularly relevant in OPVs based on amorphous low energy band-gap

polymers in which large relative fractions of fullerenes are often used. This specific issue is partly addressed in the following chapter. The results demonstrate therefore that the optimum annealing temperature of an OPV device based on a polymer:fullerene blend is a function of the relative composition of the blend; an effect that is related to the phase transition properties of the film and in particular its glass transition temperature. This is an important observation, as it indicates that the characterisation of phase transitions in unexplored polymer-fullerene systems should be performed in parallel with device optimisation studies, with the glass-transition temperature of each particular polymer-fullerene blend film providing a strong indication of the minimum annealing temperature beyond which changes in device efficiency can be anticipated.

SECTION 6.6: REFERENCES

1. Pearson, A. J.; Wang, T.; Jones, R. A. L.; Lidzey, D. G.; Staniec, P. A.; Hopkinson, P. E.; Donald, A. M., Rationalizing Phase Transitions with Thermal Annealing Temperatures for P3HT:PCBM Organic Photovoltaic Devices. *Macromolecules* 2012, 45 (3), 1499-1508.
2. (a) Zhao, J.; Swinnen, A.; Van Assche, G.; Manca, J.; Vanderzande, D.; Van Mele, B., Phase Diagram of P3HT/PCBM Blends and Its Implication for the Stability of Morphology. *J Phys Chem B* **2009**, 113 (6), 1587-1591; (b) Hopkinson, P. E.; Staniec, P. A.; Pearson, A. J.; Dunbar, A. D. F.; Wang, T.; Ryan, A. J.; Jones, R. A. L.; Lidzey, D. G.; Donald, A. M., A Phase Diagram of the P3HT:PCBM Organic Photovoltaic System: Implications for Device Processing and Performance.

- Macromolecules* **2011**, *44* (8), 2908-2917; (c) Muller, C.; Ferenczi, T. A. M.; Campoy-Quiles, M.; Frost, J. M.; Bradley, D. D. C.; Smith, P.; Stingelin-Stutzmann, N.; Nelson, J., Binary organic photovoltaic blends: A simple rationale for optimum compositions. *Advanced Materials* **2008**, *20* (18), 3510-3515.
3. (a) Ma, W. L.; Yang, C. Y.; Gong, X.; Lee, K.; Heeger, A. J., Thermally stable, efficient polymer solar cells with nanoscale control of the interpenetrating network morphology. *Advanced Functional Materials* **2005**, *15* (10), 1617-1622; (b) Li, G.; Shrotriya, V.; Huang, J. S.; Yao, Y.; Moriarty, T.; Emery, K.; Yang, Y., High-efficiency solution processable polymer photovoltaic cells by self-organization of polymer blends. *Nature Materials* **2005**, *4* (11), 864-868.
4. (a) Jo, J.; Kim, S. S.; Na, S. I.; Yu, B. K.; Kim, D. Y., Time-Dependent Morphology Evolution by Annealing Processes on Polymer:Fullerene Blend Solar Cells. *Advanced Functional Materials* **2009**, *19* (6), 866-874; (b) Agostinelli, T.; Lilliu, S.; Labram, J. G.; Campoy-Quiles, M.; Hampton, M.; Pires, E.; Rawle, J.; Bikondoa, O.; Bradley, D. D. C.; Anthopoulos, T. D.; Nelson, J.; Macdonald, J. E., Real-Time Investigation of Crystallization and Phase-Segregation Dynamics in P3HT:PCBM Solar Cells During Thermal Annealing. *Advanced Functional Materials* **2011**, *21* (9), 1701-1708; (c) Li, G.; Shrotriya, V.; Yao, Y.; Yang, Y., Investigation of annealing effects and film thickness dependence of polymer solar cells based on poly(3-hexylthiophene). *Journal of Applied Physics* **2005**, *98* (4), 043704.
5. Padinger, F.; Rittberger, R. S.; Sariciftci, N. S., Effects of postproduction treatment on plastic solar cells. *Advanced Functional Materials* **2003**, *13* (1), 85-88.
6. (a) Baek, W. H.; Yoon, T. S.; Lee, H. H.; Kim, Y. S., Composition-dependent phase separation of P3HT:PCBM composites for high performance organic solar cells. *Org. Electron.* **2010**, *11* (5), 933-937; (b) van Bavel, S. S.; Barenklau, M.; de

With, G.; Hoppe, H.; Loos, J., P3HT/PCBM Bulk Heterojunction Solar Cells: Impact of Blend Composition and 3D Morphology on Device Performance. *Advanced Functional Materials* **2010**, *20* (9), 1458-1463.

7. Wienk, M. M.; Kroon, J. M.; Verhees, W. J. H.; Knol, J.; Hummelen, J. C.; van Hal, P. A.; Janssen, R. A. J., Efficient methano[70]fullerene/MDMO-PPV bulk heterojunction photovoltaic cells. *Angewandte Chemie-International Edition* **2003**, *42* (29), 3371-3375.

8. (a) Mihailetchi, V. D.; Wildeman, J.; Blom, P. W. M., Space-charge limited photocurrent. *Physical Review Letters* **2005**, *94* (12); (b) Goodman, A. M.; Rose, A., Double Extraction of Uniformly Generated Electron-Hole Pairs from Insulators with Noninjecting Contacts. *Journal of Applied Physics* **1971**, *42* (7), 2823.

9. Keddie, J. L.; Jones, R. A. L.; Cory, R. A., Size-Dependent Depression of the Glass-Transition Temperature in Polymer-Films. *Europhys Lett* **1994**, *27* (1), 59-64.

10. Wang, T.; Pearson, A. J.; Lidzey, D. G.; Jones, R. A. L., Evolution of Structure, Optoelectronic Properties, and Device Performance of Polythiophene: Fullerene Solar Cells During Thermal Annealing. *Advanced Functional Materials* **2011**, *21* (8), 1383-1390.

11. Fakhraai, Z.; Forrest, J. A., Probing slow dynamics in supported thin polymer films. *Physical Review Letters* **2005**, *95* (2) 025701.

12. Parnell, A. J.; Dunbar, A. D. F.; Pearson, A. J.; Staniec, P. A.; Dennison, A. J. C.; Hamamatsu, H.; Skoda, M. W. A.; Lidzey, D. G.; Jones, R. A. L., Depletion of PCBM at the Cathode Interface in P3HT/PCBM Thin Films as Quantified via Neutron Reflectivity Measurements. *Advanced Materials* **2010**, *22* (22), 2444-2447.

13. Germack, D. S.; Chan, C. K.; Kline, R. J.; Fischer, D. A.; Gundlach, D. J.; Toney, M. F.; Richter, L. J.; DeLongchamp, D. M., Interfacial Segregation in

Polymer/Fullerene Blend Films for Photovoltaic Devices. *Macromolecules* **2010**, *43* (8), 3828-3836.

14. Tillack, A. F.; Noone, K. M.; MacLeod, B. A.; Nordlund, D.; Nagle, K. P.; Bradley, J. A.; Hau, S. K.; Yip, H.-L.; Jen, A. K. Y.; Seidler, G. T.; Ginger, D. S., Surface Characterization of Polythiophene:Fullerene Blends on Different Electrodes Using Near Edge X-ray Absorption Fine Structure. *ACS Applied Materials & Interfaces* **2011**, *3* (3), 726-732.

15. Nguyen, L. H.; Hoppe, H.; Erb, T.; Gunes, S.; Gobsch, G.; Sariciftci, N. S., Effects of annealing on the nanomorphology and performance of poly(alkylthiophene): fullerene bulk-heterojunction solar cells. *Advanced Functional Materials* **2007**, *17* (7), 1071-1078.

16. Verploegen, E.; Mondal, R.; Bettinger, C. J.; Sok, S.; Toney, M. F.; Bao, Z. A., Effects of Thermal Annealing Upon the Morphology of Polymer-Fullerene Blends. *Advanced Functional Materials* **2010**, *20* (20), 3519-3529.

17. Watts, B.; Belcher, W. J.; Thomsen, L.; Ade, H.; Dastoor, P. C., A Quantitative Study of PCBM Diffusion during Annealing of P3HT: PCBM Blend Films. *Macromolecules* **2009**, *42* (21), 8392-8397.

18. He, C.; Germack, D. S.; Kline, R. J.; Delongchamp, D. M.; Fischer, D. A.; Snyder, C. R.; Toney, M. F.; Kushmerick, J. G.; Richter, L. J., Influence of substrate on crystallization in polythiophene/fullerene blends. *Solar Energy Materials and Solar Cells* **2011**, *95* (5), 1375-1381.

19. Woo, C. H.; Thompson, B. C.; Kim, B. J.; Toney, M. F.; Frechet, J. M. J., The Influence of Poly(3-hexylthiophene) Regioregularity on Fullerene-Composite Solar Cell Performance. *Journal of the American Chemical Society* **2008**, *130* (48), 16324-16329.

20. Chirvase, D.; Parisi, J.; Hummelen, J. C.; Dyakonov, V., Influence of nanomorphology on the photovoltaic action of polymer-fullerene composites. *Nanotechnology* **2004**, *15* (9), 1317-1323.
21. Erb, T.; Zhokhavets, U.; Gobsch, G.; Raleva, S.; Stuhn, B.; Schilinsky, P.; Waldauf, C.; Brabec, C. J., Correlation between structural and optical properties of composite polymer/fullerene films for organic solar cells. *Advanced Functional Materials* **2005**, *15* (7), 1193-1196.
22. (a) Treat, N. D.; Brady, M. A.; Smith, G.; Toney, M. F.; Kramer, E. J.; Hawker, C. J.; Chabynyc, M. L., Interdiffusion of PCBM and P3HT Reveals Miscibility in a Photovoltaically Active Blend. *Advanced Energy Materials* **2011**, *1* (1), 82-89; (b) Collins, B. A.; Gann, E.; Guignard, L.; He, X.; McNeill, C. R.; Ade, H., Molecular Miscibility of Polymer,âFullerene Blends. *The Journal of Physical Chemistry Letters* **2010**, *1* (21), 3160-3166.

CHAPTER 7: CORRELATING PHASE BEHAVIOUR WITH OPTICAL AND ELECTRONIC PROPERTIES IN PCDTBT:PC₇₀BM OPV DEVICES

SECTION 7.1: INTRODUCTION

In this chapter, the relationship between film nanostructure and opto-electronic properties for blends of poly[N-9'-heptadecanyl-2,7-carbazole-alt-5,5-(4',7'-di-2-thienyl-2',1',3'-benzothiadiazole) : [6,6]-phenyl-C71-butric acid methyl ester (PCDTBT:PC₇₀BM) is investigated ¹. As discussed in chapter 2, section 2.6, PCDTBT is part of a new generation of materials that have been synthesised to improve the efficiency and operational stability of OPVs over previous blend systems (for example, P3HT:PCBM). In sections 7.2 & 7.3, PCDTBT and PCDTBT:PC₇₀BM thin films are characterised using a variety of techniques to give an overview of this system. Whereas P3HT is a semi-crystalline polymer (thus capable of forming relatively pure nanodomains even in blend films), PCDTBT is relatively amorphous, with weak evidence of self-organisation only seen in pure PCDTBT thin films. Upon blending PCDTBT with PC₇₀BM, the as-cast thin films are also largely amorphous, indicating a high degree of miscibility between the two materials. It is argued that such a morphology provides a partial rationalisation for photoluminescence (PL) measurements in which PCDTBT fluorescence is quenched more efficiently by PC₇₀BM molecules relative to the fluorescence quenching that occurs in P3HT:PC₇₀BM blends. Steady state PL measurements are used to estimate a solubility

limit for PC₇₀BM in PCDTBT, by identifying a threshold concentration above which PC₇₀BM molecules can form relatively pure nanodomains. Hole mobility measurements using the space-charge limited current (SCLC) technique show an increase in hole mobility in blend thin films with a greater PC₇₀BM wt%, a result in qualitative agreement with other amorphous polymer:fullerene blends. Lastly, the influence of blend composition on the power conversion efficiency of OPVs is explored. OPVs with a peak power conversion efficiency of 4% are achieved for a 1:4 (wt%) PCDTBT:PC₇₀BM blend cast from CHCl₃.

In section 7.4 the effects of thermal annealing on the structure and electronic characteristics of PCDTBT:PC₇₀BM thin films and devices are explored. The highest efficiency PCDTBT:PC₇₀BM OPV devices reported in the literature have demonstrated that apparently optimised morphologies can be created in this system during the film casting process alone, without the need for any post-deposition treatment². Neutron Reflectivity (NR) experiments on as-cast PCDTBT:d-PCBM thin films with an optimised blend composition are presented to demonstrate that fullerene molecules are distributed with a concentration gradient through the depth of the thin film, with the surface being composed of almost pure d-PCBM. Such a vertical composition profile is highly fortuitous for conventional OPV architectures. By constructing a partial phase diagram for PCDTBT:PC₇₀BM blends focusing on the glass transition temperature, of PCDTBT, the temperature is identified beyond which changes in film nanostructure (and consequently device efficiency) can be anticipated. It is shown that annealing protocols used for P3HT:PCBM OPVs lead to a reduction in device efficiency, with the onset approximately coincident with the T_g of the blend. Additionally thermal annealing decreases the mobility of holes within the blends and

reduces the glass transition temperature of the film, observations that provide a partial explanation for the reduced power conversion efficiency in OPVs. Grazing-incidence wide-angle X-ray scattering (GIWAXS) of pure PCDTBT thin films show that thermal annealing above T_g results in an increase in disorder in the material, a result that may explain the observed reduction in photovoltaic efficiency in blend thin film devices. The final part of this chapter, section 7.5, looks at the conditions under which PC₇₀BM aggregation occurs. In-situ monitoring of PCDTBT:PC₇₀BM blend thin films on silicon / native oxide during thermal annealing using spectroscopic ellipsometry (SE) show that a threshold temperature of 155°C is needed to induce PC₇₀BM aggregation. This indicates that the morphology of PCDTBT:PC₇₀BM blend thin films have an improved degree of thermal stability compared to blend films of P3HT:PCBM. However, coarse phase-separation driven by thermal annealing at temperatures at or above 155°C will further decrease the efficiency of photocurrent generation in this system.

SECTION 7.2: OPTICAL AND STRUCTURAL PROPERTIES OF PCDTBT THIN FILMS

The chemical structure of PCDTBT is shown in Figure 7.1, alongside an AFM phase image ($1 \mu\text{m}^2$) of the thin film surface & measurements of the optical density and photoluminescence. Here, as for all samples prepared for this chapter, the thin films are cast from CHCl_3 . In Figure 7.1(b), it can be seen that the structures present on the surface of the sample are at or below the size of the AFM tip ($\sim 7\text{-}10 \text{ nm}$). As will be shown from GIWAXS measurements, the absence of any domain-like structures in PCDTBT larger than several nm is a probable consequence of the amorphous nature of this polymer.

In Figure 7.1(c), the optical density (O.D.) and photoluminescence (PL) spectra from pure PCDTBT are presented. The O.D. spectrum is characterised by two absorption bands, centred at 570 nm ($\pi\text{-}\pi^*$ absorption band of the first excited state S_1) and 400 nm ($\pi\text{-}\pi^*$ absorption band of the second excited state S_2)³. These bands are thought to arise from the donor-acceptor nature of the polymer. Yi et al.⁴ have demonstrated these bands may shift in energy for derivatives of PCDTBT, in which additional thiophene units have been included beside the TBT unit. Upon optical excitation of the polymer at either absorption band, a relative broad emission spectrum is measured, characterised by a peak centred at 690 nm.

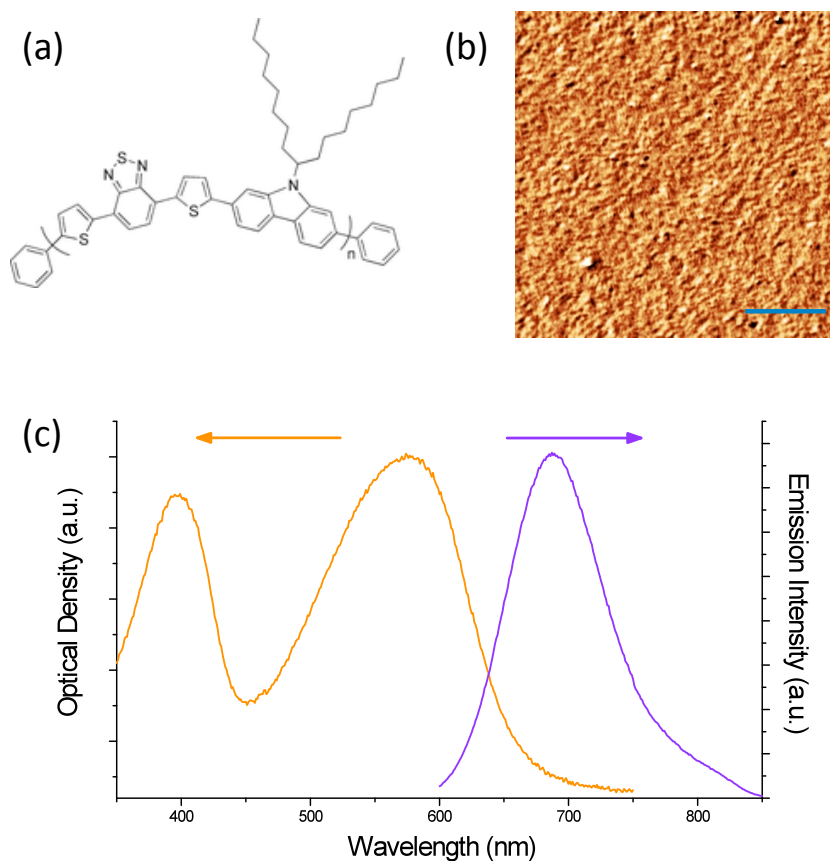


Figure 7.1: (a) The chemical structure of the PCDTBT monomer. An AFM tapping-mode phase map of the surface of a PCDTBT thin film is presented in part (b). Here the scale bar corresponds to 250 nm. Steady-state optical density and photoluminescence spectra are presented in part (c).

GIWAXS has been used to probe the nanoscale structure of as-cast PCDTBT thin films, with results presented in Figure 7.2. As can be seen from Figure 7.2(a), two broad rings are discernable in the scattering pattern. From Figure 7.2(b), it can be seen that in the in-plane direction these peaks are located at $q_x = 0.31 \text{ \AA}^{-1}$ and 1.45 \AA^{-1} . These are attributed to the chain spacing between PCDTBT backbones along the alkyl

side-chains (20.3 Å) and the distance between planar π -stacked backbones (4.3 Å) respectively⁵.

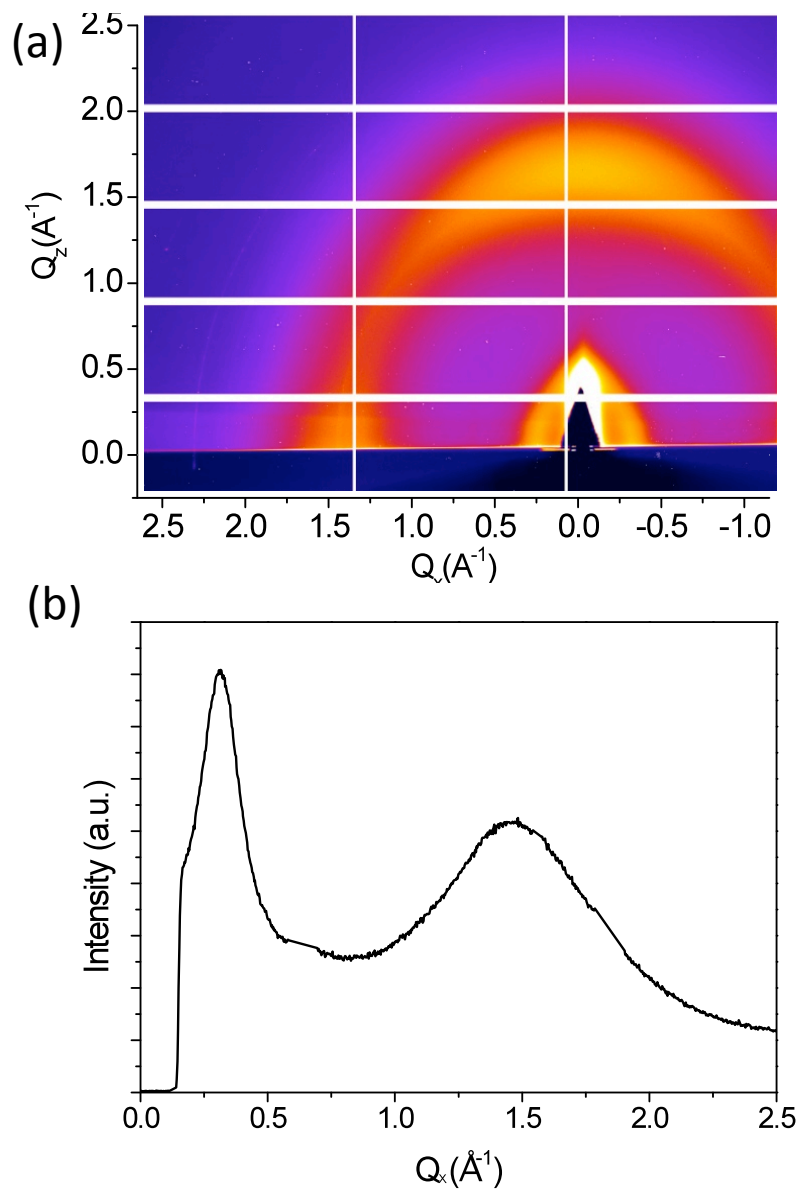


Figure 7.2: (a) 2D GIWAXS scattering pattern from a pure PCDTBT thin film, collected with the sample facing 0.11° into the incident X-ray path. A line profile of the scattering pattern, taken along the in-plane (Q_x) direction is presented in part (b). The region of low intensity at low Q_x corresponds to the beam stop seen in part (a).

This result is consistent with powder diffraction studies on this material ^{5a}, which suggested that PCDTBT is largely amorphous. As can be seen from Figure 7.2(a) however, there is a weak preference for the polymer to stack ‘face-on’ with respect to the substrate, as the outermost ring (corresponding to the π - π stacking of PCDTBT chains) is most intense in the out-of-plane direction. This is in contrast to P3HT, which preferentially stacks ‘edge-on’ with respect to the substrate (i.e the π - π planes are orientated perpendicular to the substrate). Nevertheless, the coherence length (L) of PCDTBT in this sample is low. Using the relationship $L = 2\pi/\Delta q$, where Δq is the full-width-at-half-maximum (FWHM) of a scattering signal, values of 57 Å and 12 Å are obtained from the alkyl side group and π - π plane scattering signals respectively. This corresponds to approximately three times the inter-chain spacing along these directions. Such small length scales explain the absence of any resolvable features in the AFM data presented in Figure 7.1(b).

SECTION 7.3: OPTICAL, STRUCTURAL AND ELECTRONIC PROPERTIES OF PCDTBT:PC₇₀BM BLEND THIN FILMS

In Figure 7.3, O.D. and AFM phase measurements are presented for blend films, the latter technique applied to blend films having a fullerene concentration of 20, 40, 60 & 80 wt%.

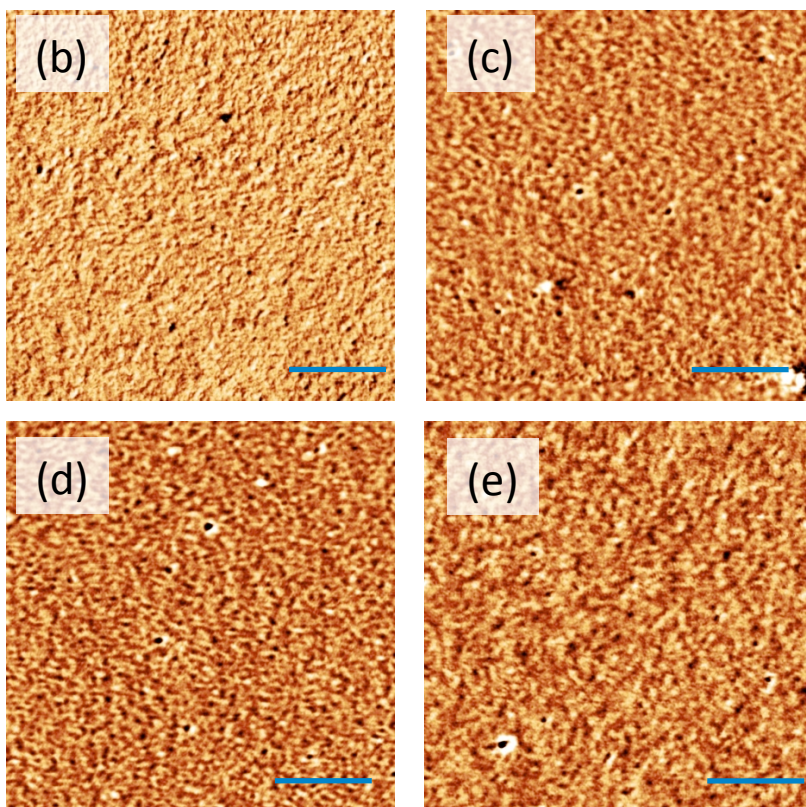
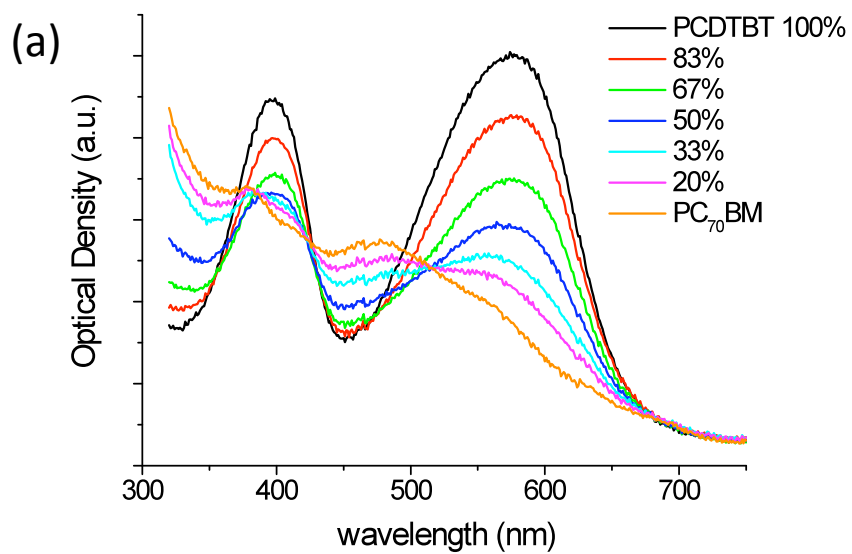


Figure 7.3: (a) Absorption spectra of as-cast PCDTBT:PC₇₀BM blend thin films as a function of PCDTBT wt%. In parts (b) to (e), AFM tapping-mode phase maps of the surface of as-cast blend thin films with PC₇₀BM wt% of 20%, 40%, 60% & 80% respectively. The scale bar in all images corresponds to 250 nm.

From Figure 7.3(a), it can be seen that the absorption bands of PCDTBT do not undergo any significant shift in wavelength upon blending with PC₇₀BM. The reduction in overall absorption as the concentration of PC₇₀BM is increased in the film is consistent with the weak absorption strength of PC₇₀BM relative to PCDTBT over the wavelength range measured ⁶. The observation that the absorption peaks of PCDTBT do not undergo any shift in energy suggests PC₇₀BM has a negligible effect on the conformation or effective conjugation length of PCDTBT. This is in contrast to blends of P3HT:PCBM, where the data presented in chapters 4 to 6 and the Appendix (Figure A.1) has linked changes in the absorption spectrum to a disruption in the self organisation and effective conjugation length of P3HT.

In Figure 7.3 parts (b) to (e), it can be seen that AFM measurements of the surfaces of the thin film blends show no evidence of phase separation (at least on the surface of the samples) over a length scale greater than ~10 nm. This clearly indicates the existence of a finely mixed morphology. Given the structure of the polymer and the results of empirical device studies to determine an optimised blend composition for PCDTBT:PC₇₀BM OPVs, it is possible that fullerene concentrations below 50 wt%, the molecules are located between the alkyl side-groups of PCDTBT, thus forming a molecularly mixed phase. Cates *et al.* ⁷ and Mayer *et al.* ⁸ have demonstrated this type of organisation in blends of PBTTT:PCBM where molecular mixing is evidenced using GIWAXS through an increase in the spacing of adjacent polymer backbones.

To determine whether the miscibility between PCDTBT and PC₇₀BM can be inferred using an indirect probe, attention now turns to steady-state measurements of the

photoluminescence from blend thin films. In Figure 7.4, the relative photoluminescence intensity from a PCDTBT:PC₇₀BM blend is presented as a function of PC₇₀BM wt%. Here the data has been normalised against the emission intensity of a thin film of pure PCDTBT, to provide an estimate of the quenching efficiency of PC₇₀BM molecules. Shown alongside this data are identical measurements recorded from RR-P3HT:PC₇₀BM thin films. These samples were cast from CB solvent and not subject to any post-deposition treatment. It is apparent that PC₇₀BM is a very efficient quencher of photogenerated excitons on PCDTBT, as emission from the polymer is quenched by 99% upon addition of only 9 wt% PC₇₀BM. Identical measurements on RR-P3HT:PC₇₀BM indicate that emission quenching in these samples is approximately an order of magnitude less efficient. It is possible that these results are consistent with the amorphous nature of PCDTBT:PC₇₀BM blend thin films, which results from a high degree of miscibility, particularly at low PC₇₀BM wt%. In contrast, the ability of RR-P3HT to undergo partial phase separation in a blend is likely to decrease the efficiency of exciton quenching.

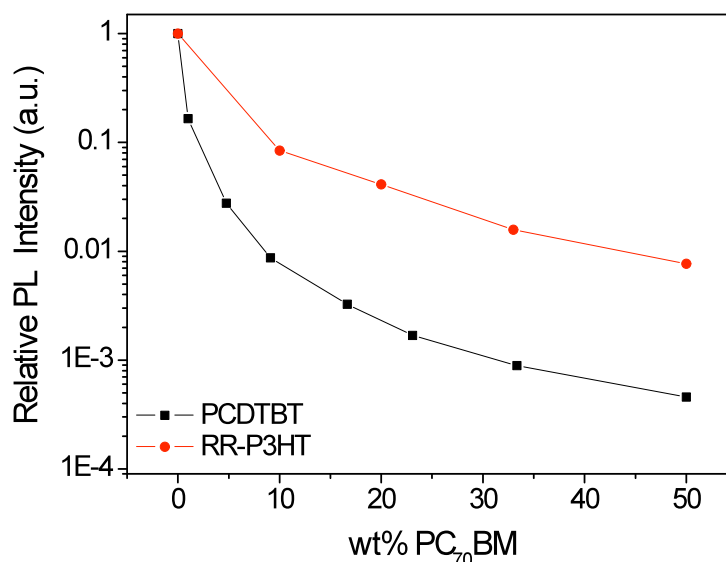


Figure 7.4: Photoluminescence emission intensity from thin films of PCDTBT or RR-P3HT blended with PC₇₀BM, as a function of wt% PC₇₀BM. For each sample set the emission from each sample has been normalised to the emission from a pure polymer thin film.

In Figure 7.5, PL spectra for PCDTBT/PC₇₀BM blend thin films for each composition are presented. For clarity, the intensity of each spectra spectrum has been normalised to unity. Over the composition range 0 to 50 wt% PC₇₀BM, it can be seen that emission from PCDTBT progressively blue-shifts as the wt% of PC₇₀BM is increased. For blend thin films with a PC₇₀BM fraction above 50 wt%, emission at 710 nm is detectable & is identified as singlet emission from the fullerene⁹. This suggests that at such high concentrations, a fraction of photogenerated excitons residing on PC₇₀BM cannot diffuse to a PCDTBT molecule within their lifetime to undergo dissociation. This suggests that over this composition range, PC₇₀BM domains are formed whose size must be commensurate with the exciton diffusion length in PC₇₀BM (a lower bound for the exciton diffusion length in PCBM has been estimated as 5 nm¹⁰). This observation is consistent with empirical device studies that demonstrate that in this

blend system, a PC₇₀BM wt% of at least 50% is needed to allow the formation of pure, interconnected, fullerene domains that permit the efficient extraction of photogenerated charge¹¹.

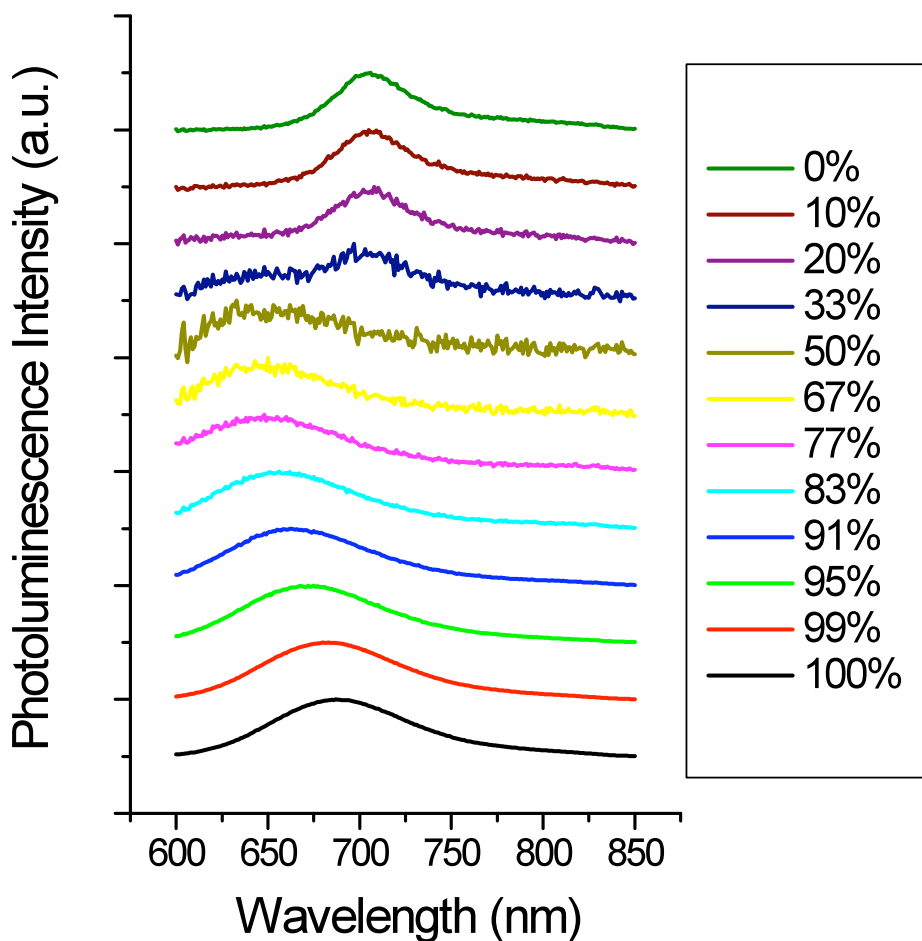


Figure 7.5: Photoluminescence spectra from PCDTBT(wt%):PC₇₀BM blend thin films, shown for PCDTBT wt% between 100 & 0%. All spectra were obtained after film excitation at 400 nm.

It can be seen that there is only a relatively small shift (710 to 705 nm) in singlet emission wavelength from PC₇₀BM as the PCDTBT wt% in the film is increased.

This suggests that relatively pure nanodomains of the fullerene are formed. In contrast however, there is a significant (690 up to 650 nm) shift in emission wavelength from PCDTBT upon addition of PC₇₀BM. This may result from the close proximity between donor and acceptor materials. Etzold *et al.*^{3a} also noted a blue-shift in emission energy from PCDTBT between pure and blend thin films, the latter containing 66 wt% PCBM. It is possible that the measurements here and in ref [1a] are consistent with fullerene molecules disrupting the energetic migration of excitons within the PCDTBT density of states.

The role of the blend morphology on hole mobility, μ_h , was investigated using the device architecture ITO/PEDOT:PSS/active layer/Au. The hole mobility is estimated at room temperature using space-charge limited current (SCLC) measurements as outlined in chapter 2, section 2.4. In Figure 7.6(a), μ_h in a PCDTBT:PC₇₀BM blend as a function of PC₇₀BM concentration is presented. This data was obtained by fitting the dark-current measurements over the range $5 < V < 9$ to the SCLC model. Here the effective bias is calculated by subtracting the built-in voltage¹ across the device from the applied bias. It can be seen that μ_h increases with increasing wt% of PC₇₀BM. Indeed, an almost 9-fold increase in μ_h in a 1:4 wt% PCDTBT:PC₇₀BM blend is measured compared to the hole mobility in pure PCDTBT, increasing from 4×10^{-6} cm²/Vs to 3.5×10^{-5} cm²/Vs. This trend is in qualitative agreement with the findings of Cates *et al.*¹³ who measured μ_h by SCLC methods for a number of amorphous polymer: functionalized fullerene blends, with an increase of up to 10^3 in μ_h measured for a number of amorphous polymer:fullerene systems relative to unblended polymer

¹ Estimated as the difference between the work function of Au (4.7eV) and PEDOT:PSS (4.85eV)

control devices. It was suggested that molecular mixing between fullerene molecules and polymer side-groups inhibited the coiling of the polymer chains and thus increased their effective conjugation length and thereby increased μ_h .

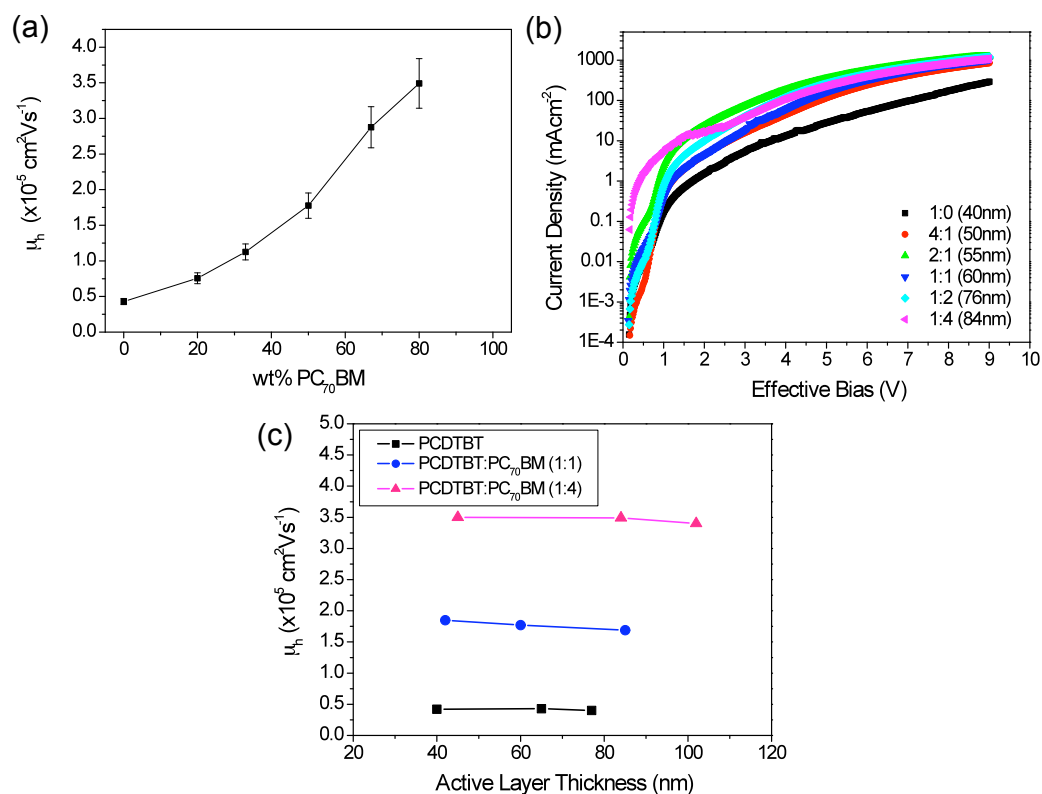
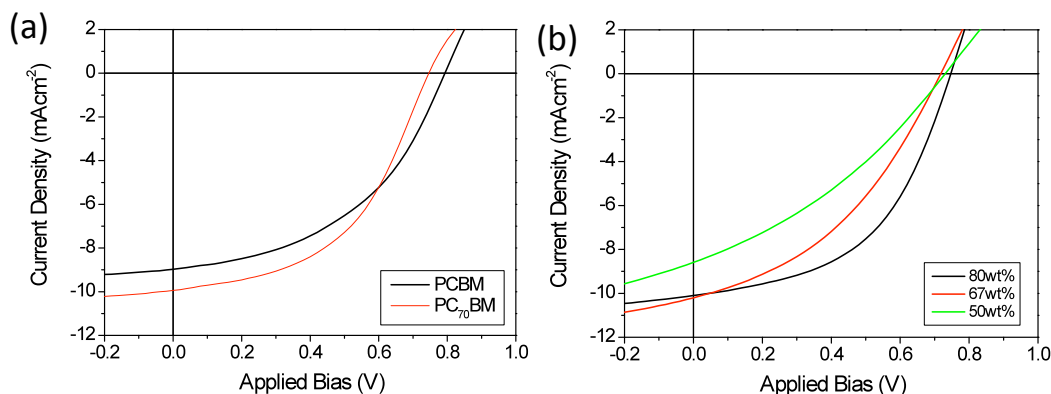


Figure 7.6: (a) Hole mobility for PCDTBT:PC₇₀BM blend Au top-contact devices, as a function of PC₇₀BM wt%. These values are extracted from the dark-current measurements presented in (b). The thickness of each blend is given in parenthesis. The average hole mobility obtained for devices with different active layer thicknesses, for a number of semiconducting layer compositions, is shown in part (c).

Clearly a significantly smaller increase in μ_h is observed here on blending PCDTBT with PC₇₀BM than was observed on the systems explored by Cates *et al.* From the results presented in Figure 7.3 it is apparent that mixing PCDTBT with PC₇₀BM does not result in any significant modification in the structure of the absorption spectrum of

the polymer. This may indicate that changes in the conformation of the polymer are relatively limited. Hole mobilities as high as $10^{-3} \text{ cm}^2/\text{Vs}$ have been reported for PCDTBT with a M_w of 28kDa (comparable to the 31kDa M_w PCDTBT used here) in an OFET device architecture¹⁴. This is in contrast to the polymers studied by Cates *et al.* (for example, MDMO-PPV) that had hole mobilities of the order of $10^{-7} \text{ cm}^2/\text{Vs}$. It is possible therefore that the small improvement in μ_h measured here is due to PCDTBT already being a good hole transporter, relative to other amorphous polymers.

A series of photovoltaic devices were fabricated to determine an efficient blend composition for device application using the batch of PCDTBT available for this research project. From the literature, all OPV studies have focused on blends containing a wt% excess of PC₇₀BM. As noted, the relatively large separation between adjacent side groups on the backbone of PCDTBT is likely to permit fullerene molecules to mix at a molecular level with PCDTBT. Hence a threshold amount of PC₇₀BM is required to provide a percolated network for electron transport towards the cathode in a practical OPV. In Figure 7.7(a), current voltage (*JV*) characteristics are presented for PCDTBT OPVs using either PCBM or PC₇₀BM as acceptor. Figure 7.7(b) shows *JV* characteristics as a function of PC₇₀BM acceptor concentration. Device metrics are presented in the accompanying table. Note that the use of post-deposition heat treatments are explored in Section 7.4 of this chapter. Here, all OPVs are as-cast and unannealed.



Acceptor	J_{sc} (mAcm ⁻²)	FF (%)	V_{oc} (V)	PCE (%)
PCBM (80nm)	-8.9	46	0.79	3.3
PC ₇₀ BM (87nm)	-9.9	49	0.75	3.6
Blend (70nm)				
1:1	-8.6	33	0.73	2.1
1:2	-10.2	41	0.71	2.9
1:4	-10.1	51	0.75	3.8

Figure 7.7: Current density-voltage characteristics of PCDTBT:acceptor (1:4 wt%) OPVs using either PCBM or PC₇₀BM as the acceptor (a), or PCDTBT:PC₇₀BM OPVs with varying wt% of PC₇₀BM (b). Average device metrics are presented in the table, with the uncertainty in PCE representing the standard deviation in efficiencies across 6 devices. The thickness of each active layer (\pm 4nm) is given in parenthesis.

From Figure 7.7(a), it can be seen that the substitution of PCBM for PC₇₀BM leads to an improvement in device efficiency, principally through an increase in short-circuit current density. This is consistent with the greater optical density of PC₇₀BM compared to PCBM over the visible wavelength region; an effect that compensates

for the relatively low absorption density of PCDTBT over the wavelength range 420 to 520 nm (see Figure 7.3(a)).

To test the effect of film composition on device performance, OPVs with a PC₇₀BM wt% ranging from 50 to 80% were fabricated. Owing to the relatively low fill-factor of the 1:4 wt% OPV with an active layer thickness of (87 ± 4 nm) (49%), thinner active layers were used (70 ± 4 nm) in an attempt to improve the efficiency of charge extraction. For an OPV with a blend composition of 1:4 wt% PCDTBT:PC₇₀BM, a PCE of 3.8 ± 0.2 % was achieved with an active layer thickness of 70 nm. The improvement in Fill-Factor with increasing PC₇₀BM wt% over the range investigated is consistent with an increase in electron mobility and reduction in bimolecular recombination. Note however that the optimum film composition used here (80 wt% PC₇₀BM) is in slight excess of other studies to have used CHCl₃ as the casting solvent (a wt% closer to 67% is most often used). However, studies by Alem *et al.*¹⁵ & Park *et al.*^{11a} noted that domains ~50 to 100 nm in size were apparent on the surface of the blend thin films studied, as inferred from phase measurements obtained by tapping mode AFM. Alem *et al.* correlated an increase in apparent domain size with increasing PC₇₀BM wt% in the blend and tentatively identified such features as being fullerene domains. Such features are not however observed in the samples explored here (as shown earlier in Figure 7.3). Since the solubility of fullerenes is relatively low in chloroform relative to other solvents commonly used in OPV processing (for example, chlorobenzene, dichlorobenzene or trichlorobenzene)¹⁶, the blend solutions I have used here may be prone to aggregation and are consequently unstable over long periods of storage at ambient conditions. Variations in solution preparation conditions between this work and others may therefore explain any differences obtained.

SECTION 7.4: INFLUENCE OF THERMAL ANNEALING ON FILM NANOSTRUCTURE AND PHOTOVOLTAIC PROPERTIES OF PCDTBT:PC₇₀BM BLENDS

From the previous section it is apparent that relatively efficient OPVs can be prepared without the need for further post-deposition treatment. This is a remarkable characteristic of this blend system, as films cast from CHCl₃ dry in only a few seconds. This is in contrast to the P3HT:PCBM system, where device PCEs of roughly 1% were obtained for as-cast devices, as shown in previous chapters. To provide some insight into why PCDTBT:PC₇₀BM blends form efficient morphologies simply through the casting process alone, I have participated in a study of blend thin films using neutron reflectivity (NR)^{5b}. As with the study on P3HT:PCBM blend thin films using this technique, the fullerene is substituted for deuterated PCBM (d-PCBM) to increase its contrast against the polymer. Here, a 1:4 (wt%) PCDTBT:d-PCBM blend thin film cast from CHCl₃ was studied. A summary of the data is presented in Figure 7.8.

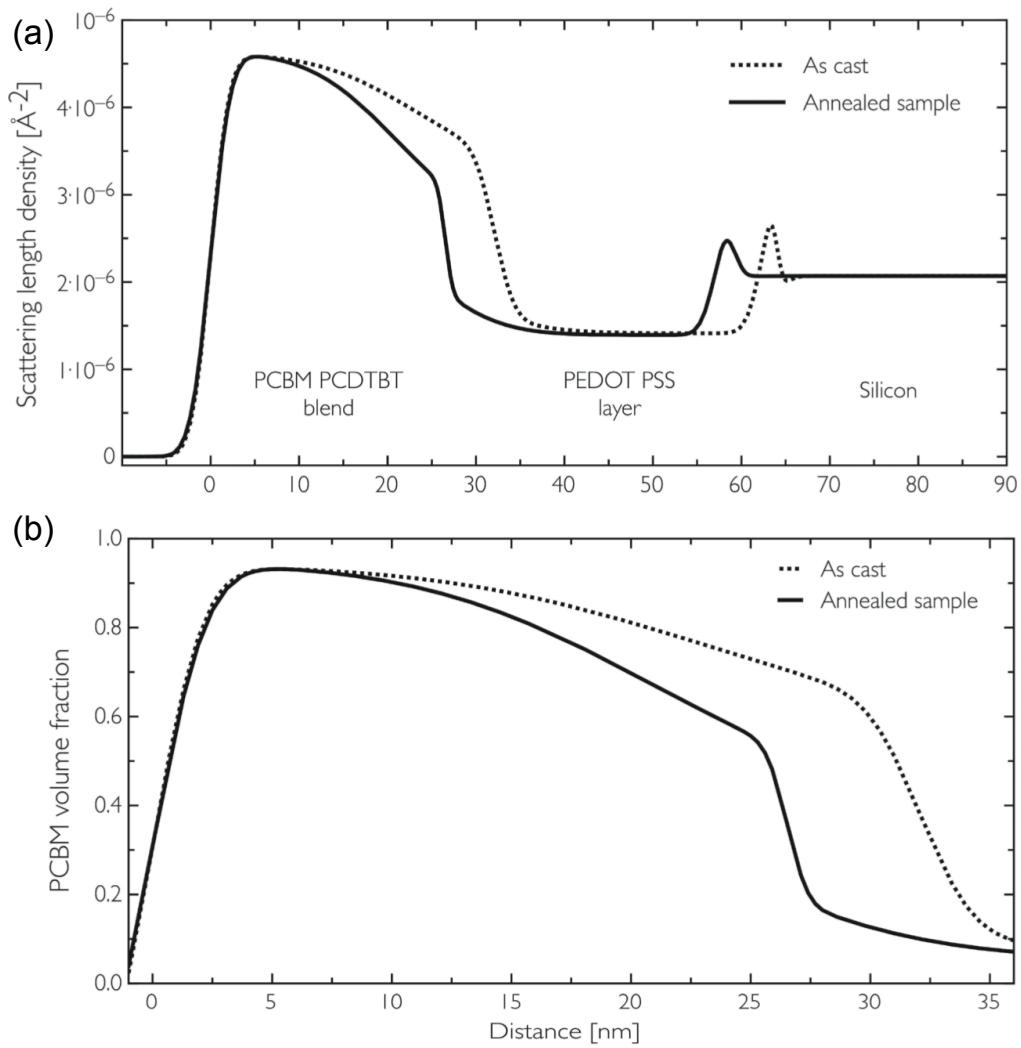


Figure 7.8: Part (a) shows the modelled scattering length density profile for a 1:4 (wt%) PCDTBT:d-PCBM film cast from CHCl₃ on PEDOT:PSS. The profile has been acquired by fitting neutron reflectivity measurements from the sample with a gradient interface model. An expanded view is provided in part (b). The measurements and analysis were undertaken by Andy Parnell on samples prepared by myself. Here, the annealing protocol was 70°C for 60 minutes.

As can be seen, the profile of scattering length density versus film depth shows an enrichment in fullerene concentration at the free surface of the film, with the concentration of d-PCBM decreasing in an almost linear fashion towards the

PEDOT:PSS interface. Note that this profile differs substantially from the vertical composition of an optimised P3HT:PCBM blend thin film, where the best-fit to the neutron reflectivity data suggested a uniform distribution of d-PCBM throughout the entire depth of the film ¹⁷. It is important to recognise that differences in film thickness, volume concentration of d-PCBM and interaction energies between the polymers and the substrate may explain the differences between the composition profiles for the different blend systems. It is not known therefore, whether a vertical gradient of PCBM can be achieved in P3HT:PCBM blends when the wt% of PCBM is in excess of P3HT, or if the gradient in PCDTBT:PCBM blend thin films is retained if the thickness of the film is increased or if it is deposited onto a different substrate. More work is required to answer these questions and possible experiments are considered in chapter 9. Nevertheless the data presented in Figure 7.8 suggests that the vertical distribution of fullerene molecules in as-cast PCDTBT:PCBM blend thin films with an optimised composition is highly advantageous for OPVs using a conventional device architecture. The high (> 50 vol%) acceptor content throughout the film will enable efficient dissociation of excitons generated on PCDTBT chains, whilst the enrichment of d-PCBM at the surface will facilitate the extraction of electrons and act as a hole blocking layer.

Figure 7.8 also shows the modeled d-PCBM vertical composition of the film when subject to a post deposition thermal treatment at 70°C for 60 minutes. This annealing protocol represents the only annealing step reported in the literature to date for high efficiency PCDTBT:PC₇₀BM OPVs ^{11a} and provides a suitable starting point to understanding the effects of thermal annealing on this system. As can be seen, the vertical distribution of d-PCBM for the heated samples is qualitatively unchanged

compared to the control, with a similarly board interface with PEDOT:PSS and a relatively smooth surface. The absence of any significant changes in vertical composition is not a particularly surprising observation as the T_g for pure PCDTBT, as reported in the literature ^{5a} or as reported later in this chapter, is in the region of 120 to 130°C. For this reason it is difficult for d-PCBM molecules to diffuse and aggregate when the film is heated to 70°C, because at this temperature the PCDTBT phase forms a relatively rigid polymer matrix.

To determine the phase behaviour of this system, particularly the T_g of PCDTBT in a blend, a number of PCDTBT:PC₇₀BM blend thin films cast from CHCl₃ were monitored using SE during a first heating cycle. In Figure 7.9, the modeled blend film thicknesses as a function of PC₇₀BM wt% are plotted during heating (part (a)) and cooling (part (b)) with the extracted T_g values as a function of PC₇₀BM wt% presented in part (c). It can be seen that for all film compositions, a reduction in film expansion rate occurs around 70 to 75°C. This temperature range is above the boiling point, T_e , of CHCl₃ (62°C). It is likely therefore that the reduction in film expansion rate is due to the effects of solvent evaporation. Note that in this case solvent loss occurs once the film temperature exceeds the solvent boiling point. This is in contrast to blends of P3HT:PCBM, where from chapters 5 and 6 it was found that solvent loss occurs below T_e by heating a sample to a temperature which exceeds the T_g of the blend.

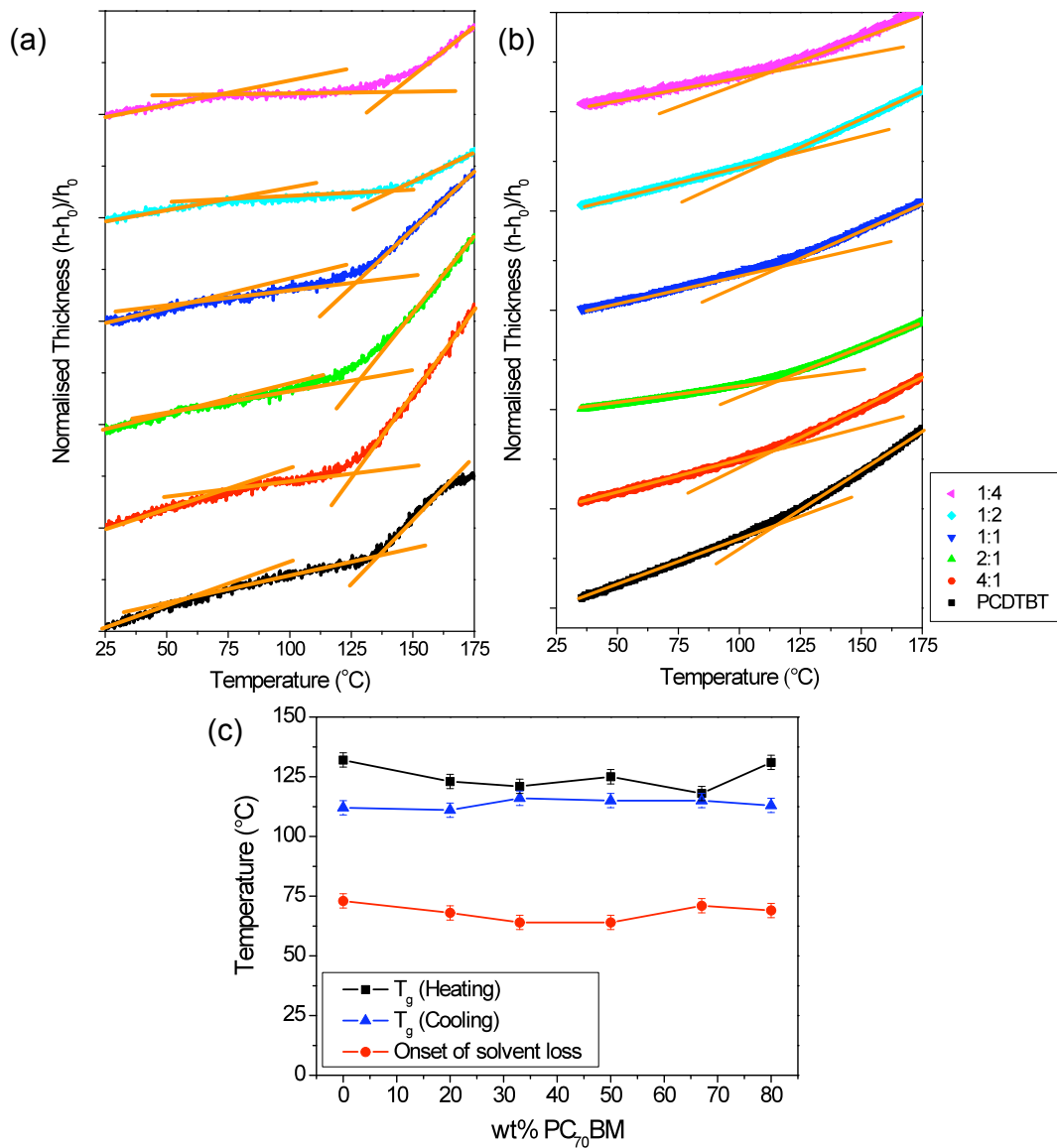


Figure 7.9: (a) Normalised thickness changes versus sample temperature for a number of PCDTBT:PC₇₀BM (wt%:wt%) blend thin films during the first heating cycle (part (a)) and first cooling cycle (part (b)). For all samples the heating / cooling rate was 5 $^{\circ}\text{C}/\text{min}$. The T_g and onset for solvent loss for each film are marked by the intersection of the linear fits to the data. In part (c) the blend T_g (s) are presented as a function of PC₇₀BM wt%. Also shown is the estimated temperature for solvent loss.

From Figure 7.9, it can be seen that the T_g of the PCDTBT used in this investigation is relatively insensitive to blend composition and any variations are mostly within uncertainty limits. At 80 wt% PC₇₀BM the T_g of the polymer is 135°C compared to the pure material (130°C). From chapter 6 section 6.3, the relative increase in T_g observed when P3HT is blended with PCBM was attributed to the fullerene molecules acting as an anti-plasticiser for the polymer, thereby increasing the cohesive interactions between materials in the film. In blends of PCDTBT:PC₇₀BM, such behaviour is not apparent. Similar results have been reported in blends of F8TBT:PCBM¹⁸ (F8TBT is almost identical in structure to PCDTBT with the exception that a carbon atom replaces the nitrogen atom and the carbazole unit thus becomes fluorinated). The authors attributed the relative insensitivity of F8TBT T_g with blend composition [only varying from 110°C to 100°C as the PCBM loading was increased from 0 to 80 wt%] to its good miscibility with PCBM. In PCDTBT:PC₇₀BM blend thin films, the insensitivity of T_g to film composition is also true for thin films cast from a DCB solvent, and for films cast onto a PEDOT:PSS coated substrate¹. For these samples however there are deviations in the value of T_g , compared to samples cast from CHCl₃, suggesting that PCDTBT chains may form a different molecular conformation whilst in DCB solution (for example, a more open configuration), or arrange themselves differently at the sample/substrate interface. Upon cooling, it is apparent that the measured T_g for films of pure PCDTBT and PCDTBT:PC₇₀BM blends is reduced to approximately 110 to 115°C. As will be discussed later in this section, the insensitivity between blend T_g and fullerene concentration provides an indirect probe of blend film nanostructure for samples to have undergone thermal annealing.

In chapter 6, DMTA measurements of P3HT:PCBM films are referred to, in which thermal transitions related to PCBM could be measured when the fullerene concentration in the film exceeded 60 wt%. Here some of the thermal transitions of PC₇₀BM are explored. Figure 7.10 shows the thermal expansion of a 110 nm thick film of pure PC₇₀BM cast from CHCl₃ onto a silicon / native oxide substrate. It can be seen that two transitions are detectable during the first heating cycle and occur at 112°C and 152°C.

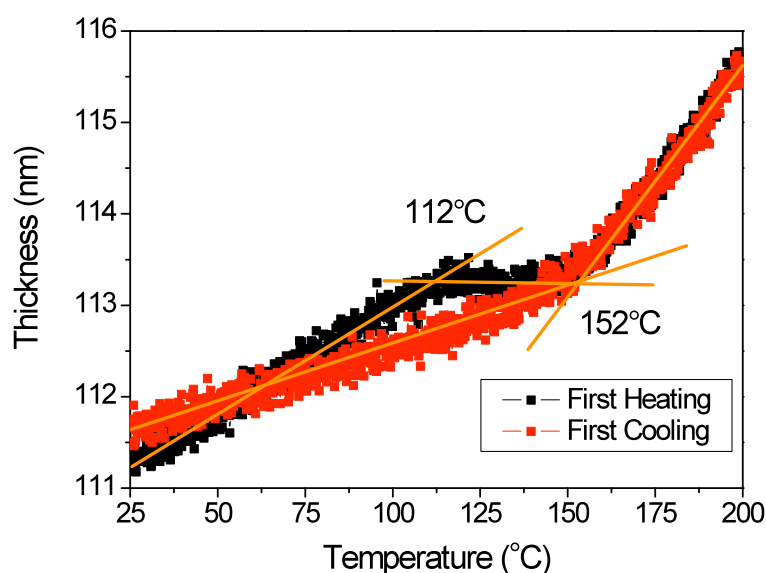


Figure 7.10: Thickness evolution of a pure PC₇₀BM thin film cast from CHCl₃ during first heating and first cooling cycles. The rate for each ramp was 5°C/min. Orange markers provide a guide to the eye of the thermal expansion or contraction rate of the sample, the intersections of which correspond to thermal transitions.

It is apparent that the lower temperature transition observed at 112°C is non-reversible. As PCBM is known to be hygroscopic, this feature may originate from the

removal of trapped moisture¹⁹. The higher temperature thermal transition (152°C) is however reversible, and is observed during first heating and first cooling cycles. The melting temperature of PC₇₀BM is known to exist above 250°C¹⁹, suggesting the thermal transition at 152°C is a solid-solid transition. Note that a transition at around 155°C has also been observed in P3HT:PCBM blend films using dynamic mechanical thermal analysis¹⁹. In Figure 7.9(b) a transition in this temperature range is not observed in any of the spectroscopic ellipsometry experiments performed on the blends. The apparent absence of this transition again supports the proposition that as-cast films of PCDTBT and the PC₇₀BM are relatively intimately mixed. Note however, at high PC₇₀BM loadings, (above 50 wt%) PC₇₀BM nanodomains are expected to form (see Figure 7.5 and the related discussion), thereby facilitating efficient electron transport in optimised PCDTBT:PC₇₀BM OPVs as demonstrated in Figure 7.7. It appears however that in PCDTBT:PC₇₀BM blends such nanodomains are sufficiently small that the solid-solid transition at 152°C is suppressed.

It is apparent from the previous discussion, and from the results presented in chapters 5 & 6, that significant changes in active layer morphology are unlikely to be anticipated in PCDTBT:PC₇₀BM blend thin films subject to a thermal anneal at a temperature below the T_g of the polymer (~120°C). However, application of a thermal anneal at a temperature above the boiling point of CHCl₃ may permit any solvent trapped in the thin films during casting to evaporate. To explore the influence of thermal annealing on PCDTBT:PC₇₀BM OPVs, devices were thermally annealed for 30 minutes at temperatures ranging from 70°C to 180°C. The results are presented in Figure 7.11. The weight fraction of PC₇₀BM in the active layer was varied from 50 to 80% and the film thickness was kept constant at 70 nm. As can be seen from Figure

7.11, annealing close to or above the T_g of the blend decreases the PCE relative to unannealed controls. For OPVs annealed at 70°C, any improvements are within measured spread of device efficiencies measured. It appears therefore that a thermal treatment at 70°C applied to PCDTBT:PC₇₀BM OPVs prepared from CHCl₃ solution can only result in a minor improvement in efficiency at best.

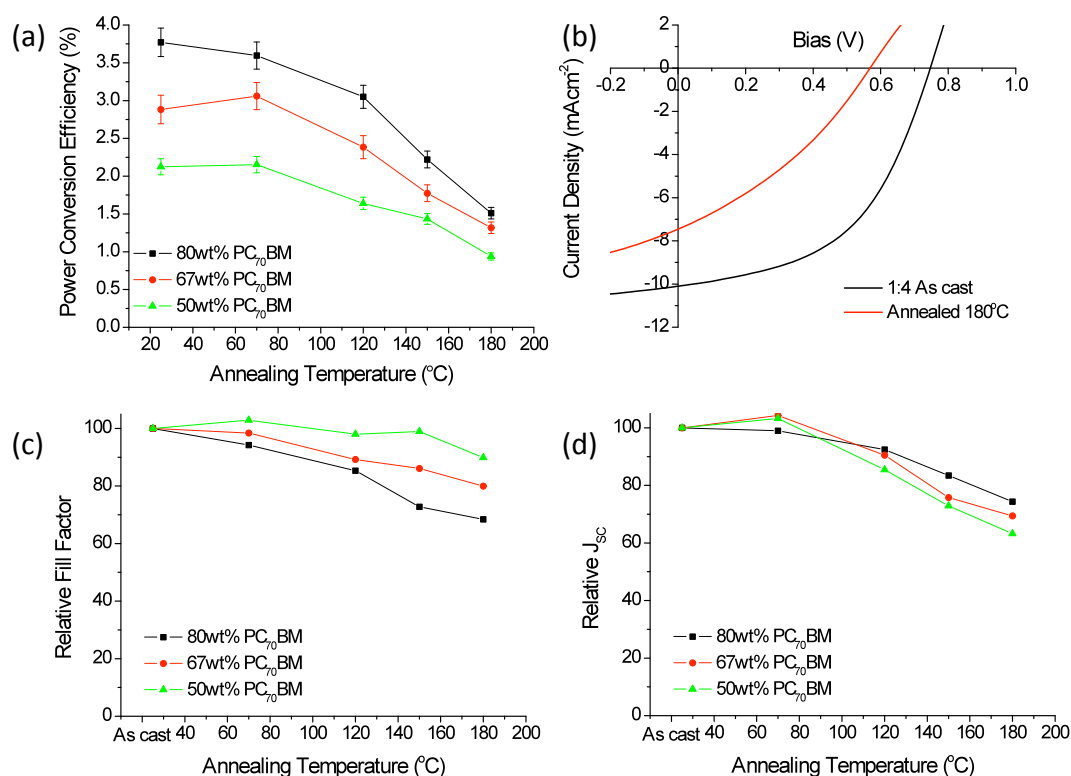


Figure 7.11: (a) Power conversion efficiency of PCDTBT:PC₇₀BM (wt%) OPVs as a function of annealing temperature. Typical current density-voltage measurements are presented in part (b) to provide an example of how thermal annealing reduces device efficiency. Here the active layer composition for all devices is 1:4 wt%. Parts (c) and (d) show the average fill-factor and short-circuit current densities of all devices as a function of annealing temperature, normalised to the values measured for the unannealed devices.

The relative changes in J_{sc} and FF of devices to have undergone thermal annealing are presented in Figure 7.11 parts (c) and (d) respectively. It is apparent that the data in Figure 7.11(a) masks differences between the different active layer compositions and the cause for lower PCEs. For example, devices with 80 wt % PC₇₀BM in the active layer undergo the largest relative reduction in FF but the smallest relative reduction in J_{sc} upon annealing, compared to unannealed controls.

To further explore the electrical characteristics of thermally annealed PCDTBT:PC₇₀BM blends, devices having a Au top electrode were measured under the SCLC regime, following the method described in section 7.3. As shown from Figure 7.12, μ_h decreases for samples annealed at or above 120°C for 30 minutes. It appears therefore that one explanation for the reduction in OPV power conversion efficiency seen in Figure 7.11(a) results from a reduction in hole mobility within the active semiconducting layer of the devices.

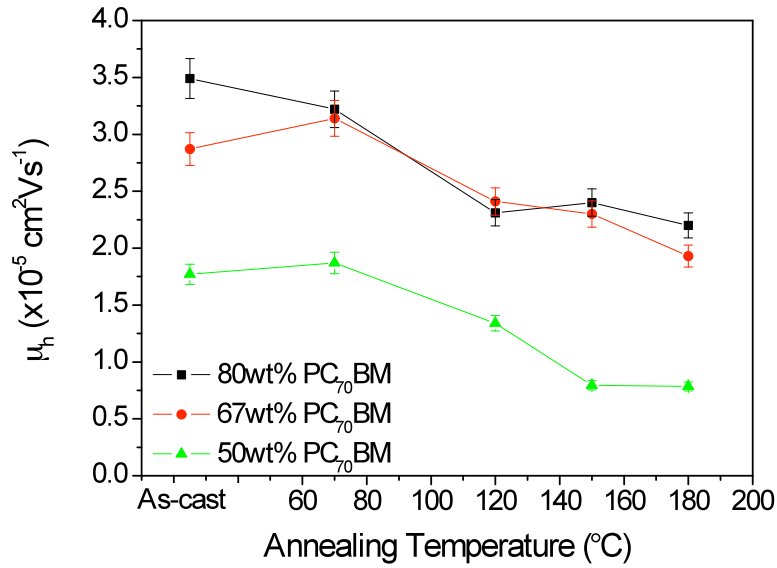


Figure 7.12: Hole mobility for PCDTBT:PC₇₀BM blend Au cathode devices, as a function of device annealing temperature.

My studies on P3HT:PCBM blend OPVs in chapter 6, section 6.4, correlated a reduction in PCE due to thermal annealing with a combination of coarse phase separation by PCBM and a reduction in the effective conjugation length (inferred from absorption measurements) of P3HT. Given the relatively high loading of PC₇₀BM in the OPVs studied in this chapter, it is possible that coarse phase separation of PCBM may occur in OPVs annealed above the T_g of PCDTBT. However that this is not the case. Tapping-mode AFM phase images, taken from measurements of the surface of the blend thin films deposited onto PEDOT:PSS, are presented in Figure 7.13. It can be seen that there is no evidence for large-scale fullerene aggregation, even after annealing at 180°C for 30 minutes. Note however that coarse phase separation can result from extended thermal annealing at lower temperatures for blend

thin films deposited onto silicon/native oxide substrates, as will be shown in the next section.

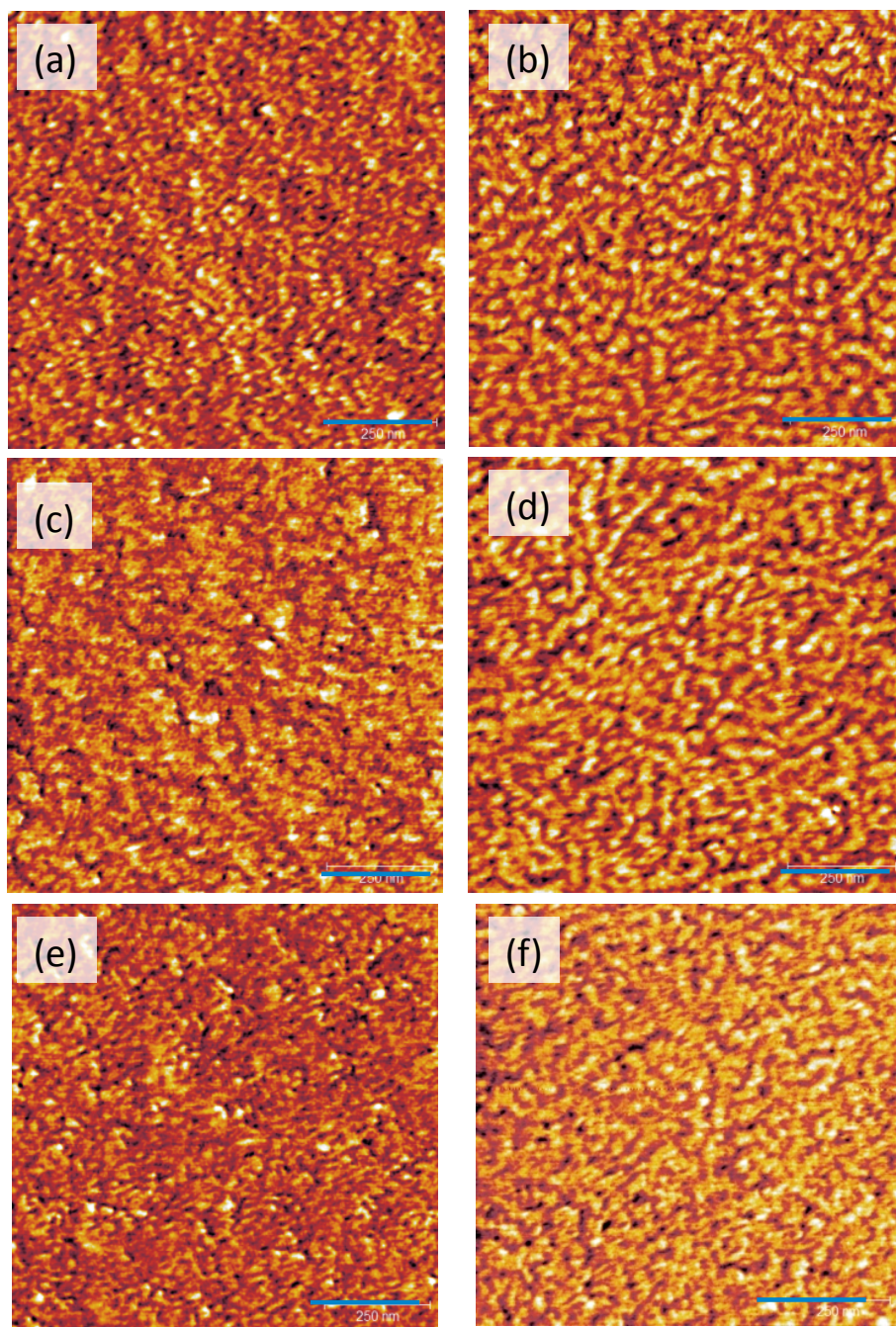


Figure 7:13: Tapping mode AFM phase images ($1 \mu\text{m}^2$) of PCDTBT:PC₇₀BM blend thin films left as-cast (left column) or after annealing at 180°C for 30 minutes (right column). The film compositions are 1:1 wt% (parts (a) and (b)), 1:2 wt% (parts (c) and (d)), 1:4 wt% (parts (e) and (f)). The scale bar in all images corresponds to 250 nm.

To identify a mechanism for the reduction in hole mobility in annealed PCDTBT:PC₇₀BM blend thin films, the nanoscale structure of annealed PCDTBT thin films was studied using GIWAXS. Specifically, the FWHM of the scattering ring at $q_z = 1.57\text{\AA}^{-1}$ (corresponding to scatter from the π - π stacking plane of the polymer, as shown in Figure 7.2) was used to calculate the coherence length of PCDTBT in thin films annealed at temperatures up to 250°C. The results are presented in Figure 7.14.

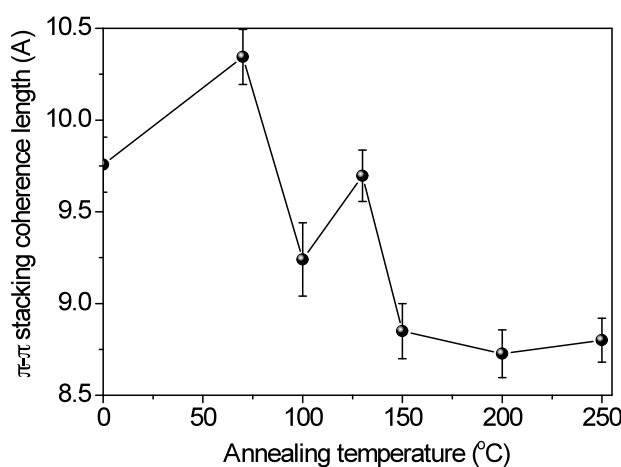


Figure 7.14: Coherence length of PCDTBT chains along the π - π stacking plane. Samples were measured after annealing at various temperatures for 30 minutes. Coherence length values were calculated from a line profile of a 2D GIWAXS image taken along an out-of-plane (normal to the substrate) direction.

As can be seen, a small increase in coherence occurs after annealing PCDTBT to 70°C. As this temperature is above the boiling point of the casting solvent used, it is possible that volume relaxation due to residual solvent loss explains this change. For PCDTBT thin films annealed at or above a temperature of 100°C the coherence length is reduced relative to the unannealed control. Similar results have been

reported by Beiley *et al.*²⁰ who studied a higher molecular weight batch of PCDTBT (120 kDa compared to the 33 kDa material used in this study). Both results suggest therefore that thermal annealing increases disorder in PCDTBT thin films. It is important to recognise however that both studies have examined thin films of pure PCDTBT, and thus the influence of PC₇₀BM in encouraging or inhibiting conformational changes in PCDTBT remains unknown. However, from Figure 7.9(b) it was shown that the T_g of PCDTBT in a blend film is reduced after heating, a result also found for a film of the pure polymer. Wang *et al.*²¹ have shown that for thin films of PCDTBT (below 80 nm) a depression in T_g relative to the bulk T_g value occurs. This observation was correlated with an increase in the relative volume fraction of a disordered surface layer as the film thickness was reduced. Thus the reduction in blend T_g upon annealing suggests a more disordered polymer phase in the blend films, behaviour which is not strongly influenced by PC₇₀BM concentration. This link may help to explain the decrease in hole mobility and power conversion efficiency measured for OPV devices as discussed previously.

SECTION 7.5 DETERMINING THE ONSET OF PC₇₀BM AGGREGATION IN PCDTBT:PC₇₀BM BLEND THIN FILMS

From Figure 7.13 it is apparent that the morphology of the PCDTBT:PC₇₀BM blends show a relatively high degree of thermal stability – the coarse phase separation (as seen in P3HT:PCBM blend thin films) is apparently suppressed in the samples measured here. To explore the conditions under which the aggregation of PC₇₀BM can occur, a combination of SE & GIWAXS was used to characterise thermally

annealed PCDTBT:PC₇₀BM blends; the results of which form the final part of this chapter.

Figure 7.15 shows the change in thickness of a PCDTBT:PC₇₀BM 1:4 wt% blend film determined using spectroscopic ellipsometry as a function of time during a thermal ramp from 25°C (a heating rate of 90°C/min was used here), and an isothermal soak. The normalised thickness is calculated in an identical manner to that used in Figure 4.10, where h & h_0 are the modeled thickness of the sample at a time t & t_0 respectively. Data is plotted for three different isothermal soak temperatures (130, 150 and 155°C), with part (a) focusing on the first 300s of the experiment, whilst part (b) plotting data recorded over the duration of the entire experiment (3,750s). Here, the return to room temperature can be seen at the end of the experiment. It can be seen in part (a) that the film undergoes a period of contraction in thickness after $t = 25$ s, corresponding to a temperature of 63°C; a temperature coincident with the boiling point of CHCl₃. During the isothermal soak, a slow reduction in the overall thickness of the film can be seen. This process has also been observed in P3HT:PCBM blend thin films as shown in section 5.2 Figure 5.2, and was ascribed to the process of volume relaxation. This process concludes when the system reaches an equilibrium state. It is apparent that the reduction of film thickness is initially relatively rapid, but then slows with a pseudo-plateau being reached. The time required to reach this pseudo-plateau is dependent on the annealing temperature and occurs more rapidly as the temperature is raised.

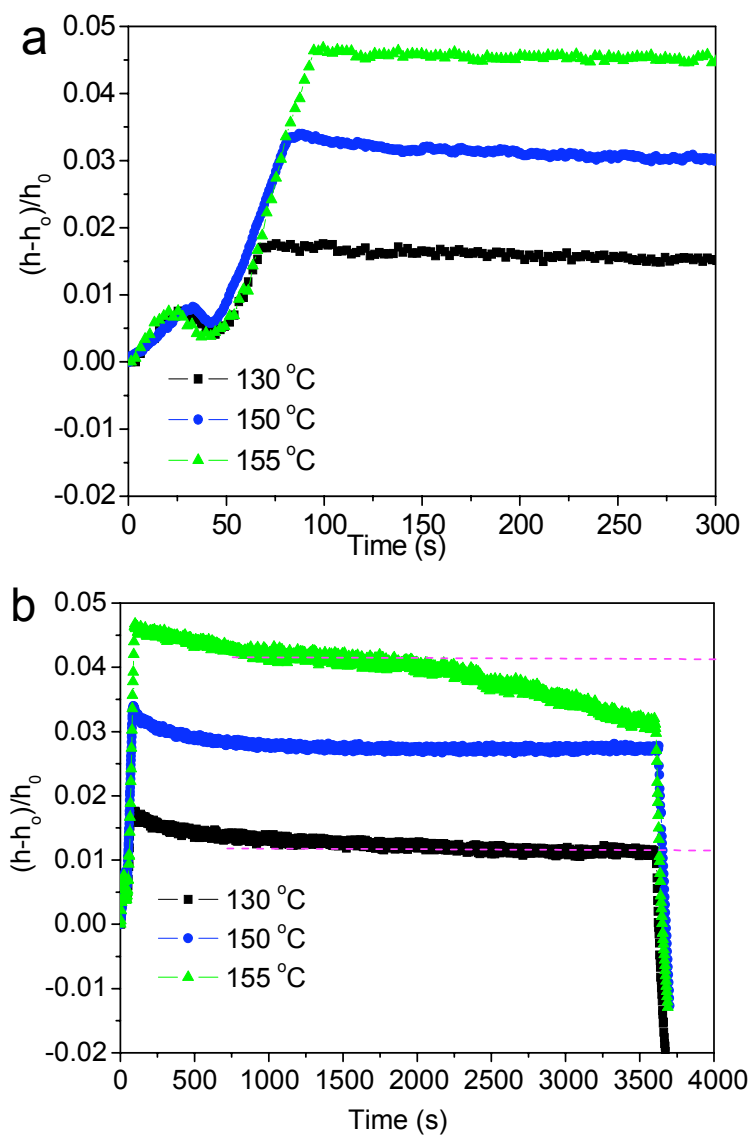


Figure 7.15: Thermal expansion changes for PCDTBT:PC₇₀BM (1:4 wt%) thin films during heating, isothermal annealing at 130°C, 150°C or 155°C and cooling. For all samples the heating rate was 90°C/min. The relative reduction in films thickness due to residual solvent loss is highlighted in part (a). Dashed lines in part (b) are a guide to the eye.

Turning to Figure 7.15(b), it can be seen that when the PCDTBT:PC₇₀BM blend film is annealed at 130 or 150°C, the pseudo-plateau that is established exists for the entire

duration of the annealing process. In contrast however, when a film is annealed at 155°C, there is an additional reduction in film thickness that occurs at a time $t > 2,100$ s. The measurements on P3HT:PCBM blends in chapter 5, section 5.2, demonstrated that this reduction in thickness was correlated with the coarse phase-separation of P3HT and PCBM. In particular, it was argued that the depletion of material from the bulk combined with the formation of micron-sized crystallites reduces the average film thickness and increases film roughness. As will be discussed, a very similar process occurs here. In Figure 7.16, a series of optical microscopy images of PCDTBT:PC₇₀BM blend films are presented. In part (a) the micrograph corresponds to an as-cast thin film, whilst parts (b), (c) and (d) show a similar film annealed at 130, 155 and 200°C for one hour respectively. It can be seen in Figure 4.16(b) that when films have been annealed at 130°C and cooled to room temperature, no apparent structure is observed (although structure may well be present at a length-scale below the resolution of the optical microscope). When however, the film is annealed at 155°C (Figure 4.16(c)), structures (assumed to be PC₇₀BM crystallites) are visible. Such structure becomes significantly coarser when films are annealed at 200°C (see Figure 4.16(d)). The correlation of the appearance of crystallisation in a film annealed at 155°C for one hour with the reduction in thickness shown in Figure 7.15(b) suggests that the onset temperature for this process is the solid-solid transition of PC₇₀BM determined via ellipsometry as shown in Figure 7.14(b). This solid-solid transition at roughly 155°C is likely to be the cold-crystallisation temperature of PC₇₀BM in the blends, suggesting that the cold-crystallisation of PC₇₀BM facilitates phase separation in the blends.

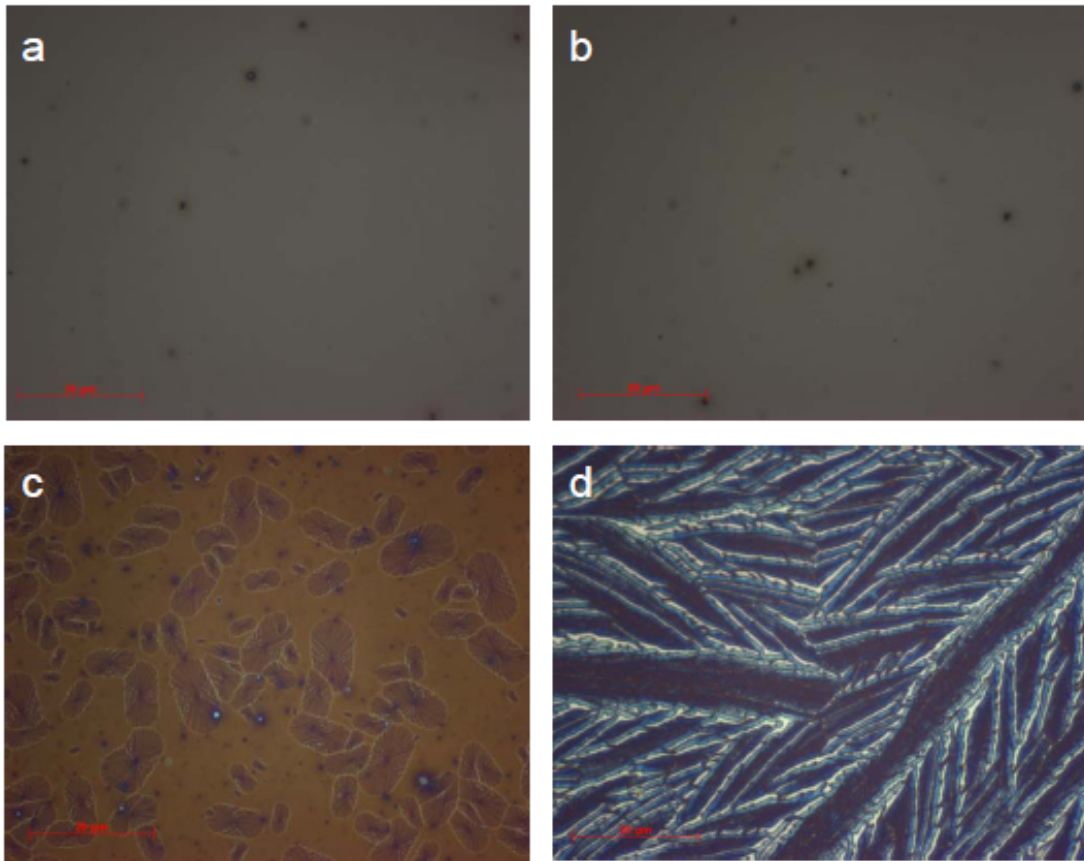


Figure 7.16: Optical micrographs of PCDTBT:PC₇₀BM (1:4 wt%) blend thin films cast on silicon/native oxide substrates left as-cast (a), or after thermal annealing at 130°C (b), 155°C (c) or 200°C (d) for one hour. The scale bar represents 20 μm.

To complement the ellipsometry studies, GIWAXS has been used to probe *ex-situ* changes in sample nanostructure that occur due to thermal annealing for a PCDTBT:PC₇₀BM (1:4) wt% blend thin film cast onto silicon/native oxide. These results are presented in Figure 7.17. In part (a), the scattering pattern for an as-cast film is shown. It can be seen that three distinct scattering rings are visible, having q_x values of 0.67, 1.36, and 2.0 Å⁻¹. These broad, diffuse rings suggest the presence of amorphous (nanoscale) PC₇₀BM domains^{5b}.

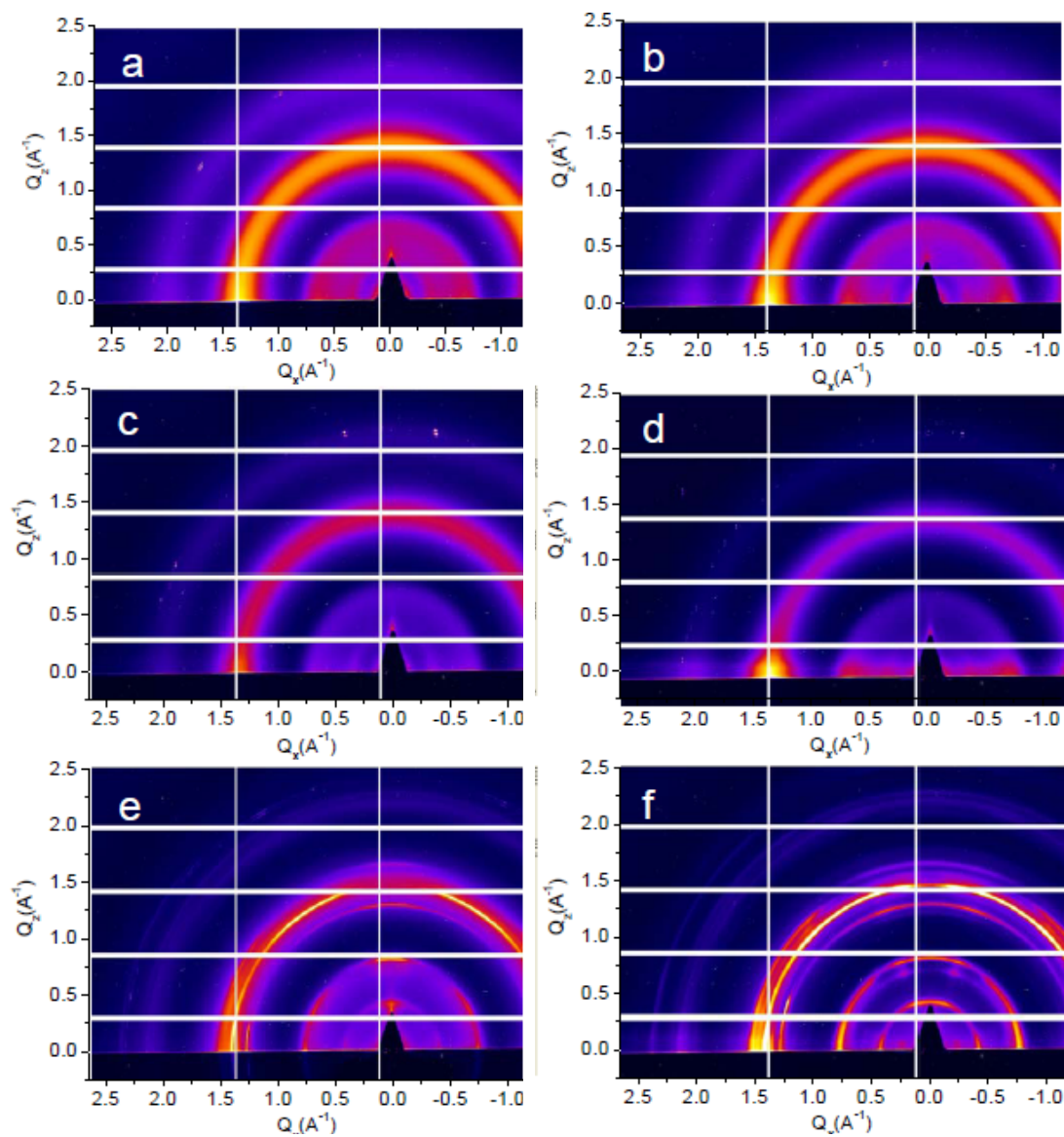


Figure 7.17: 2D-GIWAXS images of PCDTBT:PC₇₀BM (1:4 wt%) thin films cast onto silicon / native oxide substrates. Part (a) represents an as-cast film, with later parts corresponding to samples after thermal annealing at 70°C for 1 hr (b), 130°C for 1 hr (c), 155°C for 30 minutes (d), 155°C for 1 hr (e) and 200°C for 1 hr (f).

In Figure 7.17 parts (b), (c) and (d) scattering patterns for similar films that have been annealed at 70°C and 130°C for 1 hour, or 155°C for 30 minutes respectively are presented. In all cases the three rings remain relatively unchanged, indicating the

distribution of amorphous PC₇₀BM domains has not been changed significantly by the thermal treatments. To quantify this, Scherrer's equation²² (using a pre-factor of 0.9) is used to estimate the relative changes in the size of PC₇₀BM nanodomains in the blend thin film, using the full-width-at-half-maximum (FWHM) of the ring at $q = 1.36 \text{ \AA}^{-1}$. From the data presented in Figure 7.17, a characteristic length scale for PC₇₀BM nano-domains of 4.2 nm in the as-cast film and 4.6 nm in the films annealed at 130°C for 1 hour or 155°C for 30 minutes is obtained. This suggests that only a small increase (~10%) in size of the PC₇₀BM domains occurs after these thermal treatments.

In Figure 7.17(e) the scattering pattern of a blend film annealed at 155°C for 1 hour is presented. Here, a number of sharp rings are apparent that are identified as originating from polycrystalline PC₇₀BM. The number and relative intensity of the rings increases for a blend film annealed at 200°C for 1 hour as shown in Figure 7.17(f). These observations are again consistent with the SE and optical microscopy data, fully supporting the notion that partial crystallisation of PC₇₀BM only occurs when the film is annealed under these particular conditions.

From chapter 5, section 5.2, it was demonstrated that for a P3HT:PCBM blend (60:40 wt%) thin film annealed at 150°C, coarse phase-separation and crystallization of PCBM occurred after $t = 1000\text{s}$. From the SE data presented here, which is complimented by optical microscopy and GIWAXS measurements, it is apparent that coarse phase separation only occurs after a much longer anneal time (~2,100 s) and at a higher temperature. This may result from differences in the miscibility or diffusion

kinetics between P3HT and PCDTBT with PCBM or PC₇₀BM. It is important to also note that the glass transition temperature of P3HT (~50°C) in a blend film is at a much lower temperature relative to the isothermal annealing temperature used in the experiment (150°C) than the T_g of PCDTBT which is 130°C). It is therefore possible that when annealing a polymer:fullerene blend film at 150°C, P3HT chains may have a greater thermally-activated mobility than do PCDTBT chains, thus fullerene molecules diffuse more rapidly through the polymer matrix. Nevertheless, the delay in phase-separation and crystallisation of PC₇₀BM in PCDTBT is a further manifestation of a blend system that is thermally stable at temperatures in excess of that which would be experienced during the practical operation of an OPV cell.

SECTION 7.6: CONCLUSIONS

In this chapter I have explored some of the optical and structural properties of the polymer PCDTBT and its blends with PC₇₀BM in a thin film geometry. In contrast to blends of P3HT:PCBM which have been the focus of previous chapters, blends of PCDTBT:PC₇₀BM are apparently more efficient in photocurrent generation when devices are not subject to post deposition thermal treatments. From neutron reflectivity studies it was shown that optimised thin films exhibit an essentially ideal vertical distribution of acceptor material. Measurements of the relative photoluminescence emission from blends of different PC₇₀BM wt% showed that the quenching of emission from the polymer was significantly greater than in blends of P3HT:PCBM and, in another distinction to this system, photoluminescence emission from the fullerene and not the polymer is a small loss mechanism in optimised OPVs.

An important finding discussed in chapter 6 was how the apparent T_g of a P3HT:PCBM blend film during first heating provided a strong indication of the thermal annealing temperatures required to modify film structure. Whereas the T_g of P3HT was found to be sensitive to PCBM content, here the T_g of PCDTBT remains relatively stable, even at 80wt% PC₇₀BM, a finding that is also a further manifestation of the high degree of miscibility between these materials. Exceeding the T_g of a blend during a thermal annealing process is found to reduce hole mobility within the active layer of a device; an effect that is correlated with the onset of increased disorder in thermally annealed thin films of pure PCDTBT. Thus annealing protocols designed for P3HT:PCBM blends are not apparently applicable in PCDTBT:PC₇₀BM blends, however annealing above the boiling point of the casting solvent (for thin films cast from CHCl₃) but below T_g may offer a marginal benefit. Although thermal annealing has been shown to negatively impact upon device performance, the measurements have shown that the PCDTBT:PC₇₀BM blends have thermal stability beyond that of optimised P3HT:PCBM systems. It is likely therefore that the relative ease with which high efficiencies can be achieved, in addition to the enhanced morphological stability will make PCDTBT:PC₇₀BM blends a promising system with which to explore the scale up of organic photovoltaics.

SECTION 7.7: REFERENCES

1. Wang, T., Pearson, A.J., Dunbar, A.D.F., Staniec, P.A., Watters, D.C., Yi, H., Ryan, A.J., Jones, R.A.L., Iraqi, A., Lidzey, D.G. , Correlating Structure with Function in Thermally-Annealed PCDTBT:PC₇₀BM Photovoltaic Blends. *Advanced Functional Materials* **2012** (Accepted).

2. Chu, T. Y.; Alem, S.; Tsang, S. W.; Tse, S. C.; Wakim, S.; Lu, J. P.; Dennler, G.; Waller, D.; Gaudiana, R.; Tao, Y., Morphology control in polycarbazole based bulk heterojunction solar cells and its impact on device performance. *Applied Physics Letters* **2011**, *98* (25).
3. (a) Etzold, F.; Howard, I. A.; Mauer, R.; Meister, M.; Kim, T. D.; Lee, K. S.; Baek, N. S.; Laquai, F., Ultrafast Exciton Dissociation Followed by Nongeminate Charge Recombination in PCDTBT:PCBM Photovoltaic Blends. *Journal of the American Chemical Society* **2011**, *133* (24), 9469-9479; (b) Banerji, N.; Cowan, S.; Leclerc, M.; Vauthey, E.; Heeger, A. J., Exciton Formation, Relaxation, and Decay in PCDTBT. *Journal of the American Chemical Society* **2010**, *132* (49), 17459-17470.
4. Yi, H. N.; Al-Faifi, S.; Iraqi, A.; Watters, D. C.; Kingsley, J.; Lidzey, D. G., Carbazole and thienyl benzo[1,2,5]thiadiazole based polymers with improved open circuit voltages and processability for application in solar cells. *Journal of Materials Chemistry* **2011**, *21* (35), 13649-13656.
5. (a) Blouin, N.; Michaud, A.; Gendron, D.; Wakim, S.; Blair, E.; Neagu-Plesu, R.; Belletete, M.; Durocher, G.; Tao, Y.; Leclerc, M., Toward a rational design of poly(2,7-carbazole) derivatives for solar cells. *Journal of the American Chemical Society* **2008**, *130* (2), 732-742; (b) Staniec, P. A.; Parnell, A. J.; Dunbar, A. D. F.; Yi, H. N.; Pearson, A. J.; Wang, T.; Hopkinson, P. E.; Kinane, C.; Dalgliesh, R. M.; Donald, A. M.; Ryan, A. J.; Iraqi, A.; Jones, R. A. L.; Lidzey, D. G., The Nanoscale Morphology of a PCDTBT: PCBM Photovoltaic Blend. *Advanced Energy Materials* **2011**, *1* (4), 499-504.
6. Wienk, M. M.; Kroon, J. M.; Verhees, W. J. H.; Knol, J.; Hummelen, J. C.; van Hal, P. A.; Janssen, R. A. J., Efficient methano[70]fullerene/MDMO-PPV bulk

heterojunction photovoltaic cells. *Angewandte Chemie-International Edition* **2003**, *42* (29), 3371-3375.

7. Cates, N. C.; Gysel, R.; Beiley, Z.; Miller, C. E.; Toney, M. F.; Heeney, M.; McCulloch, I.; McGehee, M. D., Tuning the Properties of Polymer Bulk Heterojunction Solar Cells by Adjusting Fullerene Size to Control Intercalation. *Nano Letters* **2009**, *9* (12), 4153-4157.

8. Mayer, A. C.; Toney, M. F.; Scully, S. R.; Rivnay, J.; Brabec, C. J.; Scharber, M.; Koppe, M.; Heeney, M.; McCulloch, I.; McGehee, M. D., Bimolecular Crystals of Fullerenes in Conjugated Polymers and the Implications of Molecular Mixing for Solar Cells. *Advanced Functional Materials* **2009**, *19* (8), 1173-1179.

9. Morana, M.; Azimi, H.; Dennler, G.; Egelhaaf, H. J.; Scharber, M.; Forberich, K.; Hauch, J.; Gaudiana, R.; Waller, D.; Zhu, Z. H.; Hingerl, K.; van Bavel, S. S.; Loos, J.; Brabec, C. J., Nanomorphology and Charge Generation in Bulk Heterojunctions Based on Low-Bandgap Dithiophene Polymers with Different Bridging Atoms. *Advanced Functional Materials* **2010**, *20* (7), 1180-1188.

10. Cook, S.; Furube, A.; Katoh, R.; Han, L. Y., Estimate of singlet diffusion lengths in PCBM films by time-resolved emission studies. *Chemical Physics Letters* **2009**, *478* (1-3), 33-36.

11. (a) Park, S. H.; Roy, A.; Beaupre, S.; Cho, S.; Coates, N.; Moon, J. S.; Moses, D.; Leclerc, M.; Lee, K.; Heeger, A. J., Bulk heterojunction solar cells with internal quantum efficiency approaching 100%. *Nat. Photonics* **2009**, *3* (5), 297-U5; (b) Wakim, S.; Beaupre, S.; Blouin, N.; Aich, B. R.; Rodman, S.; Gaudiana, R.; Tao, Y.; Leclerc, M., Highly efficient organic solar cells based on a poly(2,7-carbazole) derivative. *Journal of Materials Chemistry* **2009**, *19* (30), 5351-5358.

12. Seo, J. H.; Cho, S.; Leclerc, M.; Heeger, A. J., Energy level alignments at poly[N-9'-hepta-decanyl-2,7-carbazole-alt-5,5-(4',7'-di-2-thienyl-2',1',3'-benzothiadiazole)] on metal and polymer interfaces. *Chemical Physics Letters* **2011**, *503* (1-3), 101-104.
13. Cates, N. C.; Gysel, R.; Dahl, J. E. P.; Sellinger, A.; McGehee, M. D., Effects of Intercalation on the Hole Mobility of Amorphous Semiconducting Polymer Blends. *Chemistry of Materials* **2010**, *22* (11), 3543-3548.
14. Cho, S.; Seo, J. H.; Park, S. H.; Beaupre, S.; Leclerc, M.; Heeger, A. J., A Thermally Stable Semiconducting Polymer. *Advanced Materials* **2010**, *22* (11), 1253-1258.
15. Alem, S.; Chu, T. Y.; Tse, S. C.; Wakim, S.; Lu, J. P.; Movileanu, R.; Tao, Y.; Belanger, F.; Desilets, D.; Beaupre, S.; Leclerc, M.; Rodman, S.; Waller, D.; Gaudiana, R., Effect of mixed solvents on PCDTBT:PC(70)BM based solar cells. *Org. Electron.* **2011**, *12* (11), 1788-1793.
16. Ruoff, R. S.; Tse, D. S.; Malhotra, R.; Lorents, D. C., Solubility of C-60 in a Variety of Solvents. *J Phys Chem-US* **1993**, *97* (13), 3379-3383.
17. Parnell, A. J.; Dunbar, A. D.; Pearson, A. J.; Staniec, P. A.; Dennison, A. J.; Hamamatsu, H.; Skoda, M. W.; Lidzey, D. G.; Jones, R. A., Depletion of PCBM at the cathode interface in P3HT/PCBM thin films as quantified via neutron reflectivity measurements. *Advanced Materials* **2010**, *22* (22), 2444-2447.
18. Muller, C.; Bergqvist, J.; Vandewal, K.; Tvingstedt, K.; Anselmo, A. S.; Magnusson, R.; Alonso, M. I.; Moons, E.; Arwin, H.; Campoy-Quiles, M.; Inganäs, O., Phase behaviour of liquid-crystalline polymer/fullerene organic photovoltaic blends: thermal stability and miscibility. *Journal of Materials Chemistry* **2011**, *21* (29), 10676-10684.

19. Hopkinson, P. E.; Staniec, P. A.; Pearson, A. J.; Dunbar, A. D. F.; Wang, T.; Ryan, A. J.; Jones, R. A. L.; Lidzey, D. G.; Donald, A. M., A Phase Diagram of the P3HT:PCBM Organic Photovoltaic System: Implications for Device Processing and Performance. *Macromolecules* **2011**, *44* (8), 2908-2917.
20. Bailey, Z. M.; Hoke, E. T.; Noriega, R.; Dacuna, J.; Burkhard, G. F.; Bartelt, J. A.; Salleo, A.; Toney, M. F.; McGehee, M. D., Morphology-Dependent Trap Formation in High Performance Polymer Bulk Heterojunction Solar Cells. *Advanced Energy Materials* **2011**, *1* (5), 954-962.
21. Wang, T., Pearson, A.J., Dunbar, A.D.F., Staniec, P.A., Watters, D.C., Yi, H., Lidzey, D.G., Jones, R.A.L., Competition between substrate-mediated π - π stacking and surface mediated disorder in conjugated polymer ultrathin films **2012** (submitted).
22. Patterson, A. L., The Scherrer formula for x-ray particle size determination. *Phys Rev* **1939**, *56* (10), 978-982.

CHAPTER 8: IMAGING THE NANOSCALE MORPHOLOGY OF SOLAR CELL BLENDS USING HELIUM ION MICROSCOPY

SECTION 8.1: INTRODUCTION

In this chapter the use of Helium Ion Microscopy (HeIM) is evaluated for imaging the nanoscale structures present in bulk-heterojunction organic photovoltaic blend thin films ¹. As discussed in chapter 2 section 2.6, bulk-heterojunction thin films have been commonly described with the aid of cartoons depicting an interpenetrating network between donor and acceptor materials. In early OPV research these polymer:fullerene blends networks could be resolved with relative clarity as the length scale for phase separation was far greater than the resolution of the imaging technique ². However, the realisation and confirmation that optimised networks must be on a length scale commensurate with the exciton diffusion length in the materials used has led to only a few high-resolution microscopy techniques being adequate to image the structures present ³. To resolve structure in organic semiconductor thin film blends at a length-scale of ~10 nm is a technical challenge, however such information may assist the development of bulk heterojunction (BHJ) OPVs having improved efficiency.

In this work, it is demonstrated that HeIM can be used to map the nanoscale distribution of materials in a thin film of a P3HT:PCBM blend. It is also shown that

buried structures within the film are accessible by using a plasma treatment to selectively remove surface material. Section 8.2 considers whether contrast variations in the images obtained from the HeIM reflect the probable chemical structure of a sample, or whether other factors adversely influence the measurement. Here the test sample is a blend thin film of P3HT:PCBM, subject to a thermal anneal prior to measurement. Additionally, blend thin films subject to different processing routes and films of the pure components are used as controls. It is shown that the apparent structures observed from the annealed blend sample are not seen in any of the control films. Also, the lack of correlation between surface topography and secondary electron yield suggest that the HeIM is capable of imaging the nanoscale variations in chemical structure (i.e. differentiating P3HT from PCBM).

Section 8.3 looks at the information that can be obtained quantitatively regarding a sample using HeIM. Although it is relatively straightforward to calculate the spatial periodicities present in an image, the nature of the blend samples do not allow an unambiguous measurement of the PCBM domain size to be calculated. Nevertheless, a conservative estimate of the PCBM domain size is in good agreement with X-ray scattering studies on this system. Overall the study suggests that HeIM is a promising instrument to compliment other techniques that can be used to characterise structure in conjugated polymer:fullerene blend thin films.

HeIM images were taken by Dr Stuart Boden at the University of Southampton on samples prepared by myself. AFM measurements and analysis of the HeIM data was

carried out by myself. I am grateful to Dr Cornealia Rodenburg for imaging my samples using SEM, as presented in section 8.3.

SECTION 8.2: IDENTIFYING THE ORIGIN OF CONTRAST IN HEIM IMAGES

As discussed in chapter 3, section 3.4.6, the HeIM can produce an image via generating secondary electron emission from a sample surface, generated due to the impact of He ions. The escape depth of secondary electrons is estimated to be $\sim 3\text{nm}$ for the samples investigated here⁴. The secondary electron emission from thin films of as-cast P3HT and PCBM is considered first. In Figure 8.1, a $1500 \times 1500 \text{ nm}^2$ HeIM scan of pure P3HT (part (a)) and PCBM (part (b)) thin films is presented. These images were acquired under identical imaging conditions with no plasma treatment or image processing applied. It can be seen that the image corresponding to a P3HT film appears relatively brighter than that of PCBM. This is confirmed quantitatively by the histogram distribution of grey levels for each image, presented in Figure 8.1(c). Included alongside is the grey level distribution for a beam-blanked image. This demonstrates that both films appear brighter than the measured background signal and that P3HT appears brighter (average grey level of 191) than PCBM (average grey level of 75) when identical microscope brightness and contrast settings are used. These observations are consistent with the work of Kishimoto *et al.* who observed that the efficiency of secondary electron emission is linked to the ratio of π - bonds to the sum of π - and σ - bonds in a molecule⁵. In particular it was observed that materials with a high proportion of π electrons emit a smaller number of

secondary electrons than those with a smaller fraction of π electrons and would therefore appear darker in an HeIM image.

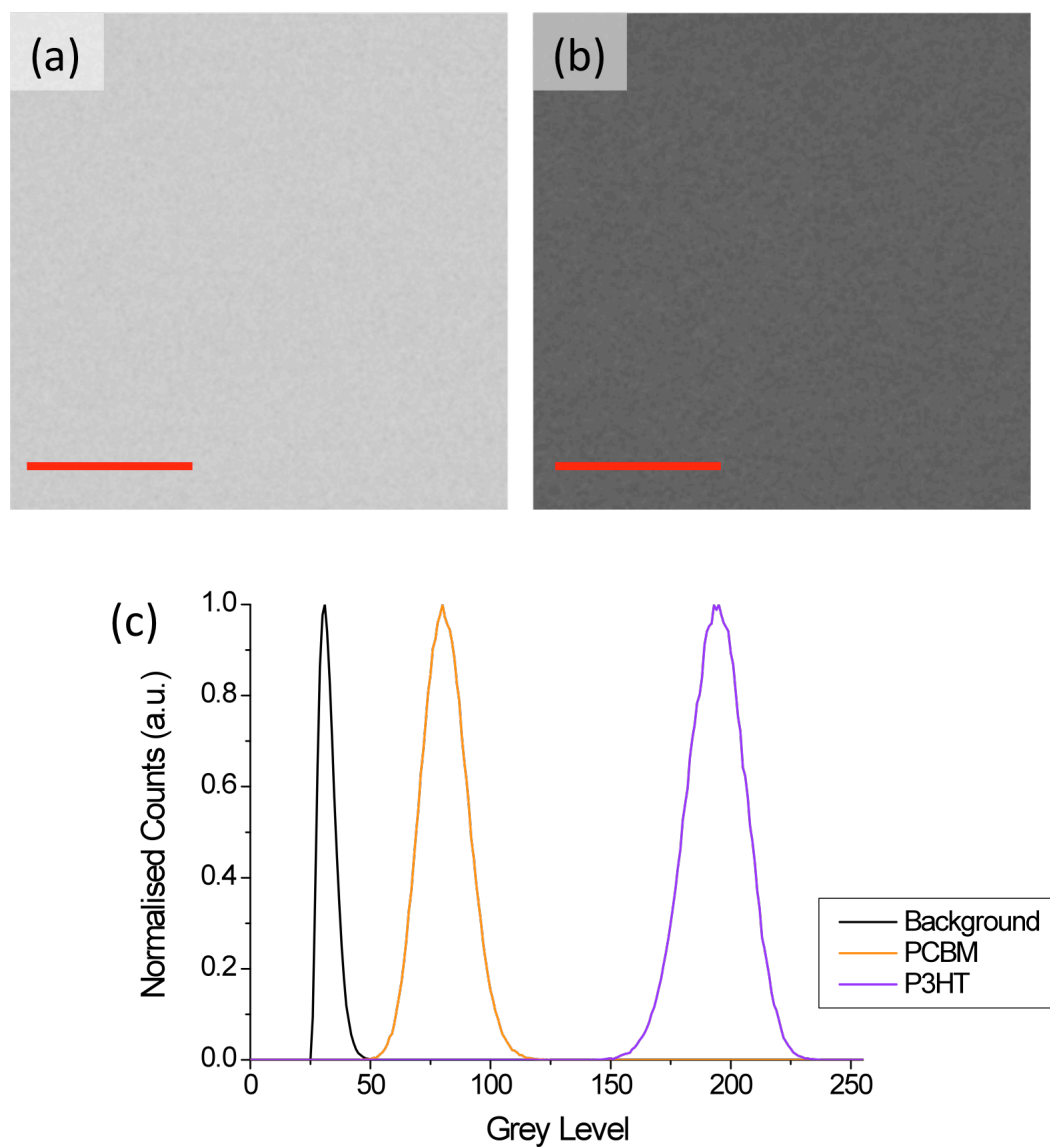


Figure 8.1: Parts (a) and (b) present low magnification HeIM images of as-cast films of P3HT and PCBM respectively prior to plasma cleaning. The scale bar represents 500 nm. Normalised grey level distributions of each sample are presented in part (c) alongside the measured background signal from a beam-blanked PCBM thin film.

In Figure 8.2 a series (parts (a) to (d)) of HeIM images are presented from P3HT:PCBM blend (60:40 by wt%) thin films having a thickness of 74 ± 2 nm. In parts (e) and (f) control images of pure PCBM and P3HT thin films are shown respectively. Prior to imaging, films shown in parts (a) to (c) were annealed at 140°C for 10 minutes in nitrogen. The annealing protocol used in this work is within the range commonly used to fabricate efficient P3HT:PCBM OPVs. As discussed in chapters 4 to 6, this step promotes phase separation between P3HT and PCBM, leading to the formation of apparently semi-crystalline nanoscale domains of these materials. All films were also subjected to a plasma etching process that was applied for a range of different times. Images shown in Figure 8.2(a) and 8.2(b) correspond to samples being exposed to the plasma etch for 3 and 6 minutes respectively, whilst films presented in Figure 8.2 parts (c) to (f) were plasma etched for 14 minutes.

As shown in Figure 8.2(a), the annealed P3HT:PCBM blend does not initially show any evidence of a phase-separated domain structure. It is possible that this may reflect the existence of a 1 – 2 nm thick P3HT wetting layer located at the film surface⁶ that is believed to exist even after a thermal annealing step which encourages PCBM migration to the surface⁷. It is also important to acknowledge that prior to imaging, all samples were briefly exposed to air and that HeIM imaging is not conducted under ultra-high vacuum. The absence of any spatial variations in contrast from the annealed film may therefore arise from a combination of vertical stratification of P3HT and the presence of surface contaminants. Previous imaging of a 20 nm thick P3HT:PCBM film using energy filtered transmission electron microscopy (EFTEM) was also unable to provide images of nanoscale phase separation, with structure only being observable in films whose thickness exceeded 100 nm⁸.

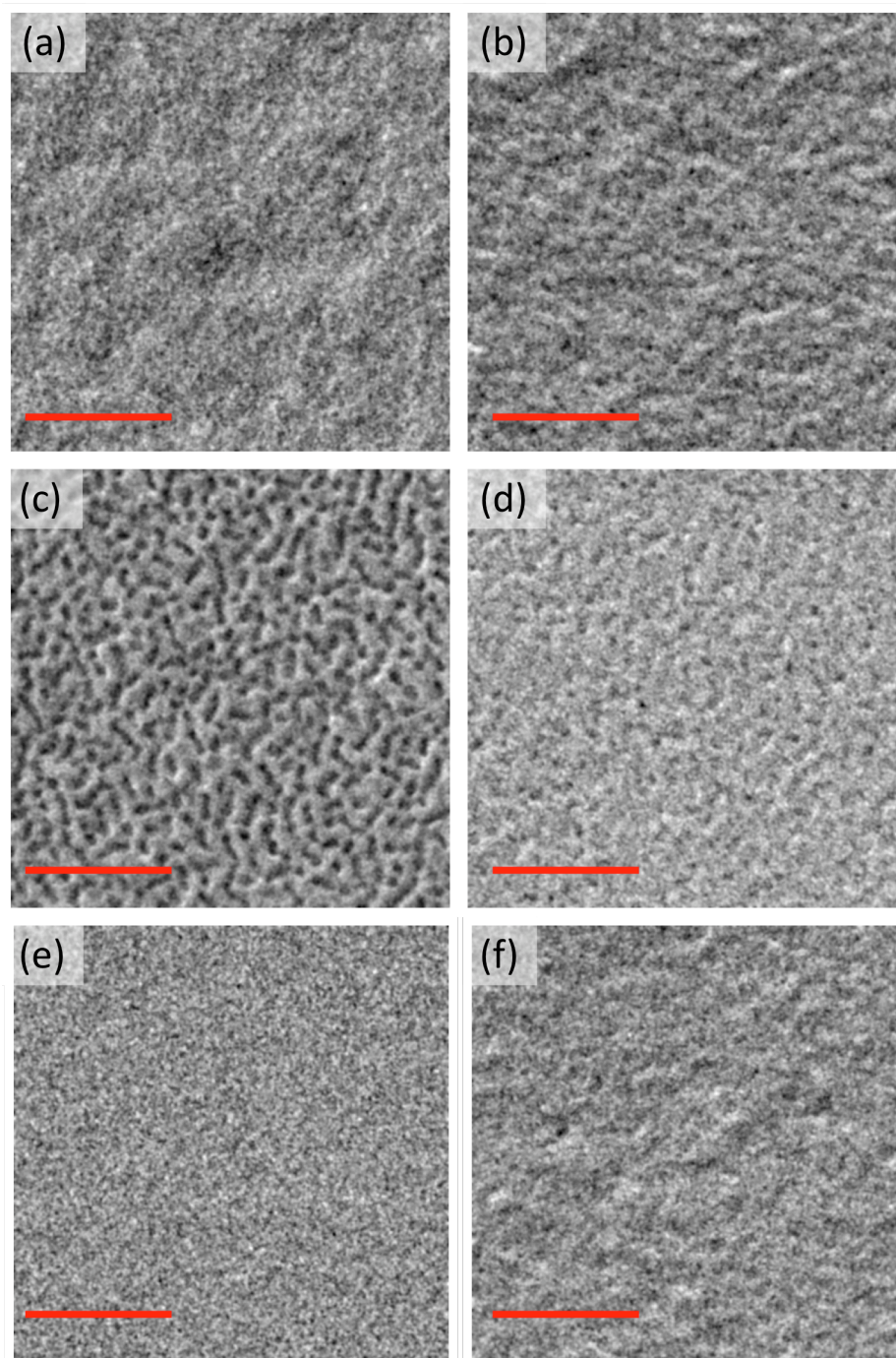


Figure 8.2: HeIM images of an annealed P3HT:PCBM blend thin film subject to plasma cleaning for a period of (a) 3 minutes, (b) 6 minutes and (c) 14 minutes. The scale bar represents 150 nm. A thin film of as-cast (unannealed) P3HT:PCBM, subject to 14 minutes plasma cleaning is presented in part (d). Thin films of PCBM and P3HT imaged at the same magnification as the blends after subject to plasma etching for 14 minutes are presented in parts (e) and (f) respectively.

To determine whether a phase-separated domain structure exists within the bulk of the films, a plasma-etching treatment was used to selectively remove material from the film surface. The effect of the plasma treatment is immediately apparent as shown in Figures 8.2 parts (b) and (c), where a distribution of bright and dark regions is observed. This is in direct contrast to the image presented in Figure 8.2(a) of an otherwise identical film that was only subjected to a short (3 minutes) plasma etch. Using atomic force microscopy (AFM) to measure the thickness of an etched sample and a control sample not subject to etching, it was determined that the 14 minute etch process removed the top 26 ± 4 nm of the film.

A consequence of the plasma etch is to increase the RMS surface roughness of the P3HT:PCBM blend film (as measured by AFM) from 0.7 to 1.5 nm. It is expected that surface topography can influence secondary electron emission yield from an otherwise chemically homogeneous sample. For example, secondary electron yields will be higher from prominent features on the sample surface, as relative less material is in the surrounding area to potentially attenuate secondary electron emission. For depressed features the opposite will occur. To determine whether the image in Figure 8.2(c) derives from spatial variations in the chemical composition of the blend film, or if it simply reflects variations in surface height resulting from the plasma treatment, images of an annealed (Figure 8.2(c)) and an unannealed (Figure 8.2(d)) P3HT:PCBM blend film are compared with films of pure PCBM and P3HT (Figures 8.2(e) and (f) respectively). Despite all samples undergoing the same plasma etch process, it can be seen that the corrugated surface observed in Figure 8.2(c) (annealed P3HT:PCBM blend) is not observed in either the unannealed blend or in the control P3HT and PCBM films, suggesting that the nanoscale variations in secondary

electron emission observed from the annealed blend appear to be intrinsic. For the unannealed blend thin film, the lack of any prominent nanoscale structure most likely results from the presence of a molecularly mixed morphology. Here, the rapid drying time of films cast from a volatile solvent (chlorobenzene) limits the time available for phase separation. It is possible that during the course of image acquisition, sputter or radiolytic damage by incident He ions may occur. To test the repeatability of the measurements, the image acquisition process was repeated for a P3HT:PCBM blend thin film, with results in Figure 8.3. As can be seen from the line profiles, acquired over an identical area in each scan, the distribution and relative intensity of grey levels appears to be consistent, in spite of the slightly increased average intensity that may be indicative of damage. To minimise errors as a result of changes in average intensity, images used for analysis were always collected from a first scan. In addition, auto scaling was used during the image analysis to avoid any influence of any average intensity variations between experiments.

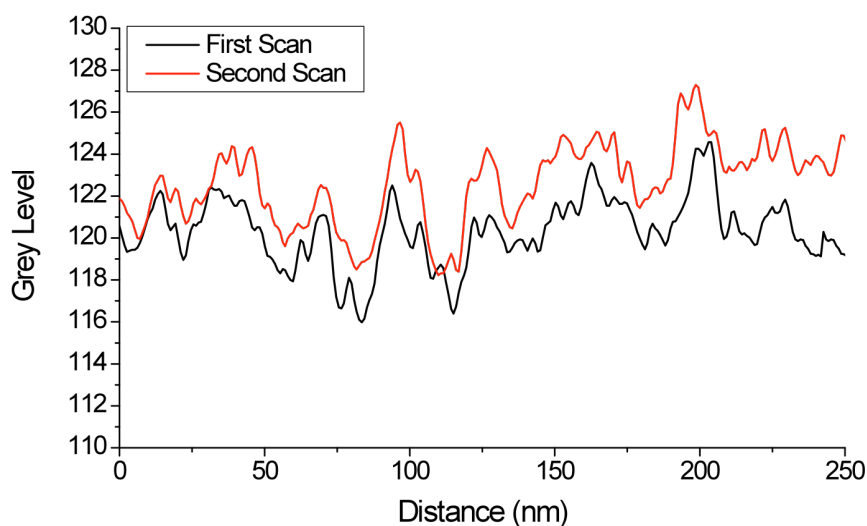


Figure 8.3: Line profiles extracted from HeIM images of a P3HT:PCBM annealed blend thin film. Images were acquired in succession and under identical imaging conditions.

To explore further the extent to which variations in the secondary emission yield of the annealed P3HT:PCBM sample results from differences in chemical composition and not as a result of surface topography, the spatial periodicities present in the HeIM image are compared to AFM tapping-mode scans of the same sample recorded over a comparable scan area. This data is presented in Figure 8.4. In Figure 8.4(a), line profiles taken from an HeIM image averaged over 10 pixels (20 nm) perpendicular to the profile axis show grey level (secondary electron) variations that have a much higher spatial frequency than variations in height as inferred using AFM as shown in Figure 8.4(b). This does not result from the limited lateral resolution of the AFM tip, as phase imaging using the same setup shows that finer features can still be resolved (see Figure 8.4(c)). The absence of a correlation between height variations seen in AFM and features seen in the HeIM image is interpreted as evidence that the HeIM images most likely derive from variations in the chemical structure of the film and that variations in surface topography have a minimal influence. From the results presented in Figures 8.1(b) and (c), the relatively bright areas observed in Figure 8.2(c) are tentatively ascribed to regions rich in P3HT, with areas that are relatively dark to domains predominantly composed of PCBM, with phase separation between the materials occurring as a consequence of the thermal annealing process.

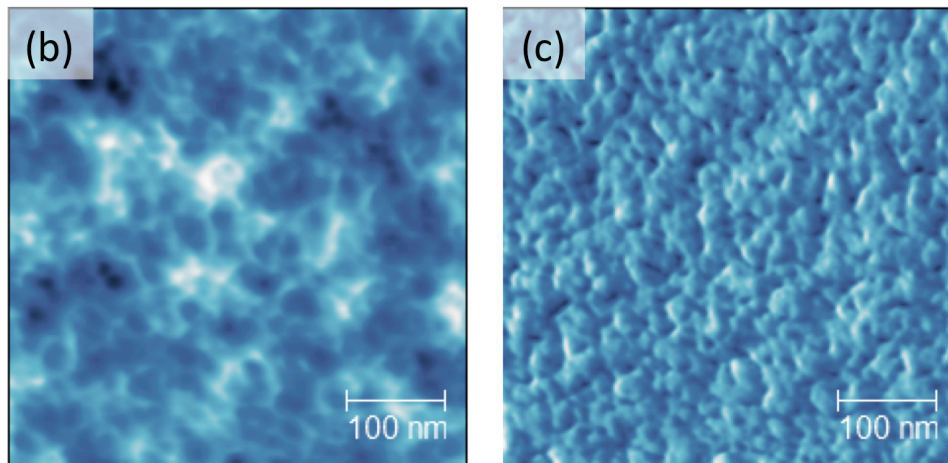
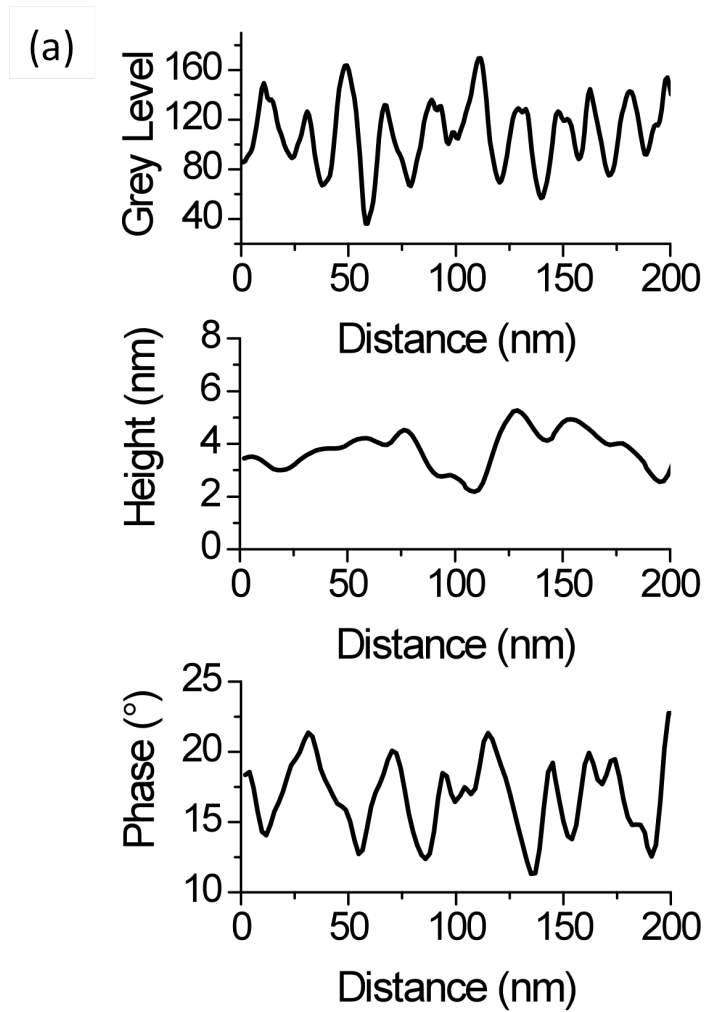


Figure 8.4: (a) Line profiles of the HeIM image (top), AFM height (middle) and AFM phase (bottom) images, illustrating the differences in spatial periodicity measured by the three techniques. AFM height (b) and phase (c) images of the annealed P3HT:PCBM blend thin film after 14 minutes of plasma etching. The colour scale in (b) is 10 nm.

SECTION 8.3: CALCULATING THE DOMAIN SIZE IN P3HT:PCBM BLEND THIN FILMS FROM HEIM MEASUREMENTS

The spatial periodicities present in the annealed blend thin film are estimated by calculating the power spectral density (PSD) and autocorrelation function (ACF)⁹ of the image data shown in Figures 8.2 parts (c) and (d), as presented in Figure 8.5. Note that a line profile of raw ACF or PSD image data presumes that there is a preferential direction of domains along that direction in order for the results to be considered representative. It is not possible to make such assumptions based upon the data used in this work alone, instead a radial average of the 2D ACF and PSD data is considered. As presented in Figure 8.5, both methods suggest a prominent periodicity of 20 ± 4 nm for the annealed blend sample. From the ACF data, this value originates from the position of the first peak away from the origin, thus representing a measure of the average distance between domain centres. In comparison the data corresponding to the unannealed sample (Figure 8.2(d)) does not exhibit a clear periodicity, in line with expectations. It is apparent therefore that an interface between P3HT and PCBM rich regions can be found within ~ 10 nm of any location of the sample area. Although it is not possible to directly compare the apparent domain size in this sample with other studies due to differences in sample preparation history, a number of small-angle X-ray scattering studies have determined a domain size of 8 to 18 nm in P3HT:PCBM blends with 40 to 50 wt% PCBM annealed at temperatures between 140°C and 150°C ¹⁰; a result in very good agreement with the value obtained here.

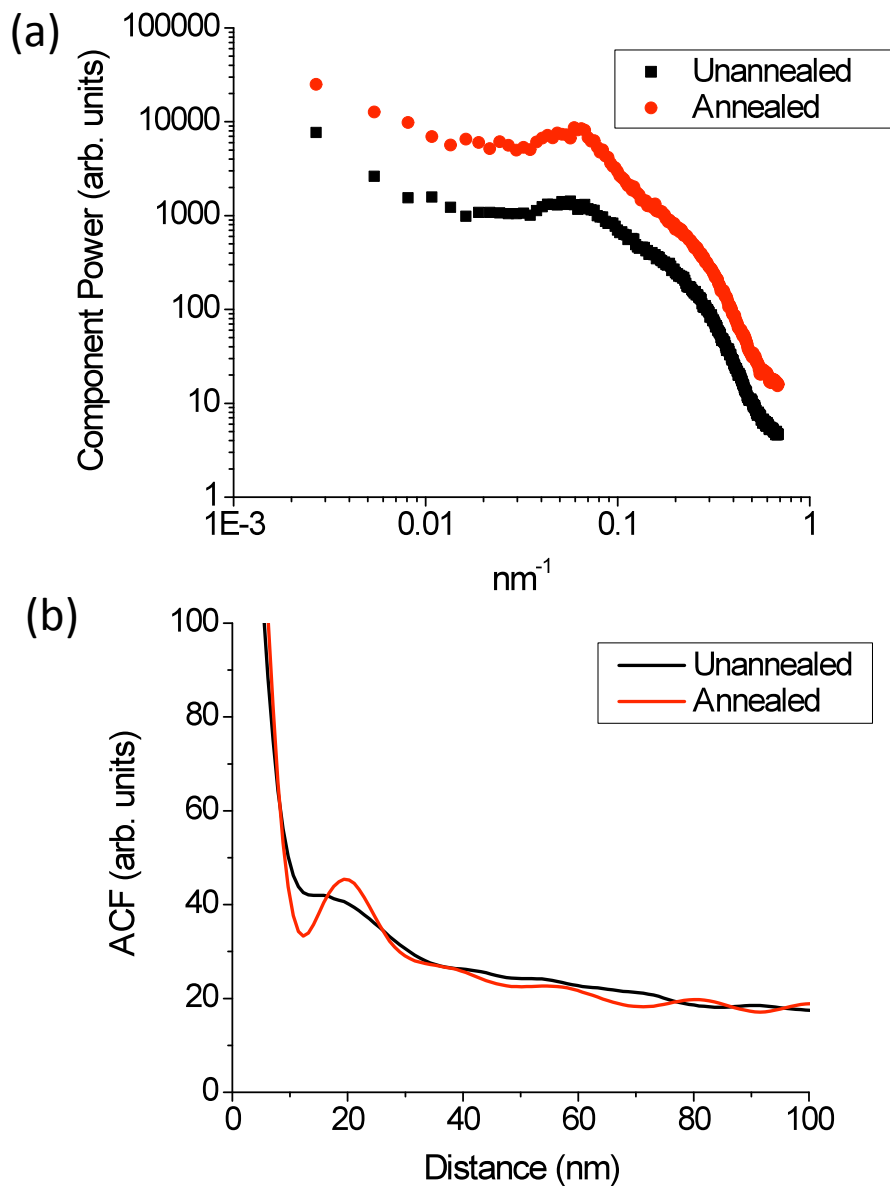


Figure 8.5: Power spectral density (a) and autocorrelation functions (b) of the annealed and untreated sample images presented in Figures 8.2 parts (c) and (d) respectively.

To determine whether the size of PCBM domains can be inferred from secondary electron emission, the autoscaled grey level distributions obtained from the HeIM images are considered and are presented in Figure 8.6. In Figure 8.6(a), histograms of the grey level distribution of the annealed and as-cast blend thin films are shown

using data extracted from the images presented in Figures 8.2 parts (c) and (d) respectively. It can be seen that the distribution of grey levels from the annealed sample is bi-modal, whereas an approximately normal distribution is found in the unannealed sample. The observation of a normal distribution of grey-levels is also found in films of the pure components as shown in Figure 8.6(b). This observation suggests a normal distribution of grey levels in the HeIM images corresponds to a chemically homogenous sample, or one in which any phase separation occurs at a length-scale below the resolution of the instrument. As shown in Figure 8.6(c), data from the annealed sample can be deconvoluted into two peaks, the smaller of which comprises 18% of the distribution area. As this peak is located towards the low end of the greyscale (thus corresponding to areas of a sample with relatively low secondary electron emission), it most likely reflects the presence of regions of pure or almost pure PCBM in the HeIM image.

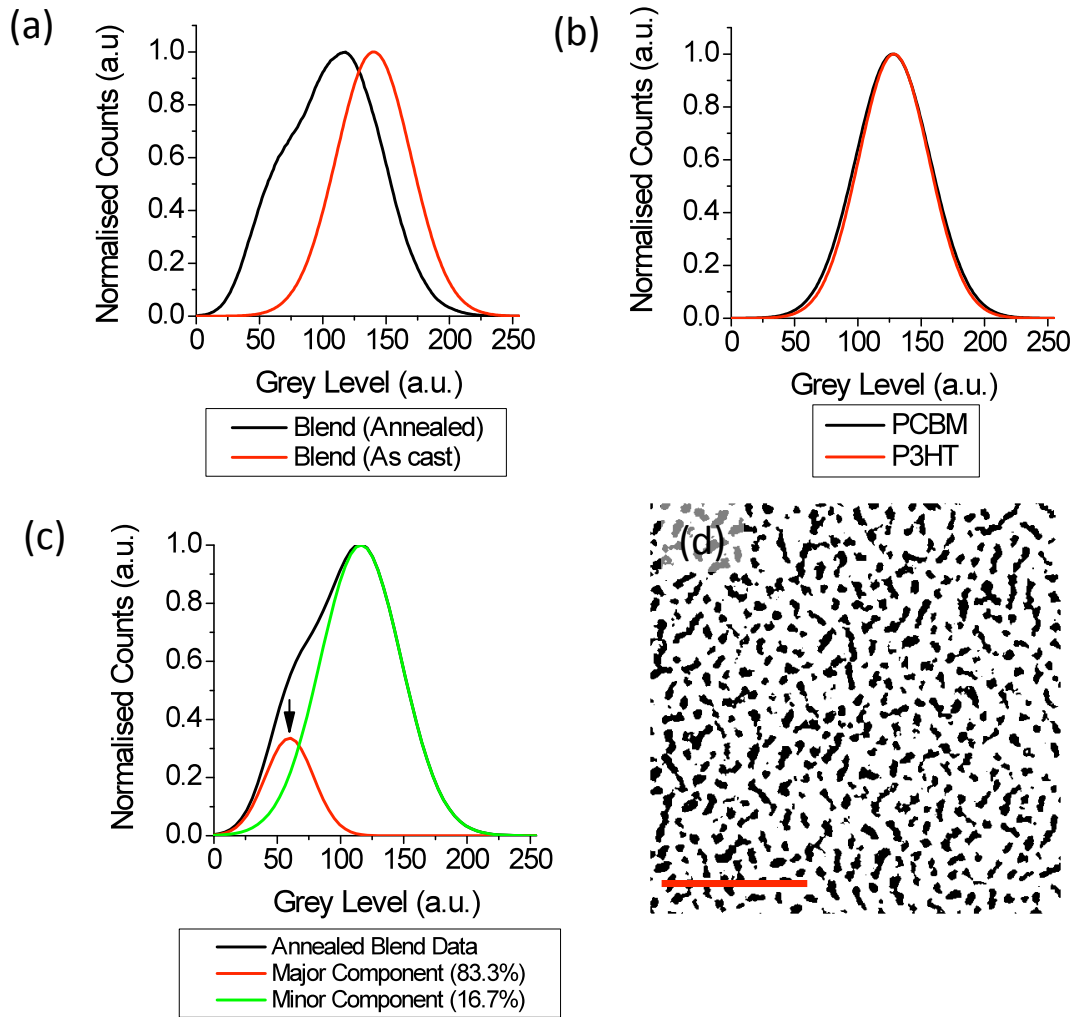


Figure 8.6: Part (a) shows grey level distributions of the annealed and as-cast blend samples, with part (b) showing grey-level distributions for the pure P3HT and PCBM films. Part (c) shows a fit of the annealed sample data shown in part (a) to two Gaussian functions. Here, a threshold level defined using an arrow is used to create a threshold image as shown in part (d). Black areas in the threshold image are attributed to PCBM rich regions. The scale bar represents 150 nm.

The densities of P3HT and PCBM are estimated to be 1.1 g cm^{-3} and 1.5 g cm^{-3} respectively¹¹. Thus a film composition of 60:40 P3HT:PCBM by wt% corresponds to a volume composition of nearly 2:1. Assuming a homogeneous distribution of pure domains, the spatial distribution of materials should be in close agreement with the

volume composition of the sample, i.e. any image should be composed ~33% PCBM by area. Note however that thin film blends of P3HT:PCBM rarely correspond to a two-phase system. Rather, in addition to pure, semi-crystalline phases of each material, a third phase of PCBM molecules mixed between amorphous P3HT chains is also believed to exist¹². To estimate the possible size of pure PCBM domains in our annealed blend sample, a binary representation of Figure 8.2(c) is produced with a threshold set to the peak position of the minor component, as shown in Figure 8.6(c). The binary image is shown in Figure 8.6(d), and permits a lower bound of the size of the pure PCBM clusters to be estimated, without including a significant fraction of the major contribution of the histogram data (which most probably corresponds to the remaining two phases within the sample). Particle analysis of the threshold image, assuming the entire range of possible circularities and discounting any particles which overlap with the edge of the image, suggests a distribution of slightly elongated PCBM domains, having an average major and minor axis length that is 12 ± 8 nm and 6 ± 3 nm respectively. The greater uncertainty in the length along the major axis is a reflection of the fact that PCBM domains form clusters, resulting in a nanoscale network within the blend instead of a distribution of isolated domains. Note that by setting a threshold at the peak of the minor histogram component, the estimate suggests that approximately 18% of the total area of the image corresponds to pure PCBM. Clearly the choice of a higher threshold would return a higher value of the PCBM domain size. Nevertheless, despite such uncertainty, the size of the PCBM clusters that can be extracted from the threshold particle analysis is in reasonable agreement with the spatial periodicity values determined earlier 20 ± 4 nm and results published elsewhere. I concede however that these values must be taken as an approximate estimate of the true size of PCBM domains within an annealed

P3HT:PCBM blend thin film, as it is not possible to determine with this technique alone the relative volume fractions of the pure material and mixed material phases.

Finally, to explore the influence of thermal annealing on the nanoscale morphology of P3HT:PCBM blend thin films, a blend sample that has been thermally annealed at 170°C for 10 minutes was measured using HeIM, with the results presented in Figure 8.7.

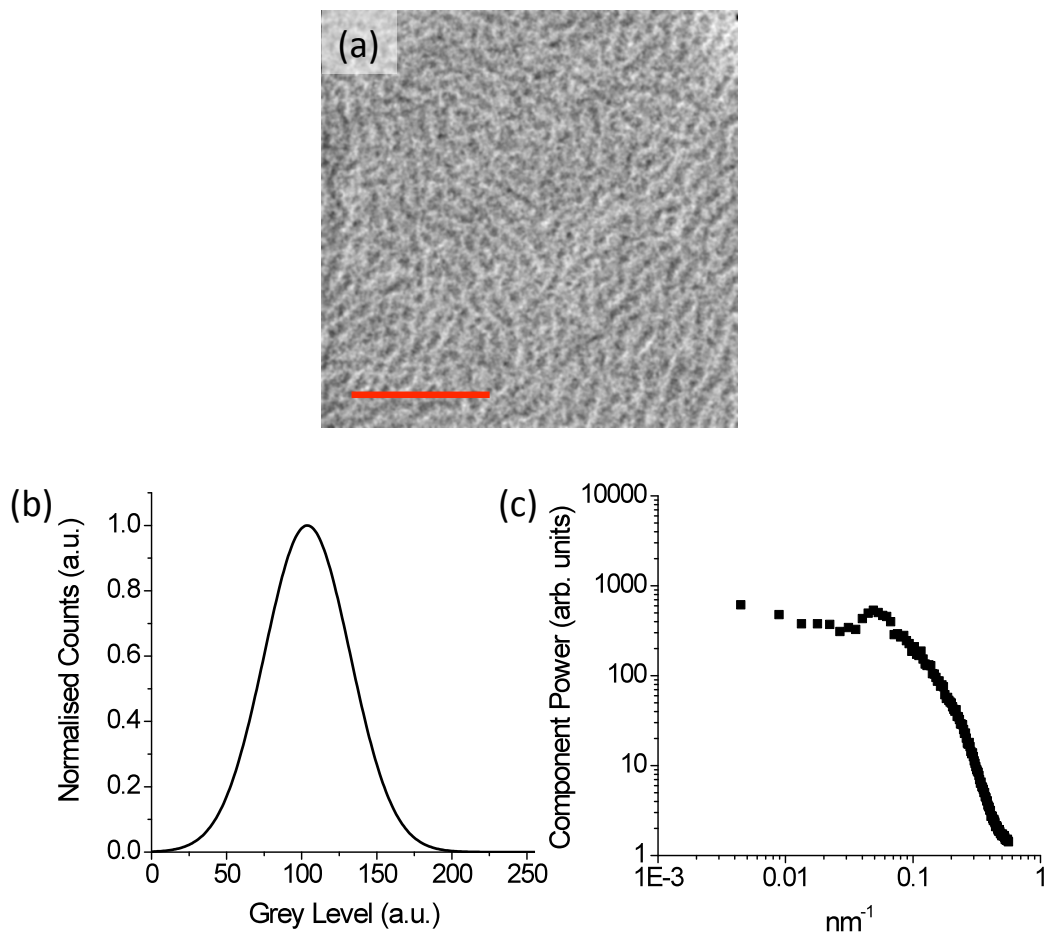


Figure 8.7: (a) HeIM image of a P3HT:PCBM blend thin film annealed at 170°C, where the scale bar represents 150 nm. (b) Grey level distribution and (c) power spectrum density of the image data.

As can be seen in Figure 8.7(a), the HeIM image again shows evidence of phase separation, with relatively bright and dark regions being present. The distribution of grey levels and the PSD of spatial frequencies are presented in Figure 8.7 parts (b) and (c) respectively. The PSD of the image data suggests a length scale for phase separation of 23 ± 3 nm, which is comparable to that observed in the sample annealed at 140°C . However these regions appear less pronounced, than the sample annealed at 140°C (see Figure 8.2(c)), suggesting a weaker degree of phase separation between P3HT and PCBM. This observation is supported by a histogram of grey levels that does not show a strong bimodal distribution. Scanning electron microscopy (SEM) images of a sample that had undergone an identical annealing treatment evidenced a large population of micron scale PCBM aggregates that are present on the surface of the blend thin film, as shown in Figure 8.8. Upon annealing an identical blend thin film at a temperature of 140°C no such structures are observed on the surface of the sample. I propose therefore that the presence of micron scale PCBM aggregates in the sample annealed at 170°C induces a depletion of PCBM across the bulk of the film. Consequently this effect limits the relative purity of the PCBM rich regions observed using HeIM at much finer length-scales and explains the relative weakness of phase-separation observed in Figure 8.7(a).

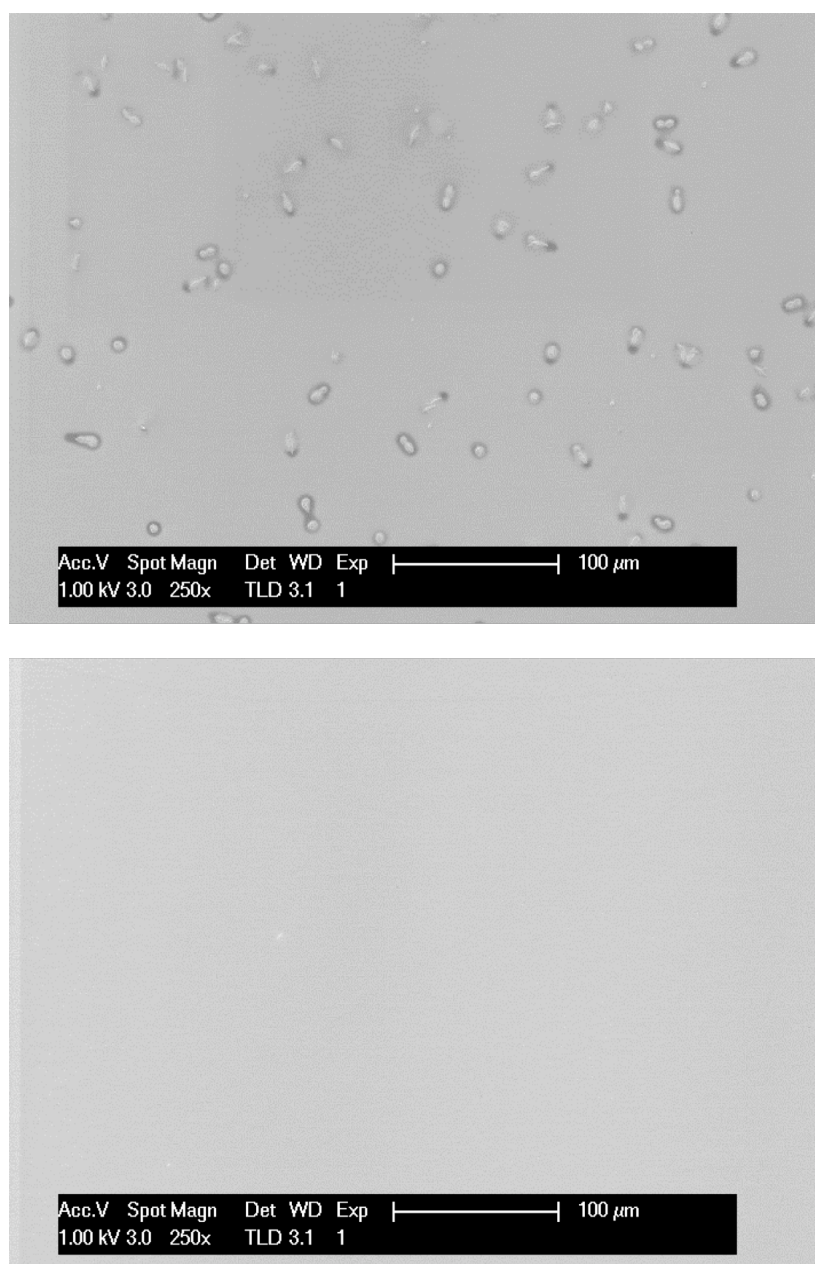


Figure 8.8: Scanning electron micrographs of P3HT:PCBM blend (60:40 wt%) thin films to have undergone thermal annealing at 170°C (top) and 140°C (bottom). For both samples the annealing time was 10 minutes, followed by a rapid cool to room temperature.

SECTION 8.4: CONCLUSIONS

The use of HeIM has been demonstrated to image the nanoscale chemical variations in thin film blends relevant to organic optoelectronic devices, using blend thin films of P3HT:PCBM as a test system. The results suggest variations in measured secondary electron emission (i.e. contrast) from the sample are intrinsic with effects resulting from the plasma treatment necessary to access the bulk structure being minimal. In a 60:40 (wt%) P3HT:PCBM blend thin film that has undergone post deposition annealing at 140°C, the spatial periodicity of the size of phase separated domains is estimated to be approximately 20 nm. Additional analysis of the grey-level distribution of the HeIM images suggest that PCBM domains are slightly elongated in shape and (in the films studied here) have a length of 12 ± 8 nm. These length-scales are commensurate with the diffusion length of excitons in P3HT and PCBM and therefore provide a partial explanation for why this annealing protocol can be used to optimise the power conversion efficiency of P3HT:PCBM OPV devices, as discussed. However the fact that in addition to phase separated P3HT and PCBM domains, the film will also be composed of amorphous regions that contain mixtures of P3HT and PCBM, means that the domain size calculations have to be taken with caution without additional supporting evidence. The results demonstrate however that HeIM is a promising complimentary technique for the characterisation of organic semiconductor thin films.

SECTION 8.5: REFERENCES

1. Pearson, A. J.; Boden, S. A.; Bagnall, D. M.; Lidzey, D. G.; Rodenburg, C., Imaging the Bulk Nanoscale Morphology of Organic Solar Cell Blends Using Helium Ion Microscopy. *Nano Letters* **2011**, *11* (10), 4275-4281.
2. Hoppe, H.; Niggemann, M.; Winder, C.; Kraut, J.; Hiesgen, R.; Hinsch, A.; Meissner, D.; Sariciftci, N. S., Nanoscale morphology of conjugated polymer/fullerene-based bulk-heterojunction solar cells. *Advanced Functional Materials* **2004**, *14* (10), 1005-1011.
3. Spadafora, E. J.; Demadrille, R.; Ratier, B.; Grevin, B., Imaging the Carrier Photogeneration in Nanoscale Phase Segregated Organic Heterojunctions by Kelvin Probe Force Microscopy. *Nano Letters* **2010**, *10* (9), 3337-3342.
4. Chua, L. L.; Dipankar, M.; Sivaramakrishnan, S.; Gao, X. Y.; Qi, D. C.; Wee, A. T. S.; Ho, P. K. H., Large damage threshold and small electron escape depth in X-ray absorption spectroscopy of a conjugated polymer thin film. *Langmuir* **2006**, *22* (20), 8587-8594.
5. Kishimoto, Y.; Ohshima, T.; Hashimoto, M.; Hayashi, T., A Consideration of Secondary-Electron Emission from Organic-Solids. *J Appl Polym Sci* **1990**, *39* (10), 2055-2066.
6. Tillack, A. F.; Noone, K. M.; MacLeod, B. A.; Nordlund, D.; Nagle, K. P.; Bradley, J. A.; Hau, S. K.; Yip, H.-L.; Jen, A. K. Y.; Seidler, G. T.; Ginger, D. S., Surface Characterization of Polythiophene:Fullerene Blends on Different Electrodes Using Near Edge X-ray Absorption Fine Structure. *ACS Applied Materials & Interfaces* **2011**, *3* (3), 726-732.

7. Parnell, A. J.; Dunbar, A. D.; Pearson, A. J.; Staniec, P. A.; Dennison, A. J.; Hamamatsu, H.; Skoda, M. W.; Lidzey, D. G.; Jones, R. A., Depletion of PCBM at the cathode interface in P3HT/PCBM thin films as quantified via neutron reflectivity measurements. *Advanced Materials* **2010**, *22* (22), 2444-7.
8. Drummy, L. F.; Davis, R. J.; Moore, D. L.; Durstock, M.; Vaia, R. A.; Hsu, J. W. P., Molecular-Scale and Nanoscale Morphology of P3HT:PCBM Bulk Heterojunctions: Energy-Filtered TEM and Low-Dose HREM. *Chemistry of Materials* **2011**, *23* (3), 907-912.
9. Moon, J. S.; Lee, J. K.; Cho, S. N.; Byun, J. Y.; Heeger, A. J., "Columnlike" Structure of the Cross-Sectional Morphology of Bulk Heterojunction Materials. *Nano Letters* **2009**, *9* (1), 230-234.
10. (a) Szarko, J. M.; Guo, J. C.; Liang, Y. Y.; Lee, B.; Rolczynski, B. S.; Strzalka, J.; Xu, T.; Loser, S.; Marks, T. J.; Yu, L. P.; Chen, L. X., When Function Follows Form: Effects of Donor Copolymer Side Chains on Film Morphology and BHJ Solar Cell Performance. *Advanced Materials* **2010**, *22* (48), 5468-5472; (b) Wu, W. R.; Jeng, U. S.; Su, C. J.; Wei, K. H.; Su, M. S.; Chiu, M. Y.; Chen, C. Y.; Su, W. B.; Su, C. H.; Su, A. C., Competition between Fullerene Aggregation and Poly(3-hexylthiophene) Crystallization upon Annealing of Bulk Heterojunction Solar Cells. *Acs Nano* **2011**, *5* (8), 6233-6243; (c) Parnell, A. J.; Cadby, A. J.; Mykhaylyk, O. O.; Dunbar, A. D. F.; Hopkinson, P. E.; Donald, A. M.; Jones, R. A. L., Nanoscale Phase Separation of P3HT PCBM Thick Films As Measured by Small-Angle X-ray Scattering. *Macromolecules* **2011**, *44* (16), 6503-6508.
11. Beal, R. M.; Stavrinadis, A.; Warner, J. H.; Smith, J. M.; Assender, H. E.; Watt, A. A. R., The Molecular Structure of Polymer-Fullerene Composite Solar Cells and Its Influence on Device Performance. *Macromolecules* **2010**, *43* (5), 2343-2348.

12. (a) Treat, N. D.; Brady, M. A.; Smith, G.; Toney, M. F.; Kramer, E. J.; Hawker, C. J.; Chabinyc, M. L., Interdiffusion of PCBM and P3HT Reveals Miscibility in a Photovoltaically Active Blend. *Advanced Energy Materials* **2011**, *1* (1), 82-89; (b) Collins, B. A.; Gann, E.; Guignard, L.; He, X.; McNeill, C. R.; Ade, H., Molecular Miscibility of Polymer, ïFullerene Blends. *The Journal of Physical Chemistry Letters* **2010**, *1* (21), 3160-3166.

CHAPTER 9: CONCLUSIONS

In this thesis, two polymer:PCBM blend systems for OPV applications have been studied in order to address how the photovoltaic properties of a blend are influenced by film processing conditions. The first system, P3HT:PCBM, is an example of a blend where both components have a relatively strong propensity to self-organise. In chapter 4, it was shown how the casting process of a P3HT:PCBM blend thin film can be monitored in-situ using SE or GIWAXS. Crystallisation of P3HT is found to take place only when the total solids concentration in the drying film exceeds a certain threshold. Crystallite growth is not a linear process, instead it develops over two stages of rapid and slow evolution as the film dries. By comparing data recorded from both techniques, the results support a link between the relative degree of crystallinity and the strength of the electronic transition in the P3HT absorption spectrum at 600 – 605 nm. Owing to the favourable photovoltaic characteristics of semi-crystalline P3HT, a degree of order is necessary in an OPV blend thin film for efficient device operation. From a device study on P3HT:PCBM blend films prepared using different solvents, as-cast films with apparently crystalline P3HT are limited in the extent to which further improvements in photovoltaic efficiency can be expected. The greatest improvements in the photovoltaic efficiency of P3HT:PCBM OPVs are found when an as-cast blend film is initially relatively amorphous (and thus shows little initial promise) and subsequently subject to solvent vapour annealing and thermal annealing protocols.

In chapters 5 and 6 the use of thermal annealing as a post film-deposition treatment on blend films has been studied. In chapter 5 the motivation was to study the process dynamically, using the same methodology as in chapter 4. Using SE, the evolution of film thickness and optical extinction coefficient of P3HT:PCBM blend films were measured, and it was found that effects relating to residual solvent loss, volume relaxation, phase separation and crystallisation could be observed. A key result from this chapter was the observation that residual solvent loss can be mediated by exceeding the glass transition of the blend. Secondly, a relatively slow cooling rate from an isothermal anneal above the blend T_g was found further improve the degree of electronic conjugation in P3HT; an effect that had a small positive impact on the efficiency of OPVs subject to isothermal annealing at 150°C.

In chapter 6, SE was used to determine the glass transition in P3HT:PCBM blend films which were prepared in an identical manner to those used in an OPV. This approach provided a rational framework with which to further understand the thermal annealing process, specifically the minimum temperature needed to alter the morphology of the blend films. In a thin film geometry, it was argued that as-cast blend films can exhibit two glass transitions, an observation tentatively ascribed to the existence of compositionally distinct amorphous phases. It was found that the higher temperature T_g closely correlates with the minimum annealing temperature necessary to improve the photovoltaic efficiency of an OPV. This reinforced the results of a previous study on this system using DMTA, in which it was found that this phase transition exists at a higher temperature in films with a greater wt% of PCBM. In addition, it was also demonstrated how the optimum annealing temperature for highest device efficiency was found to decrease with increased fullerene loading.

These trends may help to improve the design of annealing protocols for as yet unexplored OPV blends.

In chapter 7 the blend PCDTBT:PC₇₀BM was studied; a system that offers a number of advantages over blends of P3HT:PCBM toward the scale-up of OPVs for commercial applications. In contrast to P3HT, PCDTBT is largely amorphous. Its molecular structure also results in a greater relative solubility of fullerene molecules. These characteristics partly rationalise the design rules for maximizing the power conversion efficiency of this system, but do not exclude the use of post-treatment protocols to further improve device efficiency. Using a similar methodology to chapter 6, it was have shown that thermal annealing above the T_g of PCDTBT encourages greater disorder in the polymer; an effect correlated with a reduction in photovoltaic efficiency in blend OPVs. However, the enhanced thermal stability of the blend relative to P3HT:PCBM, highlights the promising nature of this system for the potential use in the scale-up OPVs. Furthermore the presence of PC₇₀BM in a blend film results in a strong quenching of photogenerated excitons on PCDTBT, in addition to a blue-shift in emission wavelength relative to fluorescence from a film of pure PCDTBT. This suggests a distinctly different donor phase in these films compared to blends of P3HT:PCBM, where relatively pure P3HT domains are thought to exist. These observations motivate future experiments using time resolved fluorescence spectroscopy, to compare polymer:fullerene blends where the polymer may be semi-crystalline or amorphous in nature.

A trend in this thesis has been to present new techniques and methods for the characterization of blend thin films (for example the use of GIWAXS or SE as dynamic probes). This has been shown explicitly in chapter 8, where I have evaluated HeIM for imaging P3HT:PCBM thin films. The ability to distinguish materials based upon their chemical structure suggests that HeIM is a promising technique to compliment other probes of film nanostructure, for example GIXRD. Data has also been included in this thesis from Neutron Reflectivity experiments that have probed the vertical composition of blend films. Although the technique has only been applied here to an optimised blend composition, there is clear potential to probe a broader range of parameter space to understand the influence of processing conditions on film structure, for example film composition, film thickness and the influence of the substrate.

APPENDIX

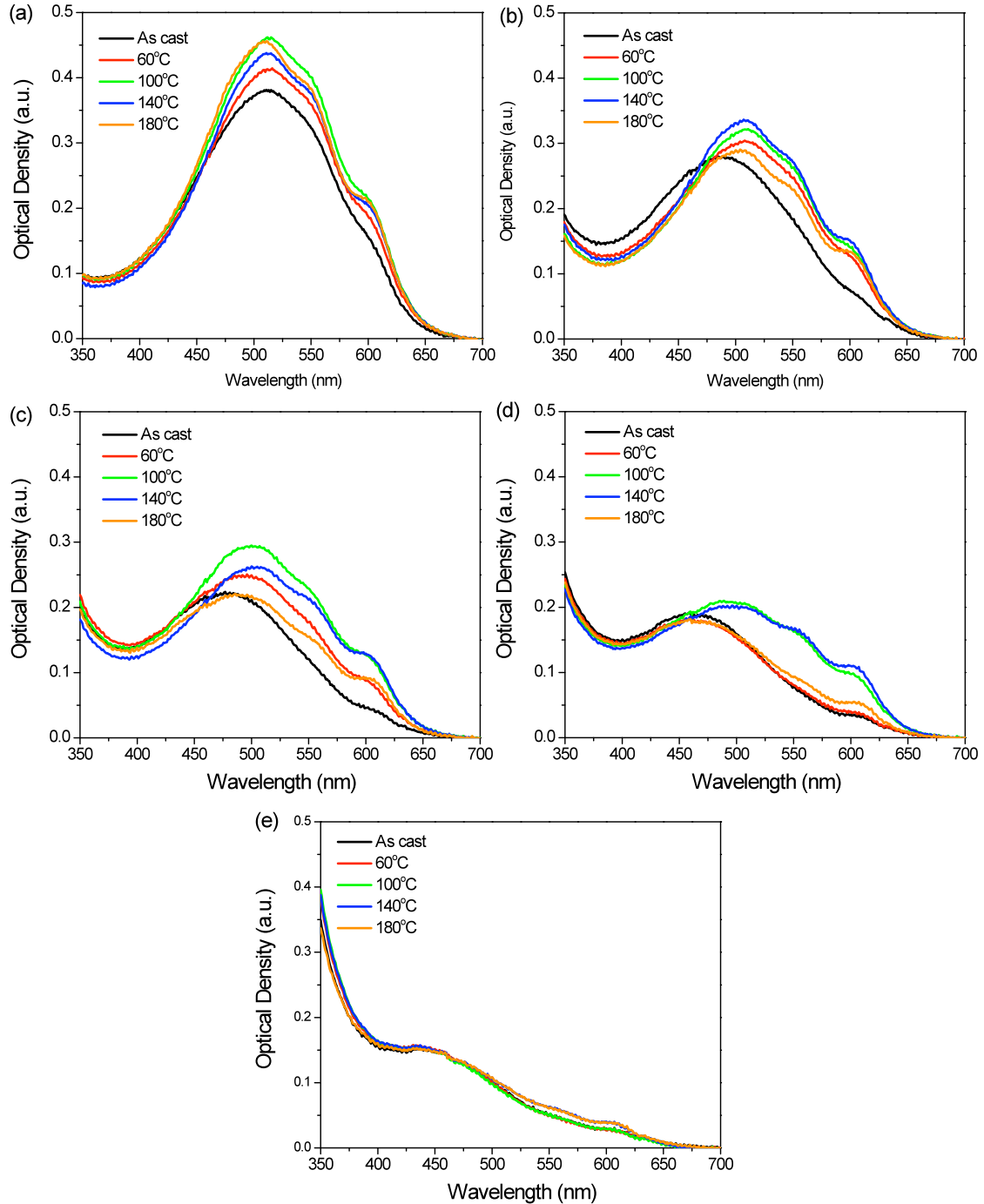


Figure A1: Optical Density spectra for a P3HT:PCBM(wt%) blend thin films after annealing. (a) 20wt% PCBM, (b) 40wt% PCBM, (c) 50wt% PCBM, (d) 60wt% PCBM and (e) 80wt% PCBM. For clarity, the thin films annealed at the other temperatures investigated in this work are not shown.

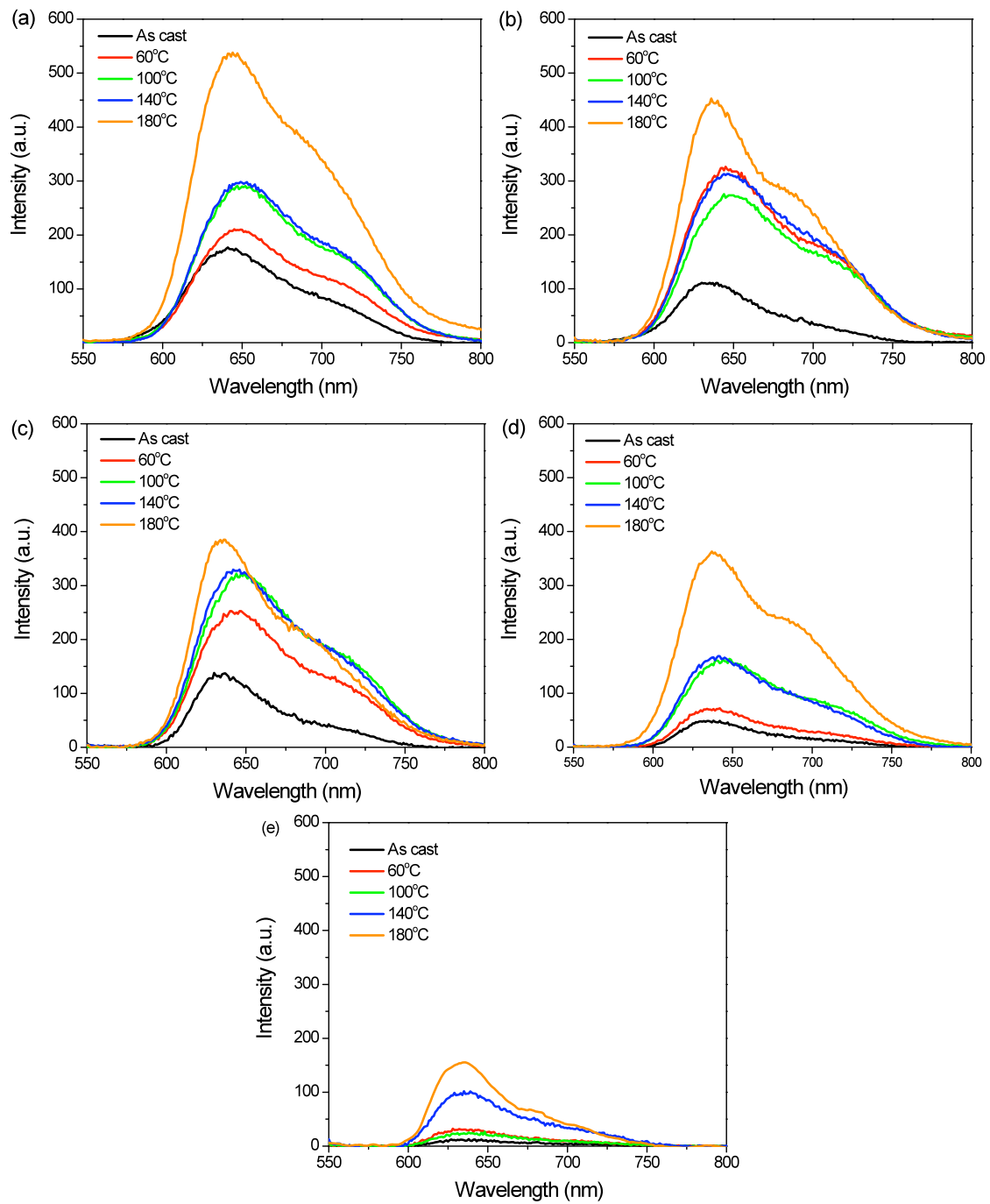


Figure A2: Photoluminescence spectra for a P3HT:PCBM(wt%) blend thin films after annealing. (a) 20wt% PCBM, (b) 40wt% PCBM, (c) 50wt% PCBM, (d) 60wt% PCBM and (e) 80wt% PCBM. For clarity, the thin films annealed at the other temperatures investigated in this work are not shown. Presented spectra have been corrected for sample absorption effects.